

DISSERTATION  
in  
PHYSICS  
for the degree  
DOCTOR RERUM NATURALIUM

---

THE CASCADE  $^{10}\text{B}$  THERMAL NEUTRON DETECTOR  
AND  
SOIL MOISTURE SENSING BY COSMIC-RAY NEUTRONS

---

---

ON THE PHASE FRONT OF NEUTRON DETECTION

---

by  
DIPL. PHYS.  
MARKUS OTTO KÖHLI

Supervisor  
PROF. DR. ULRICH SCHMIDT  
Nuclear and Neutron Physics Division  
Precision Experiments in Nuclear and Particle Physics  
Physikalisches Institut  
Department of Physics and Astronomy

ALMA MATER  
UNIVERSITAS RUPERTO-CAROLA HEIDELBERGENSIS



**Reviewers:**

Prof. Dr. Ulrich Schmidt (Physikalisches Institut, Heidelberg University)

Prof. Dr. Ulrich Uwer (Physikalisches Institut, Heidelberg University)

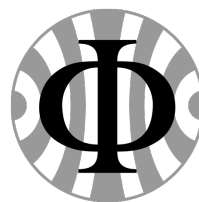
**Thesis Commitee:**

Prof. Dr. Matthias Bartelmann (Institute of Theoretical Astrophysics, Heidelberg University)

Prof. Dr. Ulrich Glasmacher (Institute of Earth Sciences, Heidelberg University)

---

Physikalisches Institut  
Fakultät für Physik und Astronomie  
Ruprecht-Karls-Universität  
Heidelberg  
Germany



Submission: March 25<sup>th</sup>, 2019  
Defense: June 5<sup>th</sup>, 2019



## Abstract

This work connects the three domains of experimental nuclear physics, computational physics and environmental physics centered around the neutron. The CASCADE thermal neutron detector is based on a combination of solid  $^{10}\text{B}$  coatings in several layers, GEMs as gas amplification stages, a microstructured readout, multichannel ASICs and FPGA hardware triggered data acquisition. The detailed analysis to improve the system in terms of time-of-flight resolution for Neutron Resonance Spin Echo Spectroscopy required for a simulation model of the detector. The limitations of existing codes led to the development of the Monte Carlo transport code URANOS, which fully integrates the detector components and features a voxel-based geometry definition. The simulation could then successfully be applied to precisely understand neutron transport within the frame of Cosmic-Ray Neutron Sensing. This novel and interdisciplinary method offers the possibility to non-invasively measure soil moisture on the hectare scale using neutrons of the environmental radiation. The endeavor of this work led to the development of the footprint weighting function, which describes the neutron density change by different hydrogen pools in the air-ground interface. Significant influences of the near-field topology around the sensor were predicted by this work, experimentally verified and correction methods were successfully tested.

## Zusammenfassung

Die vorliegende Arbeit befasst sich mit den drei Disziplinen der experimentellen Kernphysik, der computergestützten Physik und der Umweltphysik mit dem Neutron als Pivotelement. Der zur Messung von thermischen Neutronen entwickelte CASCADE Detektor besteht aus einer Kombination aus mehreren Ebenen von  $^{10}\text{B}$  Schichten, GEMs zur Gasverstärkung, eine mikrostrukturierte Auslese, Vielkanal-ASICs und einer FPGA-gestützten digitalen Datenverarbeitung. Die detaillierte Analyse um das System hinsichtlich seiner Flugzeitauflösung zur Anwendung in der Neutronen-Resonanz-Spin-Echo-Spektroskopie zu verbessern, erforderte ein Simulationsmodell des Detektors. Die Limitationen bestehender Softwarelösungen führten zur Entwicklung des Monte-Carlo Neutronentransportprogramms URANOS, welches alle wesentlichen Komponenten des Detektors abbildet und über eine voxelbasierte Geometrie-Engine verfügt. Die Simulation konnte erfolgreich angewendet werden um den Neutronentransport im Rahmen des Cosmic-Ray Neutron Sensings präzise zu verstehen. Diese neuartige und interdisziplinäre Methode bietet die Möglichkeit der nichtinvasiven Bodenfeuchtebestimmung auf der Hektarskala mit Hilfe von Neutronen aus der kosmischen Höhenstrahlung. Das Bestreben dieser Arbeit führte zu der Ausarbeitung der Flächengewichtungsfunktion, welche die Neutronendichteänderung hinsichtlich verschiedener Wasserstoffpools an der Luft-Boden-Schnittstelle beschreibt. Der maßgebliche Einfluss der Topologie des unmittelbaren Nahbereichs um den Sensor herum wurde in dieser Arbeit vorhergesagt, experimentell bestätigt und Korrekturmethode wurden untersucht.



An den Mistral





# CONTENTS

---

<b>I THE PHYSICS OF NEUTRONS AND CHARGED PARTICLES</b>	
<b>1 THE PHYSICS OF NEUTRONS</b>	<b>7</b>
1.1 About the neutron	7
1.1.1 Fundamentals	7
1.1.2 Historical overview	8
1.2 Neutron interactions	9
1.3 Units and definitions	10
1.3.1 Kinematics	10
1.3.2 Neutron flux	11
1.4 Neutron transport	13
1.4.1 Slowing down	14
1.4.2 Thermal neutrons	16
<b>2 THE PHYSICS OF ELECTROMAGNETIC INTERACTIONS</b>	<b>19</b>
2.1 Energy loss in the medium	19
2.1.1 Energy loss by ionization	19
2.1.2 Bremsstrahlung	20
2.1.3 Multiple scattering	21
2.2 Processes in gaseous media	21
2.2.1 Ionization	21
2.2.2 Energy resolution	22
2.2.3 Drift and diffusion	22
2.2.4 Gas gain	24
<b>II NEUTRON SOURCES</b>	
<b>3 NATURAL SOURCES: COSMIC NEUTRONS</b>	<b>27</b>
3.1 From supernovae to sea level	27
3.2 Analytical description of the cosmic ray neutron spectrum	32
<b>4 ARTIFICIAL HIGH FLUX SOURCES</b>	<b>33</b>
4.1 Overview of facilities	33
4.2 Research centers	35
4.3 The FRM II source	36
<b>III URANOS MONTE CARLO TRANSPORT CODE</b>	
<b>5 MODELING AND MONTE CARLO APPROACH</b>	<b>41</b>
5.1 Sampling	41
5.1.1 Random number generation	41
5.1.2 Sampling free path length	42
5.1.3 Sampling thermal velocity distributions	43
5.1.4 Evaluated Nuclear Data Files	44
5.2 Neutron Monte Carlo codes	47
5.2.1 General purpose packages	47
5.2.2 Specific neutron interaction codes	48
<b>6 URANOS</b>	<b>49</b>
6.1 URANOS concepts	50
6.2 Computational structure	52
6.2.1 Startup	52
6.2.2 Geometry	54

6.3	Sources and energy	56
6.3.1	The cosmic neutron source	57
6.3.2	General sources	57
6.4	Calculation scheme	58
6.4.1	Loop nodes	58
6.4.2	Tracking in finite geometry regions	59
6.4.3	Interaction channels	62
6.5	Detector configurations	65
6.5.1	Scoring options for CRNS	65
6.5.2	Neutron conversion evaluation for boron detectors	66
6.6	Basic performance examples	71
6.6.1	Diffusion length in water	71
6.6.2	Bonner Sphere evaluation	72
6.6.3	Cosmic spectrum evaluation	74
6.6.4	Performance benchmarks	76

#### IV COSMIC-RAY NEUTRON SENSING

7	INTRODUCTION	153
7.1	Soil moisture sensing techniques	153
7.2	Cosmic-Ray neutron sensing: the technique	154
7.2.1	The COSMOS sensor	154
7.2.2	Signal corrections	155
7.2.3	Soil moisture determination	156
8	UNDERSTANDING THE COSMIC-RAY NEUTRON DETECTOR	159
8.1	The detector model	159
8.2	The energy response function	161
8.3	Energy dependence	161
8.4	Detection probability within the case	162
8.5	Uncertainty analysis	163
8.6	Implications of the sensitivity analysis	163
9	FOOTPRINT INVESTIGATION	165
9.1	Footprint prelude	165
9.1.1	The cosmic-ray neutron spectrum assembly	165
9.1.2	Experimental verification	167
9.1.3	A closer look at the air-ground interface	169
9.1.4	Model setup	170
9.1.5	Soil moisture and above-ground neutron density	171
9.1.6	Tracking cosmic-ray neutrons in soil and air	174
9.2	Cosmic-Ray neutron transport analysis	176
9.2.1	Theoretical description by neutron transport equations	176
9.2.2	Footprint definition	178
9.2.3	Analytical characterization of the footprint	180
9.2.4	Analytical description of the penetration depth	181
9.2.5	Pressure dependency	182
9.2.6	Height dependency	183
9.3	Results	184
9.3.1	Intensity relation	185
9.3.2	Penetration depth scaling	185
9.3.3	Footprint	186
9.3.4	Where do neutrons come from?	188
9.3.5	Inhomogeneous terrain: roads	189

## V SUMMARY AND CONCLUSION

## VI APPENDIX

A	LITERATURE AND REFERENCES	199
A.1	Journal publications	199
A.2	Conference contributions	200
A.3	Bibliography	201
B	ADDENDUM	221
B.1	URANOS Monte Carlo simulation	222
B.1.1	Geometrical calculations	222
B.1.2	Elements, isotopes and reaction types	223
B.1.3	Material codepages	224
B.1.4	Parameters for generating the cosmic neutron spectrum	225
B.1.5	Simulation models of the CRNS detectors	226
B.1.6	Simulation of the neutron source room	227
B.2	Cosmic Ray Neutron Sensing	229
B.2.1	Modeling the footprint	229
B.2.2	Modeling the depth distribution	233
B.2.3	Uncertainty analysis of the CRNS transport problem	234
B.2.4	The road correction function	237
B.3	The URANOS graphical user interface	238
C	ACKNOWLEDGEMENTS	241



## P R E F A C E

---

The world of neutron detection is changing.

Much of what once was established technology has been discarded. For them now alternative ones have been presented. It began with production of tritium and peaked at the crisis of helium-3. Part of that was given to sciences for basic or applied research. Part for the industry, exploring oil deep in the rocks. And the largest part was given to homeland security, which above all demanded for it for the protection against hazards. After the stockpile was nearly exhausted, alerts on the future supply, which are especially critical to perspectives of the European Spallation Source led to developments of replacement technologies, most of them adapted from particle physics. The CASCADE thermal neutron detector is such a new generation system, which was designed specifically for the purposes of Neutron Spin Echo (NSE) spectroscopy. This method and its successors, Neutron Resonance Spin Echo (NRSE) and MIEZE (Modulation of Intensity by Zero Effort), demanded a highly granular and time-resolved detector to be operated efficiently at high rates. Contrary to triple-axis spectrometry or standard time-of-flight measurements, NRSE methods can achieve a high energy resolution using wavelength distributions of up to 20 % width. In a research field, where beam intensity in general is scarce due to limitations in the upscaling of the source, this technology offers in combination with a high-end detector the benefits which are looked for.

The CASCADE design is based on a combination of solid  $^{10}\text{B}$  coatings in several layers, GEMs as gas amplification stages, a microstructured readout, multichannel ASICs and FPGA hardware triggered data acquisition. The developments of this work successfully brought the CASCADE detector into operation at the Forschungs-Neutronenquelle Heinz Maier-Leibnitz at the instruments RESEDA and MIRA.

The world of neutron simulations is changing.

What once was the most demanding domain for high performance computing infrastructures can meanwhile be realized on a modern personal computer. Along with this loss of exclusivity the heritage of those system architectures can be abandoned: Fortran-based ASCII interfaces, which aim for criticality calculations. And set back the scope to focus on the neutron as a probe to the otherwise invisible and impenetrable. What makes neutrons to messengers for hidden orders in matter, makes them likewise hard to control and hard to describe. They are produced randomly, their momentum and their interaction appear to be stochastic. While being less abundant than photons or electrons but far from few-body systems in terms of numbers, the Monte Carlo simulation is the most suitable tool bridging the gap between thermodynamic flux models and analytical calculations. Neutrons also interact with volumes rather than with surfaces. Hence, the essential unit to comprehend and implement a geometry model is the voxel, a three-dimensional pixel.

The URANOS Monte Carlo simulation has been created based on this computational philosophy and has been realized in a collaboration with environmental physics as a valuable community tool.

The world of neutron applications is changing.

What began with the fission of uranium as source of energy and peaked with the development of a thermonuclear arsenal has been discarded. Large-scale research centers with most recently the European Spallation Source being built are shaping the research infrastructure to consequently stretch out the scope of fundamental research to other

science domains. Sources like the FRM II, ILL, SNS or ISIS are equipped with dozens of different experiments to investigate structures on the nanoscale from complex crystals to polymers or biomolecules, to image the magnetic ordering of superconductors or skyrmion lattices, to provide direct insights into storage cells or artifacts of cultural heritage and also to support the production of radio-isotopes and the medical treatment of cancer.

Since the recent initiative of Desilets and Zreda the method of Cosmic-Ray Neutron Sensing is gaining momentum. It allows to determine soil moisture on the hectare scale by the density of neutrons created in the atmosphere and reflected from the ground. It represents a technology to quantify non-invasively the most essential resource in food production: water. The effect that soil moisture influences the above-ground neutron flux had been known at least since the 1960s. Several attempts, however, failed to comprehensively understand the signal dependencies due to the lack of resources and interest to address the complexity of the transport problem. With the development of URANOS using computationally efficient the nowadays available off-the-shelf hardware, the model dependencies within the environmental system have been tracked down in extensive simulations. This work manages to unfold the intricacy of the cosmic-ray neutron transport, discovering the solution of a 50-year old problem and enabling CRNS to become an established hydrological method.

The world of neutrons is changing.

This is the phase front.

## INTRODUCTION

---

### COSMIC-RAY NEUTRON SENSING - THE CHALLENGE

From 2008 on the method of Cosmic-Ray Neutron Sensing rapidly developed. Its intriguing aspects are the possibility to measure soil moisture non-invasively at so-called intermediate scales, which cannot be accessed by other technologies, but especially match typical soil water correlation lengths. The method relies on the fact, that in collisions with hydrogen neutrons are stopped much more efficiently than with any other element due to the high cross section and the equal masses of the projectiles. High energetic cascades in the upper atmosphere generate neutrons, which finally tend to be reflected by dry soil or get moderated under wet conditions. A significant amount of data could be collected by deploying a network of standardized Cosmic-Ray Probes. Such are detectors sensitive to epithermal neutrons and similar in the buildup to Bonner Spheres with a one inch moderator around a proportional counter filled with a converter gas. However, it became clear that the data sets could not be fully understood and several attempts of analyzing the soil response using the Monte Carlo tool MCNPX failed. In 2013, the pioneers of the method, Desilets and Zreda, published a paper, in which they stated the footprint of the method would be approximately 30 ha and not significantly depend on the soil moisture content. As the data not at all showed evidence for such a relation, the interest rose for an accurate understanding of the system. The already existing code URANOS could be tailored to address the neutron transport problem in the air-ground interface, yet requiring some modifications on the scattering and scoring kernel and the implementation of additional processes like inelastic scattering. Initial calculations showed already promising results as the simulation could reproduce experimental data already better than the results presented by the authors of the mentioned paper. However, it turned out, that whereas some parts of the problem like the above-ground neutron intensity follow rather simple laws, others like the radial distribution revealed complex dependencies on different hydrogen pools. The sophisticated neutron transport problem, which indeed has remained unexplained for nearly 50 years, along with the possible fundamental impact of the method paved the ground for the necessity of a plain and conclusive analysis of the CRNS signal formation in this work.





Part I

THE PHYSICS OF NEUTRONS AND CHARGED  
PARTICLES



## THE PHYSICS OF NEUTRONS

### 1.1 | ABOUT THE NEUTRON

#### 1.1.1 | FUNDAMENTALS

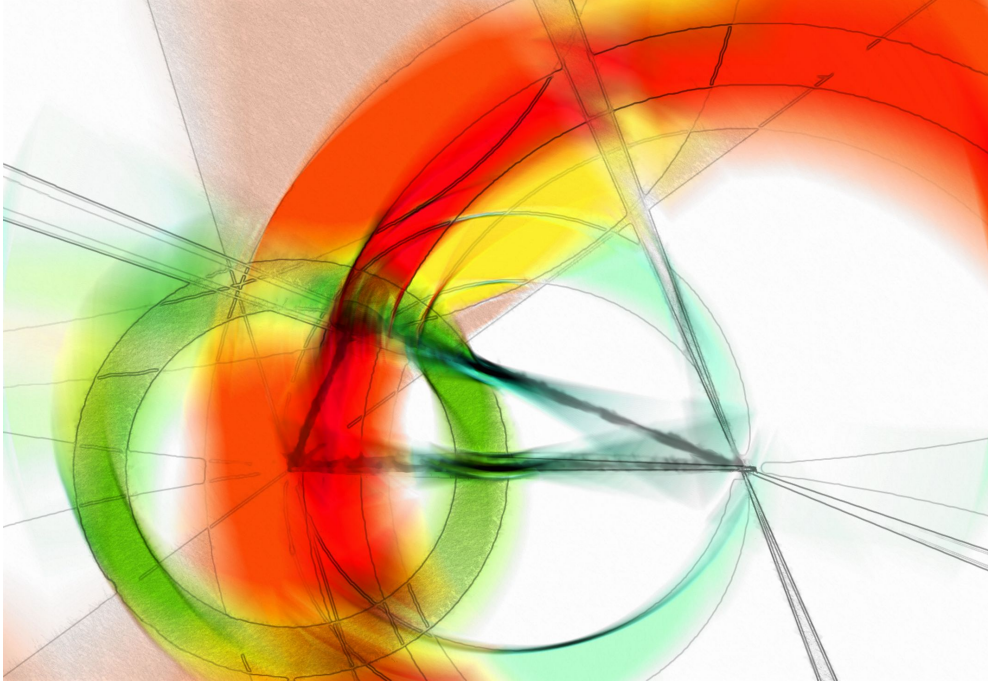
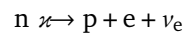


Figure 1: Artistic adaptation of measurement constraints on the CKM matrix [1, 2], inspired by results from [3]. The element  $V_{ud}$  [4], which is located in the lower left corner of the unitarity triangle, represents the transition probability for up and down type quarks. It is, among others [5], linked to nuclear beta decay and can be derived from neutron lifetime measurements.

Mass	$m = 1.0086649159(5) \text{ u}$ $m = 939.565413(6) \text{ MeV}$
Spin	$s = 1/2 \hbar / (2\pi)$
Lifetime	$\tau = 880.2(1.0) \text{ s}$
Mean-square charge radius	$\langle r_N^2 \rangle = -0.1161(22) \text{ fm}^2$
Charge	$q = -0.2(8) 10^{-21} e$
Magnetic moment	$\mu = -1.9130427(5) \mu_N$
Electric dipole moment	$d_N < 0.30 10^{-25} \text{ ecm (90 \% CL)}$

Table 1: Basic physical properties of the neutron [1].

The neutron has a net charge of zero and a spin of  $1/2 \hbar / (2\pi)$ . Its dipole moment is expected to be  $d_N \approx (10^{-37} - 10^{-40}) \text{ ecm}$  according to the standard model and measurements with nuclear bound states and sensitivities up to  $10^{-32} \text{ ecm}$  so far confirm this value [6]. Yet, they have a magnetic moment caused by small loop currents [7]. Its rest mass is slightly higher than the one of the proton, therefore it can decay weakly [4] into an electron and an electron antineutrino by



with a maximum kinetic energy transfer of 781.32 keV and a lifetime of approximately 15 min [8]. Thus there are nearly no free neutrons in the universe as the only stable condition available is the bound state in a nucleus.

The term 'Neutron' describing an electrically neutral entity of matter appeared as early as the end of the 20<sup>th</sup> century [9]. It was mainly discussed as an assumed bound state of the electron and its counterpart, which could for example make up the ether<sup>[a]</sup> and explain the results of experiments with cathode rays [10]. Though Rutherford<sup>[b]</sup> empirically discovered in 1911 [11] and theoretically described the nuclei of atoms, the neutron was proposed to be a particle comprised of a proton and an electron [12]<sup>[c]</sup>. Albeit in the late 1920s the newly developed quantum mechanics raised serious questions about such a model of nuclear electrons regarding the incorrectly predicted spin of this compound and the escape probability of the electron due to its large wavelength, the fundamental questions about nuclei stayed unanswered.

Experiments in 1930 by Bothe<sup>[d]</sup> [14] showed evidence of an at that time unknown type of reaction. In a test series of exposing light elements to alpha particles, beryllium showed the production of hard gamma rays, which originated as they supposed from nuclear excitations, producing furthermore a new type of neutral radiation. It could knock off protons with kinetic energies of several MeV from a hydrogen-rich material through several centimeters of lead. In 1932, based on the experiments of Curie<sup>[e]</sup> and Joliot<sup>[f]</sup> [15], it was quickly understood by kinetic considerations that this radiation is made of particles as heavy as the proton - in terms of comments reported first of Majorana<sup>[g]</sup> [16], then of Chadwick<sup>[h]</sup> [17]. Iwanenko<sup>[i]</sup>, who had theoretically worked on the problems of spin statistics before, realized that the neutron could also be a constituent of the nucleus [18], which was then confirmed [19] and celebrated as the birth of the neutron. This discovery was the key to understand the structure of atoms as composed of a shell and a small nucleus which itself is made up of protons and neutrons [20].

It is notable that in the first series of experimental trials boron has its first mention as a neutron absorber [21] and furthermore that the cosmic radiation soon after its discovery has been proposed to be partially made up of neutrons [22].

---

[a] to be noted: there was neither a common conception of the ether nor a consistent framework of theories. However, as in the case of the invention of the special relativity theory, this heritage can be considered an important foundation.

[b] Ernest RUTHERFORD, \*1871-†1937, New Zealand, United Kingdom of Great Britain.

[c] Rutherford himself, however, had already mentioned in 1904 in a sidenote of his book 'Radio-activity' [13] a proper description of the neutron appearing as a form of radiation.

[d] Walther Wilhelm Georg BOTHE, \*1891-†1957, German Empire.

[e] Irène JOLIOT-CURIE, \*1897-†1956, France.

[f] Frédéric JOLIOT-CURIE, \*1900-†1958, France.

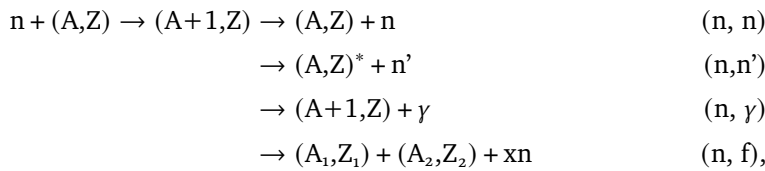
[g] Ettore MAJORANA, \*1906-?1938, Kingdom of Italy.

[h] Sir James CHADWICK, \*1891-†1974, United Kingdom of Great Britain.

[i] Дмитрий Дмитриевич Иваненко., \*1904-†1994, Russian Empire.

Neutron interactions are mainly governed by the nuclear force. Due to the small extension of nucleon potentials in the order of femtometers, the de Broglie<sup>[j]</sup> wavelength of the (slow) neutron instead defines the range for the interaction. Typical cross sections can be related to the geometric size of the nucleus and therefore path lengths in matter can easily be in the order of centimeters<sup>[k]</sup>. In this work the kinetic energy is limited to 1 GeV and neutrons are treated as a single particle, which means that they are neither subject to Coulomb<sup>[l]</sup> forces due to a net charge of zero nor to strong forces acting on the parton level in deep inelastic scattering and beyond. It is of importance, that, besides the participation of (strong) nuclear forces, interactions with nuclei are dominated by the probability of a neutron joining and forming a compound. For the production of such a state energy and momentum, including spin, relations have to be conserved. Furthermore, nuclear resonance widths are small compared to their separation, especially for low energies and light elements, and the transition probabilities depending on the small overlap integrals appear to be small.

Absorption and scattering are described in a similar interaction picture, except for the final state. For an absorption reaction the compound is produced as real state by requiring that its excitation energy is of the same magnitude as the binding energy of the neutron. Therefore, the nucleus also decays predominantly by emitting a neutron again - or by a photon in case that process is suppressed if the potential difference slightly exceeds the binding energy like for the capture of slow neutrons. This gives rise to the fact that typically the cross section for elastic scattering is the most dominant. Inelastic scattering leaves the target in an excited state and so differs from elastic scattering only by the recoil to the neutron minus the excitation energy. In the case of fission a heavy nucleus decays by deformation into fragments due to the energy gained from the additional neutron. The declaration scheme is the following (see also Fig. 2):



where (n,n) denotes elastic and (n,n') inelastic scattering off a nucleus with mass number A and atomic number Z.

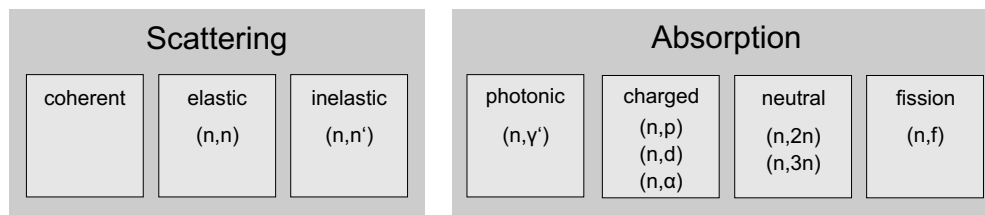


Figure 2: Types of neutron interactions and their classification.

Typical interactions neutrons undergo can be classified as either with one neutron in the initial and final state:

- Coherent Scattering describes the interference of incoming neutrons in terms of wave mechanics, therefore leading to distinct spatial distributions like in the

[j] Louis Victor Pierre Raymond, 7e duc DE BROGLIE, \*1892-†1987, France.

[k] Neutrons, when treated as a form of radiation, are often compared to x-rays in common literature. This is understood from an engineering point of view in terms of the mean free path in materials. Such a number can be derived for both types of interactions, but it cannot be compared in its quality as neither the interaction partners are the same nor the action principle. The only valid direct link can be shown for the case of diffraction.

[l] Charles-Augustin de COULOMB, \*1736-†1806, France.

case of Laue<sup>[m]</sup> diffraction. Originally coming from crystallography there is a distinction between elastic scattering, which refers to the prior mentioned process, and inelastic scattering, which refers to the additional excitation of phonons in the sample. This definition is ambiguous in its terminology<sup>[n]</sup> taking into account the further mentioned interaction types. Furthermore, quasi-elastic scattering applies to the case of (thermal) motion of the atoms giving rise to a significant contribution blurring the observed line shape.

- Elastic Scattering is the predominant mechanism of losing energy and can be understood as an elastic collision with energy and momentum conservation in the center-of-mass frame.
- Inelastic Scattering is an inelastic collision with the nucleus leaving it in an excited state. The allowed energy transfer is determined by the available nuclear excitation levels and therefore this process is mostly suppressed for kinetic energies below 1 MeV.

or such altering the target nucleus:

- Radiative Capture brings the nucleus into a A+1-state, which de-excites by emission of a photon.
- Charged Capture means that after absorbing a neutron the nucleus will decay by emitting either electrons, protons or larger compounds like helium ions, which in the case of light elements can be considered as fragments of the nucleus.
- Neutral Capture appears as an inelastic collision with similar initial and final states. Due to the absorption process and the following decay time constants and kinematics are different.
- Fission can occur for heavy elements absorbing a slow neutron if the final state energy budget is in favor of several fragments. Besides those, typically an energy dependent number of neutrons is emitted which are not any more needed to stabilize the smaller nuclei.
- Spallation is not limited incoming neutron. Any high energetic projectile with energies larger than approximately 100 MeV can induce the total breakup of a nucleus, which is described as a hadron shower.

## 1.3 | UNITS AND DEFINITIONS

### 1.3.1 | KINEMATICS

The possible reactions heavily depend on the energy of the neutron, which therefore is classified by its energy domain. The kinetic energy  $E$  of a neutron can be described in the non-relativistic limit by its wavelength  $\lambda$  derived from the de Broglie relationship

$$\lambda = \frac{h}{m_n v} \quad \kappa \rightarrow \quad E = \frac{1}{2} m_n v^2 = \frac{h^2}{2m_n \lambda^2}, \quad (1)$$

where  $h$  is the Planck<sup>[o]</sup> constant,  $v$  and  $m_n$  velocity and mass of the neutron. The neutron's energy regimes are described as follows.

[m] Max Theodor Felix VON LAUE, \*1879-†1960, German Confederation.

[n] This work will not refer to lattice structure analysis in particular and therefore will not make use of this naming scheme.

[o] Max Karl Ernst Ludwig PLANCK, \*1858-†1947, German Empire.

	kinetic energy [eV]	wavelength [Å]	velocity [m/s]
ultra cold	$< 3 \cdot 10^{-7}$	$< 520$	$< 7.5$
very cold	$3 \cdot 10^{-7} - 5 \cdot 10^{-5}$	$520 - 40$	$7.5 - 100$
cold	$5 \cdot 10^{-5} - 5 \cdot 10^{-3}$	$40 - 4$	$100 - 1000$
<b>thermal</b>	$5 \cdot 10^{-3} - 5 \cdot 10^{-1}$	$4 - 0.4$	$1000 - 10000$
thermal peak	$25.3 \cdot 10^{-3}$	$1.8$	$2200$
epithermal	$5 \cdot 10^{-1} - 10^3$	$0.4 - 0.01$	$10^3 - 4.4 \cdot 10^5$
intermediate	$10^3 - 10^5$	$0.01 - 0.001$	$4.4 \cdot 10^5 - 4.4 \cdot 10^6$
fast	$10^5 - 2 \cdot 10^7$	$0.001 - 6 \cdot 10^{-5}$	$4.4 \cdot 10^6 - 6.2 \cdot 10^7$
high energy	$> 2 \cdot 10^7$	$< 6 \cdot 10^{-5}$	$> 6.2 \cdot 10^7$

Table 2: Classification of neutrons by kinetic energy and corresponding interaction distances.

The most widely used definitions of the energy range, especially the thermal regime with the standard wavelength of  $1.8 \text{ \AA}$ , are derived from the temperature  $T$  of the medium the neutrons are interacting with. According to the kinetic theory of ideal gases the velocities  $v$  of the particles in the system can be described by a Maxwell<sup>[p]</sup>-Boltzmann<sup>[q]</sup> distribution<sup>[r]</sup>

$$f_M(v) = \sqrt{\left(\frac{m}{2\pi k_B T}\right)^3} 4\pi v^2 \exp\left(-\frac{mv^2}{2k_B T}\right), \quad (2)$$

where  $m$  is the particle's mass and  $k_B$  the Boltzmann constant. The typical speed of particles  $v_p$  at the maximum of this probability distribution can be related to the temperature by

$$\frac{df_M(v)}{dv} = 0 \quad x \rightarrow v_p = \sqrt{\frac{2k_B T}{m}} \quad \text{and} \quad T = \frac{mv_p^2}{2k_B} \quad (3)$$

and therefore, assuming the energy of neutrons can be described as  $k_B T$  in a statistical thermodynamical interpretation, temperature models are applied.

### 1.3.2 | NEUTRON FLUX

Let  $n(\vec{r}, \Omega, E)$  be the neutron density as a function of space  $\vec{r}$ , direction  $\Omega$ <sup>[s]</sup> and energy  $E$ . Then  $n(\vec{r}, \Omega, E) dV d\Omega dE$  is called the differential density of neutrons in a volume  $V$ . The total number density of neutrons at point  $\vec{r}$  is obtained by integration over all energies and angles

neutrons/cm<sup>3</sup>

$$n(\vec{r}) dV = \int_{4\pi} \int_0^\infty n(\vec{r}, \Omega, E) dV d\Omega dE. \quad (4)$$

The differential neutron flux, defined by  $F(\vec{r}, \Omega, E) d\Omega dE = n(\vec{r}, \Omega, E)v d\Omega dE$ , leads to the number of neutrons per second by taking into account the individual velocities  $v$

neutrons/cm<sup>2</sup>/s

[p] James Clerk MAXWELL, \*1831-†1879, Scotland.

[q] Ludwig Eduard BOLTZMANN, \*1844-†1906, Austrian Empire.

[r] Nota bene: for a single direction, say  $v_z$ , the distribution is  $f_M^{(1)}(v_z) = \sqrt{\frac{m}{2\pi k_B T}} \exp\left(-\frac{mv_z^2}{2k_B T}\right)$ , as by integrating over all directions the spherical volume element given by  $dV = v^2 \sin \vartheta d\vartheta d\phi dv$  is needed.

[s] Often the unit vector  $\Omega$  is expressed in spherical coordinates, especially for scattering interactions. Then it is composed of the mean direction angle  $\vartheta$  at the mean azimuthal angle  $\phi$ . For many special cases a canonical axis of the neutron beam direction is used.

and therefore represents the total path length covered by all neutrons. The quantity

$$\Phi(\vec{r}) = \int_{4\pi} F(\vec{r}, \Omega) d\Omega = n(\vec{r})\bar{v} \quad (5)$$

is called the total neutron flux and

$$\varphi(\vec{r}) = \int \Phi(\vec{r}) dt. \quad (6)$$

*neutrons/cm<sup>2</sup>* defines the neutron fluence. The terms fluence rate and flux are often used equivalently.

The integral neutron flux takes the whole ensemble of energies into account, as it assumes an equilibrium (thermalized) state of the system. Therefore, it is necessary to introduce the energy dependent flux quantity

$$\tilde{\phi}(\vec{r}, E) = \frac{d\Phi(\vec{r}, E)}{dE}, \quad (7)$$

which is called the neutron spectrum. However, most interaction processes lead to a partial energy transfer proportional to the initial energy. Therefore, the number of particles per logarithmic energy decrement ratio is a constant and the neutron spectrum can be depicted as an energy weighted spectrum

$$\phi(\vec{r}, E) = E \frac{d\Phi(\vec{r}, E)}{dE}. \quad (8)$$

Nota bene:

- In general the term 'flux' describes a directionality in the particle transport by an underlying vector field. In the field of neutron sciences it is a scalar quantity. However, the corresponding vector quantity, which is obtained by the gradient of the flux, is called a current  $J^{[t]}$ . This misalignment in terminology is of historic origin and has to be kept in mind.
- Additionally, as a consequence there is also a subtle difference between flux and fluence rate. As the latter is the time derivative of an integral quantity there is no information about directionality, contrary to the flux, which in the picture of neutron motion with gain and loss effects, still has a directional dependence.
- In the following the term 'neutron spectrum' will not specifically refer to (7), but rather be used as a synonym to the energy weighted neutron spectrum, which will be the standard representation.

---

[t] This quantity is not used in this work.



Neutron transport theory describes the flux through a medium by a Boltzmann equation in order to model the neutron field by conserving the total number of particles. This balance is kept by the four terms

- leakage out of the volume ①,
- loss due to absorption and scattering out of the volume or energy range ②,
- in-scattering from outside the volume and/or a different energy ③,
- gain by a source inside the volume ④.

$$\begin{aligned} \frac{\delta n(r, \Omega, E)}{\delta t} &= -v\Omega\nabla n(r, \Omega, E) && \textcircled{1} \\ &- (\Sigma_a(E) + \Sigma_s(E))vn(r, \Omega, E) && \textcircled{2} \\ &+ \int_{4\pi} \int_0^\infty \Sigma_s(\Omega' \rightarrow \Omega, E' \rightarrow E)vn(r, \Omega', E') d\Omega' dE' && \textcircled{3} \\ &S(r, \Omega, E). && \textcircled{4} \quad (9) \end{aligned}$$

with the macroscopic cross sections, which are also called linear attenuation coefficients, for absorption  $\Sigma_a$  and scattering  $\Sigma_s$ . Both are combined to the total macroscopic cross section  $1/cm$

$$\Sigma_t = \Sigma_a + \Sigma_s (+ \dots). \quad (10)$$

The macroscopic cross section  $\Sigma$  can be derived from the microscopic cross section<sup>[u]</sup>  $\sigma$ ,  $cm^2$  which defines the probability of interaction in a mass element divided by the product of interaction centers and the fluence:

$$\Sigma = \rho N_A \frac{\sigma}{M}, \quad (11)$$

where  $\rho$  denotes the density of a material with atoms of molar mass  $M$  and  $N_A$  the Avogadro<sup>[v]</sup> or also called Loschmidt<sup>[w]</sup> constant. On a microscopic level vice versa the microscopic cross section is described as

$$\sigma = \frac{1}{nl}. \quad (12)$$

It has the dimension of an area and is defined as the inverse of the product number density  $n = \rho N_A / M$  and the mean free path  $l$ , which by themselves describe the interaction opacity of the material<sup>[x]</sup>. The typical unit is the barn:  $1 \text{ b} = 10^{-28} \text{ m}^2$ .

As reactions can depend on parameters like the incoming energy or the (emission) angle, one introduces the differential cross section  $\frac{d\sigma}{d\Omega}$ .

The cross section can be composed like the attenuation coefficient of a sum energy dependent absorption  $\sigma_a$  and scattering  $\sigma_s$  contributions

$$\sigma(E) = \sigma_a(E) + \sigma_s(E) (+ \dots). \quad (13)$$

[u] In this work the term cross section will always refer to  $\sigma$ . For the macroscopic cross section the term attenuation coefficient is preferred.

[v] Lorenzo Romano Amedeo Carlo AVOGADRO, Conte di Quaregna e Cerreto, \*1776-†1856, Italian Empire.

[w] Johann Josef LOSCHMIDT, \*1821-†1895, Austrian Empire.

[x] To be noted: Macroscopic cross sections have the dimension of a reciprocal length, microscopic cross sections the dimension of an area.

In case of a compound with weight fractions  $w_i$  of  $n$  elements the weighted sum of cross sections is evaluated:

$$\Sigma_t = \rho N_A \sum_{i=1}^n w_i \frac{\sigma_i}{M_i}. \quad (14)$$

Therefore, the occurrence probability of an interaction type at an element can be calculated by the relative fraction of the cross sections  $\sigma_i/\sigma$  and is called reaction rate.

In a homogeneous medium the mean free path<sup>[y]</sup> between two interactions is

$$l(E) = \frac{1}{\Sigma_t(E)}. \quad (15)$$

Therefore, in case of dominant absorption, the abundance of neutrons follows the Beer<sup>[z]</sup>-Lambert<sup>[aa]</sup> attenuation law.

The probability distribution function can be denoted as

$$p(l, E) dl = \Sigma_t(E) \exp(-\Sigma_t(E)l) dl. \quad (16)$$

Integrating over a finite length leads to the number of neutrons  $N$  in a distance  $L$

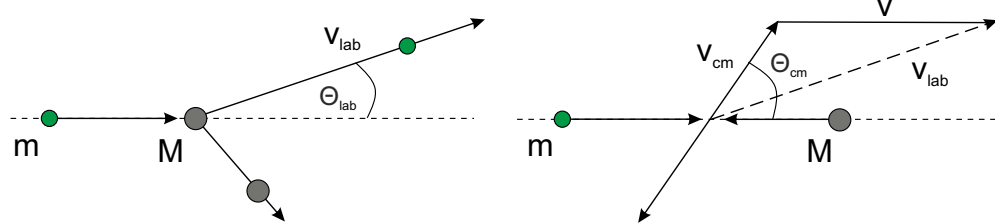
$$\frac{N(L, E)}{N_0} = \int_0^L p(l, E) dl = \int_0^L \Sigma_t(E) \exp(-\Sigma_t(E)l) dl = 1 - \exp(-\Sigma_t(E)L). \quad (17)$$

Therefore, the percentage of neutrons traversing a thin layer of thickness  $d$  without interaction is  $\exp(-\Sigma_t(E)d)$ .

#### 1.4.1 | SLOWING DOWN

Neutrons of typical energies up to 200 MeV can be treated non-relativistically for collisions by energy and momentum conservation. As for elastic interactions only the relative rather than the absolute masses are required, the neutron can be considered of mass 1 and a nucleus of mass  $A$ . It is furthermore convenient to transform the collision

Figure 3: Kinematics of an elastic collision in the laboratory (left) and center-of-mass frame (right).



from the laboratory (lab) into the center-of-mass (cm) frame as in such the angular distribution is isotropic. The velocity of the cm system with velocities of the neutron  $v$  and the nucleus  $V$  can be calculated as follows

$$v_{cm} = \frac{1}{1+A} (v_1 + AV_1) = \frac{v_1}{1+A} \quad (18)$$

[y] also called the distance to the next collision.

[z] August BEER, \*1825-†1863, German Empire.

[aa] Johann Heinrich LAMBERT, \*1728-†1777, France.

and within the cm system the velocities of the particles are

$$v_c = v_1 - v_{\text{cm}} = \frac{A}{A+1}v_1 \quad (19)$$

$$V_c = -v_{\text{cm}} = -\frac{1}{A+1}v_1 \quad (20)$$

The energy of the neutron in the cm system  $E_c$  can be derived as well according to

$$E_c = \frac{1}{2}v_c^2 + \frac{1}{2}AV_c^2 = \frac{A}{A+1} \frac{1}{2}v_1^2 = \frac{A}{A+1}E_1. \quad (21)$$

In the cm frame the absolute values of velocities of the particles do not change, so  $v'_c = v_c$ . The angles can be calculated as

$$\tan \vartheta_1 = \frac{v'_c \sin \vartheta_c}{v_{\text{cm}} + v'_c \cos \vartheta_c} = \frac{\sin \vartheta_c}{\frac{1}{A} + \cos \vartheta_c} \quad (22)$$

or by trigonometric transformation

$$\cos(\pi - \vartheta_c) = \frac{(v'_c)^2 + (v_{\text{cm}})^2 - (v_1')^2}{(A+1)^2}. \quad (23)$$

Using (18) the kinetic energy after scattering can be derived as

$$\frac{\frac{1}{2}(v_1')^2}{\frac{1}{2}(v_1)^2} = \frac{E'_1}{E_1} = \frac{A^2 + 1 + 2A \cos \vartheta_c}{(A+1)^2} = \frac{(1+\alpha) + (1-\alpha) \cos \vartheta_c}{2} \quad (24)$$

with

$$\alpha = \left( \frac{A-1}{A+1} \right)^2. \quad (25)$$

From (24) it can be derived that the angle in the cm system, and therefore also in the lab frame, is correlated to the energy loss. This is maximized for

- $\vartheta_c = \pi$ , a central 'head-on' collision, and
- $A = 1$ , a hydrogen nucleus consisting only of a proton of equal mass.

Under these conditions the kinetic energy of a neutron can be transferred to the target nucleus in one single collision. Typically the energy loss depends on the impact parameter, which can be assumed as randomly distributed, so following the standard representation for elastic scattering the probability for a neutron to scatter<sup>[ab]</sup> into a cone of  $2\pi \sin \vartheta_c d\vartheta_c$  around  $\vartheta_c$  from energy  $E$  to a range of energies  $dE'$  around  $E'$  is

$$\sigma_s(E)P(E \rightarrow E') dE' = -\sigma_{\text{cm}}(E, \vartheta_c) 2\pi \sin \vartheta_c d\vartheta_c. \quad (26)$$

Using (24) yields

$$P(E \rightarrow E') = \frac{4\pi - \sigma_{\text{cm}}(E, \vartheta_c)}{(1-\alpha)E\sigma_s(E)} \quad \text{for } \alpha E \leq E' \leq E \quad (27)$$

or zero otherwise. The scattering can mostly be considered isotropic (except for high energies, see also sec. 6.4.3.1) in angle, so  $\sigma_{\text{cm}}(E, \vartheta_c) = \sigma_s(E)/4\pi$  leading to

$$\sigma_s(E \rightarrow E') = \sigma_s(E)P(E \rightarrow E') = \frac{\sigma_s(E)}{(1-\alpha)E} \quad \text{for } \alpha E \leq E' \leq E. \quad (28)$$

[ab] an increase in the scattering angle means a larger energy loss.

With the probability for each angle and consecutively for the corresponding energy transfer, the average energy loss can be calculated as

$$\overline{\Delta E} = E - \int_{\alpha E}^E dE' E' P(E \rightarrow E') = \frac{1}{2}(1 - \alpha)E \quad (29)$$

and the important quantity of the average logarithmic energy loss as

$$\xi = \int_{\alpha E}^E dE' \ln\left(\frac{E}{E'}\right) P(E \rightarrow E') \quad (30)$$

$$= 1 + \frac{\alpha}{1 - \alpha} \ln \alpha = 1 - \frac{(A - 1)^2}{2A} \ln\left(\frac{A + 1}{A - 1}\right). \quad (31)$$

The logarithm represents the fact, that by elastic collisions not an absolute quantity but always a fraction of the kinetic energy is lost. Therefore, the moderation power of a material is defined as the average number of collisions from an initial energy, say  $E_o = 10$  MeV, until entering the thermal regime at 1 eV

$$n_{\text{col}} = \frac{u}{\xi} = \frac{\ln(E_o/E)}{\xi}, \quad (32)$$

where the lethargy  $u$  is defined as

$$u = \ln\left(\frac{E_o}{E}\right). \quad (33)$$

So  $\xi$  represents the average change in lethargy per collision. According to (31) this property of a material decreases with nuclide mass and the slowing down requires more collisions.

#### 1.4.2 | THERMAL NEUTRONS

In the previous chapter 1.4.1 it has been assumed that the target nucleus is at rest. Yet, as soon as the kinetic energy of the neutron is

- comparable to the mean kinetic energy of atoms in a gas phase or
- in the order of the binding energy or excitation of modes of additional degrees of freedom in molecules

the process has to be extended. As thermal neutron transport has been worked out elaborately by many authors, this chapter summarized the key ideas. For further reading and derivation chapter 10 of [23] is recommended. In the case of gases the velocity distribution of the particles is known - it is assumed that atoms follow a Maxwell-Boltzmann distribution (2), which allows for a straightforward treatment of the interaction. This effect of thermal motion on the scattering process is discussed in detail in sec. 5.1.3.

For a relative velocity between target and neutron before the collision of  $v_r = \|\vec{v} - \vec{V}\| = \sqrt{v^2 + V^2 - 2vV \cos \vartheta}$ , the velocity in the laboratory system after the collision will be

$$v' = \sqrt{v_{\text{cm}}^2 + \left(\frac{A}{A+1}\right)^2 v_r^2 + 2v_{\text{cm}} \frac{A}{A+1} v_r \cos \vartheta} \quad (34)$$

and the largest and smallest velocities are

$$v_{\max} = v_{\text{cm}} + \frac{A}{A+1} v_r \quad \text{and} \quad v_{\min} = v_{\text{cm}} - \frac{A}{A+1} v_r. \quad (35)$$

The total cross section as to the third term of (9) is obtained by integrating the microscopic cross section

$$d\sigma(v', V, \cos \vartheta) = \frac{1}{2} \frac{v_r}{v'} \sigma_s^{\text{free}} p(V) dV d\cos \vartheta, \quad (36)$$

which relates the free elastic scattering cross section  $\sigma_s^{\text{free}}$  to the probability of interacting with a target nucleus having a velocity distribution  $p(V)$ . So the probability of a velocity change of the neutron  $v \rightarrow v'$  is represented by the modified cross section

$$\sigma(v \rightarrow v') dv = \frac{1}{2} \frac{1}{v'} \int_0^\infty dV \int_{-1}^1 v_r d\cos \vartheta \sigma_s^{\text{free}} p(V) g(v' \rightarrow v) dv \quad (37)$$

with

$$g(v' \rightarrow v) = \begin{cases} 0, & v < v_{\min} \text{ OR } v > v_{\max} \\ \frac{2v}{v_{\max}^2 - v_{\min}^2}, & v_{\min} < v < v_{\max}. \end{cases} \quad (38)$$

By integrating (36) over  $V$  and  $\cos \vartheta$  and substituting velocities by energy the total cross section can be obtained<sup>[ac]</sup>:

$$\sigma_s(E') = \sigma_s^{\text{free}} \frac{1}{\beta^2 \sqrt{\pi}} \Psi(\beta), \quad (39)$$

where  $\beta^2 = AE'/k_B T$  and

$$\Psi(\beta) = \beta \exp(-\beta^2) + (2\beta^2 + 1) \frac{\sqrt{\pi}}{2} \text{erf}(\beta). \quad (40)$$

The  $\Psi(\beta)$  function is originating from kinetic gas theory, therefore using  $\beta$  as a variable. For  $\beta < 1$  the cross section can roughly be approximated by  $\sigma_s(E') \sim \sigma_s^{\text{free}} / \sqrt{E'} \sim \sigma_s^{\text{free}} / v$ .

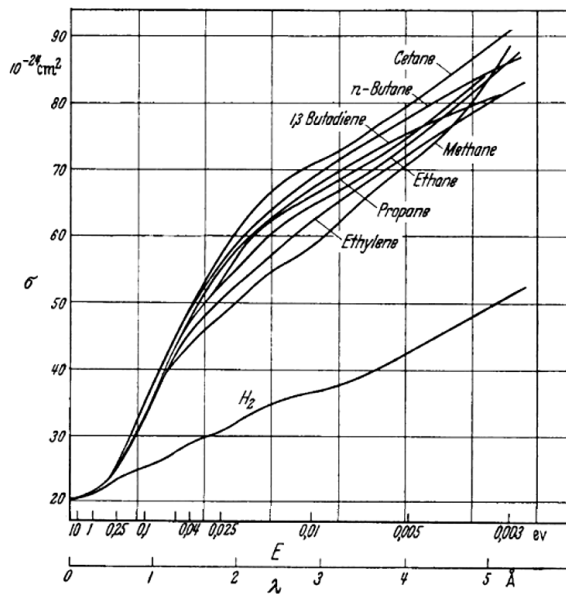


Figure 4: Cross section of protons bound in various hydrocarbons ( $C_X H_Y$ ) and in hydrogen gas  $H_2$ , modified from [24]. For  $H_2$  the deviation from the unbound cross section is small.  $H_2O$  scales nearly as the presented curve for cetane ( $C_{16}H_{34}$ ). In complex molecules the interaction probability around thermal energies and below strongly depends on the binding type and the associated degrees of freedom.

[ac] As  $\sigma_s(E') = \int_0^\infty \sigma_s(E' \rightarrow E) dE$ .



## THE PHYSICS OF ELECTROMAGNETIC INTERACTIONS

All charged particles dissipate energy while crossing a medium. Depending on the particle species and the material, different processes play a role. The most important processes are in ascending order of the energy range: Electron excitation of atoms, ionization, Bremsstrahlung, pair production, nuclear excitation and following the relativistic processes like Čerenkov and transition radiation, which are not relevant here.

### 2.1 | ENERGY LOSS IN THE MEDIUM

#### 2.1.1 | ENERGY LOSS BY IONIZATION

The Bethe<sup>[a]</sup>-Bloch<sup>[b]</sup> equation describes the energy loss  $dE$  per length  $dx$  in a medium:

$$-\frac{dE}{dx} = 2\pi N_A r_e^2 m_e c^2 \rho \frac{Z}{A} \frac{z^2}{\beta^2} \left( \ln \left( \frac{2m_e \gamma^2 c^2 \beta^2 W_{\max}}{I^2} \right) - 2\beta^2 - \delta - 2\frac{C}{Z} \right). \quad (41)$$

$r_e$	classical electron radius	$\rho$	weight density
$m_e$	electron mass	$z$	projectile charge
$N_A$	Avogadro number	$\beta$	$= v/c$ projectile velocity
$I$	mean excitation potential	$\gamma$	$= (1 - \beta^2)^{-1/2}$
$Z$	charge number	$\delta$	density correction
$A$	atomic weight	$C$	shell correction

The scaling constants are often combined to

$$\kappa = 2\pi N_A r_e^2 m_e c^2 \frac{Z}{A} \frac{1}{\beta^2}. \quad (42)$$

The maximum energy transfer  $W_{\max}$  possible in a single head-on collision for an incident projectile of mass  $m_A$  can be calculated as follows:

$$W_{\max} = \frac{2m_e c^2 \beta^2 \gamma^2}{1 + 2\frac{m_e}{m_A} \sqrt{1 + \beta^2 \gamma^2} + \frac{m_e^2}{m_A}}. \quad (43)$$

For  $m_A \gg m_e$  the energy transfer can be approximated as

$$W_{\max} \approx 2m_e c^2 \beta^2 \gamma^2. \quad (44)$$

The density factor is a correction for projectiles of high energies and describes the polarization of the atoms in the medium along the path, whereas the shell correction accounts for projectiles which have a velocity in the order of or smaller than those of

[a] Hans Albrecht BETHE, \*1906-†2005, German Empire.

[b] Felix BLOCH, \*1905-†1983, Switzerland.

the electrons orbiting the target atoms. These empirical constants are mainly important for relativistic particles. The mean excitation potential can be approximated by

$$I \approx 16 \text{ eV} \cdot Z^{0.9}. \quad (45)$$

Fig. 5 shows exemplarily the energy deposition for the counting gas argon and the neutron converter boron.

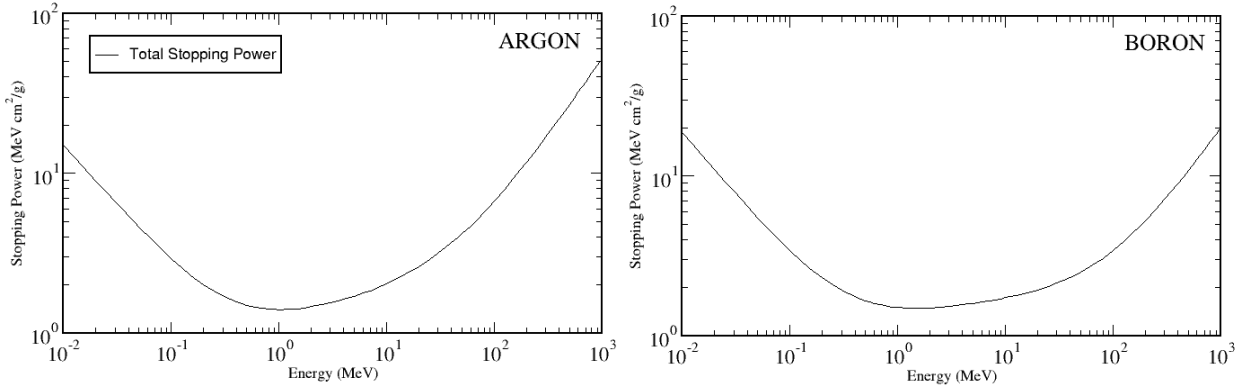


Figure 5: Energy loss  $dE$  per unit length  $dx$  for electrons in argon (NTP) and boron, modified from [25].

The process of energy loss is of statistical nature and (41) describes the mean energy deposition. Its energy dependent function, as shown in Fig. 5, is specific to the particle species and the medium. Yet, the Bethe-Bloch equation has a minimum for all particles which satisfy  $\beta\gamma \approx 3$ . Such are called **minimum ionizing particles (MIP)**. The ionization density increases towards small momenta, which is equivalent to a projectile losing a large fraction of the kinetic energy on a close range at the end of its trajectory. This is called the Bragg<sup>[c]</sup> peak.

The Bethe-Bloch-equation provides a good approximation for heavy particles, e.g. ions. For light particles like electrons Bremsstrahlung has to be taken into account as well.

### 2.1.2 | BREMSSTRAHLUNG

Particles in a medium are deflected by the Coulomb potential of the host atoms. Accelerated particles radiate photons, therefore this effect has to be considered in addition to ionization. For (light) particles with large kinetic energy this effect is called Bremsstrahlung, see also the Feynman<sup>[d]</sup> graph of Fig 6 and for electrons one can derive for the mean energy loss

$$-\frac{dE}{dx} \approx 4\alpha N_A r_e^2 z^2 E \frac{Z^2}{A} \ln\left(\frac{183}{Z^{1/3}}\right). \quad (46)$$

The coupling constant  $\alpha = e^2/(2ch\epsilon_0)$  with the electric charge  $e$  and the electric field constant  $\epsilon_0$ , represents the strength of the Coulomb interaction. Compared to ionization (41) there is an explicit energy dependence in (46), which makes this effect not only dependent on the surrounding medium, but also the momentum of the particle.

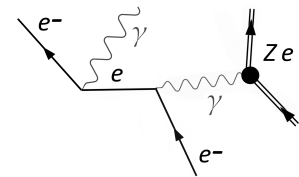


Figure 6: First order Feynman graph for Bremsstrahlung.

[c] William Lawrence BRAGG, \*1890-†1971, Australia.

[d] Richard Phillips FEYNMAN, \*1918-†1988, USA.



Therefore one can summarize all constants of (46) under the term radiation length  $X_0$  and write

$$-\frac{dE}{dx} = \frac{E}{X_0}. \quad (47)$$

As the differential equation (47) can be solved by an exponential function of the form  $\exp(-x/X_0)$ , the radiation length defines the distance in which the energy of the particle drops to  $1/e$  of its original value.

### 2.1.3 | MULTIPLE SCATTERING

Multiple Scattering describes a manifold of Coulomb deflections. Such are mostly weak, which means that the trajectory of a particle keeps its general direction. A simplified model [26] of this statistical process leads to a particle of momentum  $p$  after a distance  $x$  to a gaussian<sup>[e]</sup> distribution of the scattering angles around the original axis of the trajectory  $\vartheta = 0$  with a width of

$$\sigma_\vartheta = \frac{13.6 \text{ MeV}}{\beta c p} \sqrt{\frac{x}{X_0}}. \quad (48)$$

## 2.2 | PROCESSES IN GASEOUS MEDIA

Particles can be detected via their ionization track in a gas. In the case of neutrons a so-called converter captures the uncharged particle by nuclear absorption and then either fragments or releases excitation or binding energy in form of radiation. This chapter summarizes the relevant physics starting from the ionization track to the transport and gas gain, which is necessary to detect the electron cloud.

### 2.2.1 | IONIZATION

In a small finite volume the Landau<sup>[f]</sup> distribution [27] describes the possible energy transfer to a host atom. The Landau distribution approximates the energy loss for thin absorbers, which do not significantly reduce the overall momentum of the propagating particle. Due to the large amount of collisions with small momentum transfer, the Landau distribution has a maximum at low values and has a positive skew towards higher values, which model the unlikely hard collisions with large energy transfers. It takes the following form

$$f(\Lambda) = \frac{1}{\sqrt{2\pi}} e^{-\frac{1}{2}(\Lambda + e^{-\Lambda})}, \quad (49)$$

whereas for a length element  $x$  of an absorber of a density  $\rho$  the quantity  $\Lambda = (\Delta E - \Delta E_p)/(\kappa \rho x)$  describes the deviation of a possible energy loss  $\Delta E$  from its most probable value  $\Delta E_p$ , which is the maximum of the Landau distribution. It can be calculated by [26]

$$E_p = \kappa \rho x \left[ \ln \left( \frac{2m_e c^2 \beta^2}{I(1-\beta^2)} \right) + \ln \left( \frac{\kappa \rho x}{I} \right) + 0.2 - \beta^2 - \delta \left( \frac{\beta}{1-\beta^2} \right) \right]. \quad (50)$$

[e] Johann Carl Friedrich GAUSS, \*1777-†1855, Holy Roman Empire.

[f] Лев Давидович Ландау, \*1908-†1968, Russian Empire.

### 2.2.2 | ENERGY RESOLUTION

The energy deposition for the primary ionization along the trajectory of a charged particle can be described by a Poisson<sup>[g]</sup> distribution. However in case the full energy is transferred, there is no variance and hence there is a correlation between the single processes of energy deposition. Then, the usage of Poisson statistics is inadequate. Instead of a variance of  $\sigma^2 = N$  for  $N$  ionization processes, a material- and energy-dependent correction term  $F$ , with  $F \leq 1$ , is introduced, which is called Fano<sup>[h]</sup> factor [28]:

$$\sigma^2 = FN. \quad (51)$$

Due to the variance reduction the resolution is improved by a factor of  $\sqrt{F}$ . As an example for an electron with a kinetic energy  $O(1 \text{ keV})$  in argon a Fano factor of  $F = 0.16$  can be calculated [29].

The factual mean energy  $W$  for creating an electron-ion pair indeed is higher than the minimum ionization potential  $I$  as additional energy is transferred to vibration modes or kinematics. For gases the approximation  $W \approx (2-3) I$  [27] can be assumed.

Using  $W$  allows to calculate the number of free charge carriers  $n_t$  released by a process of energy  $\Delta E$  by  $n_t = \Delta E/W$ . For a gas mixture of different fractions  $c_i$  one has

$$n_t = \Delta E \sum_i \frac{c_i}{W_i}. \quad (52)$$

This is the total number of primary electrons due to primary and secondary ionization for a given energy deposition  $\Delta E$ .

### 2.2.3 | DRIFT AND DIFFUSION

Charged particles in a gas can be accelerated under the influence of electromagnetic fields. Yet, decelerating effects like scattering off atoms in the medium lead to a balance in the forces and so to an on average constant propagation. This is called drifting. The non-deterministic and omnidirectional transport by interaction with other particles at rather thermal energies is called diffusion.

Under the influence of an electric  $\vec{E}$  and a magnetic field  $\vec{B}$  the trajectory of a charged particle is described by the Langevin<sup>[i]</sup> equation. The solution for constant drift velocities  $\vec{v}_D$  can be denoted as

$$\vec{v}_D = e \frac{\tau}{m} \frac{1}{1 + \omega^2 \tau^2} \left[ \vec{E} + \omega \tau \frac{\vec{E} \times \vec{B}}{|\vec{B}|} + \omega^2 \tau^2 \frac{(\vec{E} \cdot \vec{B})}{|\vec{B}|^2} \cdot \vec{B} \right]. \quad (53)$$

$\omega$  denotes the cyclotron frequency with  $\omega = (e/m)|\vec{B}|$ .  $\tau$  represents the mean time between two collisions with atoms of the medium.

For electrons in the absence of a magnetic field (53) can be simplified to

$$\vec{v}_D = \frac{e}{m} \tau \vec{E}. \quad (54)$$

[g] Siméon Denis POISSON, \*1781-†1840, France.

[h] Ugo FANO, \*1912-†2001, Italian Empire.

[i] Paul LANGEVIN, \*1872-†1946, France.

For ions a different parametrization of the motion of the particles is used, as for such the ratio of the actual pressure  $p$  to standard pressure  $p_o$  has a strong influence on the kinetics. Therefore one uses

$$\vec{v}_D = \mu \vec{E} \frac{p_o}{p}. \quad (55)$$

Due to their higher mass, the drifting of ions is typically three order of magnitude lower than the drift velocity of electrons and therefore is characterized by the mobility  $\mu$ .

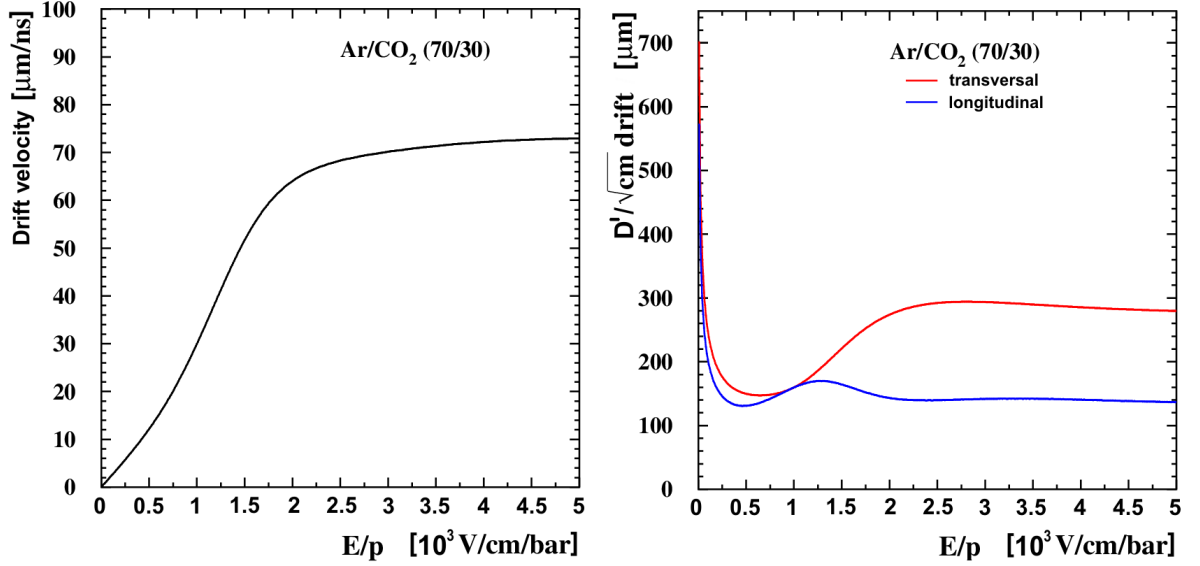


Figure 7: Drift velocity for electrons in argon:CO<sub>2</sub> as a function of electric field strength and pressure (left) and (right) simulations of the diffusion constant  $D'$  for the same functional dependencies and gas mixture, modified from [30].

Without fields or gradients, charged particles like neutrons are carrying out a random-walk propagation by collision with other atoms. This diffusion leads to a gaussian-shaped spatial particle density of the form

$$\rho(r, t) = \left( \frac{1}{\sqrt{4\pi Dt}} \right)^3 \exp\left(-\frac{r^2}{4Dt}\right). \quad (56)$$

Its width  $\sigma_D = \sqrt{2Dt}$  increases over time  $t$ .  $D$  denotes a diffusion constant and depends on the medium, but also on the electric field strength. Therefore, charge diffusion is typically modeled using a longitudinal and a transverse component with respect to the field. If the transverse axis with the diffusion constant  $D_T$  is denoted by the spatial coordinates  $x$  and  $y$  and the longitudinal axis coordinate with  $D_L$  is described by  $z$ , one writes

$$\rho(r, t) = \left( \frac{1}{\sqrt{4\pi D_T t}} \right)^2 \left( \frac{1}{\sqrt{4\pi D_L t}} \right) \exp\left(-\frac{x^2 + y^2}{4D_T t} - \frac{(z - v_D t)^2}{4D_L t}\right). \quad (57)$$

The diffusion constant can be defined as a function of drift velocity  $D' = \sqrt{2D/v_D}$ , yielding

$$\sigma_{D'} = D' \sqrt{x}. \quad (58)$$

#### 2.2.4 | GAS GAIN

Typically the primary ionization is often not sufficient to generate a signal large enough for detection. A gaseous medium allows for applying the principle of charge multiplication. If electrons, e.g. the primary charge carriers, can be accelerated to energies, which are high enough to ionize other atoms of the medium, an avalanche effect occurs, which can increase the number of electrons by a factor of  $10^4$  to  $10^6$ . The so created additional electron-ion pairs  $dN$  for an actual number of electrons  $N$  satisfies the differential equation

$$dN = \alpha(r)N(r)dr, \quad (59)$$

whereas  $\alpha$  denotes the Townsend<sup>[j]</sup> coefficient, which depends on the track length coordinate  $r$  as far as the electric field strength changes. The solution for an initial number of final charge carriers  $N_{\text{total}}$  for an initial number of charge carriers  $N_0$  takes the following form

$$N_{\text{total}} = N_0 \exp\left(\int_{r_1}^{r_2} \alpha(r)dr\right). \quad (60)$$

The ratio  $G = N_{\text{total}}/N_0$  is called gas gain.

---

[j] Sir John Sealy Edward TOWNSEND, \*1868-†1957, Ireland.

Part II

NEUTRON SOURCES



## NATURAL SOURCES: COSMIC NEUTRONS

Due to the limited lifetime of approximately 15 minutes, all free neutrons, naturally abundant or from laboratory sources, originate from an ongoing production mechanism - either the interaction of cosmic radiation with the atmosphere and the soil or natural radioactivity, which can sometimes even scale up to so-called „natural reactors“ [31]. The following section presents a short overview about how cosmic neutrons are created. A good summary can also be found in [32].

### 3.1 | FROM SUPERNOVAE TO SEA LEVEL

Cosmic rays consist mostly of ionized atomic nuclei with protons being the most abundant species with a contribution of 90% of the total measured particle number, followed by helium ions. The fraction of electrons, positrons, antiprotons, gamma rays and neutrinos can be considered negligible. The net charge of the cosmic radiation is highly positive with protons being overrepresented with a ratio of 10:1 [33]. While in general sources, also on galactic scales [34], are charge conserving, the reason for this asymmetry is inverse Compton scattering [35]. This effect leads to especially light charged particles like electrons losing energy by interactions with photons of the cosmic microwave background and therefore being slowed down more efficiently than their hadronic partners.

The cosmic ray spectrum, see Fig. 8, extends from the MeV regime up to ZeV energies with meanwhile more than a dozen candidates of extremely high energies of  $\sim 10^{20}$  eV, observed by the Fly’s Eye detector [36].

The lowest part of the spectrum is result of the solar wind,  $\sim 10^{36}$  particles per second released from the plasma of the Sun’s corona and especially from solar flares [38]. Particles in the range of 1 GeV to  $\sim 100$  TeV mostly come from supernova remnants. Therefore, the cosmic ray flux has one component of extragalactic origin overlaid by the charge emission from the Sun with a separation of low energy and high energy contributions. Theoretical considerations of the diffusive shock acceleration<sup>[a]</sup> needed to achieve such energies [39] as well as observations from the Crab nebula<sup>1</sup> can heavily support these generators, see also the overview in [40]. For higher energies the production and transport mechanisms change around the points, which in the log-log plot

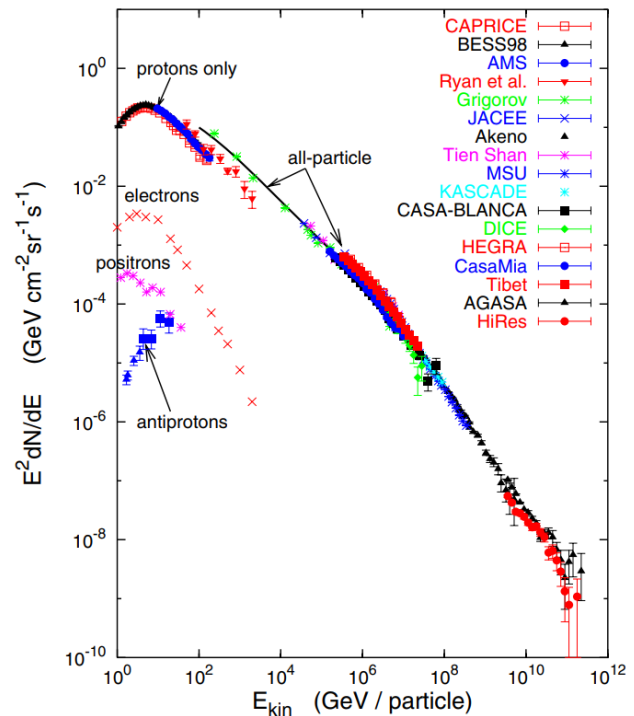


Figure 8: Energies and rates of the primary cosmic ray particles before entering the atmosphere from various experiments [37].

[a] thermal cosmic rays passing a dense matter distribution in which the strong magnetic gradient leads to an acceleration by turning several times around the ‘shock’ region.

<sup>1</sup> NGC 1952

are called 'knee' and 'ankle'. Below the knee at around  $3 \cdot 10^{17}$  eV the spectrum follows approximately an  $E^{-2.7}$  power law and beyond  $\sim E^{-3.1}$ . Between these two points the typical composition changes towards more massive particles. Yet, for the identified sources, like a reacceleration in the galactic wind termination shock [41] or neutron stars [42], the theoretical understanding has not condensed to an accepted answer. For Ultra High Energy Cosmic Rays the discussion around the proposed sources is even broader, see also the overview in [43]. The direct observation of such phenomena is suppressed by the diffusive motion of particles on the galactic scale in the interstellar medium. This leads to an almost isotropic and time-independent flux of cosmic radiation - which is then influenced by the solar activity.

As the former experiences an energy decrement from the outward gradient of the Sun's particle flux this leads to an inverse proportional relation between solar activity and cosmic ray flux. There are several mechanisms influencing the measured particle density with the most prominent being the 11-year intensity modulation cycle, which is due to the underlying solar magnetic field activity of the 22-year Hale<sup>[b]</sup> cycle, see also Fig. 9. Yet, modulations with larger period lengths can also be identified [44] as well as shorter cycles like 27 days caused by the Sun's rotation around its own axis [45]. Due to their low energy these particles have a minor direct influence on the Earth except in case of large plasma releases, called coronal mass ejections. These can cause a sudden increase in the cosmic ray intensity, which are measured in the form of ground level enhancements [46]. However, these events can also lead to an increase in the activity of the Sun and consequently a drop in cosmic ray intensity, called Forbush<sup>[c]</sup> decrease [47].

The cosmic ray intensity measured on Earth varies on average around 20 %, occasionally reaching 30 %. During periods of high solar activity, coronal mass ejections can appear several times per day and in periods of low solar activity once in a few days. Since the beginning of the global recordings by neutron monitors, see sec. ??, around 70 ground level enhancements and 40 Forbush decreases have been observed.

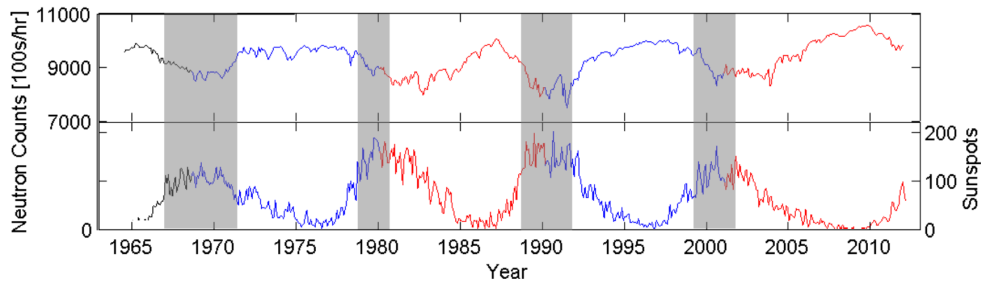


Figure 9: Time series of the cosmic ray flux (top) measured by the neutron monitor McMurdo, Antarctica, and the number of sun spots (below). Colors indicate the heliospheric magnetic field in near-Earth space and gray boxes the polarity change thereof, modified from [48].

The magnetic field of the Earth exhibits in the first order a dipole structure tilted by 11 degrees with respect to the rotation axis. It deflects and reflects charged particles entering from the outside, especially the low energetic part from the solar wind. The Lorentz<sup>[d]</sup> force leads to an equation of motion for a particle with charge  $q$ , mass  $m$  and velocity  $\vec{v}$  in the presence of a magnetic field  $\vec{B}(r)$

$$\frac{d\vec{v}}{dt} = \frac{q}{\gamma m} \vec{v} \times \vec{B}(r), \quad (61)$$

[b] George Ellery HALE, \*1868-†1938, USA

[c] Scott Ellsworth FORBUSH, \*1904-†1984, USA

[d] Hendrik Antoon LORENTZ, \*1853-†1928, Netherlands



where  $\gamma = 1/\sqrt{1 - v^2/c^2}$  is the Lorentz factor. Depending on the inclination angle to the field a particle spirals around the field lines with a radius  $r$

$$q\vec{v} \times \vec{B}(r) = \gamma m \frac{\vec{v}^2}{r}, \quad (62)$$

which can be written in scalar form as

$$Br = \frac{\gamma mv}{q} = \frac{p}{q} \quad (63)$$

using the momentum  $p$  of the particle. The quantity  $Br$  is called magnetic rigidity and can be expressed in units of  $\text{GV}^{[e]}$ , momentum per unit charge. Depending on incoming direction and destination location there is an energy threshold for which the particle flux due to magnetic shielding on the ground becomes zero. This parameter, the cutoff rigidity  $r_c$ , characterizes the local deflection capability of a magnetic field. On the Earth the cutoff rigidity ranges from a few hundred MV at the poles, where particles are barely deflected due to being orthogonally incident with respect to the field, to nearly 18 GV around the equator, where the Lorentz force is maximized. The cutoff rigidity

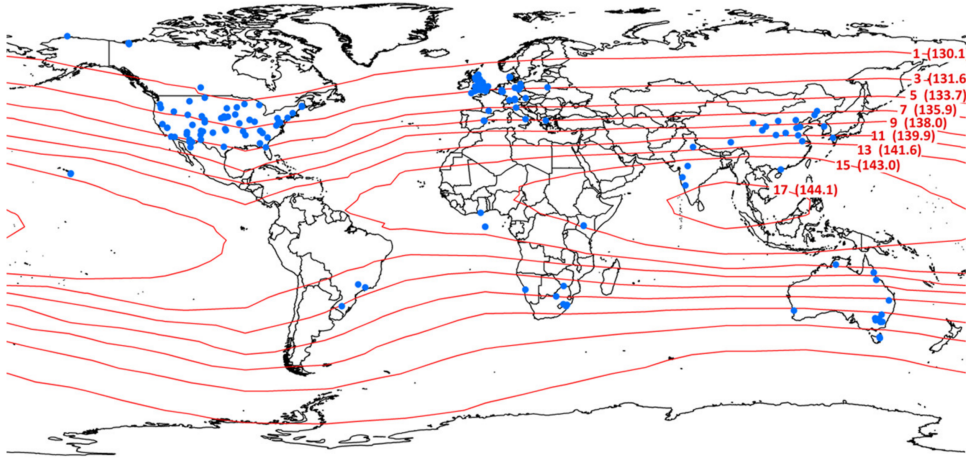


Figure 10: Vertical cut-off rigidity contours of the International Geomagnetic Reference Field calculated for the year 2010 (red countour lines with rigidities in GV and atmospheric attenuation lengths) based on the work of [49], and locations of all cosmic ray stations (blue) listed in 2017. The slow changes of the magnetic field of the Earth also alters the cutoff rigidity regions. [50]

can be used to estimate [51] the particle flux  $N$  entering the atmosphere by

$$N(r_c) = N_o \left( 1 - \exp\left(-\alpha r_c^{-k}\right) \right), \quad (64)$$

with the parameters  $\alpha \approx 9.02$  and  $k \approx 1.05 \text{ GV}^{-1}$ .

Those highly energetic particles then create air showers of elementary particles by interacting with molecules of the atmosphere, that can be regarded as a large calorimeter<sup>[f]</sup> [53]. Such showers consist partly or entirely of an electromagnetic and an hadronic cascade, which both feature a different phenomenology, see also Fig. 11. Electromagnetic showers, governed by the Coulomb interaction, consist of leptons and photons with electron and muon bremsstrahlung together with pair production being the dominant processes. This leads to the cascade being dependent mainly on the charge number  $Z$  - for example the electromagnetic radiation length  $X_o$  can roughly be estimated [54] by

$$X_o \approx \frac{710 \text{ MeV}}{Z + 0.92}, \quad (65)$$

[e] conveniently leaving the  $1/c$  factor.

[f] the term refers to an energy measurement - as the principles compare well to detectors for calorimetry in nuclear and particle physics, see also [52]. Yet, although its integral, height dependent, properties can be well estimated, its variation in time is a large uncertainty.

which leads to  $X_0^{\text{air}} \approx 86 \text{ MeV} \approx 37 \text{ g/cm}^2 \approx 310 \text{ m}$  for dry air [55]. One can compare this value to the total scale height of the atmosphere  $h_o \approx 8400 \text{ m}$ , known from the barometric pressure formula. Therefore, a substantial part of a shower will be absorbed in the atmosphere. Hadronic showers are mainly created in collisions of protons with other nuclei. They can also be comprised of an electromagnetic component<sup>[g]</sup> but mainly consist of particles, which interact by the strong force, like pions. Unlike cascades governed by Coulomb force, hadronic interactions at high energies are much more complicated in their event topology and less well understood on the level of perturbative quantum chromo dynamics. However, a number of phenomenological models have been developed. For energies in the lower GeV range soft multiparticle production with small transverse momenta are the dominant feature [56]. At higher energies of the projectile additionally hard scattering of partons carrying only a small fraction of the momentum of the hadron can take place, which leads to smaller sub-cascades [57]. For much higher energies gluon interactions finally start to compete with quark-quark interactions.

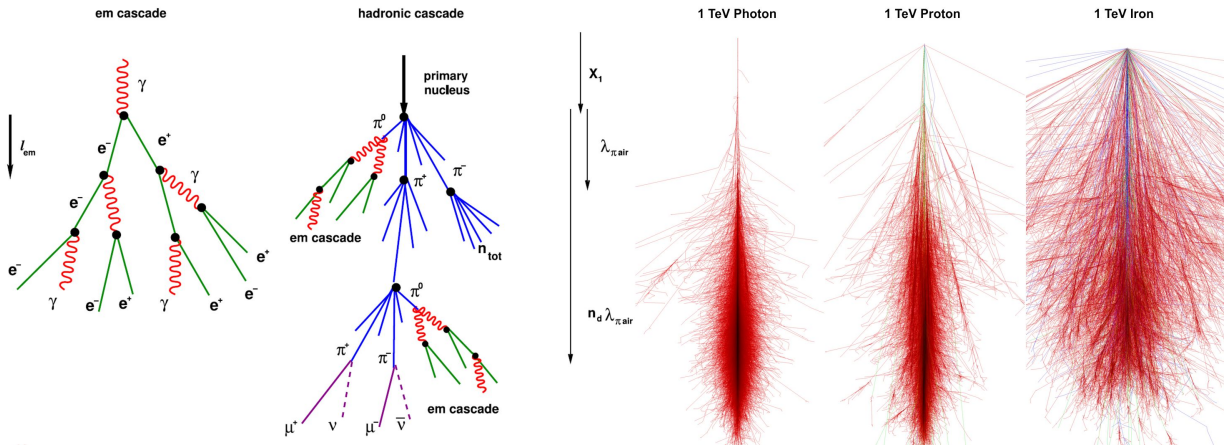


Figure 11: Air showers: (left) Feynman graph representation of electromagnetic and hadronic cascades with the typical interaction lengths [58] and (right) simulation of leptons, hadrons and heavy nuclei in the atmosphere (same scale) [59].

The hadronic interaction length  $\lambda_{\text{had}}$  therefore mainly depends on the atomic number  $A$  and their corresponding cross section.

$$\lambda_{\text{had}} \sim \frac{1}{n\sigma_o A^{2/3}}, \quad (66)$$

whereas the mean cross section  $\sigma_o$  being specific for the particle species. For example the interaction length for GeV pions in air amounts to  $\lambda_{\text{had}}^{\pi} \approx 120 \text{ g/cm}^2$  [55]. This leads to hadronic showers in general developing faster due to the multiplicity and lasting longer as the hadronic cross section is smaller than in the electromagnetic case.

One of the by-products in these cascades are neutrons. Although neither being present in cosmic radiation nor being the dominant production channel neutrons make up a large part of the particles at ground level as their interaction probability is smaller compared to charged particles and their lifetime is long enough to traverse the atmosphere, see also Fig. 12. The neutron density increases until a height of around 20 km or (50-100)  $\text{g/cm}^2$ , the so-called Pfozter<sup>[h]</sup> maximum [60], by spallation reactions in the upper atmosphere, and beyond it follows a simple exponential law as a function of atmospheric depth. As seen in Fig. 12, the initial flux decreases by several orders of magnitude with only marginal deviations of the base spectrum until reaching the ground level.

[g] Muons are for example primarily produced by pion decay, which is mediated by the weak force.

[h] Georg PFOTZER, \*1909-†1981, German Empire

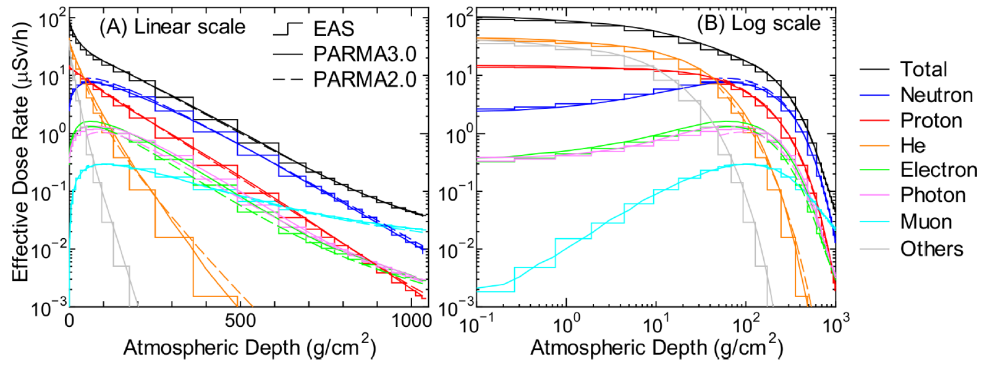


Figure 12: Atmospheric depth dependencies of effective dose rates at  $r_c = 0$  GV for solar minimum conditions in log-linear (left) and log-log representation (right), calculations carried out using PARMA [61].

The spectrum of cosmic-ray induced neutrons, see Fig. 13, offers some distinct features with three prominent peaks, which originate from the physics involved from the process of creation until absorption, see here sec. 1.4. Highly energetic neutrons at  $\approx 100$  MeV are produced as secondary particles by intra-nuclear cascades and pre-equilibrium processes [62]. When high-energy neutrons or protons interact with atoms of the atmosphere, the excited nuclei evaporate neutrons at a lower energy. This process manifests itself at the peak at  $\approx 1$  MeV and shows additional absorption fine structure due to distinct resonances of non-hydrogen atoms, especially oxygen, compare also the cross sections in Fig. 31. Neutron interactions in the sub-MeV region are entirely dominated by elastic collisions, in which the energy loss is correlated to the mass of the target nucleus. Due to the mass of hydrogen being nearly equal to the one of the neutron, this energy band is most sensitive to water and organic molecules and thus most relevant for the method of cosmic ray neutron sensing. Below  $\approx 1$  eV the kinetic energy of the target, which is usually in thermal equilibrium at  $k_B T \approx 25$  meV, significantly contributes to the neutron's energy during a collision. As a consequence, neutrons finally become thermalized at  $\approx 25$  meV. Since neutrons cannot leave the thermal equilibrium they perform a random walk until they are absorbed<sup>[i]</sup>.

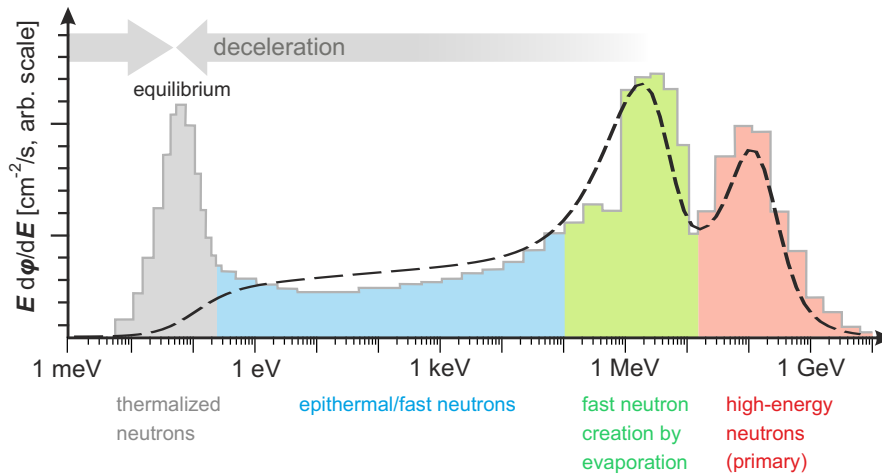


Figure 13: The cosmic ray neutron spectrum with its different domains. Data (histogrammed) from [65] and analytical description (dashed line) by [66].

[i] The dominant channel [63] is absorption by nitrogen,  $^{14}\text{N} + n \rightarrow ^{14}\text{C}$ , being the main source of atmospheric carbon-14 used in radiocarbon dating for inferring the chronometric age for materials recovered from archeological contexts [64].

Cosmic ray propagation in the atmosphere has been modeled extensively by Sato et al. [66] using PARMA [67], which is based on PHITS [68], see also sec. 5.2.1. They provide an energy spectrum of cosmic ray neutrons for a variety of altitudes, cutoff rigidities, solar modulation potentials and surface conditions. These simulations have been validated with various independent measurements, i.e. [65] and [69], at different altitudes and locations on Earth. Moreover, the analytical formulations of the spectra turned out to be effective in use for subsequent calculations. The presented energy-dependent flux  $\phi(E)$  is described by a mean basic spectrum  $\phi_B$ , a function for neutrons below 15 MeV  $\phi_L$ , an extension for thermal neutrons  $\phi_{th}$ , and a modifier  $f_G$  for the geometry of the interface, which is defined by the ratio in comparison to a hypothetical spectrum of a semi-infinite atmosphere:

$$\phi(s, r_c, d, E, w) = \phi_B(s, r_c, d, E) \cdot (f_G(E, w) + \phi_{th}(E, w)) \cdot \phi_L(s, r_c, d). \quad (67)$$

The individual terms are

$$\begin{aligned} \phi_B(s, r_c, d, E) = & \\ & 0.229 \left( \frac{E}{2.31} \right)^{0.721} \exp\left(-\frac{E}{2.31}\right) + c_4(d) \exp\left(-\frac{(\log(E) - \log(126))^2}{2(\log(2.17))^2}\right) \\ & + 0.00108 \log\left(\frac{E}{3.33} 10^{12}\right) \\ & \cdot \left(1 + \tanh\left(1.62 \log\left(\frac{E}{9.59} 10^8\right)\right)\right) \left(1 - \tanh\left(1.48 \log\left(\frac{E}{c_{12}}\right)\right)\right), \end{aligned} \quad (68)$$

$$\log(f_G(E, w)) = -0.0235 - 0.0129 (\log(E) - g_3(w)) \left(1 - \tanh\left(0.969 \log\left(\frac{E}{g_5(w)}\right)\right)\right), \quad (69)$$

$$\phi_L(s, r_c, d) = a_1(r_c) (\exp(-a_2(r_c)d) - a_3(r_c) \exp(-a_4(r_c)d)), \quad (70)$$

and

$$\phi_T(E_T, w) = \frac{0.118 + 0.144 \exp(-3.87w)}{1. + 0.653 \exp(-42.8w)} \left(\frac{E}{E_T}\right)^2 \exp\left(\frac{-E}{E_T}\right), \quad (71)$$

denoting the solar modulation potential  $s$ , cutoff rigidity  $r_c$ , the weight fraction of water  $w$  and atmospheric depth  $d$ .  $E_T = k_B T$  represents the thermal energy. The calculation of the individual parameters is described in appendix B.1.4 by (160). For some parameters the solar modulation potential can be set to a minimum and a maximum condition, whereas here the latter has been chosen allowing to already expand many numerical values.

## ARTIFICIAL HIGH FLUX SOURCES

## 4.1 | OVERVIEW OF FACILITIES

The earliest research with neutron sources, see sec. 1.1.2, was based on natural  $\alpha$  emitters interacting with targets like beryllium. Nuclear fission quickly became the standard source yielding a high flux of up to  $10^{15}$  n/cm<sup>2</sup>s. Meanwhile, in the 21<sup>st</sup> century, pulsed sources based on accelerator, apart from the design exception of the IBR-II in Dubna, started to outperform the existing reactors.

In 1968, Brugger [70] reviewed the progress in flux intensity as a function of time. In this plot, see also Fig. 14, which has been updated over decades [71, 72], two phenomena can be observed: that every baseline technology levels off, sooner or later, and that there is belief, that, although recent trends indicate stagnation, upcoming projects would succeed to achieve tremendous steps forward.

In neutron physics up to now only three (Radioisotopes with  $\alpha$  particles, fission and spallation) out of five (fusion and photofission) main production methods are used efficiently as sources for large-scale research centers. Technological trends and limitations, the leveling-off, can for example be observed in the history of particle accelerators. In this related field, having a larger variety of acceleration mechanisms, the beam energy of charged particle experiments saturated very quickly and so in most facilities one can find them as boosters chained one after the other. Yet, as a consequence of reviewing only a limited time frame, this engineering principle has been disregarded in particle physics, when extrapolating the „energy frontier“ exponentially like Moore's<sup>[a]</sup> law<sup>[b]</sup> [73]. Although the original publication showed the contrary, see Fig. 16, this expected trend is often displayed as a Livingston<sup>[c]</sup> plot. The conclusion, which can be drawn instead, is, that rather a new technology can introduce a boost to outperform existing systems instead of the upscaling of already established methods.

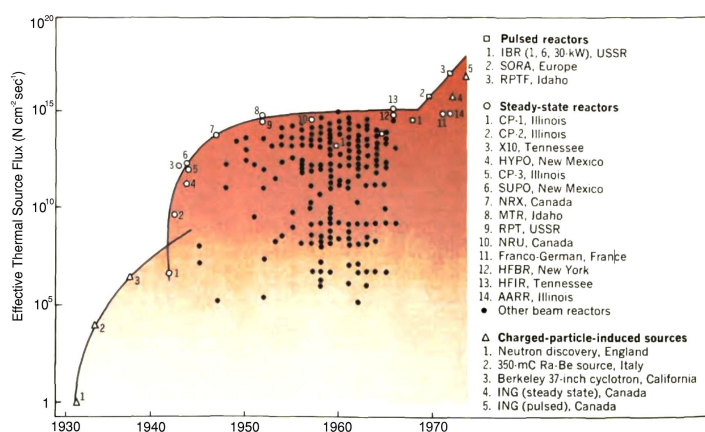


Figure 14: Neutron sources with their thermal neutron flux plotted by the initial year of operation (Note: the axis is not scaled correctly). The optimistic extrapolation presented by Brugger [70] in 1968 calls for a next generation of sources based on novel technologies.

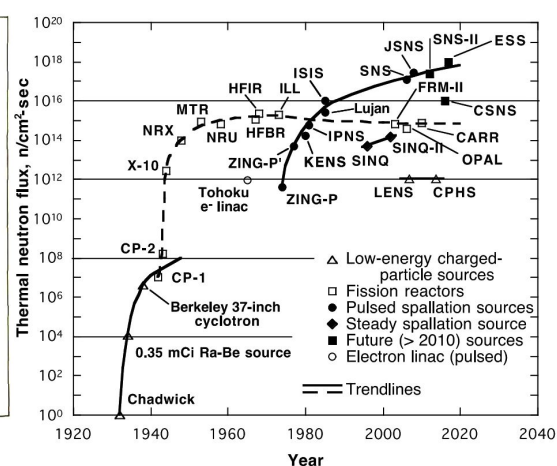


Figure 15: Highest flux sources as a function of initial year of operation and grouped by production method. The initial plot by Carpenter [71] has been updated in 2009.

[a] Gordon Earle MOORE, \*1929, USA

[b] The paradigm of the semiconductor industry that since the 1970s the packing density of integrated circuits doubles in a period often referred to as 18 months.

[c] Milton Stanley LIVINGSTON, \*1905-†1986, USA

To understand the limitations of actual neutron sources in their intensity, the characteristics of the production mechanisms are summarized in the following. Spallation and fission differ in their released neutron energy spectrum, which is significantly harder for spallation. Both also contrast in their production mechanism. The overall number of neutrons released per fission event is on average 2.4 for  $^{235}\text{U}$ , which is less than the incoming beam energy dependent 10-20 neutrons for spallation. Furthermore, in fission one neutron is required to sustain the chain reaction and in typical fuel elements nearly half of the remaining fraction of  $^{239}\text{U}$  ends in the production of plutonium. For fission around 180 MeV is deposited as heat, for spallation in tungsten it is around 32 MeV. In a fission process the average gamma energy deposited is 12 MeV, whereas for spallation it is 2 MeV per neutron. Yet, for spallation the kinetic energy of the incident ion beam, which is dumped in the target, has to be added to the heat budget. Finally the limitation for the overall intensity is a trade-off between the source geometry, which focuses on maximizing the neutron flux in the surrounding moderator by minimizing self-absorption, and the cooling capabilities for a compact source or target. This effectively limits the thermal design power to  $\approx 100\text{ MW}^{[d]}$  and the total neutron flux to  $\approx 10^{15}\text{ n}/(\text{cm}^2\cdot\text{s})$ . Spallation sources can operate in a pulsed mode and therefore achieve a much higher peak flux within the duty cycle.

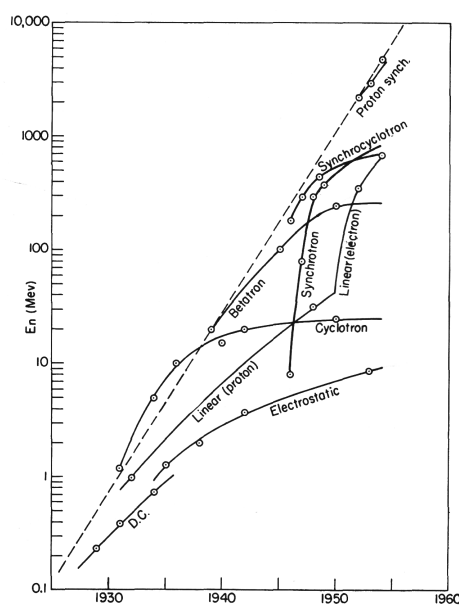


Figure 16: The original Livingston plot [74] shows the collision energy of of different charged particle accelerators. The non-proton labeled entities denote electron machines.

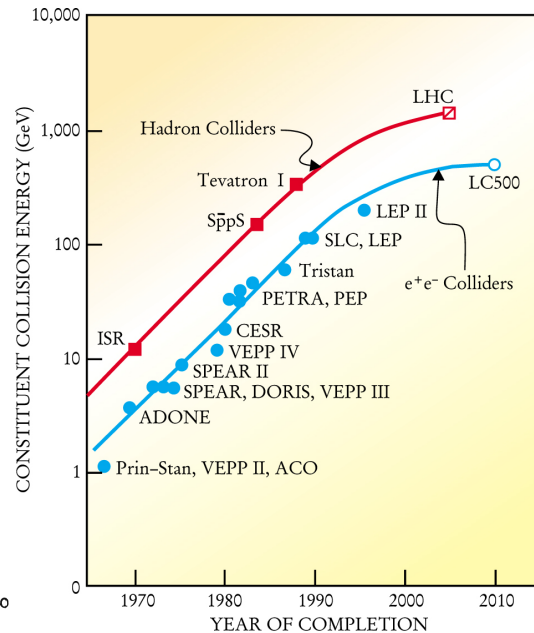


Figure 17: One of the rare graphs showing that hadron and lepton synchrotrons and storage rings are reaching their technological limits in the 21<sup>st</sup> century [75].

[d] compared to 1500 MW per block for conventional nuclear power plants.

The following neutron research centers in Europe directed towards scattering methods are currently operating a research reactor, see the map presented in Fig. 18.

A detailed overview is given in tab. 3. Spin-Echo instruments are available at FRM II,



Figure 18: Overview: Sites of neutron sources of scattering facilities in Europe organized in the ENSA association, collected in [76].

ILL, LLB, ISIS and formerly at BER II and BNC.

Facility	Organization	Country	Type	Year
ESS	ERIC Consortium	Sweden	Spallation	2025
ISIS	Rutherford Appleton Laboratory	England	Spallation	1985
SINQ	Paul Scherrer Institute	Switzerland	Spallation	1996
PIK	Petersburg Nuclear Physics Institute	Russia	100 MW	2018
ILL	Institute Laue-Langevin	France	58 MW	1971
FRM II	Heinz Maier-Leibnitz Zentrum	Germany	20 MW	2004
WWR-M	Petersburg Nuclear Physics Institute	Russia	18 MW	1960
LLB	CEA/CNRS	France	14 MW	1980
BNC	Budapest Research Centre	Hungary	10 MW	1992
BER-II	Helmholtz-Zentrums Berlin	Germany	10 MW	1973
JEEP-II	Institute for Energy Technology	Norway	2 MW	1967
RID	Delft University of Technology	Netherlands	2 MW	1963
IBR-2	Frank Laboratory of Neutron Physics	Russia	2 MW	1982
RPI	Instituto Superior Técnico	Portugal	1 MW	1960
RIC	Jožef Stefan Institute	Slowenia	250 kW	1966
TRIGA II V	Atominstitut Wien	Austria	250 kW	1962
FRMZ	Johannes Gutenberg University Mainz	Germany	100 kW	1967

Table 3: Neutron research facilities in Europe with their operational period ordered by type and thermal design power as a rough estimator for the total neutron flux [76][77][78].

The total amount of research facilities and training reactors in Europe is 48, this also includes the n\_TOF facility at CERN. In addition the Russian Federation keeps currently another 63 reactors in operation [78].

The Forschungs-Neutronenquelle Heinz Maier-Leibnitz<sup>[e]</sup>, FRM II, is a research reactor cooled by light water with a heavy water moderator. The compact fuel element [79], see Fig. 19 (left), has specifically been developed in order to achieve the highest thermal neutron flux [80] for its nominal power of 20 MW. The active core, see Fig. 19 (right), consists of 113 curved  $\text{AlMg}_3$  embedded  $\text{U}_3\text{Si}_2$  fuel elements between a cylinder 6.75 cm (for the control rod) and 11.2 cm with an active region of 70 cm. The uranium is enriched to 93 % of  $^{235}\text{U}$ . A maximum of unperturbed thermal neutron flux of  $8 \cdot 10^{14}$  n/cm<sup>2</sup>/s can be achieved, whereas typically a fuel element can be operated non-stop for 60 days until the power density cannot be held any more, which means that the control rod is at its maximum position. Neutrons are extracted by guides which are directed towards the region of highest flux but perpendicular to the line of sight to the reactor core. This tangential arrangement significantly reduces the background of gamma radiation and fast neutrons. Several dedicated moderators tailor the neutron energy to the needs of specific instruments. Besides the room temperature ( $\sim 320$  K) of the deuterium moderator there is a hot and a cold source, see below and Fig. 20. The hot source consists of a cylindrical graphite block of 14 kg heated to 2300 K and the cold source of a spherical containment for 12 l of liquid deuterium at 18 K. A fission neutron converter can in turn again produce MeV-neutrons for the fast neutron tomography station [81]. Most of the eleven beam tubes (SR) supply experiments in the Experimental Hall, which require the highest flux, and some are fanned out into the Neutron Guide Hall (SR-1 split into six guides NL-1 to NL-6). The Spin Echo instruments RESEDA [82] and MIRA [83] are located at the end of NL-5 and NL-6, respectively. The HEiDi [84] single crystal diffractometer aims at the hot source.

The spectrum of a moderator can be described in a first order approximation by a Maxwell-Boltzmann distribution (99), see also sec. 1.3.1. Fig. 20 shows the results of simulations of the neutron flux density at the beginning of the respective beam tubes. The  $\text{D}_2\text{O}$  thermal neutron source can be well approximated by a distribution with a temperature of 318 K - as the heavy water moderator is sufficiently large to achieve a thermally equilibrated flux. For the description of the hot and cold source the fit has to be carried out by a sum of Maxwell-Boltzmann functions. As for technical reasons both vessels are limited in size the results are undermoderated spectra, which do not correspond to the temperature of the moderators but can be described by a thermal spectrum with shifts towards a cold or a hot thermal bath. Experiments then limit the phase space by wavelength selectors like choppers or monochromators.

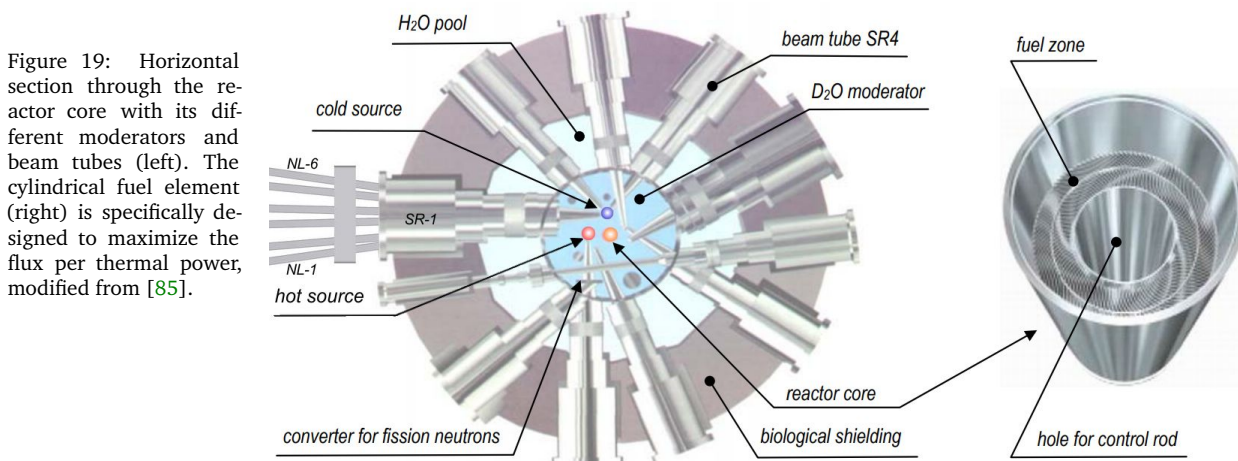


Figure 19: Horizontal section through the reactor core with its different moderators and beam tubes (left). The cylindrical fuel element (right) is specifically designed to maximize the flux per thermal power, modified from [85].

[e] Heinz MAIER-LEIBNITZ, \*1911-†2000, Germany



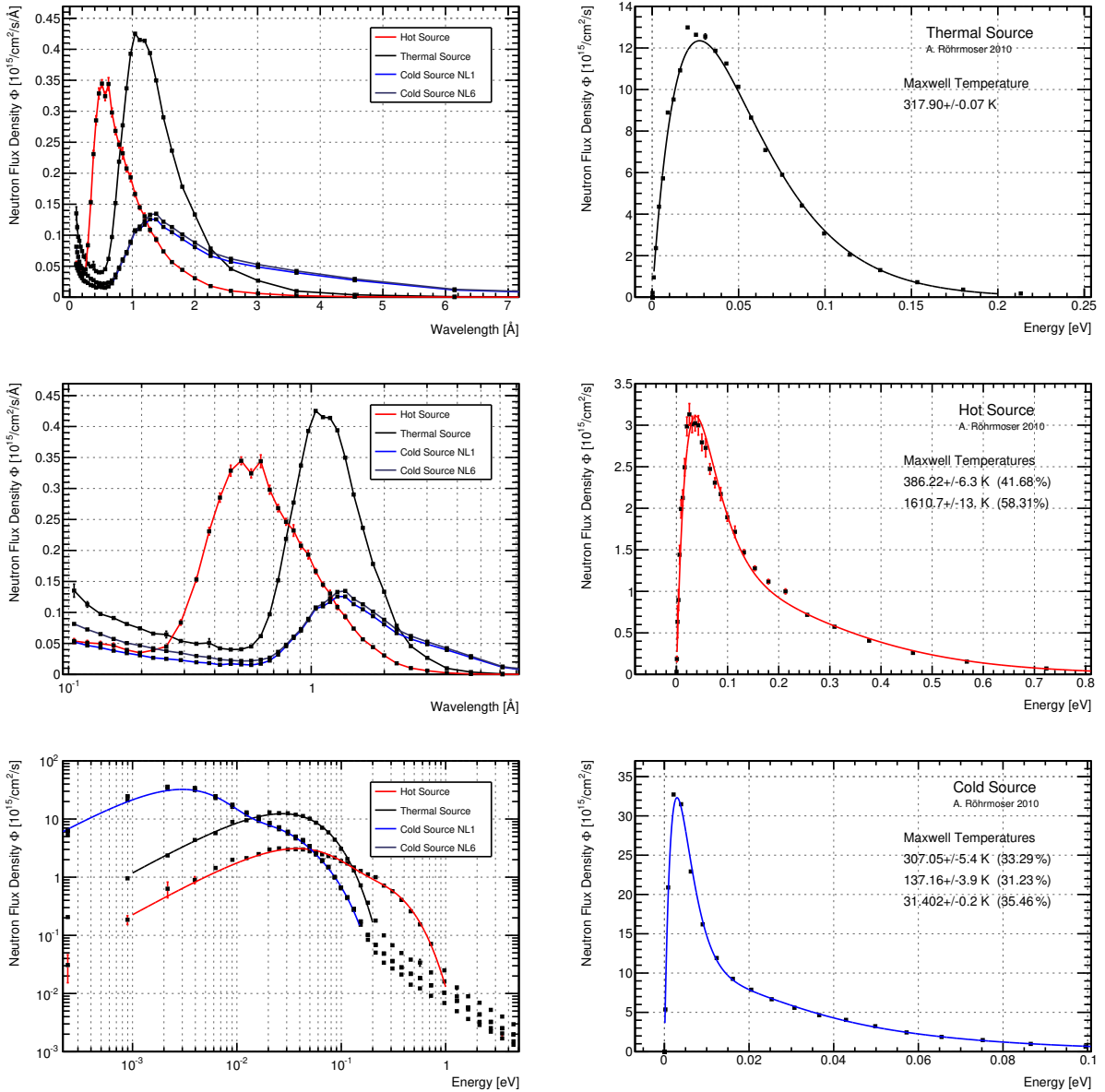


Figure 20: Monte Carlo simulations of the neutron flux at the FRM-II for different moderators relevant in this work. The left column shows from top to bottom the results for all sources as a function of wavelength, logarithmic wavelength and logarithmic energy. The right column shows each flux distribution as a function of energy fitted by one or more Maxwell-Boltzmann functions (99) in order to describe the spectrum. These fits are also shown in the same color in the left column.



Part III

URANOS MONTE CARLO TRANSPORT CODE



## MODELING AND MONTE CARLO APPROACH

---

The Monte Carlo [86] method is a brute-force calculation technique, which is used for complicated problems consisting of well-defined or independent sub-tasks. The method retains a close relation to the problem it is trying to solve by repeated random sampling from a set of initial conditions. Although especially in high-energy physics the modeling of complicated particle interactions and transport problems by means of such simulations have even become an own discipline, it has to be noted, that the first realization of this method in physics was carried out by the initiative of Fermi<sup>[a]</sup> in order to solve problems of neutron transport. His FERMIAC [87], an analog computer, consisted of an adjustable trolley, which was able to ray-trace neutron paths on a two dimensional technical drawing. In the same year, 1947, von Neumann<sup>[b]</sup> then set up similar programs [88] on the first entirely digital computer, the ENIAC [89], in order to calculate thermonuclear reactions in spherical symmetric geometry [90].

### 5.1 | SAMPLING

The Monte Carlo approach is a stochastic method, in which a randomly chosen subset of a system is used as an estimator for specific parameters, observables of the system. The requirements are

- the sample space  $S$  is defined,
- the values associated with the sample space need to be accessible, either by a known probability distribution function  $f(x)$  or an invertible cumulative probability distribution  $F(x) = \int_{-\infty}^x f(t) dt$ ,
- a method for the generation of random numbers.

After one or more random numbers  $\xi_i$  have been chosen there are two methods for evaluation. The sampling by rejection accepts a random number if

$$f(\xi_1) < \xi_2, \quad (72)$$

*sampling by rejection*

whereas for real  $\xi \in [0, 1]$  the support and the codomain of the function should be normalized accordingly, i.e.  $\|f\|_{\max} \leq 1$ . Then the result will be  $x = \xi$ .

The sampling by the inverse cumulative distribution function calculates the resulting number by

$$x = F^{-1}(\xi). \quad (73)$$

*sampling by the inverse cumulative function*

#### 5.1.1 | RANDOM NUMBER GENERATION

The pseudo-random number generator TRandom3 uses the Mersenne<sup>[c]</sup>-Twister algorithm MT 19937 [91] based on the Mersenne prime number 19937. It has the following features:

[a] Enrico FERMI, \*1901-†1954, Kingdom of Italy.

[b] John VON NEUMANN, \*1903-†1957, Austro-Hungarian Empire.

[c] Marin MERSENNE, \*1588-†1648, France.

- a very long period of  $p = 2^{19937} - 1 \approx 4.3 \cdot 10^{6001}$ <sup>[d]</sup>,
- low correlation between subsequent numbers (k-distributed for the output sequence),
- relatively fast, as it generates the output sequence of 624 32bit integers at once.

The random generator is seeded at the initialization of the program by the system time in milliseconds. This is taken as the first integer of the seed sequence, the remaining 623 numbers<sup>[e]</sup> are generated by the multipliers from [92].

### 5.1.2 | SAMPLING FREE PATH LENGTH

According to the definition of the macroscopic cross section  $\Sigma_t$ , which in general is energy dependent, see sec. 1.4, the probability  $p$  of an interaction on a distance  $dx$  in a homogeneous material can be stated as

$$dp = \Sigma_t dx. \quad (74)$$

Solutions of this type of differential equation are exponential functions. For the non-interaction probability one therefore can write

$$p(x) = \exp(-x\Sigma_t). \quad (75)$$

The probability distribution function for the distance to the next collision (75) assuming conditional probabilities transforms to

$$p(x) dx = \Sigma_t \exp(-x\Sigma_t) dx. \quad (76)$$

The free path length  $l$  is obtained by the cumulative probability distribution function of (76)

$$\int_0^l p(x) dx = \int_0^l \Sigma_t \exp(-x\Sigma_t) dx = 1 - \exp(-\Sigma_t l) = P(l). \quad (77)$$

Now, in order to retrieve a path length, (77) can be sampled using the inversion method (73). This means, that the normalized cumulative function is set equal to a random number  $\xi$  on a unit interval:

$$l = -\frac{\ln(1 - \xi)}{\Sigma_t} = -\frac{\ln(\xi)}{\Sigma_t}. \quad (78)$$

As  $\xi$  is uniformly distributed in  $[0, 1)$  the same holds true for  $1 - \xi$ , justifying the latter transformation.

It is assumed in (78) that the material is homogeneous and the cross section and therefore the energy stay constant. In case of an inhomogeneous material it is possible that the integral cannot be resolved in a closed form. The solution is to split the domain into entities of homogeneous materials and only evaluate the path to the respective border. This procedure is equal to the prerequisite already stated in (76), that the probability at any point  $x$  does not depend on the individual path history.

[d] A typical URANOS run can easily require more than  $2^{32}$  random numbers. TRandom3 takes approximately 10 ns for each random number on a modern architecture, e.g. the one presented in sec. 6.6.4.

[e] If too many zeros are in the initial seed tuple it can take up to  $10^5$  calls until the output vector is equidistributed.

In order to describe scattering processes with thermal neutrons an algorithm has to be applied which preserves the thermally-averaged reaction rate. Such has been introduced by [93], whereas this modified version follows the implementation by [94] and [95]. Besides sampling a Maxwell-Boltzmann distribution, see also (2), for the velocity of the target nuclide it has to be taken into account, that velocities that lead to relative velocities which correspond to a high cross section will have a larger effect on the reaction rate. Therefore, by using the effect of thermal motion on the interaction probability

$$v\bar{\sigma}(v, T) = \int v_r \sigma(v_r) f_M^{(1)}(V) d\vec{V}, \quad (79)$$

one has to conserve the reaction rate (integrand of (79))

$$R(V) = \|\vec{v} - \vec{V}\| \sigma(\|\vec{v} - \vec{V}\|) f_M^{(1)}(V), \quad (80)$$

whereas  $f_M^{(1)}(V)$  denotes the speed distribution as in (2) for target nuclei of temperature  $T$ , velocity  $\vec{V}$  and magnitude of velocity  $V$ . The CM system of the collision of a neutron with velocity  $\vec{v}$  moves at  $v_r = \|\vec{v}_r\| = \|\vec{v} - \vec{V}\| = \sqrt{v^2 + V^2 - 2vV \cos \vartheta}$ . Such a probability function can be constructed by

$$p(V) dV = \frac{R(V) dV}{\int R(V) dV}. \quad (81)$$

Defining the denominator of (81) as the normalization factor  $C$  and

$$\beta = \sqrt{\frac{m}{2k_B T}} \quad (82)$$

as well as  $\mu = \cos \vartheta$  one obtains

$$p(V, \mu) dV d\mu = \frac{4\sigma(v_r)}{\sqrt{\pi}C'} \sqrt{v^2 + V^2 - 2vV\mu} \beta^3 V^2 \exp(-\beta^2 V^2) dV d\mu. \quad (83)$$

In order to obtain a sampling scheme one can divide (83) into two parts such that

$$\begin{aligned} p(V, \mu) &= g_1(V, \mu) g_2(V) & (84) \\ g_1(V, \mu) &= \frac{4\sigma(v_r)}{\sqrt{\pi}C'} \frac{\sqrt{v^2 + V^2 - 2vV\mu}}{v + V} \\ g_2(V) &= (v + V) \beta^3 V^2 \exp(-\beta^2 V^2). \end{aligned}$$

Here the reason for dividing and multiplying (83) by  $v + V$  is that  $g_1$  is bounded. As  $\|\vec{v} - \vec{V}\|$  can take on arbitrarily large values, dividing by the sum of the speeds as the maximum value ensures it to be bounded. In general a probability distribution function  $q(x) = g_1(x)g_2(x)$  can be sampled by sampling  $x'$  from a normalized distribution  $q(x)$

$$q(x) dx = \frac{g_2(x)}{\int g_2(x)} \quad (85)$$

and accepting it with a probability of

$$p_{\text{accept}} = \frac{g_1(x')}{\max[g_1(x)]}, \quad (86)$$

with  $g_1(x)$  bounded. In order to determine  $q(V)$  it is necessary to integrate  $g_2$  into (84)

$$\int_0^{\infty} dV (v + V) \beta^3 V^2 \exp(-\beta^2 V^2) = \frac{1}{4\beta} (\sqrt{\pi} \beta v + 2), \quad (87)$$

leading to sampling the probability distribution function

$$q(V) dV = \left( \frac{4\beta^4 v V^2}{\sqrt{\pi} \beta v + 2} + \frac{4\beta^4 V^3}{\sqrt{\pi} \beta v + 2} \right) \exp(-\beta^2 V^2). \quad (88)$$

By substituting  $x = \beta V$ , likewise  $dx = \beta dV$ , and  $y = \beta v$  leads finally to

$$q(x) dx = \left[ \left( \frac{\sqrt{\pi} y}{\sqrt{\pi} y + 2} \right) \frac{4}{\sqrt{\pi}} x^2 \exp(-x^2) + \left( \frac{2}{\sqrt{\pi} y + 2} \right) 2x^3 \exp(-x^2) \right] dx. \quad (89)$$

The terms outside the parentheses are normalized probability distribution functions which allow to be sampled directly and the expressions inside the parentheses are always  $< 1$ .

The **thermal neutron scattering sampling scheme** therefore is the following:

A random number  $\xi_1$  is sampled from  $[0, 1)$  and if

$$\xi_1 < \frac{2}{\sqrt{\pi} y + 2}, \quad (90)$$

the function  $2x^3 \exp(-x^2)$  is sampled using method (72), otherwise  $4/\sqrt{\pi} x^2 \exp(-x^2)$ . The retrieved  $x$  gives the value for  $V$  by dividing by  $\beta$ .

For this velocity it has to be decided to accept it based on (86). The cosine of the angle can be sampled by another random number  $\xi_2$  in  $[0, 1]$  by

$$\mu = 2\xi_2 - 1 \quad (91)$$

and as the maximum of  $g_1$  is  $4\sigma(v_r)/\sqrt{\pi} C'$  another sampling random number  $\xi_3$  can be used to accept speed and angle by

$$\xi_3 < \frac{\sqrt{v^2 + V^2 - 2vV\mu}}{v + V}. \quad (92)$$

If this condition is not met speed and cosine of the angle have to be resampled.

#### 5.1.4 | EVALUATED NUCLEAR DATA FILES

Experimental and theoretical results on neutron-nuclear interactions and their subsequent products are collected in libraries. The main data base is the Experimental Nuclear Reaction Data Library (EXFOR) [96], which stores most of the accepted published results in a scheme of general observables. Such measurements are often not comprehensive or contradictory, therefore so called evaluated data bases exist, which assess the literature especially regarding the intercomparison of different results and compress them to standardized and consistent values. The maintained data bases, which are used for this work are the United States Evaluated Nuclear Data File (END-F/B) [97] and the Japanese Evaluated Nuclear Data Library (JENDL) [98].



#### 5.1.4.1 DATA FORMATS

The standard reference data is provided in the ENDF-6 format [99], which for reasons of downward compatibility uses 80-character records and variables in FORTRAN form. A typical file could look like the following example

```
#LIBRARY      JENDL-4.0
#REACTION     H-1(N,EL)H-1-L0,SIG
#NUCLEUS      H-1
#MF           3
#MT           2
#EN-MIN       1e-05
#EN-MAX       2e+07
#E,eV         Sig,b                Interpolation
1E-05         1156.94              Lin-Lin
1.1024E-05   1101.91              Lin-Lin
...           ...                  ...
```

Table 4: Example for an ENDF card: the elastic scattering cross section of hydrogen.

The header describes the data according to the parameters: Energies are given in eV,

Library	Collection (JENDL) and version (4.0)
Reaction	Element (H), Isotope (H-1), Projectile (Neutron), Reaction type (elastic scattering) and data type (cross section)
MT	Type of the reaction (elastic scattering)
MF	Subdivision of MT into data types (cross section)
Range	Minimum and maximum of the energy

angles in dimensionless cosines of angles, cross sections in barns and temperatures in Kelvin. For the data types the important numbers are MF=3, which is the reaction cross section, and MF=4, which is the angular distribution of the emitted particles. The MT numbers necessary for this work are given in table 5.

MT	Description
1	Neutron total cross section
2	Elastic Scattering
3	Sum of non-elastic processes
4	Sum of inelastic cross sections
5	Sum of processes without any MT number
16-21	Neutron final state reactions (incl. fission)
22-26	Neutron and charged particle final state
50+i	Inelastic scattering to the <i>i</i> th excited state
102	Radiative capture
103-117	Neutron capture with charged particle emission
208-210	Pion ( $\pi^+$ , $\pi^-$ , $\pi^0$ ) production
211,212	Myon ( $\mu^+$ , $\mu^-$ ) production

Table 5: Selection of relevant MT numbers and designated purpose [99].

### 5.1.4.2 INTERPOLATION LAWS

Cross sections are treated by the following rules given in table 6. As seen, the extrapolation rules take into account the typical logarithmic behavior of the cross section. Nevertheless there is no hyperbolic law supposed to be applied, which would take into account especially the  $1/v$  behavior in the thermal regime; instead, the values are tabulated in very short intervals.

Table 6: Interpolation rules for tabulated cross sections.

law	Description	law	Description
const	$\sigma$ is constant (a histogram)	lin-log	$\sigma$ is linear in $\ln x$
lin-lin	$\sigma$ is linear in $x$	log-lin	$\ln \sigma$ is linear in $x$
log-log	$\ln \sigma$ is linear in $\ln x$		

Angular distributions are described by normalized probability distributions. That means a process describing an incident particle of energy  $E$  into an interval  $d\mu$  around the angular cosine  $\mu = \cos \vartheta$  by a probability function  $f(\mu, E)$  with

$$\int_{-1}^1 f(\mu, E) d\mu = 1.$$

Due to the azimuthal symmetry of the distribution, they are represented by Legendre<sup>[f]</sup> polynomial series<sup>[g]</sup>

$$f(\mu, E) = \frac{2\pi}{\sigma_s(E)} \sigma(\mu, E) = \sum_{l=0}^N \frac{2l+1}{2} a_l(E) P_l(\mu), \quad (93)$$

where the number  $l$  denotes the order of a Legendre polynomial with coefficient  $a_l$ . The zero order factor  $a_0 = 1$  is implicitly assumed. So the cross section is obtained by

$$\sigma(\mu, E) = \frac{\sigma_s(E)}{2\pi} \sum_{l=0}^N \frac{2l+1}{2} a_l(E) P_l(\mu). \quad (94)$$

### 5.1.4.3 INTERPOLATION ALGORITHM

Data in structures defined by the ENDF cards are stored by points and corresponding interpolation laws, see chapter 5.1.4.2. Therefore, in order to calculate a cross section as a function of energy, the upper and lower tabulated values have to be selected from the arrays they are stored in. These are found by an interpolation search algorithm [100]. The performance is  $O(n)$  in a general case, but  $O(\log \log n)$  on linear data set. As some cross sections are stored in files with a mixed metric, consisting of a point matrix of fluctuating density regarding a linear energy scale, if the interval limits during the algorithm are not changed fast enough, the algorithm changes to logarithmic interval search. This improves the performance in case the cross section does not change between 20 MeV and 1 GeV.

Interpolation search defines upper and lower limits of the interval  $L$  and  $R$ , starting at the minimum and maximum of the data set, and compares the value at  $(L+R)/2$  to the search value  $x$ . Then the  $L$  or  $R$  limit is set to  $(L+R)/2$ , dependent on in which of interval  $x$  is located. If  $L+1 = R$ , the search is stopped and result provided is determined either by a linear or a logarithmic interpolation of the values at  $L$  and  $R$  according to their relative position compared to  $x$ .

[f] Adrien-Marie LEGENDRE, \*1752-†1833, France.

[g] with up to 20 coefficients.

Among the existing Monte Carlo tools, most codes do have a long history and strong aim towards nuclear fuel calculations. Besides dedicated programs, the most widely used in neutron physics is MCNP, especially for purposes of the ESS, GEANT4 can be considered the most important.

### 5.2.1 | GENERAL PURPOSE PACKAGES

MCNP (**Monte Carlo N-Particle**) was developed in Los Alamos as a general purpose software to treat neutrons, photons, electrons<sup>[h]</sup> and the coupled transport thereof. Versions until MCNP4 [101] were capable of simulating neutrons up to 20 MeV, which is the maximum of most of the cross sections available in the evaluated data bases, and were written in FORTRAN 77 [102], which was until the mid-90s considered the standard in scientific computing. With version 5 [103] the development was forked to the MCNPX [104](MCNP eXtendend) branch, which converted the code to Fortran 90 [105] and included the LAHET [106] framework. This especially introduced the extension of the energy range for many isotopes up to 150 MeV and some to GeV by using the continuously improved Cascade-Exciton Model (CEM) [62] and on top the Los Alamos Quark-Gluon String Model (LAQGS) [107]. It also can treat (heavy) ion transport for charged particles with energies larger than 1 MeV/nucleon by tabulated ranges. The actual version 6 [108] re-merged the X-branch into the main development branch. Since it also provides an optional cosmic-ray source [109] it has gotten large attention for the calculation of the cosmic neutron spectrum as seen in [110].

USA

A more recent general purpose tool is PHITS [68] (**Particle and Heavy Ion Transport code System**), as extension of the high energy particle transport code NMTC/JAM [111], which, besides the features mentioned above, also supports charged particles in magnetic fields,  $dE/dx$  calculations in the **Continuous-Slowing-Down Approximation** [112] (CSDA) and intra-nuclear cascade (JAM) [113] (**Jet AA Microscopic Transport**) models up to 1 TeV. PHITS is also typically linked against the JENDL-4/HE(High Energy) data base, consisting of files evaluated by CCONE [114], which is a more sophisticated model compared to INCL [115] and JAM. However, it comes along with many adjustable parameters for each nucleus, which often leads to a better accuracy compared to other physics models. PHITS also features a rudimentary graphical user interface. Like MCNP and the following codes it is also written in Fortran. One of the recent follow-up developments is PARMA [67] (**PHITS-based Analytical Radiation Model in the Atmosphere**). It calculates the spectra of leptons and hadrons providing effective models for fluxes of particles of different species, especially with the aim of dose estimations.

Japan

The FLUKA [116](**FLUktuierende KAskade**) code is mostly oriented towards charged hadronic transport and nuclear and particle physics experiments. For neutron calculations, the full spectrum is divided into 260 energy groups, which are not directly linked to an evaluated data base, but operate on their own set of reprocessed and simplified mean values. Especially for neutrons and geometrical representations, it contains implementations from the MORSE [117] neutron and gamma ray transport code.

CERN

GEANT4 [118] (**GEometry ANd Tracking**) can be regarded as FLUKA's successor, based on multithreaded C++ and OpenGL visualizations. It is designed specifically for the needs of high energy and accelerator physics. GEANT4 especially excels in describing a complex geometry of the setup. Since 2011, also driven by requests from the European Spallation Source, an increasing number of low energy neutron calculation capabilities

CERN

[h] MCNP does not handle magnetic fields for charged particles.

were introduced. Meanwhile the software has advanced to a level where there is a good agreement with other codes like MCNP for fast neutrons [119] as well as slow neutrons [120].

### 5.2.2 | SPECIFIC NEUTRON INTERACTION CODES

- USA* VIM [121] is a continuous energy neutron and photon transport code written mainly in Fortran 90. It is developed by Argonne National Laboratory for reactor physics and shielding. The geometry is limited to hexagonal or rectangular lattices of combinatorial unit cells and especially focuses on the description of critical states.
- France* TRIPOLI [122] is a neutron, photon and electron transport code written in FORTRAN 77 and C by the Commissariat à l'énergie atomique, Saclay. It uses, unlike VIM, not only the ENDF data bases but is able to extract cross sections from several libraries by a specific interface allowing for example neutron energies up to 150 MeV.
- USA* Similar to both mentioned programs there are a number of codes with approximately the same scope allowing photon and neutron transport. Among them are TART [123] with 700 energy groups up to 1 GeV, but neutron calculations only up to 20 MeV. Whereas earlier versions were written in LRLTRAN, a language unique to the Lawrence Livermore National Laboratory to run on their Cray supercomputers<sup>[i]</sup>, the releases after 1995 were ported to Fortran. It's successor, MERCURY [124], then was rewritten in C with improvements in geometry definitions by XML steering files. Furthermore, with dedicated scope on reactor analysis there are PRIZMA [125] and Shift [126], which partly includes also deterministic codes, Serpent [127], which does not only use the average interaction length calculations, but also the Woodcock delta-tracking method [128] that continues across geometrical borders by pseudo fictitious steps in the subsequent material. This feature is also included in RMC [129] (Reactor Monte Carlo) and MORET [130]. These codes were developed at governmental institutions and mostly for the research program pursued. For the MONK [131] code there also have been made the approach to commercialize such a tool. The only German contribution to be mentioned in the field of reactor analysis is KAMCCO [132], a pseudo Monte Carlo transport code, which was developed in Karlsruhe for the fast breeder reactor in the 1970s [133].
- Russia*  
*USA*  
*Finland*  
*China*  
*France*  
*UK*  
*Germany*
- USA* The most recent development is the publicly available MIT OpenMC [94]. Although mostly written in Fortran 90, it features a Python [134] API and XML geometry definition files as well as Jupyter [135] notebook parsers.

[i] Still holding the claim that TART would be the fastest Monte Carlo available.

## URANOS

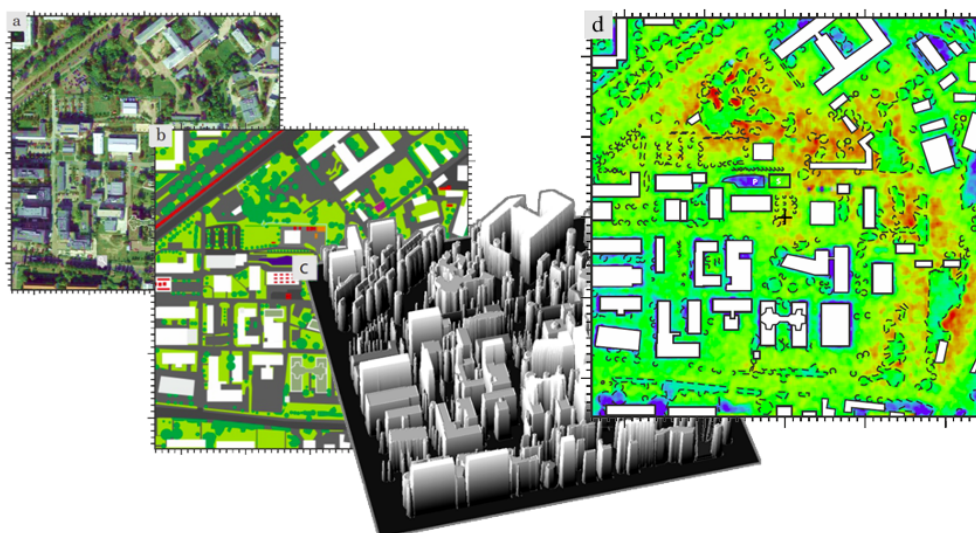


Figure 21: URANOS modeling process, exemplarily for a neutron density in an urban environment: a) Choice of a simulation context, b) Transfer to a (layered) pixelated image, c) Extrusion of a voxel model by the geometry unit and d) Export of the result - here: the above-ground neutron density in a chosen energy interval.

The acronym URANOS stands for **Ultra Rapid Neutron-Only Simulation**. The program is designed as a Monte Carlo tool which simulates exclusively contributions in a detection environment from neutron interactions. The standard calculation routine features a ray casting algorithm for single neutron propagation and a voxel engine. The physics model follows the implementation declared by the ENDF database standard and was described by OpenMC [94]. It features the treatment of elastic collisions in the thermal and epithermal regime, as well as inelastic collisions, absorption and emission processes such as evaporation. Cross sections, energy distributions and angular distributions were taken from the databases ENDF/B-VII.1 [97] and JENDL/HE-2007 [98]. The entire software is developed in C++ [136], linked against CERN's analysis toolbox ROOT [137], whereas the GUI uses the QT cross-platform framework [138]. This section focuses on the computational and physical description, the user interface is explained and displayed in appendix B.3.

The choice for creating an own independently operating Monte Carlo based program apart from the software mentioned in section 5.2 was based on evaluating the specific demands of understanding the physics of neutron detectors. The key ideas are:

- Most of the existing codes are not publicly available and fall under the export control law for nuclear related technology - whereas the underlying data bases are free of access. High precision detector development is not a use case which is envisaged by the authorities.
- Most of the existing codes were developed in the 1970s or 1980s. Written in the procedural programming language Fortran, which has been proven useful in the ages of limited execution orders and memory, but nowadays suffers the drawback of requiring sophisticated and time consuming code tuning, these tools in the best case received wrappers in C, rarely in C++. Today, facing multithreading, distributed network topologies and distributed memory in abundance, the changes of computing technology also have a strong impact on the code design and coding strategies.

- Meanwhile even more complex mathematical operations are readily available from standard packages like the GSL [139] (GNU Scientific Library) and frameworks such as Root [137].
- The majority of codes focuses on the evaluation of radiation sources, including gamma emissions. Signal generation in a boron based hybrid detector requires two additional steps of charged particle transport mechanisms - within the conversion layer itself and subsequently in the gas. In the most cases it is not possible to integrate such a calculation path directly, but it would have to be added on top of the simulation. Furthermore, typical codes expect for the geometry objects of roughly equal size - boron layers having an aspect ratio of  $10^5$  due to the low thickness cannot be described.
- All available codes propagate a take-off amount of neutrons in time due to the fact that in typical applications concerning criticality calculations the neutrons themselves change the state of the environment, for example by generating a significant amount of heat. Therefore, the whole ensemble has to be propagated, especially until an equilibrium state is reached. Due to limited computing resources this also required the multigroup method, see also the following key point.
- The multigroup method is a technique, which allows significant improvement of the calculation speed by not treating every neutron track individually but assigning an effective weight to propagating particle. This weight gets increased for (n,xn) processes and reduced, if a neutron is absorbed or loses enough energy to drop out of a specific interval. The method is derived from solving Fermi age diffusion equations [140] and is applied in many codes. However, it requires many interactions to generate enough randomness and thus it leads to a significant bias whether or not a neutron will undergo most probably only one collision. Yet, for the study of background contributions in detectors or albedo neutrons, such a systematic error should be avoided.

The only software package which does not suffer from the mentioned drawbacks was GEANT4. But at the beginning of this work the code did not at all feature any accurate low energy neutron calculation. Materials in GEANT4 are usually described under a free gas assumption with unbound cross sections with no information about interatomic chemical bindings, this especially comes into account when treating hydrogen collisions<sup>[a]</sup>. Therefore, the main part of the relevant physics would still have to be integrated. In conclusion it has been decided to focus on a design from scratch in modular, object oriented language.

## 6.1 | URANOS CONCEPTS

The buildup of the software can be motivated based on the following general aspects:

- The geometry is represented in a 3-dimensional coordinate space.
- In typical situations the number of neutrons can easily reach  $10^9$ , whereas the relevant neutrons contributing to an observable might scale down this initial amount by more than  $10^6$ .
- Neutrons are neither as abundant nor as simple to describe as necessary to apply means of ensemble statistics.

[a] GEANT4 though can be coupled to the constantly developed models for evaluating the JEFF-3.X [141] ACE formatted thermal scattering law files. For scattering in crystal structures meanwhile the NXSG4 extension [142] has been released.

- Neither energy nor particle number is conserved, moreover both are linked to each other depending on the medium, which implies complex transport equations, that often can only be solved numerically.
- In general interactions are not deterministic but of statistical nature.
- Important parameters like cross sections cannot be derived but are to be extracted from data bases.
- Whereas possible physical interactions are numerous, the relevant ones within a specific energy interval are predominately not more than two different types.
- Secondary particles, except conversion ions, are typically not contributing.

One specific feature of URANOS is its layer geometry, which takes advantage of the symmetry of the envisaged problem. The concept is presented in Fig. 22. In one case a neutron detector has to be simulated which consists of several mostly identical layers of a boron coated substrate. Whereas along the horizontal and vertical axes the geometric scales vary significantly, the mean free path lengths are comparable. For example the absorption probability for a neutron in a 500 nm film of boron might be around 3 %, the scattering probability in a polymer foil of 100 times the thickness is approximately the same number and in the air gap of 100 times the thickness of the plastic it may be 0.3%. This also means that the spatial definitions in such a simulation should not be build on concepts requiring objects of roughly equal size. The solution of URANOS is using layers. This allows to easily build up a geometry of homogeneous materials with the main parameter being position and height of such a layer. Each layer furthermore can be sub-structured by twodimensional matrices into voxels.

URANOS uses ray casting [143], a technique, which refers to conducting a series of ray-

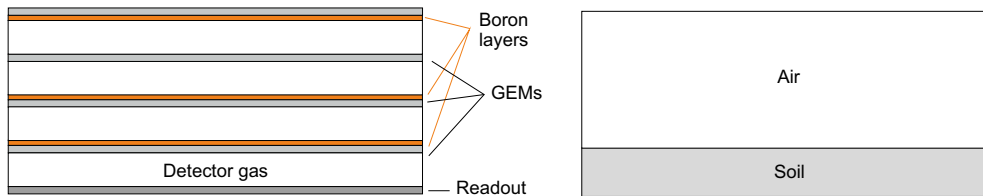


Figure 22: Idea of the URANOS layer geometry representing two problems: (left) simulation of a neutron detector consisting of a stack of substrates coated with a converter and (right) evaluating the propagation of albedo neutrons.

surface intersection tests in order to determine the first object crossed by tracks from a source. These intersections are either defined by analytical surfaces, like the layer structure, or computed from extruded voxels, which do not at all consist of surfaces. Similar types of geometry definitions with mixed volume and surface data were for example used in early computer games when no powerful hardware acceleration was available<sup>[b]</sup> and nowadays for X-ray tomography image reconstruction in material research [144], geosciences [145] and especially medical imaging [146]. The method of ray casting also allows to only record and store the variables necessary for each run. The neutron is physically propagated forward in time through the domain and flags are used as boolean operators for each possible output. If for example the recording observable is defined as the density above the surface not the whole track but only the tracklet within the layer above the ground is kept in the memory.

[b] Notable examples are the Voxel Space engine by NovaLogic or the GAIA/Paradise-Engine by Appeal.

The basic concept of URANOS relies on looping over a set of neutrons, which features initial conditions, predefined or randomized, and for each neutron a loop tracking its path through the geometry. Both entities are referred to as 'stacks'. In each step the geometrical boundaries are determined and handed over to the physics computation unit. For specific cases actual variables of the neutron or its track history are recorded emulating a real or a virtual detector. This process is called 'Scoring' and can be invoked when passing a layer or an absorption in a converter takes place. A track is defined as the shortest path between two points of interaction. It can, as will be seen later, be cut by layer or material boundaries, which dissects it into tracklets. The pseudo flow chart of Fig. 23 illustrates the entire simulation process, which will be described in the following.

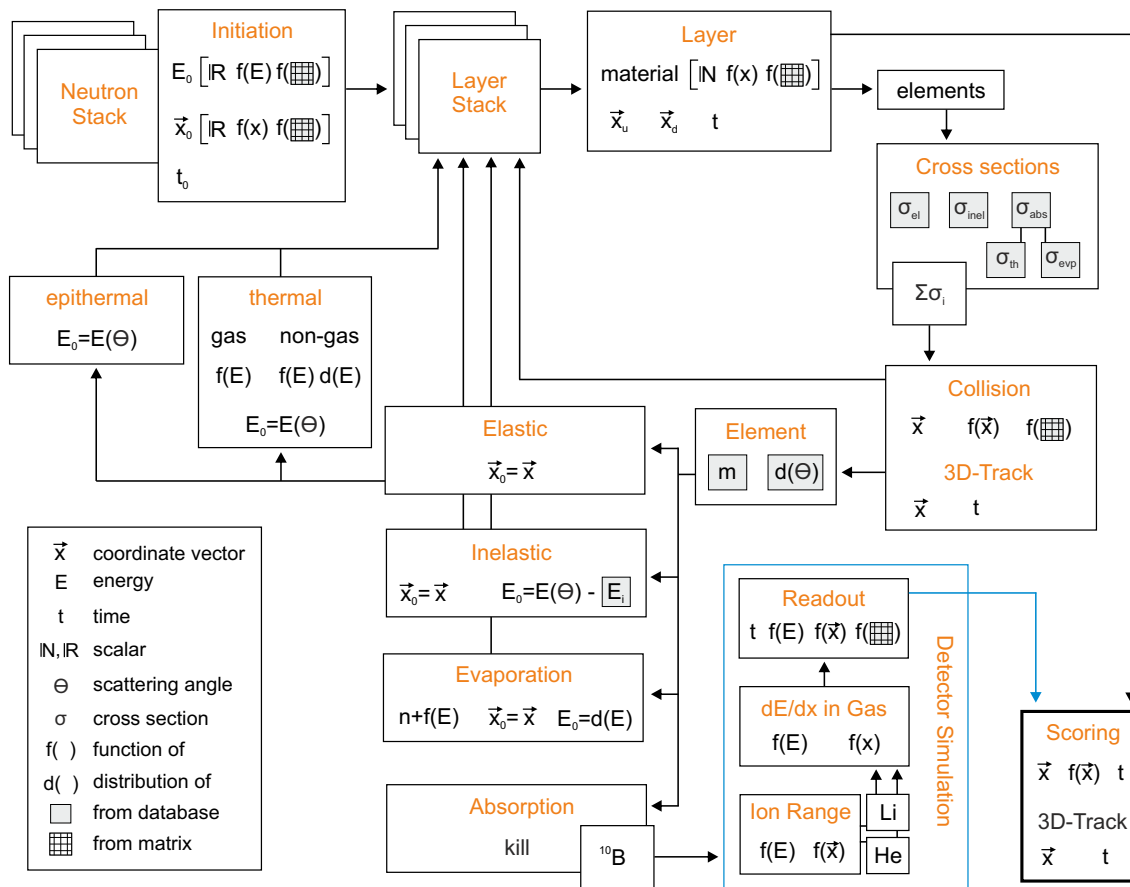


Figure 23: Pseudo flow chart of the internal buildup of URANOS. Each calculation step is represented by a block describing the structural function in orange and the corresponding physics variables.

### 6.2.1 | STARTUP

Before the main calculation routine shown in Fig. 23 three steps are performed:

- Assigning memory to objects, which will be used throughout the calculation, by creating empty containers. These are at least 50 one and two dimensional root histograms.
- Reading the configuration files, creating the geometry and, if available, reading the voxel extrusion matrices.
- Reading the necessary tables from the ENDF library [99], see also sec. 5.1.4.1.



The configuration is split into two files, one containing the basic settings for URANOS, like the number of neutrons to calculate and furthermore import and export folders for the data, and one containing information how to geometrically structure the layers, see here also the next sec. 6.2.2.

Cross sections and angular distributions are read from tabulated ENDF files, exemplarily shown in Fig. 24, grouped into absorption, elastic and inelastic scattering. Exemplarily for  $^1\text{H}$ ,  $^{10}\text{B}$  and  $^{16}\text{O}$  the selected cross sections to be loaded are shown in tab. 7, whereas the full list of available isotopes can be found in appendix B.1.2. For the selection only

Isotope	Elastic	Inelastic	Absorption
$^1\text{H}$	MT=2 (MF=3, 4)	n/A	MT=5, 102, 208-210
$^{10}\text{B}$	MT=2 (MF=3, 4)	MT=51-54	MT=107
$^{16}\text{O}$	MT=2 (MF=3, 4)	MT=51-70	MT=5, 102, 103, 107, 208-210

Table 7: Example cross sections according to [99] and chapter 5.1.4.1.

MT numbers with significant contributions are taken into account, which translates to omitting processes with overall less than  $10^{-2}$  % of the total cross section. Furthermore, the cross section tables are compressed before loaded into the program. Except for hydrogen, the algorithm skips every new value with a relative difference of less than 1 % to its non-skipped predecessor, removing 0 % (rare elements) to 98 % (iron) of data, which saves a significant amount of iteration steps in the process of the cross section lookup, see sec. 5.1.4.3. The smallest error listed on cross sections can be found for elastic scattering of hydrogen with 0.3 %, other isotopes exhibit standard deviations of 1 % and larger, which justifies the compression method. For calculating the total

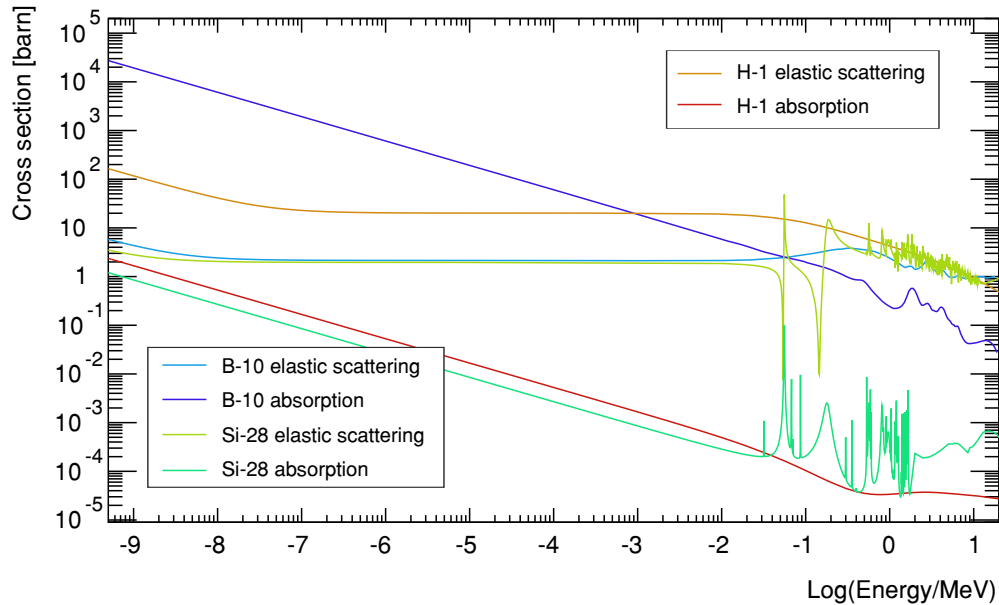


Figure 24: Examples of cross sections for the light isotopes hydrogen (efficient moderator), boron (efficient absorber) and silicon (transparent) from the ENDF library [97] from thermal energies in the meV domain to the MeV range.

macroscopic cross section the individual contributions of elastic  $\Sigma_{\text{el}}$  and inelastic  $\Sigma_{\text{in}}$  scattering as well as absorption  $\Sigma_a$  are summed up

$$\Sigma_t = \Sigma_a + \Sigma_{\text{el}} + \Sigma_{\text{in}}, \quad (95)$$

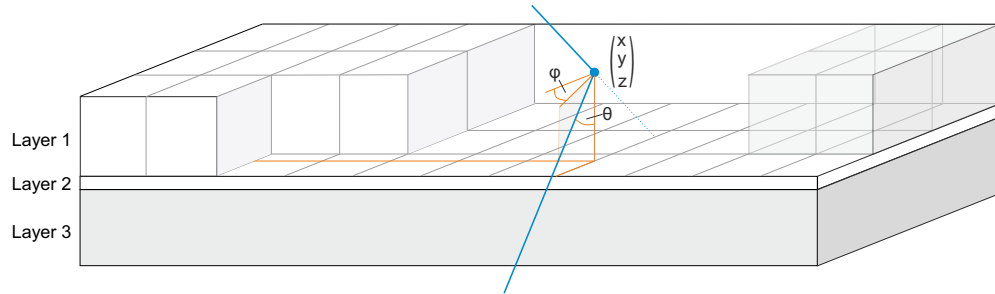
whereas for 'inelastic' cross sections the integrally mainly contributing ones are summed up, see table 14, and 'absorption' itself is understood as a sum of MT numbers stated in table 7, which can either lead to capture without consecutive particles or the creation of new neutrons by for example evaporation or charged particle ejection by converters.

URANOS uses analytical definitions and voxel geometry as introduced in sec. 6.1. The following top-down structure is applied for describing the simulation environment:

geometry  $\rightsquigarrow$  layer  $\rightsquigarrow$  voxel mesh  $\rightsquigarrow$  material  $\rightsquigarrow$  isotope

Fig. 25 illustrates the buildup of such a structure of three layers. A thick and a thin solid layer are combined with a voxel geometry creating an arbitrary arrangement of materials of different density and air. Each layer of the stack is either entirely composed

Figure 25: Schematic of the URANOS geometry definition for layers of different height (black) and tracks (blue). Layer 1 is defined by a voxel mesh, Layer 2 and 3 contain a uniformly defined material.



of a solid or subdivided into several sections using a twodimensional matrix from which voxels are extruded. The solids are filled with predefined materials. A material is a specific atomic composition of isotopes with their atomic weight and density. Table 8 provides an example of such a definition, whereas all available materials can be found in appendix B.1.3. Most compounds are taken from [147]. The voxel mesh is auto-

Material	Density	Composition
Air	1.2 kg/m <sup>3</sup> NTP	78 % <sup>14</sup> N <sub>2</sub> , 21 % <sup>16</sup> O <sub>2</sub> , 1 % <sup>40</sup> Ar
Boron	2.46 g/cm <sup>3</sup>	80.1 % <sup>11</sup> B, 19.9 % <sup>10</sup> B

Table 8: Example composition of the material 'dry air' and a neutron converter.

matically loaded if a file with a name corresponding to a layer number is found. It can be either a tab separated ASCII [148] matrix of equal row and column rank or a quadratic portable network graphics (PNG) [149] image. The integer values  $w$  or grayscale values denote the material numbers which primarily override the global layer definition. Typically solids are directly extruded from these values, yet there are three further declaration modes:

- the material is soil and  $w$  defines the amount of water in volume percent,
- the material is defined globally by the layer and  $w$  scales the density,
- the material is defined globally by the layer,  $w$  scales the height of this material and the remaining volume extended to the full layer height is filled with air.

The layers can be stacked on top of each other with individual definitions to realize complex geometries. Fig. 26 provides examples to illustrate the scope of applications (not discussed here) and the scales which can be targeted. The images of one single layer act hereby as sectional view. Especially landscapes can be modeled using the third declaration mode, an example is provided in Fig. 27. The geometry of each layer is simply defined by an array of 8 elements:

$$g = [x \text{ lower bound}, x \text{ upper bound}, y \text{ lower bound}, y \text{ upper bound}, \\ \text{upper } z \text{ position, height, material, layer number}], \quad (96)$$

whereas the lateral lower and upper bounds are defined globally and the layer number acts as an additional identifier to create subgroups within the stack. Furthermore,

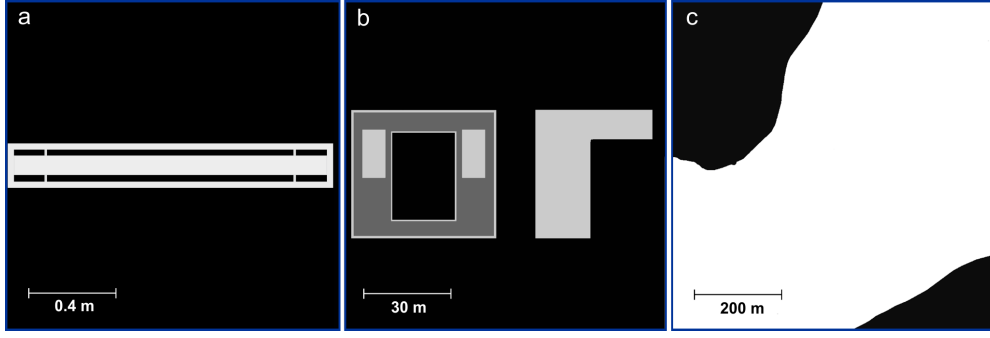


Figure 26: Examples of layers for voxel geometry definitions (all in top view): a) a moderated 2 inch proportional counter, b) the rooftop of the Physikalisches Institut in Heidelberg, c) a part of a lake where a buoy has been deployed. Grayscale values define preconfigured materials.

the forward and backward propagation direction are defined according to if the layer number along the path increases or decreases, respectively.

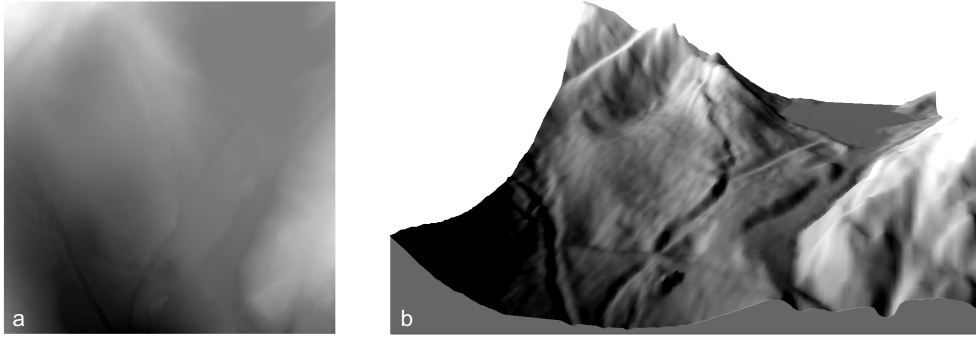


Figure 27: Example of a complex layer structure in voxel geometry for a digital environmental model (Kaunertal Glacier at N46° 52.2 E10° 42.6). (a) Grayscale image with  $500 \times 500$  pixels at a lateral resolution of 1 m and 0.5 m in height by the 8 bit gray card. (b) Shaded illustration of the resulting layered voxel structure of soil/air.

Neutron tracks  $\vec{S}$  are described by a mixed geometry definition of support vectors  $\vec{x}$  in Cartesian<sup>[c]</sup> coordinates and spherical direction vectors  $\vec{r}$ :

$$\vec{x} = \begin{pmatrix} x \\ y \\ z \end{pmatrix} \quad \text{and} \quad \vec{r} = \begin{pmatrix} r \\ \vartheta \\ \phi \end{pmatrix}, \quad (97)$$

denoting the three spatial coordinates  $x, y, z$  and the angles  $\vartheta, \phi$  with the range  $r$ . The choice for this system is due to the fact that this characterization provides direct access to the necessary observables. Examples are point sources which are randomly distributed in both angles or detector planes for which the beam inclination is an important parameter considering sensitivity. Hence new coordinates  $\vec{x}'$  are calculated by

$$\vec{x}' = \begin{pmatrix} x \\ y \\ z \end{pmatrix} + \begin{pmatrix} r \cos(\phi) \sin(\vartheta) \\ r \sin(\phi) \sin(\vartheta) \\ r \cos(\vartheta) \end{pmatrix}$$

and for determining the position on a layer at elevation  $z_L$

$$\vec{x}_L = \begin{pmatrix} x \\ y \\ z \end{pmatrix} + (z - z_L) \begin{pmatrix} r \cos(\phi) \tan(\vartheta) \\ r \sin(\phi) \tan(\vartheta) \\ 1 \end{pmatrix}.$$

[c] René DESCARTES, \*1596-†1650, France.

Time is an indirect quantity. It is derived from the geometrical position of the neutron calculated from energy and initial conditions.

In URANOS three layers can be assigned specific functions. These are source layer, detector layer and ground layer. The **source layer** defines the origin for all neutron histories. Especially all height values for starting positions, see also sec. 6.3, are restricted to be initiated here. This layer may neither be the upper- nor lowermost as otherwise neutrons would escape the computational domain. The **ground layer** is used in cosmic neutron simulations to record the spectra at the air/ground interface. In the **detector layer**, which can be superimposed to another layer, either single real or virtual detectors can be placed, or the layer itself acts as a virtual detector and records every neutron passing, see also sec. 6.5.

### 6.3 | SOURCES AND ENERGY

URANOS provides a variety of sources. A source is defined by a spatial distribution and an energy spectrum from which random values are sampled. They are either defined as

- point sources with all neutrons starting from the same coordinate vector,
- a plane source with all neutrons sharing the same  $z$  coordinate within lateral boundaries,
- a volume source, which randomly distributes neutrons in the source layer within lateral boundaries, and alternatively extends the volume source downwards to the ground layer with exponentially distributed height values<sup>[d]</sup>.

As explained in sec. 6.2.2 the source has to be placed in the source layer, which defines its  $z$ -position. For the coordinates  $(x, y) \in A$  in the source area  $A$  in case of plane or volume sources the options are:

- rectangular boundaries with either equal aspect ratio (square) or any other, sampling the origins uniformly from possible positions in  $(x, y)$ , and
- circular boundaries, sampling the origins either uniformly in radius  $r$  from the center or in  $(x, y)$ .

Furthermore, the starting angle  $\vartheta$  can be set to:

- full or half sphere, sampling  $\vartheta$  in  $[0 \dots \pi]$  or  $[0 \dots \pi/2]$ , or
- unidirectional beam, which allows to set theta to a specific inclination. Additionally a divergence  $s_\vartheta$  can be chosen. Then, the angles are sampled from a gaussian function centered around  $\vartheta$  with a width of  $s_\vartheta$ .

The starting energy for the neutrons are derived from normalized distributions, which are described in the following sections. The method of sampling by rejection is applied according to (72) in sec. 5.1. For source definitions on a linear support in  $[a, b]$ , like in sec. 6.3.2, the random variable  $\xi \in [0, 1]$  is scaled to the abscissa test quantity

$$\xi_t = a + (b - a)\xi.$$

For source definitions on a logarithmic support in  $[10^a, 10^b]$ , like in sec. 6.3.1,  $\xi$  is scaled to

$$\xi_t = 10^{a+(b-a)\xi}.$$

[d] This option is called artificial cosmic source and accounts for neutrons which are generated by physical processes URANOS is not capable of simulating like high energy protons, myons or induced cascades thereof.

### 6.3.1 | THE COSMIC NEUTRON SOURCE

The cosmic neutron source definition is specifically designed for the problem of soil moisture dependent neutron transport in the vicinity of the atmosphere-soil interface. Instead of propagating primary particles through several kilometers of atmosphere, a source definition near the ground level is chosen. Recent works, especially from Sato et al. [66], have provided analytical functions modeling cosmic-ray spectra for various conditions. As such spectra are always integrated over all trajectory angles, based on these models, which are covered in sec. 3.2, a net incoming spectrum has been reconstructed. The procedure and a detailed description can be found in sec. 9.1.1 and the result is used as the generalized cosmic neutron incoming spectrum. Further explanation about the composition and features can be found in sec. 3.1.

Fig. 28 shows the URANOS cosmic-ray neutron spectrum (cyan) and exemplarily the total spectrum above ground for dry conditions. The energy of neutrons can range over more than 12 orders of magnitude. The plot here as well as the following will be presented logarithmically in units of lethargy, see (33) in sec. 1.4.1. The intensity  $I$  or flux density per logarithmic unit of energy is given in units of

$$I = d\Phi/d(\log(E)) = E d\Phi/dE. \quad (98)$$

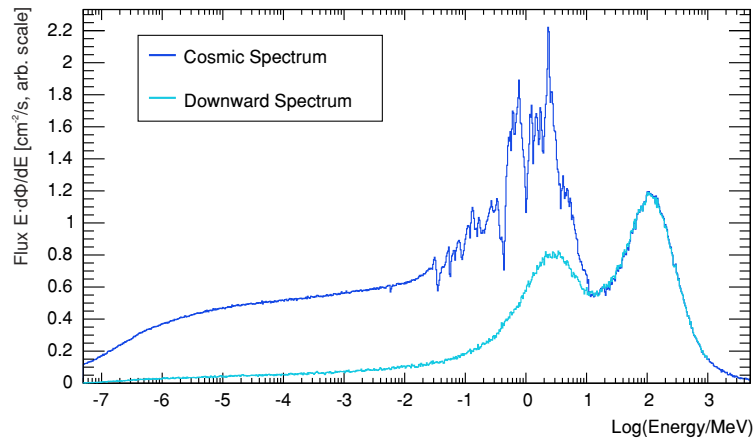


Figure 28: The URANOS Cosmic Neutron Source Spectrum: Total angular integrated flux after interaction with the soil (blue) and only incoming flux (cyan).

### 6.3.2 | GENERAL SOURCES

Besides the cosmic neutron source definition in sec. 6.3.1, which expands over several decades of energy, energy distributions for specific sources have been implemented. These available source configurations allow sampling from thermal as well as fission spectra. Exemplarily some are shown in Fig. 29.

- **Monoenergetic:** neutrons of energy  $E$  or wavelength  $\lambda$ ,
- **Thermal:** neutrons at a temperature  $T$  described by a Maxwellian distribution

$$N(E) = \frac{E}{(k_B T)^2} \exp\left(-\frac{E}{k_B T}\right). \quad (99)$$

- **Predefined:** americium-beryllium spectrum from [150],
- **Evaporation:** assuming the nucleus to form a degenerate Fermi gas [151] one can derive various forms of density distributions

$$N(E) \propto E \exp\left(-\frac{E}{k_B T}\right), \quad (100)$$

which are simply described by a temperature parameter [152]. Therefore, the energy distribution of the neutrons released by fission are commonly represented either by a Maxwellian distribution or the following Watt spectrum [153].

- **Fission:** A semi-empirical description is the Watt spectrum [154], especially used for  $^{235}\text{U}$ , which can be selected as a source although the isotope itself is not implemented,

$$N(E) = 0.4865 \sinh(\sqrt{2E}) \exp(-E), \quad (101)$$

and for  $^{252}\text{Cf}$  [155]

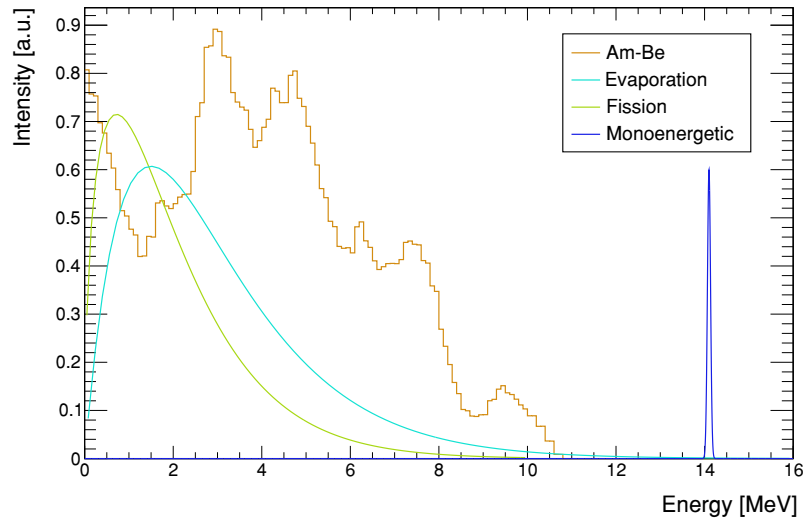
$$N(E) = \sinh(\sqrt{2E}) \exp(-0.88E), \quad (102)$$

which are both specific cases of the more general form of a Maxwellian distribution<sup>[e]</sup>, which allows a more accurate modeling by introducing the Watt parameters  $a$  and  $b$  taking into account the mean neutron kinetic energy of and those of the fission fragments:

$$N(E) = 2 \frac{\exp\left(-\frac{ab}{4}\right)}{\sqrt{\pi a^3 b}} \sinh(\sqrt{bE}) \exp\left(-\frac{E}{a}\right). \quad (103)$$

The parameters  $a, b$  are typically tabulated as a function of energy, element and isotope.

Figure 29: Different preconfigured source distribution functions in URANOS in the MeV range covering different use cases: laboratory test sources like americium-beryllium (yellow) with a variety of resonances, spontaneous fission (green), evaporation (cyan) from de-excitation and fusion (blue)



## 6.4 | CALCULATION SCHEME

### 6.4.1 | LOOP NODES

URANOS runs in the main calculation routine on two loops, these are

Neutron Stack  $\rightleftarrows$  Layer Stack

whereas both are used differently - each onset neutron is a placeholder and only initialized at runtime. Furthermore, the particle number is not conserved due to physical

[e] Although several earlier reports before [154] mention this formula, none of them states the origin.

processes generating neutrons, which are lined up in the stack. The layer stack is created at startup and consists of a fixed amount of elements which are traversed by an iterator either forwards or backwards, depending on the direction vector. The possible initial conditions for neutrons are

- energy: available source definitions from sec. 6.3, which can be either real values, normalized functions to be sampled from or lookup tables.
- geometry: definition from sec. 6.2.2, which can be either a fixed vector from a source, a distribution function to be sampled from or lookup tables, which are normalized at startup.
- time: either a real value or a function<sup>[f]</sup> to be sampled from.

Using these initial conditions the loop over the layer stack commences. Each layer, which is geometrically described in sec. 6.2.2, can either consist of a homogeneous material defined by its isotope composition, a material defined by an analytical function or an input matrix from which voxels are extruded. A comprehensive material list is provided in appendix B.1.3. The neutron iterates to the following layer if it geometrically leaves the boundaries and no change of materials can be found in the collision detection. Otherwise the layer iterator keeps its value and if the neutron has not been absorbed, the calculation procedure is repeated with an updated history.

#### 6.4.2 | TRACKING IN FINITE GEOMETRY REGIONS

For each layer the material setup is loaded according to the actual spatial position of the neutron. The definition either accounts integrally for the whole layer or for regions, which can be described by analytic functions or voxelwise. For the selected material the total macroscopic cross section  $\Sigma_t$  is composed isotope by isotope. The amount and type of reactions (MT identifiers), loaded according to sec. 5.1.4.2, depends on the element, see also the description in sec. 6.2.1 or the isotope list in appendix B.1.2. Elemental hydrogen for example cannot undergo inelastic scattering and  $^{10}\text{B}$  exhibits a negligible radiative capture, so only charged reaction paths are relevant. The selection criteria in detail are

- elastic and absorption cross sections are always calculated if available.
- inelastic cross sections are loaded for energies  $750 \text{ keV} < E < 50 \text{ MeV}$ .

Using the macroscopic cross section  $\Sigma_t$  defined by (14) the free path length  $l$  is sampled from a random number  $\xi$  as described in sec. 5.1.2 from (78):

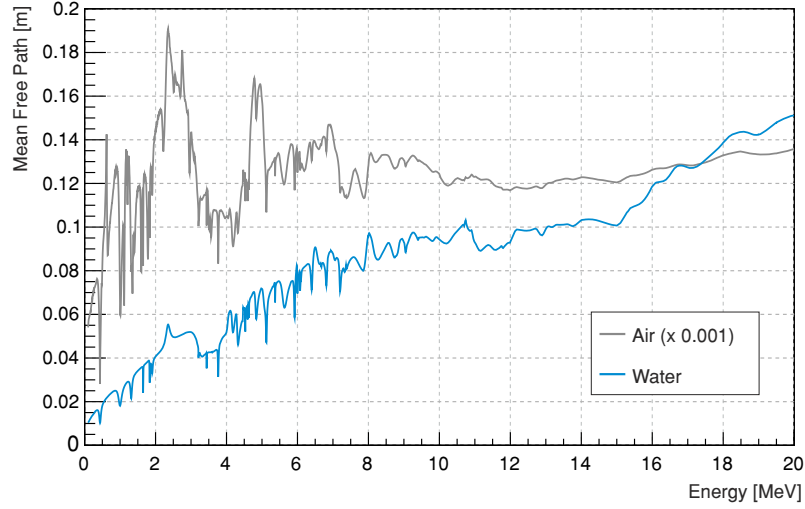
$$l = -\frac{\ln(\xi)}{\Sigma_t}. \quad (104)$$

In case the material definition contains a density multiplication factor, it is applied to  $\Sigma_t$  before evaluating (104). The distance to the border  $l_{\text{tj}}$  is calculated by the  $z$ -coordinate of the last interaction of the neutron  $z_o$  and the layer  $z$ -position  $z_l$  and height  $d_l$

$$l_{\text{tj}} = \begin{cases} \left| \frac{z_l + d_l - z_o}{\cos(\vartheta)} \right|, & \text{if already scattered within the layer and forward,} \\ \left| \frac{z_o - z_l}{\cos(\vartheta)} \right|, & \text{if already scattered within the layer and backward,} \\ \left| \frac{d_l}{\cos(\vartheta)} \right|, & \text{otherwise (crossing).} \end{cases} \quad (105)$$

[f] such a function would for example be a phase for the polarization vector in NRSE.

Figure 30: Mean free path  $1/\Sigma_t$  for neutrons in the MeV range. The dominant peaks originate from the contribution of the elastic scattering cross section, in dry air (NTP) mainly by nitrogen, in water by oxygen, see also Fig. 31.



In case the material is defined by voxels, additionally a procedure is applied, which samples the trajectory according to the underlying pixel matrix:

- determination of the z-projected length  $z_m$  of one lateral unit pixel  $s_p$  for the actual direction vector by  $z_m = s_p / \tan(\vartheta)$ . The unit pixel size is determined by the spatial extension of the domain divided by the number of pixels.
- If the material of the voxel at  $\vec{x}'$  for  $z_o \pm z_m$  is different from the actual, stop and repeat the range calculation for the actual composition and geometry. If the material does not change iterate  $\pm z_m$  until the end of the layer. The propagation direction, forward or backward, determines  $\text{sgn}(z_m)$ .

If  $l_{\text{trj}} > l$  no interaction takes place and the neutron can proceed to the following layer. If  $l_{\text{trj}} < l$  the spatial coordinates of the interaction  $\vec{x}_i$  are calculated by

$$\vec{x}_i = \begin{pmatrix} x_o \\ y_o \\ z_i \end{pmatrix} + \begin{pmatrix} \cos(\phi) |\tan(\vartheta)(z_i - z_o)| \\ \sin(\phi) |\tan(\vartheta)(z_i - z_o)| \\ 0 \end{pmatrix}, \quad (106)$$

whereas the new z coordinate is given by

$$z_i = \begin{cases} z_l + |\cos(\vartheta)l_{\text{trj}}|, & \text{if not scattered within the layer and forward,} \\ z_l + d_l - |\cos(\vartheta)l_{\text{trj}}|, & \text{if not scattered within the layer and backward,} \\ z_o + |\cos(\vartheta)l_{\text{trj}}|, & \text{if scattered within the layer and forward,} \\ z_o - |\cos(\vartheta)l_{\text{trj}}|, & \text{if scattered within the layer and backward.} \end{cases} \quad (107)$$

Consecutively the type of reaction is determined by another random number  $\xi$  by intervals of the relative fraction of the constituents of the macroscopic cross section:

$$\begin{aligned} \xi < \frac{\sigma_{\text{el}}}{\sigma} & \quad \leadsto \quad \text{scattered elastically,} \\ \frac{\sigma_{\text{el}}}{\sigma} < \xi < \frac{\sigma_{\text{el}} + \sigma_a}{\sigma} & \quad \leadsto \quad \text{absorbed,} \\ \xi > \frac{\sigma_{\text{el}} + \sigma_a}{\sigma} & \quad \leadsto \quad \text{scattered inelastically,} \end{aligned} \quad (108)$$



as the probability of selecting a reaction  $i$  from all possible reaction channels is

$$p_i = \frac{\Sigma_i}{\sum_{j=0}^n \Sigma_j} = \frac{\Sigma_i}{\Sigma_t}$$

The target interaction element is determined by a randomly choosing from a proportional lookup table. Each reaction type is accompanied by two vectors - one `<double>` represents the cumulative probability distribution  $v_s$  and one `<int>` a list of corresponding elements  $v_e$ <sup>[g]</sup>:

$$v_s[n] = \left\{ i \mid \sum_{j=0}^i \Sigma_j \right\}, \quad (109)$$

$$v_e[n] = \{i \mid \text{isotope of } i\}. \quad (110)$$

For inelastic scattering additionally the excited state of the target isotope has to be determined. One vector vector of `<double>` like in (110) contains the cumulative cross section distribution and two support vectors contain the  $q$ -values representing the energy loss in MeV in a `<float>` list and the inelastic angular distributions in a `<TMatrixF>` list.

The individual contributor, which will be used to determine the reaction target, is chosen by a random number  $\xi$ . If

$$v_s[i] \leq \xi \leq v_s[i+1], \quad \forall i > 0, \quad (111)$$

then the corresponding isotope is taken from  $v_e[i]$ <sup>[h]</sup>.

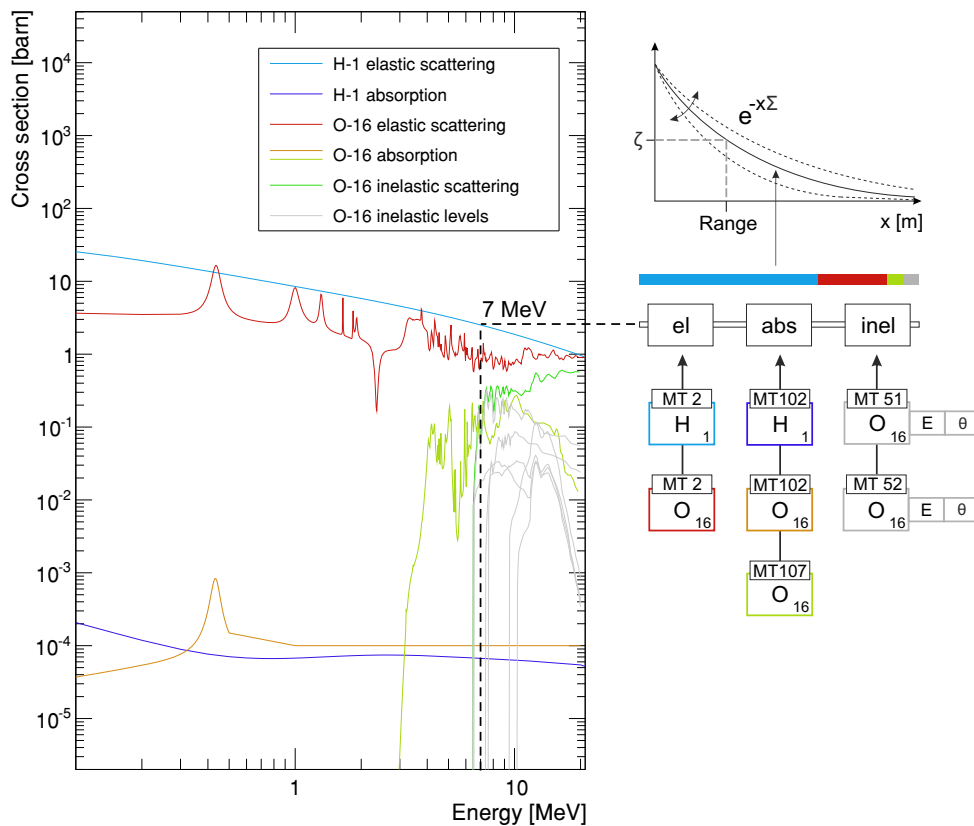


Figure 31: Range calculation in URANOS: For a given neutron energy, here in the MeV range, the cross sections from the isotope list are evaluated according to elastic, inelastic and absorption processes. Only possibly relevant ENDF [97] cards are evaluated. The left panel shows such a list of reaction probabilities for water. Inelastic levels are only displayed up to MT56 and are link additionally to energy loss and angular distribution. The cumulated cross section multiplied by the atom number density (14) yields the macroscopic cross section (10). By sampling a random number  $\xi$  as in (78), a free path length value for the range (77) is obtained.

[g] Example: Natural boron, see also tab. 8, contains  $\approx 80\%$   $^{11}\text{B}$  and  $\approx 20\%$   $^{10}\text{B}$ . For a reaction the cross section  $\Sigma_i = \Sigma_i(^{10}\text{B}) + \Sigma_i(^{11}\text{B})$  is accompanied by a vector of individual contributions  $[\Sigma_i(o), \Sigma_i(o) + \Sigma_i(i)]$  and a vector of isotopes  $[^{10}\text{B}, ^{11}\text{B}]$ .

[h] If  $i = 0$ , then  $\xi \leq v_s[1]$ .

### 6.4.3 | INTERACTION CHANNELS

For each interaction the following quantities are updated:

- the position vector  $\vec{x}$ , including time, by adding the path length  $l$  to the last position,
- the direction vector  $\vec{r}$ ,
- energy, including velocity  $v$  and wavelength  $\lambda$ .

#### 6.4.3.1 ELASTIC AND INELASTIC SCATTERING

Scattering is described by the collision of a neutron with a nucleus of mass  $A$  assuming energy and momentum conservation according to (23), (24) and (25) of sec. 1.4.1. The problem has a radial symmetry regarding the impact parameter, therefore only one angle  $\vartheta_{\text{CMS}}$  has to be calculated. The second angle can be determined by a random number  $\xi$  in  $[0, 1)$

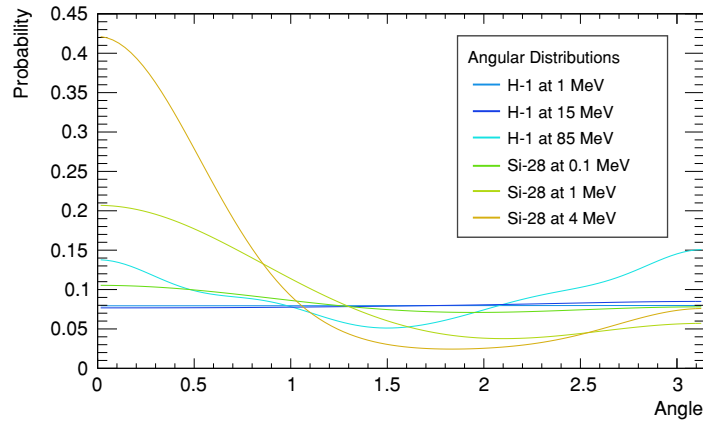
$$\phi_{\text{cm}} = \pi (2\xi - 1). \quad (112)$$

For inelastic scattering the energy loss is substituted by the  $q$ -value obtained from (111) and (110), respectively. The target velocity  $V$  can be neglected for kinetic energies  $E$  of the neutron:

$$V \approx 0 \text{ if } \begin{cases} 0.11 \text{ eV} < E < 1 \text{ MeV} & \text{in case of hydrogen,} \\ 0.15 \text{ eV} < E < 0.01 \text{ MeV} & \text{otherwise.} \end{cases} \quad (113)$$

For **lower energies** the interaction result has to be calculated by laws of thermal scattering taking into account the velocity distribution of the target material. In case of amorphous material or fluids there is no analytical form to describe such, therefore only sampling from an effective thermal spectrum like (99) is carried out. For solids with a crystal lattice Bragg scattering is the dominant channel. The kinetic theory of gases allows a cohesive description of the scattering process. For such the energy and angle are sampled according to (90), (91) and (92) in sec. 5.1.3.

Figure 32: Energy dependent representation of angular distributions in the center of mass frame for two isotopes. Above 20 MeV for hydrogen there are 12 and below 6 Legendre coefficients. For silicon 7,9 and 13 coefficients are given for the stated energies in ascending order.



In case of **higher energies** than stated in the above limits the angular distribution in the center of mass frame can be found in ENDF cards either tabulated or described by Legendre polynomials. Depending on the energy for the interaction a set of (interpolated) factors is compiled according to (93). Exemplarily Fig. 32 shows such distributions. With increasing energy the forward direction is preferred, except for

hydrogen - here the asymmetry is much weaker than for heavy elements and only for very high energies a significant deviation from an even distribution can be observed.

For inelastic scattering with an energy transfer  $E^*$  the evaluation of the angular distributions is carried out likewise, whereas the lowest energy, for which the reaction can occur, is given by the  $q$ -value. Hence, the reaction kinematics of inelastic processes share some similarities with elastic processes of corresponding kinetic energies  $E' = E - E^*$ .

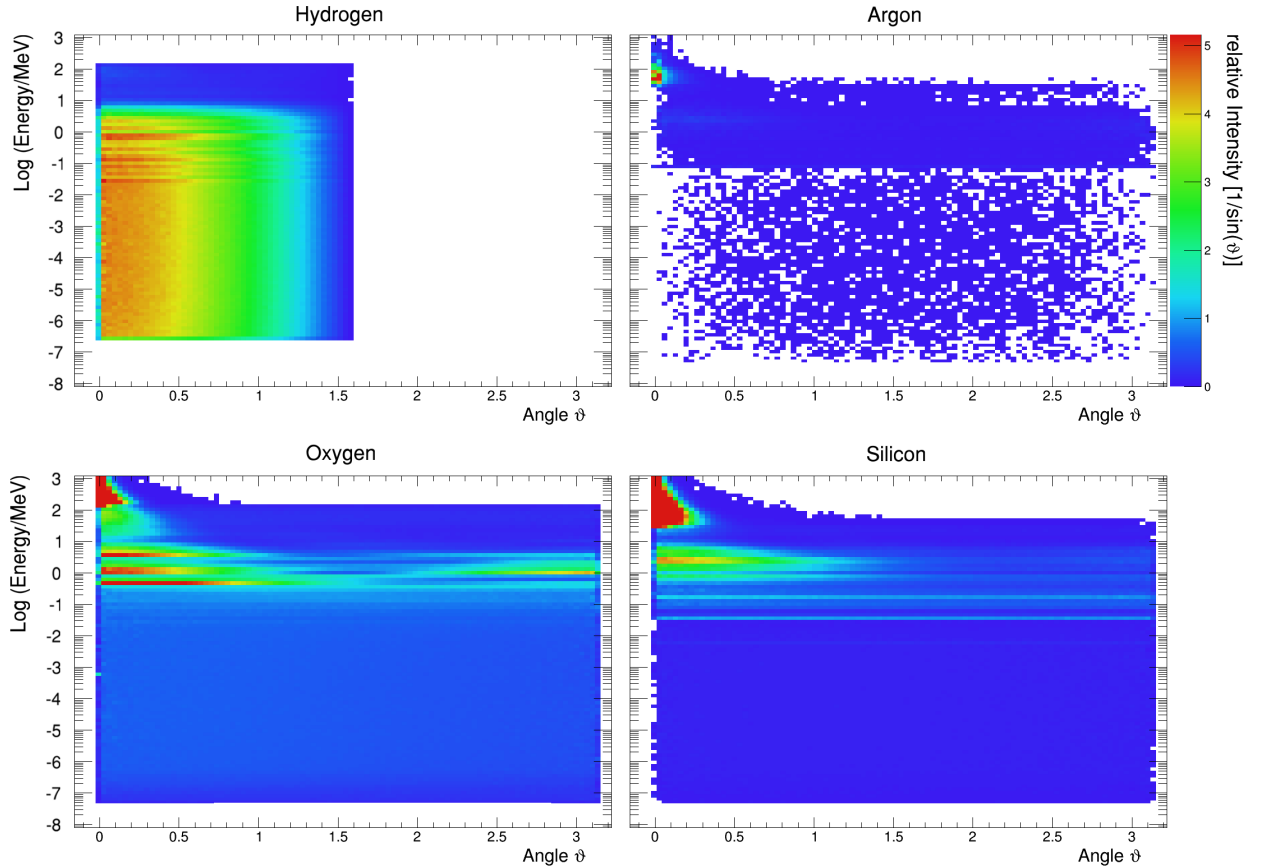


Figure 33: Relative occurrence of scattering angles in an air-ground interface for selected isotopes. The distributions in spherical coordinates are weighted by  $\sin^{-1}$  of the scattering angle for the projection onto the theta axis, see also (91). Due to the neutron having approximately the same mass as the proton in collisions with hydrogen atoms (top left) backward facing angles are not allowed as far as the relative velocity of the target is not considered (thermal cutoff). As the plots show in-situ distributions the dominant features in the MeV region for hydrogen originate from the relative abundance in the corresponding energy range by collisions with other elements, see also Fig. 28 and 31. For oxygen (bottom left) the angular sampling up to 150 MeV is carried out via Legendre polynomials, see for example Fig. 32, and above via tabulated distributions. For other elements like silicon (bottom right) the Legendre representation is typically only available up to 20 MeV.

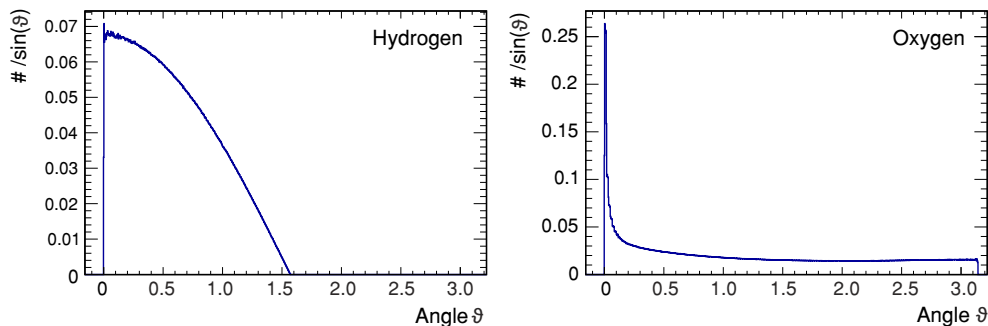


Figure 34: Projection of the weighted scattering angles of the in-situ calculations of Fig. 33 for all energies, exemplarily for H and O.

As the scattering kinematics have been calculated in the center of mass system, a transformation to the laboratory system is carried out via

$$\vartheta_1 = \arccos \left( \frac{1 + A \cos(\vartheta_{\text{cm}})}{\sqrt{A^2 + 1 + 2A \cos(\vartheta_{\text{cm}})}} \right), \quad (114)$$

and added to the existing direction vectors

$$\vartheta_u = \cos(\vartheta^{\text{old}}) \cos(\vartheta_{\text{cm}}) + \sin(\vartheta^{\text{old}}) \sin(\vartheta_{\text{cm}}) \cos(\pi + \phi_{\text{cm}}), \quad (115)$$

$$\vartheta_l^{\text{new}} = \arccos(\vartheta_u), \quad (116)$$

$$\phi^{\text{new}} = \phi^{\text{old}} \pm \arccos \left( \frac{\cos(\vartheta_{\text{cm}}) - \cos(\vartheta^{\text{old}}) \vartheta_u}{\sin(\vartheta^{\text{old}}) \sin(\vartheta_{\text{cm}})} \right). \quad (117)$$

Due to the choice of the coordinate system, see also the geometry definition (97), adding direction vectors is less convenient than the otherwise direct and intuitive declaration. The method presented here equals an Euler<sup>[i]</sup> rotation in  $\theta$  and  $\phi$  around the direction axis given by the trajectory of the particle.

#### 6.4.3.2 EVAPORATION

URANOS simplifies the calculation of the evaporation process as in the low-Z and intermediate energy range most otherwise for fissionable elements discussed quantities are approximately invariable. The mean number of evaporated neutrons can be considered constant  $\bar{n}_{\text{evap}} \approx 1$  for projectile energies below several hundred MeV and mass numbers of  $A < 100$  [156]. Furthermore, for the emission energy a Maxwellian spectrum according to (100) with a mean neutron energy of 1.8 MeV [157] and a flat angular distribution [158] is assumed<sup>[j]</sup>.

#### 6.4.3.3 ABSORPTION

The neutron is either absorbed by a non-radiating process and consequently the calculation is terminated or the material is a specific absorber, which leads to a scoring by the detection unit, see the following sec. 6.5.

A specific case is the High Energy Cascade: URANOS mainly carries out neutron interactions. For the generation of high energetic radiation in the atmosphere charged particles are also largely contributing to the production of the neutron component [159]. As far as for low energetic and albedo neutrons such can be neglected, in order to simulate more than 100 m of atmosphere the generation of the primary spectrum is emulated by an effective model: For any absorption occurring above 16 MeV leading to otherwise the generation of new particles the neutron is not eliminated if a random number  $\xi$  is below a specific value  $k_{\text{HE}}$ , receiving only a fractional energy loss and angular deviation. This value  $k_{\text{HE}}$  is tuned to emulate an effective atmospheric attenuation length  $L_{\text{prim}}$  of the primary spectrum component of  $145 \text{ cm}^2/\text{g}$ <sup>[k]</sup>.

[i] Leonhard EULER, \*1707-†1783, Old Swiss Confederacy.

[j] In order to provide upper limits in comparison:  $^{235}\text{U}$  produces on average  $\approx 2.4 + E/\text{MeV}$  neutrons per fission.

[k] Experimental values for  $L_{\text{prim}}$  are in the range of (135-155)  $\text{cm}^2/\text{g}$ , depending on the site. Here, the value from [66] is taken.

Scoring options are evaluated in the detector layer. For a spatially resolved detector this is the readout structure. For CRNS there are furthermore the following possibilities:

- scoring the coordinates of a neutron passing the upper/lower boundary or the full track within the layer,
- scoring if a neutron track intersects a predefined volume entity, called a detector, and
- scoring for any voxel, which has the material definition to be a 'detector'.

### 6.5.1 | SCORING OPTIONS FOR CRNS

In the most simple case a uniform detection efficiency  $\epsilon$  can be chosen for a specific range of energies, which is a useful configuration for CRNS detectors

$$\epsilon = \begin{cases} 1 & \text{for } E_{\min} < E < E_{\max}, \\ 0 & \text{otherwise.} \end{cases} \quad (118)$$

In order to not model a whole cosmic-ray neutron sensing system in a large environment, the detector has been modeled independently and integrated as an effective model. Fig. 35 shows the implemented functions, which represent averaged values for the whole unit. In this work cubic spline interpolation is used for describing the absolute efficiency and the angular dependence is modeled by

$$\epsilon_{\vartheta} = 1.24 - 0.254 \exp\left(\frac{x}{0.92}\right). \quad (119)$$

As far as thermal neutrons are not considered, the flux in the epithermal/fast region, see also sec. 3.2, can be considered a plateau region, justifying the established choice of (118), see also sec. 8. The options above can be applied to the whole detector layer.

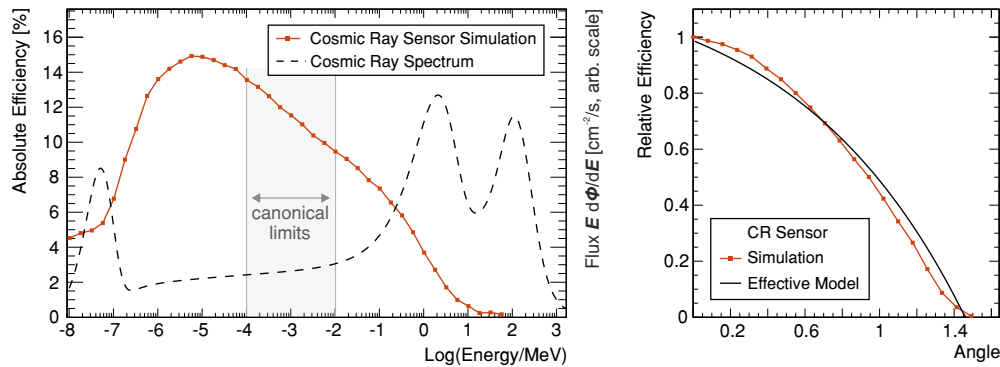


Figure 35: . Detection efficiencies for CRNS detector models. (left) Energy dependent absorption probability for perpendicular irradiation, here: simulation of a monoenergetic beam with results (red markers) averaged over the surface. (right) Energy independent, averaged, angular dependence relative to the left panel.

This allows mainly scoring the upward and downward directed flux. If for example angular resolution is required one can place two types of scoring units within the detector layer, which is either

- a plane in  $z$ -direction, a sphere or a vertical cylinder,

whereas in both cases the radius can be specified<sup>[1]</sup>. The geometrical calculation can be found in the appendix B.1.1 in (159) and (157), respectively.

[1] The cylinder height corresponds to the detector layer. If due to positioning or the choice of the radius of the sphere there is an intersection with the layer boundary only the volume inside the detector layer is taken into account.

## 6.5.2 | NEUTRON CONVERSION EVALUATION FOR BORON DETECTORS

Whereas in gaseous converters like  $^3\text{He}$  regarding the detection efficiency only the macroscopic cross section has to be taken into account, as nearly all converted neutrons can be detected, for hybrid solid state detectors the entire signal generation path has to be considered. Compared to the attenuation length at  $\lambda = 1.8 \text{ \AA}$  of  $20 \mu\text{m}$  the range within a converter layer is  $< 4 \mu\text{m}$ . Even for thin layers therefore the efficiency can be significantly reduced by inactive material. The two main absorption reactions in boron-10 are:

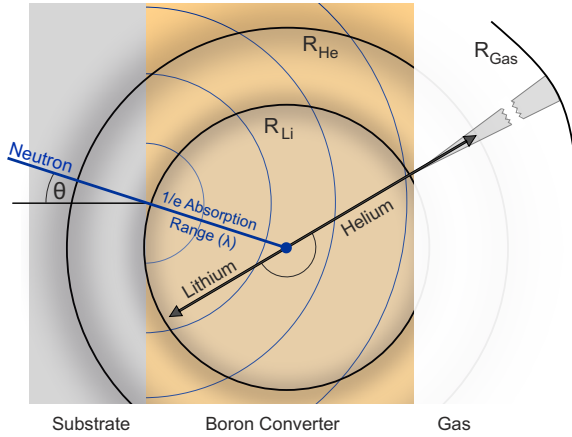
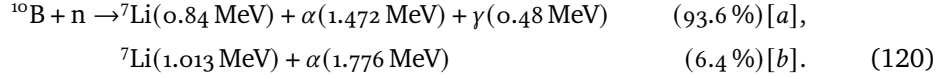


Figure 36: Physics of a hybrid boron converter layer: a neutron impinges at an angle  $\vartheta$  normal to the surface. The absorption probability is wavelength dependent. By the conversion process lithium (Li) and helium (He) ions with fixed energies are created. In the medium itself they lose energy by collisions leading to a Bragg distributed range  $R$ , different for both agents. After reaching the gas an ionization track is produced with the remaining energy at the boundary. [K2016]

In the boron medium itself the particles are emitted isotropically and back to back. Two geometries are possible: (1) the front side irradiation describes the case of the active surface being oriented towards the incoming neutrons and therefore the detection medium being situated prior in beam direction. (2) Vice versa the backside irradiation refers to the inverted geometry. Therefore, as only one of both can enter the gas, a random number  $\xi_1$  determines<sup>[m]</sup> the type of ion  $I$  and another random number  $\xi_2$  assigns the decay branch ([a] or [b]). Two more random numbers  $\xi_3, \xi_4$  determine the emission angles

$$\vartheta_I = 0.5\pi\xi_3, \quad (121)$$

$$\phi_I = \pi(2\xi_4 - 1). \quad (122)$$

The remaining distance to the layer border  $d_S$  can then be calculated either upwards or downwards. The fragments lose kinetic energy mainly by ionization. These energy-range-relations have been calculated by SRIM [160] and transferred to analytical models. For boron carbide the energy loss in the medium can be described as

$$\begin{aligned} \text{Li}^{+++}: (E_o = 1.013 \text{ MeV}) \quad E_{\text{out}} &= E_o - (-0.209d_S^2 + 0.924d_S), \\ &(E_o = 0.840 \text{ MeV}) \quad E_{\text{out}} = E_o - (-0.2195d_S^2 + 0.8574d_S), \\ \text{He}^{++}: (E_o = 1.776 \text{ MeV}) \quad E_{\text{out}} &= E_o - (-0.0165d_S^3 + 0.1003d_S^2 + 0.289d_S), \\ &(E_o = 1.472 \text{ MeV}) \quad E_{\text{out}} = E_o - (-0.0285d_S^3 + 0.1267d_S^2 + 0.3354d_S), \end{aligned} \quad (123)$$

[m] All random numbers here are assumed to cover a range within  $[0, 1)$ , hence the rule for the ion choice is  $\xi_1 < 0.5$ .

and for boron

$$\begin{aligned}
\text{Li}^{++}: (E_o = 1.013 \text{ MeV}) E_{\text{out}} &= E_o - (-0.019d_S^3 - 0.1166d_S^2 + 0.8065d_S), & (124) \\
(E_o = 0.840 \text{ MeV}) E_{\text{out}} &= E_o - (-0.1863d_S^2 + 0.7891d_S), \\
\text{He}^{++}: (E_o = 1.776 \text{ MeV}) E_{\text{out}} &= E_o - (-0.0069d_S^4 + 0.047d_S^3 - 0.0732d_S^2 + 0.3998d_S), \\
(E_o = 1.472 \text{ MeV}) E_{\text{out}} &= E_o - (-0.0115d_S^4 + 0.0581d_S^3 - 0.0634d_S^2 + 0.4189d_S).
\end{aligned}$$

These models are independent of the isotope ratio of  $^{10}\text{B}$  and  $^{11}\text{B}$  as only electromagnetic interactions contribute, the nuclear charge number and the ionization level. The average maximum ranges are from (1.69-1.90)  $\mu\text{m}$  for lithium to (3.27-4.05)  $\mu\text{m}$  for helium ions in the branches [a] and [b] of (120) with a straggling variation in the order of  $\sigma \approx 5\%$ , which are reflected by an additional relative smearing of the track length by a gaussian random number corresponding to an equal spread. Fig. 37 shows in the left panel the energy-range-relation of the conversion products, which are depicted in Fig. 36 as spheres.

The ions enter the gas volume with a broad spectrum of energies. Here, first the maximum range  $d_{g,\text{max}}$  in the medium has to be calculated. For  $\text{Ar}:\text{CO}_2$  the following descriptions are used, which are also exemplarily displayed in the right panel of Fig. 37:

$$\begin{aligned}
\text{Li}^{++}: d_{g,\text{max}} &= -6.6034E_{\text{out}}^4 + 18.215E_{\text{out}}^3 - 18.783E_{\text{out}}^2 + 11.732E_{\text{out}}, \\
\text{He}^{++}: d_{g,\text{max}} &= 4.7579E_{\text{out}}^5 - 20.64E_{\text{out}}^4 + 33.888E_{\text{out}}^3 - 25.727E_{\text{out}}^2 + 13.216E_{\text{out}}, & (125)
\end{aligned}$$

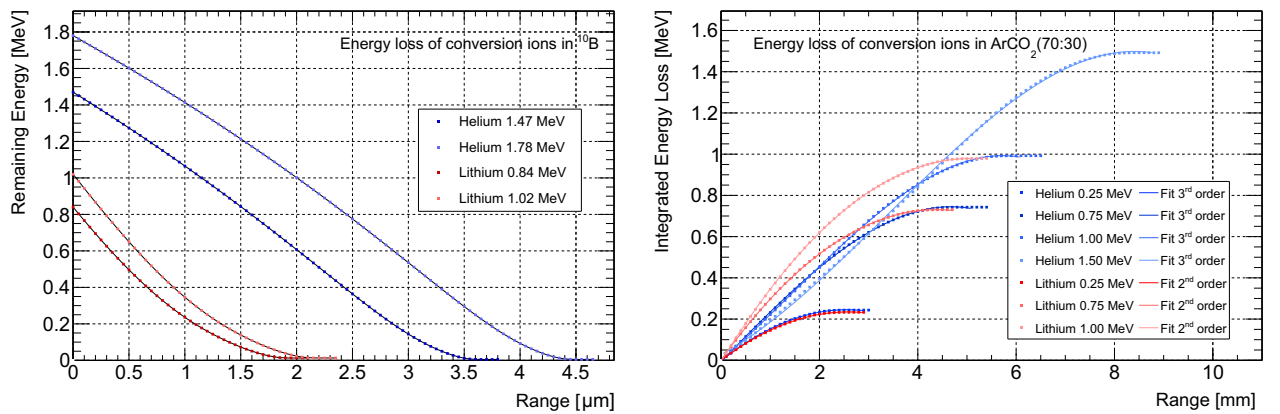


Figure 37: Calculated energy loss of helium and lithium ions from boron conversion. (Left) Energy-range relation shown for solid  $^{10}\text{B}$  and a density of  $13.05 \cdot 10^{22}$  atoms/ $\text{cm}^3$  with 4<sup>th</sup> order (helium) and 3<sup>rd</sup> order (lithium) polynomial fit functions. (Right) After leaving the conversion layer the energy spectrum of the ions is continuous, an exemplary set of energy-range relations in  $\text{Ar}:\text{CO}_2$  with 3<sup>rd</sup> order (helium) and 2<sup>nd</sup> order (lithium) polynomial functions are shown.

After determining the ionization track length the available distance to the next layer has to be calculated. Here it has to be taken into account that a grid of thickness  $h_{\text{Grid}}$  is inserted, which has an optical transparency  $T^{[n]}$ . Therefore, the track can pass the grid in case of

$$\xi < 0.5\sqrt{T} \left( 1 - \frac{\tan(\vartheta_I)}{\sqrt{T}} \right). \quad (126)$$

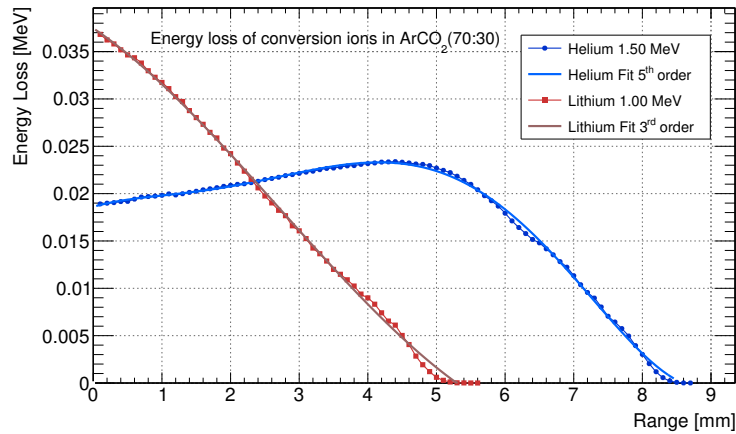
If the ionization track length is longer than the available space, the track is cut in length and in its energy deposition, otherwise both is scored unaffectedly. The result is an

[n] In general optical transparency does not equal zero-diffusion flux transparency, yet, this is the case for typical mesh geometries (thickness  $\approx 50 \mu\text{m}$  and  $\approx 100 \mu\text{m}$  pitch) and reasonably high drift fields in the order of 1 kV/cm in  $\text{Ar}:\text{CO}_2$ . [161]

ionization tracklet  $s_I$ . If no spatial resolution information is necessary, the simulation stops and calculates the geometric mean  $x$  and  $y$  values from the projected track. These are handed over to the  $n \times n$  readout matrix of a detector with  $n$  pixels and a pixel pitch of  $d_p$ .

For determining signals of a spatially resolved system it is necessary to not only know the geometry of track but also the ionization distribution  $dE/dx$ . Each of the nuclear fragments released by the absorption process exhibit a different behavior. Whereas helium ions entering the gas with energies of MeV and more still sit on the plateau regime of the Bethe-Bloch equation (41), lithium ions already start on the descending branch of the Bragg peak. Fig. 38 shows the ionization density in the Ar:CO<sub>2</sub> detector gas. In order to yield the correct energy distribution in the gas the energy loss in the boron layer has to be subtracted from the initial value, which corresponds to shifting the curves to the left. The energy loss calculated by SRIM has been fitted by polynomials

Figure 38: Energy loss per 0.1 mm in the counting gas for both conversion ions. The initial energy is chosen to be just above the maximum  $q$  value of the production channels of (120).



along the track, which is carried out as a onedimensional projection with straggling being neglected here. The following functions describe the ionization density:

$$\begin{aligned}
 \text{Li}^{++}: dE/dx &= 0.000145x^3 - 0.001185x^2 - 0.004865x + 0.037458, \\
 \text{He}^{++}: dE/dx &= 0.0000079x^5 - 0.0001455x^4 + 0.0007924x^3 \\
 &\quad - 0.0015872x^2 + 0.0021239x + 0.018607.
 \end{aligned} \tag{127}$$

Yet, the readout of the CASCADE detector, see also sec. ??, has its own specificity. The main printed circuit board features a crossed stripes design, not independent pixels, and each pixel is comprised of an interwoven comb structure with an  $x$ - and a  $y$ -component, see also the left panel of Fig. 40. Therefore, the actual energy distribution on the individual strips for the resulting event topology has to be simulated on exactly such a structure. The same principle is used as described in sec. 6.2.2. A boolean ASCII matrix  $M(x_M, y_M)^{[o]}$ , represented in the right panel of Fig. 40 by a monochromatic image, derived from the actual copper layer of the readout board, is used to project the track onto. The following steps are performed:

- randomizing the start coordinates of the track  $(x_t^S, y_t^S)$  within the innermost four detector pixels according to the metric (length per pixel),

$$x_t^S = (2\xi_1 - 1)d_p, \quad y_t^S = (2\xi_2 - 1)d_p, \tag{128}$$

[o] Representing not the entire readout but only a cutout large enough to contain a single track. These are  $12 \times 12$  pixels of the detector at  $400 \times 400$  image pixels.



- projecting the track ( $s_I$  with  $\vartheta_I$  and  $\phi_I$ ) onto the pixel matrix  $M$  by a straight line with end coordinates  $(x_t^E, y_t^E)$ ,

$$x_t^E = \sin(\phi_I) \sin(\vartheta_I) |s_I| \quad y_t^E = \cos(\phi_I) \sin(\vartheta_I) |s_I|, \quad (129)$$

- determining for every pixel in the matrix the distance to the track  $d_t$  by taking the smaller value of either the orthogonal distance to the line or the distance to its end points,
- simulating transverse charge spreading (diffusion) by assigning a relative (charge) deposit value for this image pixel  $p_i = (x_M, y_M)$ . Each is weighted by a gaussian function  $G_{p_i}(d_t, s_t)$  with an abscissa offset of  $d_t$  for the distance to the track and a width  $s_t$  representing the average track smearing width.
- Dividing the total energy deposition of the ion track in the gas by the sum of the total relative deposits on the matrix and multiplying each pixel by this factor,
- summing up all energy deposits for each strip, separately for the  $x$ - and a  $y$ -component of the readout and
- subtracting a threshold value from each strip.

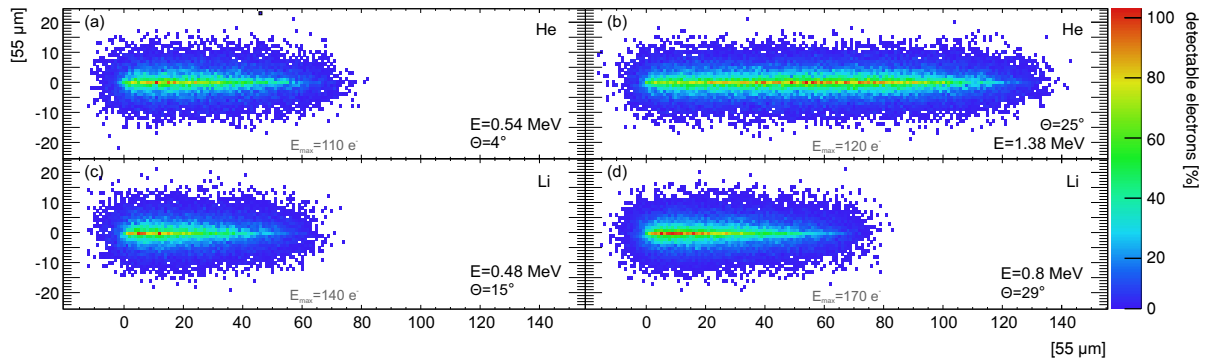


Figure 39: Simulation of four examples of helium (top) and lithium (bottom) tracks for a drift distance of 40 mm, without obstacles, a drift speed of  $10 \mu\text{m}/\text{ns}$  and a longitudinal/transverse drift constant of  $0.15 \text{ mm}/\sqrt{\text{cm}}$ . The binning is chosen in units of the smaller TimePix [162] pixel units.

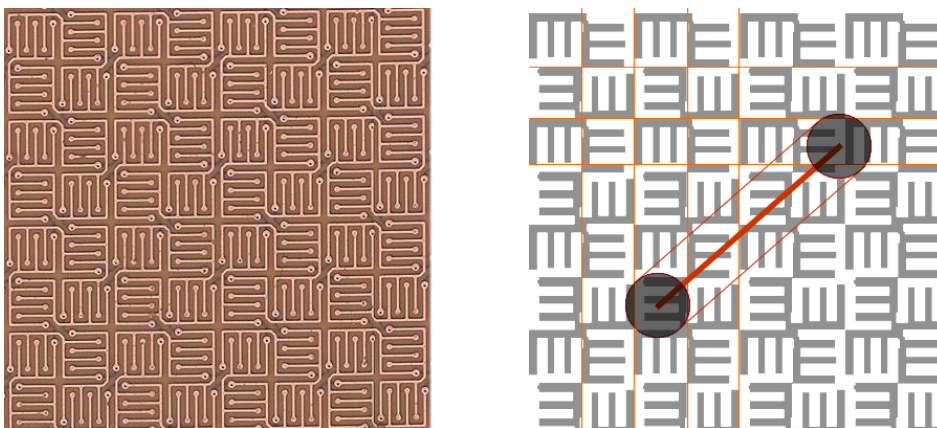


Figure 40: The readout in a cutout of  $8 \times 8$  pixels: (Left) The actual PCB, (Right) Illustration of the track projection simulation with the monochromatic input readout matrix. Orange lines mark the pixel borders. Each pixel has an  $x$ - and a  $y$ -component in white and black, respectively. A track track with its outlines symbolizing diffusion deposits the total charge according to the pixels hit.

The relative charge deposit on each image pixel  $p_i$  represents the weighted energy density deposited on the readout, as especially for crossed strips only the integrated charge along each channel plays a role. This means that in the case of the CASCADE detector the signal display is composed of two linear spatial and one time data set. In order to visualize the charge distribution, in Fig. 39 a pixelated readout has been assumed and the electron distribution is discretized. The exemplarily chosen energies

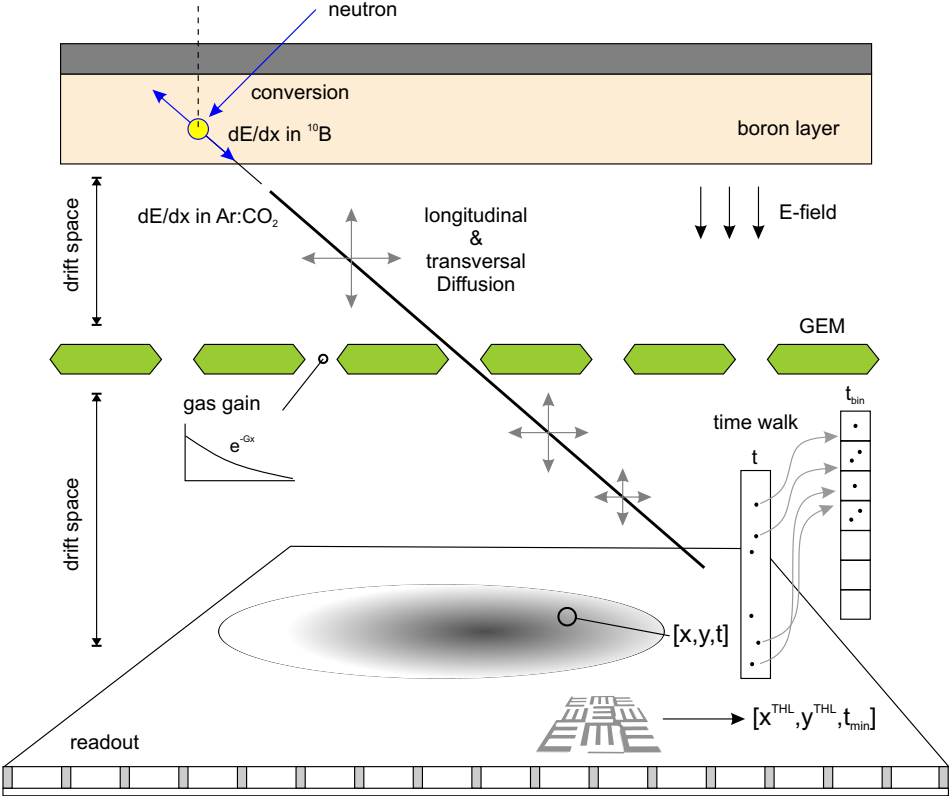
at rather slant angles visualize the spatial spread of the charge density shown in Fig. 38 for a maximum (free) drift distance of 40 mm. At the beginning and the end of the ionization tracklet the charge is effectively distributed in two dimensions, whereas in the center the distribution can be considered as only being relevant orthogonal to the main axis.

This leads to the following effects:

- the effective width of the tracklet depends on the energy loss along its axis, therefore the tail is slightly more 'pointy'-shaped than the origin, which renders a simple geometric description impossible,
- the origin is not located at the coordinate of highest  $dE/dx$  even if in the case of lithium the track has its highest ionization density at the beginning. The reason is that the diffusion leads to a relatively stronger smearing out at the ends of the track. Therefore, the origin is not directly correlated to the highest measured  $dE/dx$ .

In summary the schematic Fig. 41 describes the steps specific for calculating the geometry and the readout in the CASCADE detector in a unit-cell like picture. A track is generated from a neutron conversion inside the boron. Its length is calculated analytically by the energy loss in the converter and subsequently in the gas. Due to the narrow drift spaces of the layer geometry a track can be limited in its extension by the subsequent grid or GEM. Finally the track broadened by the diffusion in the gas is projected onto the readout with discrete spacing (pixel) and time (clock cycles) units.

Figure 41: Elements of the CASCADE detector in URANOS from the particle simulation to the signal generation with focus on the description of the charged particle track inside the gaseous volume.



In order to visualize the tracking capabilities of URANOS Fig. 42 shows two non-trivial neutrons paths from generation until absorption, exemplarily in air (left) and in the ground (right). It already acts as a demonstrator for the interactions at this specific interface. In air the main scattering partners are nitrogen and oxygen, which leads to a large amount of scatterings with small energy decrements. By the long path lengths in the thin medium the neutron also can acquire hundreds of meters of integrated travel distance. Inside the soil typical scattering lengths are far below one meter. For high energy neutrons, the main scattering partners can be silicon, aluminum and oxygen. However, due to the presence of water a few interactions with light nuclei can thermalize a neutron (blue lines). Then it will carry out a random walk which will be dominated by hydrogen scattering.

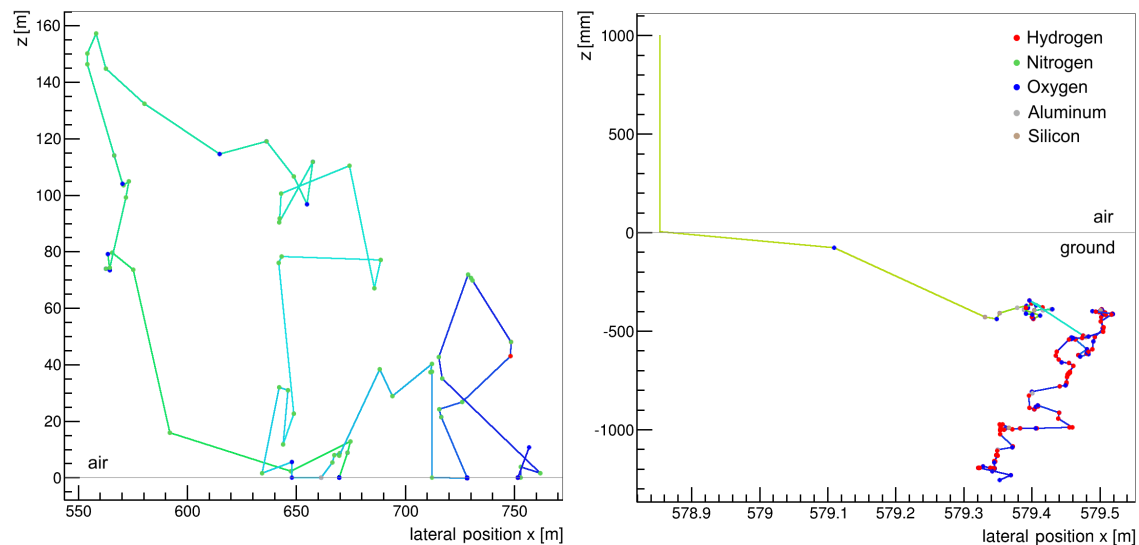


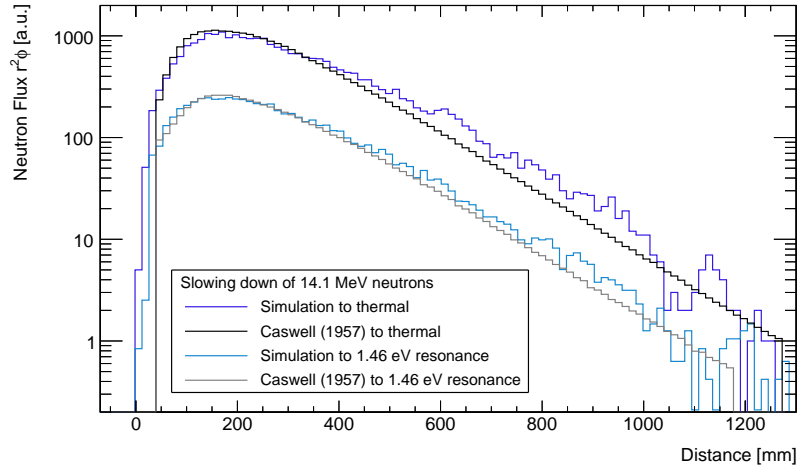
Figure 42: Projection of track calculations in an air ground interface. The simulated neutrons, which are artificially released from 1 m above the soil, are rainbow-colored according to the logarithm of the corresponding energy scaling from 10 MeV (red) to thermal (blue). Left: a neutron which mainly scatters in the air. Right: a neutron thermalizing inside the soil. To be noted: both x- and y-axes are not scaled equally.

### 6.6.1 | DIFFUSION LENGTH IN WATER

The attenuation of fast neutrons by efficient moderators is a basic example of neutron physics and the main source of thermal neutrons. Modeling the slowing down process properly requires the correct description of interaction lengths, energy loss and geometric transport. Therefore, it can be regarded as validation test of the Monte Carlo code. In public literature sources a few examples of well controlled and simple measurements can be found. CASWELL, GABBARD, PADGETT, and DOERING [163] describe an experiment of determining the radial distribution of neutrons in a water tank from 14.1 MeV to thermal energies and 1.46 eV. A deuterium beam is delivered by an aluminum tube onto a tritium target inducing fusion. The tank measures 2.4 m in length and 1.2 m in height, whereas the particle injector is located at a distance of 0.6 m from one wall and vertically centered. The flux is measured pointwise by indium foil activation, which provides data for the non-equilibrium state above 1 eV, and thermal neutron detectors with cadmium shielding. Although both energy regimes are supposed to exhibit similar range distributions they have to be treated by different methods of neutron transport. Until reaching the indium resonance a maximum mean energy loss by elastic collisions, including a few inelastic reactions, can be attributed to hydrogen interactions. Beyond

this limit the kinetic energy of the neutron is becoming dominated by thermal scattering leading to a constant average energy. This system can be easily reproduced in a model setup including the generalization of an infinitely large domain. The fluxes  $\Phi$  are scored at thermal (9-120) meV and indium resonance (1.3-1.6) eV energies on a sphere of radius  $r$  yielding a surface flux of  $r^2\Phi$ . Fig. 43 shows the measured fluxes from [163] in comparison to the simulation results. Both attenuation distributions are in good agreement. The particle density in both cases peaks at around 15 cm followed by a nearly exponential decay with similar attenuation lengths<sup>[p]</sup>.

Figure 43: Comparison of the attenuation length from [163] for deuterium-tritium fusion neutrons emitted into water. The spherical surface flux for thermal and indium resonance neutrons as a function of distance from the source is compared to the simulation results from URANOS.



## 6.6.2 | BONNER SPHERE EVALUATION

A case similar to the previous sec. 6.6.1 are Bonner Spheres, see also sec. ??, which are proportional counters surrounded by shells of polyethylene. As this spectrometer type of array is used to monitor environmental fluxes, various studies were carried out for the modeling of such [164–169]. Whereas the neutron range distribution in water in the previous example demonstrated geometric transport and collision treatment, the Bonner Sphere offers the possibility to focus on an energy-dependent comparison and on the interplay of moderator and absorber. Among the various existing technical realizations the helium-based version was chosen, equipped with a 3.2 cm spherical counter. For reasons of convenience, the whole model has been discretized in 17 layers, which are symmetrically arranged around the center and depicted in Fig. 44. Laterally the resolution by the pixel matrix was set to 1 mm, therefore the voxel size of a  $X$  inch sphere is  $1 \text{ mm} \times 1 \text{ mm} \times (X/17)''$ . For the simulation the model was irradiated by a neutron beam of the same diameter as the sphere under an angle of  $0^\circ$ .

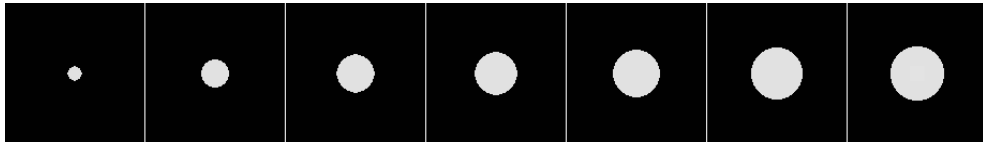


Figure 44: Discretized URANOS Input files for the upper half of a 2 inch Bonner Sphere.

Furthermore, hydrogen atoms in polyethylene have been emulated by the scattering kernel derived from the (oxygen-)bound cross section in water. This can yield exclusively for thermal energies a systematic uncertainty of around 10%. Due to the statistical nature of neutron transport the actual geometrical shape of a body has a minor influence compared to other parameters like overall volume or thickness. Exem-

[p] Fermi age transport theory, which is not taken into comparison here, can very well reproduce the attenuation at radial distances larger than 25 cm. For fluxes more close to the source the theoretical distribution peaks much earlier.

plarily for the calculation routine some track views are shown in Fig. 45 and Fig. 46 as a central cut through the model and for the whole domain.

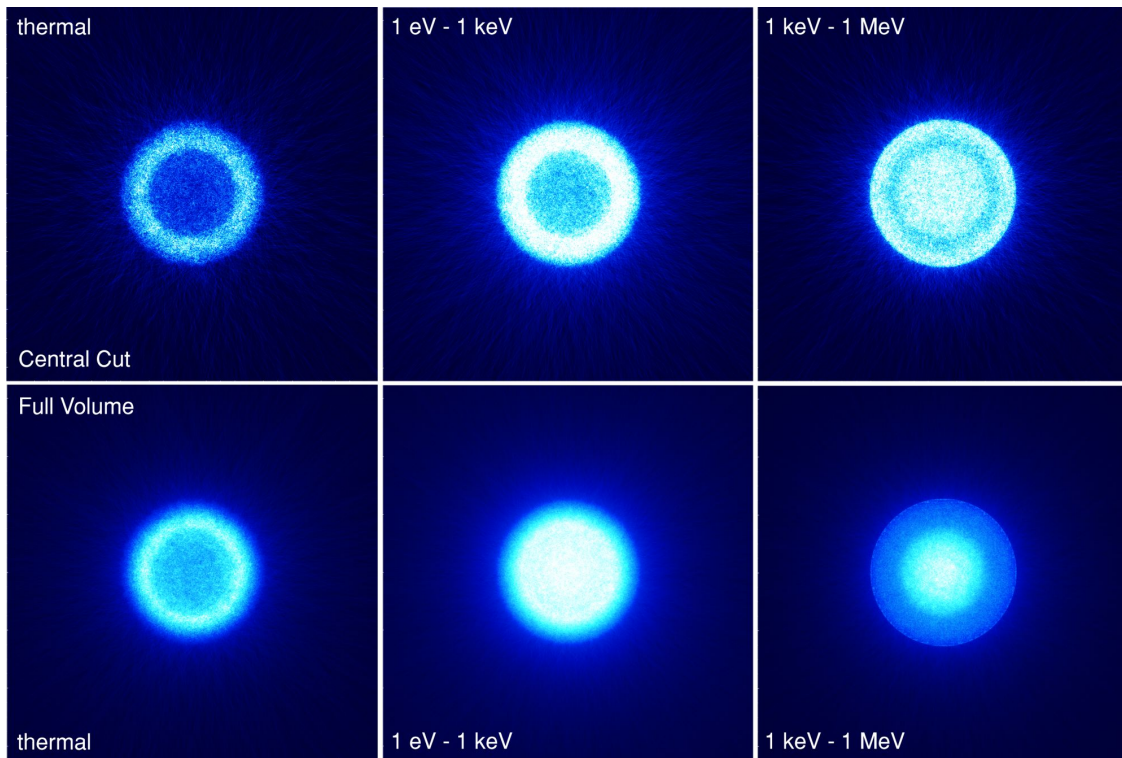


Figure 45: Flux calculation of Bonner Spheres of 2 inch diameter. The simulated neutron tracks ( $E_{\text{kin}} = 10 \text{ keV}$ ) of  $10^6$  histories are displayed in a central cross section of 3 mm height (top row) and the full domain of  $13 \text{ cm} \times 13 \text{ cm} \times 5.4 \text{ cm}$  (bottom row).

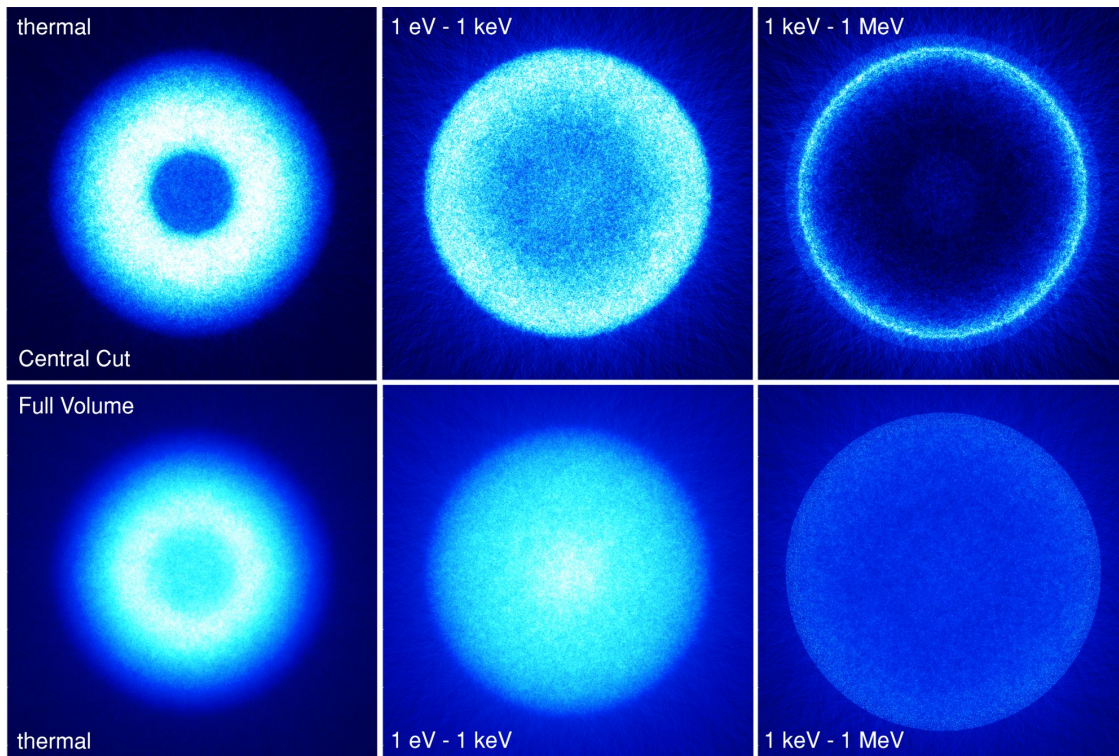
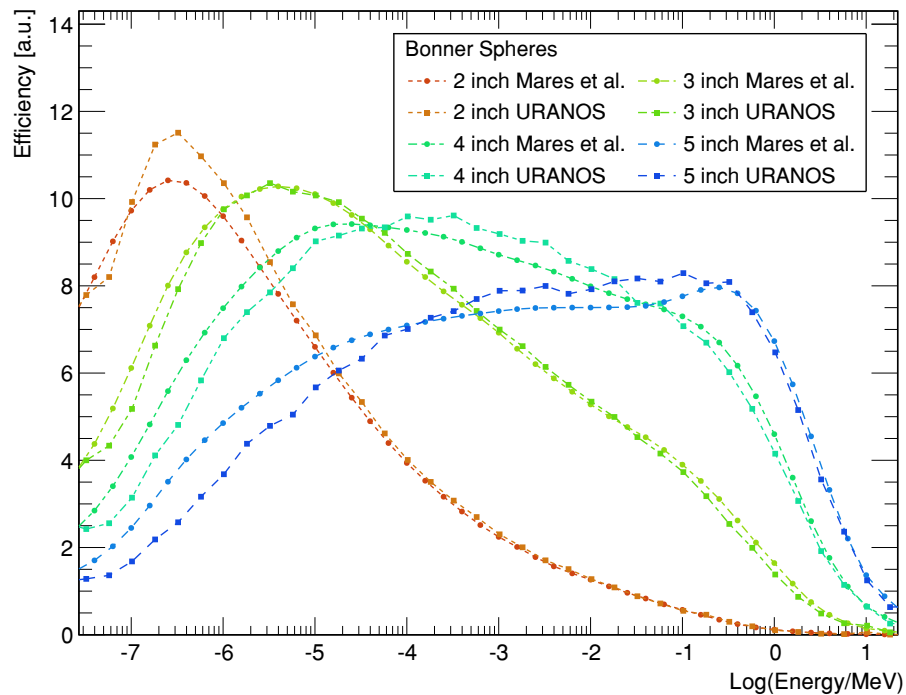


Figure 46: Flux calculation of Bonner Spheres of 4 inch diameter. The simulated neutron tracks ( $E_{\text{kin}} = 10 \text{ keV}$ ) of  $10^6$  histories are displayed in a central cross section of 6 mm height (top row) and the full domain of  $13 \text{ cm} \times 13 \text{ cm} \times 11 \text{ cm}$  (bottom row).

Comparing to calculations from [170], see Fig. 47, there is a good agreement in the energy sensitivity between response curves from literature and URANOS results. This successfully validates the simulation for basic scattering calculations.

Figure 47: Comparison of simulations of the energy dependent response function of Bonner Spheres of URANOS and MCNP calculations by MARES, SCHRAUBE, and SCHRAUBE [170]. The detectors are HDPE spheres with diameters in the range of (2-5) inch, equipped with a  $3.2\text{ cm }^3\text{He}$  counter.



### 6.6.3 | COSMIC SPECTRUM EVALUATION

Although since more than 50 years the general shape and height-dependent scaling of the cosmic-ray neutron spectrum at ground level is known [171], there is a perpetual discussion about precise features of the intensity distribution, especially at the soil interface. The reasons are:

- high-energy neutron interaction cross sections above 20 MeV were not seriously investigated nor integrated into transport codes. Their evaluation and corresponding measurements are recent developments, mainly of the 21<sup>st</sup> century.
- The invention of the Bonner Sphere, see also sec. ??, could standardize dosimetric flux evaluations, yet, by means of this type of spectrometer the neutron spectrum is determined indirectly. The experimental findings themselves are the result of unfolding algorithms [172], which rely only on a few absolute values and energy-dependent response functions from Monte Carlo models of the detectors themselves [173], which typically do not take into account the incoming angular distribution. This means that different simulations can produce slightly different weightings for different parts of the spectrum. Sometimes such unfoldings even yield physically wrong reconstructions<sup>[q]</sup>.

In the following Fig. 48 and Fig. 49 an overview of different results from the most widely used codes, see sec. 5.2, are presented along with experimental results. The main differences appear in the high energy regime, for which the usual data bases, see also sec. 5.1.4, until very recently provided only poor support. These uncertainties were partly compensated by effective nuclear interaction models, but propagate to the

[q] Seen for example in the sudden increase of flux meanwhile slowing down in the epithermal regime in [174] or [175].

lower energetic parts of the flux distribution. For now only the general shape of the spectrum has to be considered. The peak structures at around 1 MeV, which are de facto spectral lines of inelastic resonances, mostly oxygen, cannot be resolved experimentally by spectrometers and are displayed only at times. By normalizing to the intensity of the thermal peak Fig. 48 accumulates possible uncertainties and therefore maximizes the deviations between the presented evaluations. A better convergence is displayed in Fig. 49.

In order minimize this general problem URANOS uses a validated neutron spectrum near the surface as a source and releases it directly onto the ground to minimize typical uncertainties of atmospheric propagation. The implementation of the works presented by [66] and [159], which are based on [68] and [67], are discussed in sec. 6.3.1.

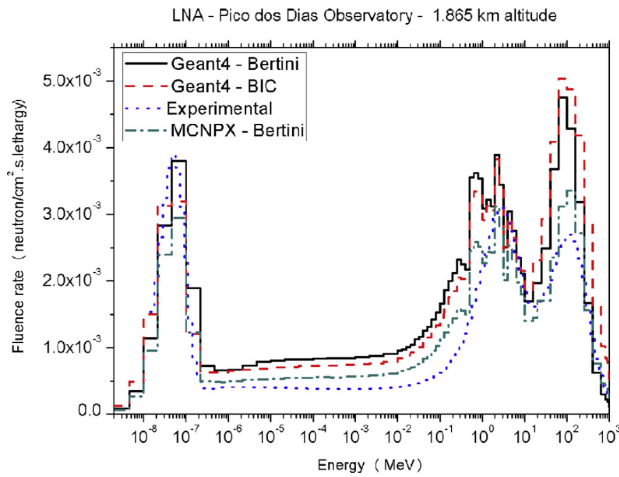


Figure 48: Energy dependent neutron flux at an altitude of 1860 m calculated by MCNPX, GEANT with the two high energy models Bertini [176, 177] and BIC [178] and determined experimentally from [179]. [180]

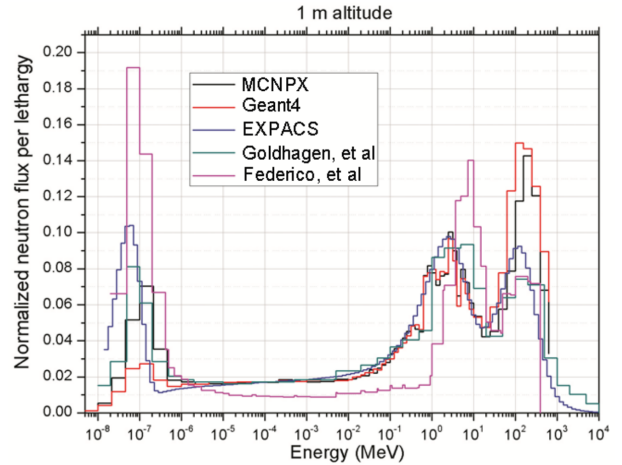


Figure 49: Energy dependent neutron flux at 1 m altitude calculated by EXPACS, MCNPX, GEANT4 and determined experimentally from [181] and from [182]. Environmental conditions are not the same. [183]

Fig. 50 presents the result from URANOS for the calculated neutron flux (black) above the surface in an infinite domain. The input is drawn in green. On the qualitative level

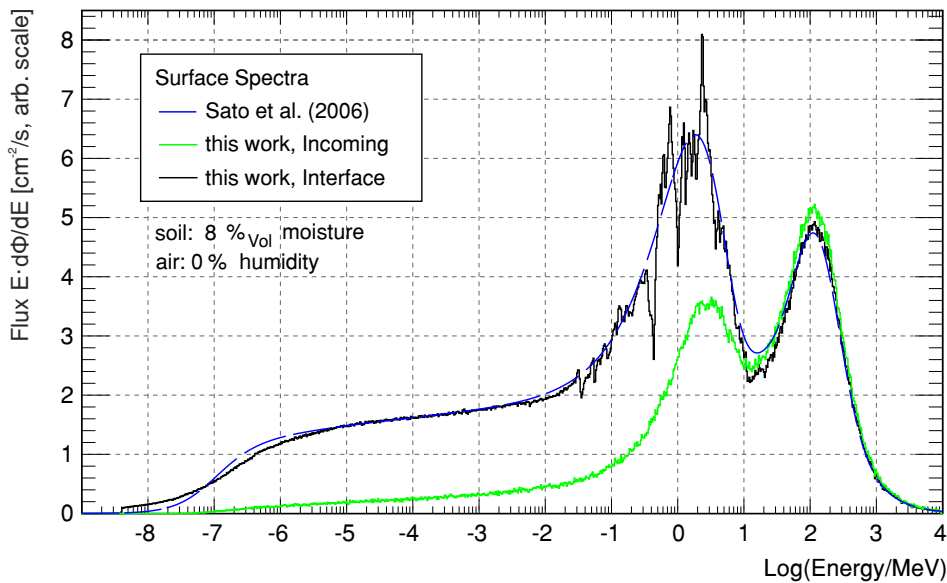


Figure 50: URANOS cosmic-ray neutron spectrum comparison. The incoming spectrum (green), which is generated from the analytical functions (68) and (69) from [66], is released onto the soil. The resulting intensity distribution, shown in black, is compared to the original spectrum for the same environmental conditions from [66] in blue.

the underlying physics model correctly calculates the response to the soil. In the high energy domain around 100 MeV the incoming flux is only reduced, no influence of backscattering can be observed. In the region around 1 MeV the evaporation peak ap-

pears correctly in width and mean energy value. The spike structure on the peak itself is result of elastic scattering on strong nuclear resonances, mainly in oxygen - for example at 435 keV<sup>[r]</sup>. As there are no significant sources in the range of 1 eV to 0.1 MeV, in a lethargy-dependent plot there is a flat plateau between neutron generation and thermalization, the latter being truncated here. This plateau can feature a slant angle in case there are significant absorption processes involved, but no other features like bumps or steps should be visible. It has to be pointed out that the resulting spectrum here requires nearly the full physics and tracking computation.

For a quantitative investigation due to the lack of a generally accepted standardized spectrum or a consensus in the literature, the evaluation of the URANOS code focuses on the capability to reproduce the above-ground cosmic neutron spectrum for typical conditions. This implies that the input spectrum released on the ground should reproduce the same densities as the input formulae (68) and (69). This test twice evaluates the computational correctness of the code - by yielding the same predictions as the Monte Carlo reference and indirectly by showing that the reverse-engineered input spectrum has been modeled correctly.

#### 6.6.4 | PERFORMANCE BENCHMARKS

The performance of the code heavily depends on the setup, which is to be simulated. The most significant contributor is the mean lifetime of neutrons in terms of scatterings within the domain. In simple configurations like for the analysis of detectors most neutrons undergo only a few interactions before either being absorbed or leaving then domain. Atmospheric neutrons can have up to hundreds of scatterings before ending up thermalized, see also later 9.1.6. Additionally, depending on the chosen materials and energy range, only a few cross sections like for elastic scattering plus absorption are evaluated. In the MeV regime adding up all inelastic channels scales up to dozens of address requests.

In order to provide some practical estimations a standard scenery can be defined as in table 9. This domain measures 900 m × 900 m with a source dimension of 840 m × 840 m. It contains a minimum configuration of six layers for analyzing a neutron density which can be considered in spatial equilibrium in the innermost 400 m × 400 m.

Layer	Position [m]	Height [m]	Material	Function
1	-1000	920	air	top buffer layer
2	-80	30	air	source layer
3	-50	47.5	air	-
4	-2.5	0.5	air	detector layer
5	-2	2	air	-
6	-0	3	soil	ground layer

Table 9: The standard setup for a layer composition in cosmic neutron sensing.

A similar setup has also been used for simulating the so-called 'UFZ site' in the publication [SK2017b] - an urban environment with many concrete buildings, streets, green spaces, a railroad line, a lake and trees. From the twelve layers in total eight contained a pixel matrix of 1800 × 1800 voxel definitions. The composition 21 introducing the URANOS chapter shows the layer model setup as well as one of the calculation results for the above-ground neutron density.

[r] The structure of the evaporation peak can rather be compared to a transmission spectrum, as those energies are missing which correspond to resonances. There neutrons are scattered off to lower energies more likely than otherwise.



The machine, on which the URANOS v0.99 $\rho$ <sup>[s]</sup> was evaluated, is based on a 4 GHz i7 central processing unit. The technical specifications relevant for this benchmark are:

CPU: Intel Core i7-6700K, 4 cores at 4 GHz (40x multiplier), 4×(32+32) KB L1-Cache, 4×256 KB L2-Cache, 8 MB L3-Cache,  
 Mainboard Chipset: Intel Z170 Skylake,  
 RAM: 16 GB DDR4, 1067 MHz, CL15, tRCD15, tRP15, tRAS36, CR2T,  
 OS: Windows 7, 64 bit (Build 7601)<sup>[t]</sup>.

The following table 10 summarizes the single core performance of the code in terms of neutrons per second. The 'standard setup' and 'UFZ site' are described above and are simulated in combination with the cosmic neutron spectrum like presented in sec. 6.6.3 Fig. 50, the detector is a rover type instrument, see sec. 7.2.1, which is a setup similar to the Bonner Sphere models presented in sec. 6.6.2 and the other benchmarks are synthetic. Without additional voxel geometry descriptions by pixel matrices one instance of URANOS requires approximately 230 MB of memory, mainly for storing ENDF data.

N <sup>o</sup>	n/s	name	description
1	3730	std. setup	water body, 5 g/m <sup>3</sup> air humidity NTP
2	1800	std. setup	like N <sup>o</sup> 1, ground with 10 % soil moisture
3	1060	std. setup	like N <sup>o</sup> 1, ground with 1 % soil moisture
4	2850	std. setup	like N <sup>o</sup> 1, with full domain tracking enabled
5	880	std. setup	like N <sup>o</sup> 3, with full domain tracking enabled
6	1030	std. setup	like N <sup>o</sup> 1, with thermal transport enabled
7	600	std. setup	like N <sup>o</sup> 2, with thermal transport enabled
8	510	std. setup	like N <sup>o</sup> 3, with thermal transport enabled
9	470	std. setup	like N <sup>o</sup> 3, with thermal transport and full domain tracking enabled
10	2000	UFZ site	with 10 % soil moisture
11	1680	UFZ site	like N <sup>o</sup> 10, without voxel geometry but same layering
12	36700	detector	thermal spectrum onto a side face with $\vartheta = 0^\circ$
13	16250	detector	like N <sup>o</sup> 12, with an americium-beryllium spectrum (see sec. 6.3.2)
14	14100	detector	like N <sup>o</sup> 12, with a 1 MeV monoenergetic beam
15	14200	water	thermal spectrum with $\vartheta = 0^\circ$ from air into a water body
16	7100	water	like N <sup>o</sup> 15, with an americium-beryllium spectrum
14	6300	water	like N <sup>o</sup> 15, with a 1 MeV monoenergetic beam

Table 10: Single core performance of URANOS (v0.99 $\rho$ ) for a number of practically relevant scenarios. The above described system with a 4 GHz i7-6700K CPU was used to evaluate the benchmarks.

[s] compiled by Qt 5.2.1 linked against ROOT 5.34.20 in Visual C++ MSVC 2010 32bit. The integration was restricted to previous versions of the library and runtime as far as no ROOT 5.34.X version provided binaries for later versions.

[t] Spectre [184] vulnerability patched.



Part IV

COSMIC-RAY NEUTRON SENSING



## INTRODUCTION

---

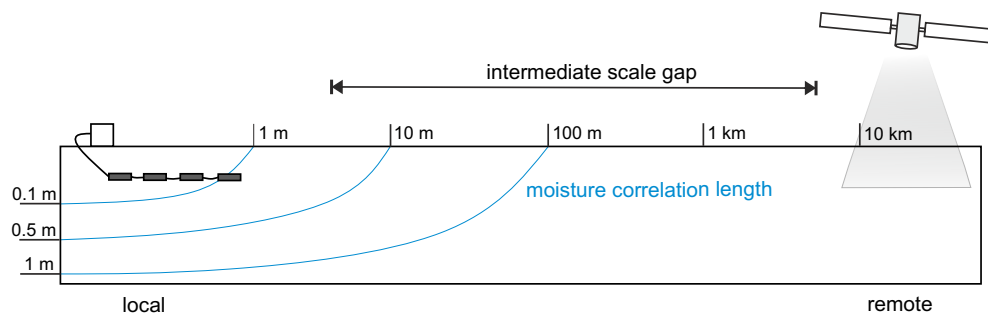
Throughout the history of Cosmic Ray discoveries 'range' was one of key observables. It started as early as 1900 when Villard<sup>[a]</sup> found a new type of radiation [185], which was later named  $\gamma$  and found to be produced by artificial sources as well as to be omnipresent in the environment. In order to disentangle ground from atmospheric effects numerous experiments were conducted, but it was not until balloon flights of Wulf<sup>[b]</sup> [186], Gockel<sup>[c]</sup> [187] and finally Hess<sup>[d]</sup> [188] from 1910-1914 studying the discharge of electrometers revealed the atmospheric contributions as the intensity did not decrease as expected by height. Although the invention of the Geiger counter and later the cloud chamber facilitated measurements by displaying and quantifying interactions of particles, the nature, intensity and composition of this cosmic radiation was subject to unsuccessful speculations. In 1933 Compton<sup>[e]</sup> concluded that the origin of this radiation are extraterrestrial high energetic particles [189], whereas Johnson's<sup>[f]</sup> experiments indicated that these would be largely positively charged [190]. During the 1930s different effects could be decomposed, so it could be understood by works of Bhabha<sup>[g]</sup> and Heitler<sup>[h]</sup> that the radiation is partly due to air showers [191] and a flux of galactic particles which alters by latitude and solar activity [192]. These highly energetic were as early as 1934 supposed to originate from supernovae [193]. The presence of neutrons in such air showers [194] was first investigated by Cocconi<sup>[i]</sup> by ground-based and airborne experiments, whereas Simpson<sup>[j]</sup> could identify nuclear disintegration as the main contributor [195] to the neutron production. As from the 1950s, based on established technologies, networks of neutron and myon monitors were set up in order to systematically study and characterize the cosmic radiation and its effects [196].

### 7.1 | SOIL MOISTURE SENSING TECHNIQUES

To date the measurement possibilities for determining the water content of the environment are either bound to local instrumentation or large-scale satellite-based technologies, both not meeting the typical correlation lengths for water resources, which has always been an issue for the interpretation of the available data [197]. This is called the intermediate scale gap [198]. Most of the local techniques are using in-situ probes which have to be installed and operated inside the soil. Although determining the water content by the electrical conductivity of the ground [199] is in general possible, this quantity depends on many other variables like salinity, temperature and nutrient content. Therefore, it is not possible to interpret such measurements without profound knowledge of the soil type. This holds true as well for similar methods, which make use of the dielectric properties of soil [200] for frequencies up to 1 GHz as the dipole moment of water is much higher than the one of other typical elements. The electri-

- 
- [a] Paul Ulrich VILLARD, \*1860-†1934, France.
  - [b] Theodor WULF, \*1868-†1946, German Empire.
  - [c] Albert GOCKEL, \*1860-†1927, German Empire.
  - [d] Viktor Franz HESS, \*1883-†1964, Austria-Hungary.
  - [e] Arthur Holly COMPTON, \*1892-†1962, United States of America.
  - [f] Thomas Hope JOHNSON, \*1899-†1998, United States of America.
  - [g] Homi Jehangir BHABHA, \*1909-†1966, British India.
  - [h] Walter Heinrich HEITLER, \*1904-†1981, German Empire.
  - [i] Vanna COCCONI-TONGIORGI, \*1917-†1997, Kingdom of Italy.
  - [j] John Alexander SIMPSON, \*1916-†2000, United States of America.

Figure 51: Ranges for different soil moisture sensing technologies with relevant scales for water distribution in the support volume.



cal properties of the soil also play the important role for **time domain transmission (TDT)** and **time domain reflectometry** [201], which make use of the change of velocity for electromagnetic signals. This property is also used for **ground penetrating radar (GPR)** [202], which uses the transmission and reflection of electromagnetic waves in the subsurface and **electromagnetic induction (EMI)** [203] based methods featuring mobile or stationary devices equipped with antennas or coils, respectively. In order to extend the scope any stationary technology can be distributed on a larger area in the form of sensor networks [204].

Among the non-invasive methods, which are typically referred to as remote sensing, there is the measurement of the blackbody emissivity of the soil in the microwave region either from ground-based stations [205], but meanwhile this technique is applied mostly from extremely high altitudes by dedicated satellites [206], most notable the recent ESA Copernicus program [207] with its Sentinel missions [208, 209]. As hydrogen also possesses the strongest nuclear magnetic moment the amount of water in the ground can also be determined by NMR devices [210]. A more sophisticated and experimental approach is the gravimetric determination of the surrounding subsurface-water by absolute microgravimeters [211]. Furthermore, the possibility to measure the water content by the reflection of GPS signals [212] is still in evaluation.

The methods mentioned mostly rely on electromagnetic properties of the soil, especially of water. Another exceptional property of hydrogen is the efficient slowing down of neutrons. Therefore, devices had been proposed which measure the thermalization of fission neutrons [213]. The absence of slow neutrons in a distance from an active source indicates the absence of water and/or the presence of a absorbers, and therefore this method suffers from the fact that already traces of isotopes like  $^{10}\text{B}$  lead to a false interpretation without chemical analysis of the soil [214]. Nevertheless, this technique is still used in oil-well logging for downhole tools which have to be operated from the inside of a drilling tube [215].

## 7.2 | COSMIC-RAY NEUTRON SENSING: THE TECHNIQUE

### 7.2.1 | THE COSMOS SENSOR

Cosmic-ray neutron sensors of type CRS<sup>[k]</sup> are commercially available in several configurations, see Fig. 52. The CRS1000 and CRS1000/B are mainly in stationary use to monitor environmental neutron fluxes, and the Rover system [216] is typically used in vehicles for spatially resolved mobile surveys, for example in applications of agricultural land use [217]. A description of the main components can be found in [218]. The sensors comprise one or two moderated detector tubes sensitive to epithermal/fast neutrons, a high voltage generator, a pulse height analyzer, and a data logger with integrated telemetry. The detector can be regarded as a Bonner Sphere, see sec. ??, its energy sensitivity will be discussed in sec. 8.3. As a neutron moderator, high-

[k] Hydroinnova LLC, USA

density polyethylene of 1 inch thickness is used to encase the proportional counter. The CRS1000 uses helium-3, while the CRS1000/B uses boron trifluoride, which requires larger detectors in order to achieve the same count rate due to its lower cross section (3837 b vs. 5330 b at 25.3 meV) [98] and pressure (0.5 bar vs. 1.5 bar) and therefore lower macroscopic cross section. The Rover is technically equivalent, but consists of significantly larger detectors than the stationary sensors and two tubes in one moderated module to increase the event rate and therefore the time resolutions [219].

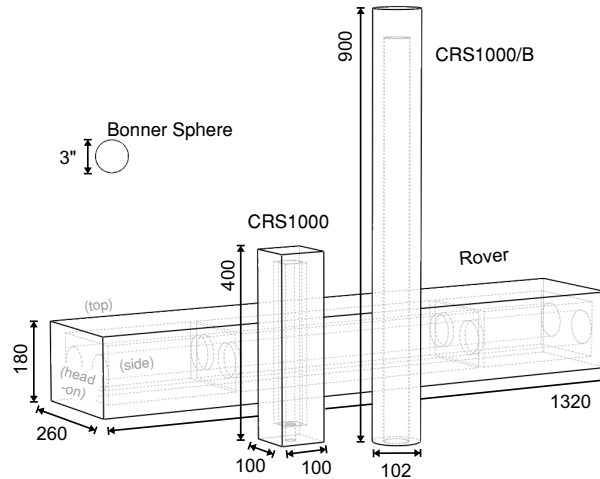


Figure 52: Variants of the cosmic-ray neutron detectors modeled in this study. Dimensions are in units of millimeters. To scale a Bonner Sphere is illustrated in comparison. [KS2018]

## 7.2.2 | SIGNAL CORRECTIONS

The cosmic-ray neutron spectrum is result of highly complex interplay of relativistic and non-relativistic particles, of leptons and baryons that create showers in the atmosphere like in a large calorimeter. Neutrons themselves as a by-product of these particle cascades make up a large part of the remaining radiation at ground level and are sensitive to the number of nucleons as long as being highly energetic and to hydrogen when being moderated. The neutron density  $N_n$  at the soil interface is influenced by various factors, which turn out to exhibit a non-linear scaling, including correlations to other relevant environmental variables. Nonetheless, in order to derive a soil moisture value  $\theta$ , there is a set of linear off-the-shelf corrections, which are used for example in time series, but have mostly been gained empirically. The fully corrected neutron count rate of a sensor  $N_{\text{corr}}$  is calculated by

$$N_{\text{corr}} = N_n \cdot C_I \cdot C_p \cdot C_h, \quad (130)$$

where  $C_I$  denotes the incoming radiation correction,  $C_p$  the atmospheric pressure correction and  $C_h$  the air humidity correction - see also [220].

As discussed in section 3.1, the cosmic radiation, which penetrates the upper atmosphere creating secondary neutrons, is not constant in its flux. Its intensity depends on the solar cycle and the vertical cutoff rigidity and other temporal variations. These fluctuations can hardly be predicted and therefore are measured by neutron monitors<sup>[1]</sup> distributed in various locations around the world. Although these detectors primarily measure the highly-energetic proton component of the incoming radiation, there is a similar dynamic assumed for neutrons [218] for regions of the same cutoff rigidity. The Neutron Monitor Data Base (NMDB)<sup>[m]</sup> provides real-time data about the incoming radiation  $I$ , which can be retrieved automatically. The established correction method

[1] see sec. ?? and the time series in Fig. 9.

[m] accessible via <http://www01.nmdb.eu/>

uses then a standardized count rate for the respective detector  $I_{\text{ref}}$  for the **incoming radiation correction**

$$C_I = 1 + \gamma \left( \frac{I_{\text{ref}}}{I} - 1 \right) \quad (131)$$

using  $\gamma = 1$ . More sophisticated correction approaches are analyzed in [221].

The incoming radiation including the secondary particles are attenuated by the atmosphere. The reference pressure  $p$  at the sensor location provides a good estimator for the mass of the air column. The **barometric pressure correction** therefore can be written using the atmospheric depth at reference pressure  $X_{\text{ref}} \approx 1000 \text{ g/cm}^2$ <sup>[n]</sup>

$$C_p = \exp \left( \frac{X - X_{\text{ref}}}{\lambda_{\text{atm}}} \right) \quad (132)$$

and the atmospheric attenuation length  $\lambda_{\text{atm}}$ . In [222]  $\lambda_{\text{atm}} = 132 \text{ g/cm}^2$  is assumed. Yet, this parameter itself depends on energy range, altitude and cutoff rigidity as it represents an average of interaction lengths of different primary and secondary air shower particles, e.g. seen in Fig. 12. Literature values of measurements range from (130-165)  $\text{g/cm}^2$ , overviews can be found in [222–225] and [226].

**Atmospheric water vapor** can account for three effects on the measured neutron signal. Firstly, it increases the area density and secondly especially the hydrogen abundance pre-moderates the spectrum. Albedo neutrons are then furthermore also scattered off these water molecules near the surface. [227] assumes, that the latter has a negligible effect<sup>[o]</sup> and proposes the following correction function:

$$C_h = 1 + \alpha_{\text{hum}} (h_{\text{abs}} - h_{\text{abs}}^{\text{ref}}) \quad (133)$$

with  $\alpha_{\text{hum}} = 0.0054 \text{ m}^3/\text{g}$ , absolute humidity  $h_{\text{abs}}$  and a reference value of  $h_{\text{abs}}^{\text{ref}} = 12 \text{ g/m}^3$ , which corresponds to 50 % relative humidity at 25 °C. Relative and absolute humidity  $h$  at a given temperature  $T$  (in K) can be approximated by

$$h(h_{\text{rel}}, T) = 1323.48 \frac{\text{g}}{\text{m}^3} h_{\text{rel}} 10^{\frac{aT}{b+T}} \quad \text{with } (a, b) = \begin{cases} (7.5, 237.3 \text{ K}), & \text{if } T > 273.15 \text{ K}, \\ (7.6, 240.7 \text{ K}), & \text{otherwise.} \end{cases} \quad (134)$$

### 7.2.3 | SOIL MOISTURE DETERMINATION

The above-ground neutron spectrum contains two parts. The pure incoming radiation  $\Phi_{\text{inc}}$  never had any contact with soil. The albedo component  $\varphi_{\text{alb}}$  is then defined as those neutrons which passed the interface at least once:

$$\Phi_{\text{tot}} = \Phi_{\text{inc}} + \Phi_{\text{alb}} \rightsquigarrow N = k_{\text{inc}} N_o + k_{\text{alb}}(\theta) N_o. \quad (135)$$

Soil moisture  $\theta$  is then inferred from the intensity change of the reflected component. As any hydrogen in the environment contributes to the signal, all water pools have to be added up, including biomass  $\theta_{\text{org}}$  and chemically bound lattice water  $\theta_{\text{lw}}$ , which is typically in the order of (1-2) % volumetric soil moisture:

$$\theta = \theta_{\text{mob}} + \theta_{\text{org}} + \theta_{\text{lw}}. \quad (136)$$

[n] standard conditions assume at sea level  $p_{\text{NTP}} = 1013 \text{ hPa}$  and  $X = \int_0^{h_{\text{max}}} \rho_{\text{air}}(h) dh = p/g$ .

[o] we will later see, that this is not the case.



Although the typical definitions of soil moisture account only for the available water  $\theta_{\text{mob}}$ , this work for reasons of simplicity implicitly assumes the extension of this term by including hydrogen contributions, which can be converted to effective soil moisture values according to  $\theta = \sum_i \theta_i$ .

In [216] the count rate of the sensor  $N$  is assumed to be derived from a reference parameter  $N_o$ , which is supposed to be the instrument count rate over entirely dry soil<sup>[p]</sup>. The neutron flux as a function of gravimetric or volumetric soil moisture  $\theta$  then follows a simple hyperbola

$$\theta(N) = \frac{a_o}{\frac{N}{N_o} - a_1} - a_2, \quad (137)$$

with the parameters  $a_o = 0.0808$ ,  $a_1 = 0.372$  and  $a_2 = 0.115$  derived from an empirical analysis in [216].  $a_1$  equals the incoming radiation fraction  $k_{\text{inc}}$ ,  $a_o$  and  $a_2$  have the units of  $\text{m}^3/\text{m}^3$  or  $\text{kg}/\text{kg}$ . Although the approach to use only the sensor-specific calibration parameter  $N_o$  leads in many cases to satisfying results, individual site conditions, however, have led authors to use slightly different sets of  $a_i$  parameters [228–230]. The reasons for these ambiguous results will be discussed later and address the understanding of neutron transport and individual contributions to the signal, yet, relation (137) can be used to estimate the error  $\sigma_\theta$

$$\sigma_\theta = \left| \frac{\delta\theta}{\delta N} \sigma_N \right| = \frac{a_o \frac{1}{N_o}}{\left( \frac{N}{N_o} - a_1 \right)^2} \sigma_N = \dots = (\theta + a_2)^2 \frac{\sigma_N}{a_o N_o}, \quad (138)$$

for which due to counting statistics  $\sigma_N = \sqrt{N}$  can be assumed. Hence, the relative error can be calculated as

$$\frac{\sigma_\theta}{\theta} = \left( 1 + 2a_1 a_2 + a_1 \theta + \frac{1}{\theta} (a_2 + a_1 a_2^2) \right) \frac{1}{\sqrt{N}}. \quad (139)$$

As  $N$  and  $\theta$  are related to each other by  $N(\theta) = N_o \cdot \left( \frac{a_o}{\theta + a_2} + a_1 \right)$ , using (137) one can replace the acquired counts by multiples of acquisition intervals of the parameter  $N_o$ .

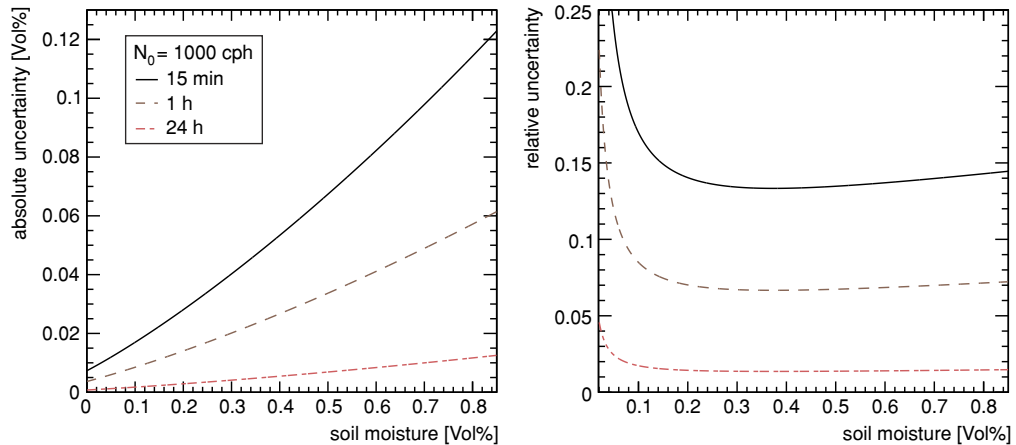


Figure 53: Absolute (left) and relative (right) errors for soil moisture determination using (137) for CRNS sensors.

[p] we will see later, that this definition has some drawbacks.



## UNDERSTANDING THE COSMIC-RAY NEUTRON DETECTOR

*Part of the results about the CRNS probe presented in this chapter have been published in [KS2018].*

In order to reduce the enormous computational effort, which inevitably goes along with the large scale differences of a  $\sim 1 \text{ m}^3$  detector in a  $\sim 1 \text{ km}^3$  environment, effective response models have to be applied rather than using the geometrical detector itself in the simulation. The solution to increase the recorded flux is to adequately scale up the volume of the detector entity. However, if the recorded flux is supposed to be increased by use of such a detector with its actual enlarged geometry (e.g. moderator and converter tube), this significantly alters its characteristics. A virtual sensor entity with an effective model allows for the upscaling of the counting volume of a detector, while still retaining the same features as the unscaled type. It also allows to set the maximum detection probability within the operation range to 100 %. However, such neutron detection models are sensitive to the specific response function of the detector [231–233]. Previous studies, where the results of this work can be related to, were based especially on the modeling of Bonner Spheres [164–168], and showed [169] that the detector response function can be approximated by the product of an energy-dependent efficiency term and an angular term. Monte Carlo models which rely on the implementation of such functions, e.g. [234], are a subclass of global variance reduction methods [235], which aim on increasing the computational efficiency, especially in undersampled regions.

### 8.1 | THE DETECTOR MODEL

The detector models, which are actually used for Cosmic-Ray Neutron Sensing have been introduced in sec. 7.2.1. In URANOS the device is modeled by a voxel geometry. The central cutout of the rover configuration is shown exemplarily in Fig. 54, the other detectors are presented in appendix B.1.5. The sensor geometry has been derived from actual devices and from supporting information provided by the manufacturer [236], see also Fig. 52. Details of the mechanical parts have been reduced to features that

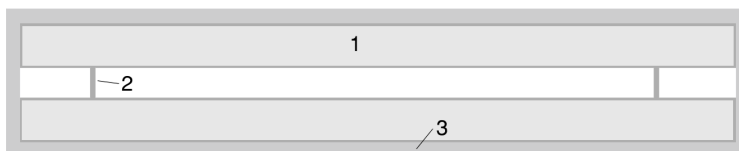


Figure 54: Cross section of the Rover detector simulation model with a length of 132 cm and a width of 26 cm. It features two gas filled proportional counter tubes in a stainless steel casing (1), aluminum mounting brackets (2) and a HDPE moderator (3). [KS2018]

have a significant influence on the neutron response, and only materials with significant macroscopic neutron cross sections have been considered. The size of the voxels has been set to  $1 \text{ mm} \times 1 \text{ mm} \times h \text{ mm}$ , whereas  $h$  denotes the layer height to which the voxel is extruded and varies from 1 mm, the generic cubic configuration, to 850 mm for the length of the CRS1000/B tube. The materials used are: high-density polyethylene

(CH<sub>2</sub>), aluminum oxide (Al<sub>2</sub>O<sub>3</sub>), steel (Fe with 20 % Cr, 20 % Ni) at 8.03 g/cm<sup>3</sup>, boron trifluoride (<sup>10</sup>B enriched BF<sub>3</sub> gas), <sup>3</sup>He enriched noble gas, and air (78 % N<sub>2</sub>, 21 % O<sub>2</sub>, 1 % Ar). The partial gas pressure has been set to 1.5 bar for helium and to 0.5 bar for boron trifluoride. See also appendix B.1.3.

The stationary systems (CRS1000 and CRS1000/B) are oriented upright, while the mobile system „rover“ is oriented horizontally. Consequently, the „top“ facing neutron flux runs from the surface upwards through the short cuboid face of the stationary sensor, and through the long cuboid face of the mobile detector. The „side“ facing fluxes run parallel to the surface through the long faces of the stationary detector and through two short and two long faces of the mobile detector.

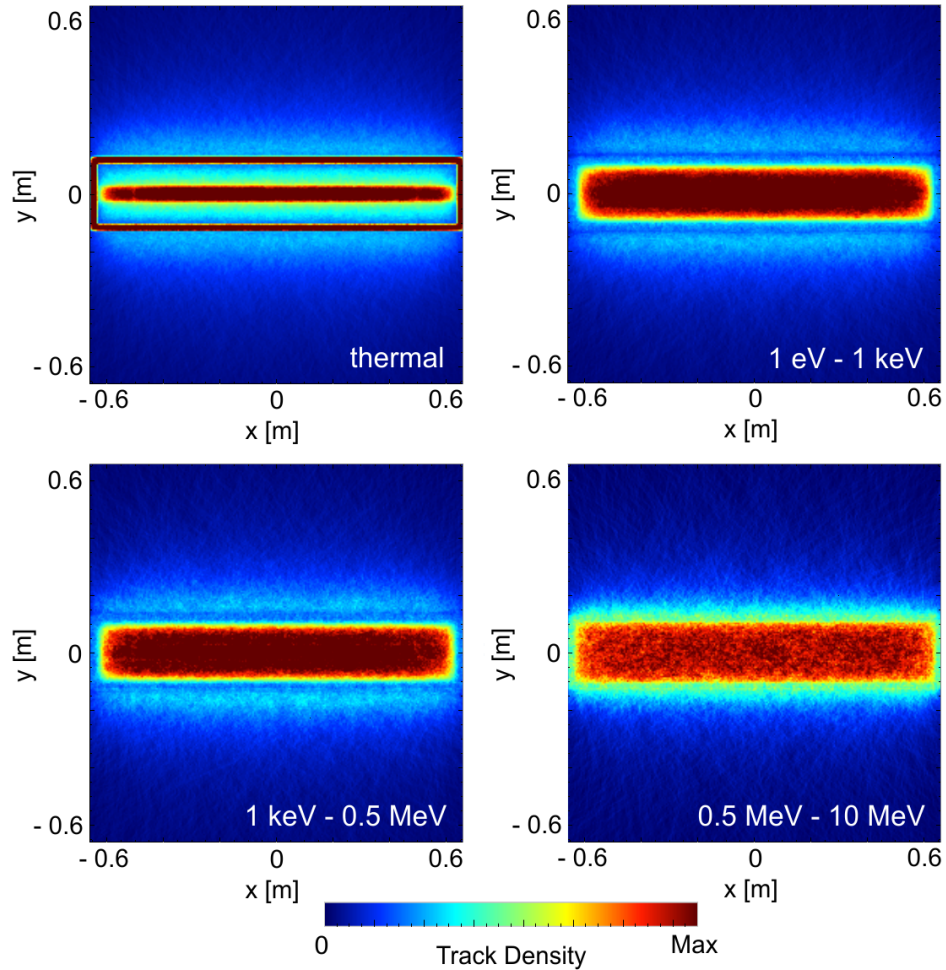


Figure 55: Track density within the <sup>10</sup>B<sub>F</sub><sub>3</sub> rover detector model using a randomly distributed flux from a plane source, illustrated for four energy regimes from thermal to MeV. The outer casing of the detector (see also Fig. 52) consists of polyethylene, which becomes visible by the outward directed flux. Neutrons of high energies (lower right panel) do not undergo enough interactions to stay contained in the casing. Thermalized neutrons (upper left panel) are scattered within the moderator and are efficiently absorbed by one of the two tubes, with a probability of  $\approx 0.5$  to be captured in either of them. [KS2018]

In order to simulate incoming cosmic-ray flux from the atmosphere, monoenergetic neutrons were released randomly from a virtual plane of the same extension as the model dimensions. The number of neutrons absorbed in the converter gas divided by the total number of neutrons released is defined as the efficiency  $R(E, \vartheta)$  of the setup, which intrinsically normalizes the efficiency to the detector area. As for the CRS1000/B with its cylindrical housing also the identical plane source definitions are used, this geometry leads to an ambiguity in the efficiency definition, which has to be considered for interpreting the results, see also [237]. That means, due to the surface

normals being different for the cubic CRS1000 and the cylinder of the /B version, the directionality of an orthogonally incident flux cannot be defined consistently for both<sup>[a]</sup>. To study the behavior of neutrons inside a detector system, the simulated neutron track density is shown exemplarily for a  $^{10}\text{BF}_3$  rover detector in Fig. 55. The tracks represent  $4 \cdot 10^7$  histories of incident neutrons with kinetic energies spanning 10 orders of magnitude. From the perspective of MeV neutrons, the path length through the polyethylene casing is in the order of the scattering length. This leads to an almost geometrically homogeneous distribution, where reflected neutrons have a negligible probability of reentry. Neutrons with  $E \geq 1$  keV exhibit shorter scattering lengths while the energy lost by moderation allows for more neutrons in the boundary region to escape the device (seen by the 'glow' at the perimeter). For smaller energies,  $E \leq 1$  keV, the leakage out of the device is minimized while the number of interactions within the moderator is maximized. In a cross section through the model (not shown) this equals the flux outside the polyethylene being lower compared to higher energy domains. As soon as neutrons are thermalized, their absorption in the converter gas gets most effective.

## 8.2 | THE ENERGY RESPONSE FUNCTION

The energy response of a detector system,  $R(E, \vartheta)$ , quantifies this sensitivity as a function of neutron energy  $E$  and incident angle  $\vartheta$ :

$$R(E, \vartheta) = \epsilon(E) \cdot g(\vartheta), \quad (140)$$

where an angle of  $\vartheta = 0$  would correspond to an orthogonal neutron incidence. Averaged over the whole surface of the detector, the incoming flux can independently be characterized as a function of these quantities. The analysis of the energy dependence is presented in the following. The results from the simulations of the angular sensitivity can be found in appendix B.1.5.2.

## 8.3 | ENERGY DEPENDENCE

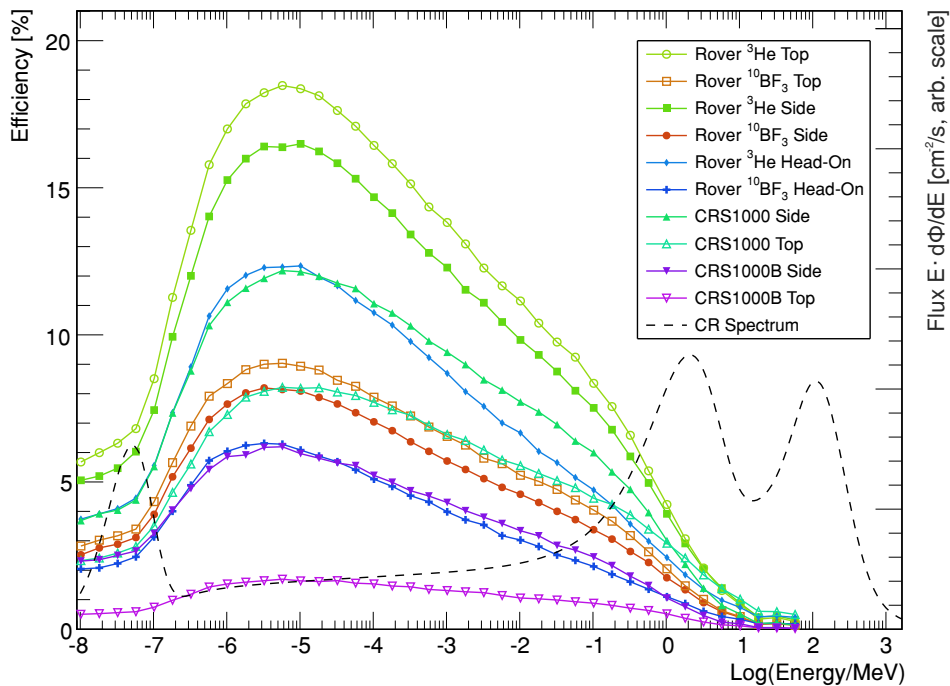
The energy-dependent component of the neutron response,  $\epsilon(E)$ , has been calculated by URANOS simulations of different detector configurations. The results presented in Fig. 56<sup>[b]</sup> show that all detector models exhibit qualitatively similar energy response in the range from 0.1 eV to 1 MeV with a maximum between 1 eV and 10 eV. The main differences in the resulting curves can be attributed to the absolute detection efficiency, which is a function of the detector model, the converter gas and casing area. The latter is influenced by the geometry and orientation of the detector, as the surface neutron flux is averaged over the exposed area. Minor qualitative deviations of the response functions are noticeable for different aspect ratios of moderator and counter tube, compare CRS1000 (top) and rover (side) in Fig. 56. The highest efficiency is achieved for neutrons in the energy range between 1 eV and 100 eV, while between 0.1 eV and 0.1 MeV average efficiencies can be found. The latter range corresponds to the 'water-sensitive domain' for the CRNS technique. The manufacturer has stated that the working energy range for the detectors is within 100 eV to 10 keV (unpublished data). This energy window appears to be too narrow compared to the results presented

[a] Nota bene: this definition is not phase space conserving under angular variation - considering a neutron beam incident onto the sensor from a specific direction, the effective projected area of the corresponding cuboid face has to be taken into account.

[b] The cosmic-ray neutron flux density is represented per logarithmic unit of energy, see (33) in sec. 1.4.1, given in units of  $d\Phi/d(\log(E)) = E d\Phi/dE$ .

here, indicating a hitherto underestimation of near-thermal neutrons. A significant contribution of eV-neutrons was also suggested by other authors using empirical [238] and modeling analysis [239]. The energy efficiency shows also remarkable similarity to reference curves of Bonner Spheres with equal moderator thickness, see Fig. 47. As an example, the rover detector system with the standard 1 inch moderator thickness approximately corresponds to a 3 inch moderator type with a 3.2 cm spherical counter [170], or to detectors equipped with a 4 mm  $^6\text{LiI}$  crystal and a 2 inch moderator [166]. This example illustrates that the main influence on the energy-dependent response can be attributed to the thickness of the moderator. Similar results also have been presented for portal monitor type detectors [120]. For the actual integration of such a response into an environmental neutron transport model a probe-specific function derived from a cubic spline interpolation of this data or in good approximation Bonner Sphere calculations can be utilized.

Figure 56: Absolute counting efficiency for various actual cosmic-ray neutron sensing devices. The results for perpendicular irradiation are averaged over the entire surface for each setup. For 'CRS1000 Side' exemplarily the effect of production-related density variations between  $0.92\text{ g/cm}^3$  (low) and  $0.98\text{ g/cm}^3$  (high) are plotted. The cosmic-ray neutron spectrum from [66] illustrates the relative abundance of neutrons above the surface. [KS2018]



#### 8.4 | DETECTION PROBABILITY WITHIN THE CASE

The results above have addressed the detector efficiency averaged over the entire detector surface. However, the detector case itself cannot be considered as a homogeneously responsive device. A neutron hitting the detector centrally has a much higher absorption probability than a neutron entering at the very edge of a moderator. The spatial distribution of the detector efficiency can be illustrated by an efficiency map. As an example, Fig. 57 shows the boron trifluoride rover system with its two proportional counter tubes for 10 eV neutrons from the side- and top-facing perspective. The color scale represents the detection probability for a normally incident neutron, showing that detection is more probable in a narrower area for sideways incident neutrons compared to neutrons incident from the top. Although for the epithermal/fast regime Fig. 54 showed a homogeneous distribution of the tracks inside the casing, the absolute efficiency varies significantly depending on the individual original impact location.

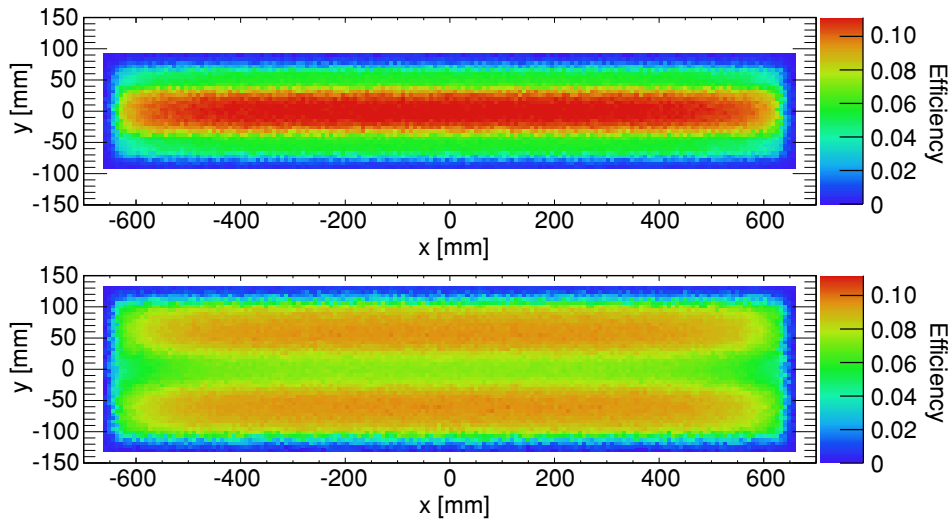


Figure 57: Efficiency map for the  $^{10}\text{BF}_3$  rover system for orthogonally incident neutrons from the side (top panel) and the top direction (bottom panel), depicting the probability of being absorbed in the converter dependent on the  $x, y$  coordinate entering the detector. [KS2018]

## 8.5 | UNCERTAINTY ANALYSIS

Simulations performed in this study were conducted with  $10^6$  released neutrons, which corresponds to a relative statistical error of the detector response  $R$  of  $s_R = 10^{-2}/\sqrt{R}$ , where  $R = R(E, \theta)$  is given in units of percent and usually stays below 1%. The good agreement with reference calculations from literature confirmed the reasonability of this approach, see also sec. 6.6.2. Systematic errors of potential relevance mainly involve the assumptions on material composition and geometry. For polyethylene the scattering kernel was emulated by water. Due to the higher mobility of water molecules, it could have biased the resulting efficiency by up to 10%, particularly in the thermal regime. The fabrication related variations of polyethylene density could further alter the macroscopic cross sections of the real detector in the order of (1-2)%, thereby shifting the actual response function towards thicker or thinner moderators. Moreover, the abstraction level used for the modeled detector geometry has been high, as only moderator, absorber, and the metal parts have been taken into account. Nonetheless, the calculations showed that even drastic changes of the arrangement had only marginal effects on the response function.

## 8.6 | IMPLICATIONS OF THE SENSITIVITY ANALYSIS

Although the internal assembly of the detector is clearly distinguishable in the impact location map of Fig. 57, the device is small compared to the diffusion length of environmental neutron fluxes, see also Fig. 30. Therefore, higher accuracy of the presented computational results would not lead to relevant information for environmental research.

Therefore, one can conclude that for the general analysis of neutron transport, a domain specified from 100 eV to 10 keV is suitable, slightly underestimating the contribution from both ends of the spectrum - fast and thermal neutrons. The implications of working with the simple model of a lower and upper threshold for the sensitive range are probably moderate. The entire spectrum from 1 eV to 0.1 MeV is dominated by elastic scattering and the cosmic-ray induced density of albedo neutrons. It is related to the environmental water content and scales uniformly in this regime [66]. Hence, the asymmetric shape of  $\epsilon(E)$  has a minor influence on the sensitivity of the device in terms of soil moisture sensing. According to additional simulations (not shown), the change of the sensor's footprint radius, which will be investigated later, is negligible. The similarity to the response of Bonner Spheres, however, explains the reported influence of

thermal neutrons on CRNS detectors [238, 239].

Given the effective detection area of the cuboid sensor and its angular response, both conformations do exhibit a different sensitivity to the neutron flux directly below the sensor. In other words, near-field effects as seen later, can be attributed to the relatively high sensitivity to the downward direction and the flux distribution around the detector. In situations of small-scale changes of the topology below the sensor as for example in the monitoring of snow cover [240] with height and snow pack variations or dense and time-varying biomass estimations [220] there is a direct influence of the external flux field to the probe response.



## FOOTPRINT INVESTIGATION

## 9.1 | FOOTPRINT PRELUDIUM

Part of the results about the footprint investigation presented in this chapter have been published in [KS2015] with complementary information in the follow-up publication [SK2017].

The aim of this work is to investigate the specific features of neutron transport at an air-ground interface. Specifically, the system can be regarded as an exponentially decreasing volume source from a low-density to a high-density region, whereas the latter slows down neutrons much faster due to the higher abundance of water. As hydrogen interactions also have a different scattering angle distribution the system behaves asymmetrically regarding the domain particle density parity. The goal of this study is to find and describe the ensemble dynamics in a highly non-linear system.

## 9.1.1 | THE COSMIC-RAY NEUTRON SPECTRUM ASSEMBLY

Continuing from the description in sec. 3.2 the focus is set on parameters for maximal atmospheric depths (low altitude)  $d_o = 1020 \text{ g/cm}^2$ , solar maximum conditions  $s = 1700 \text{ MV}$  and an exemplary cutoff rigidity of  $r_c = 10 \text{ GV}$ . This procedure might introduce small differences for different places on Earth. However, measurements [65] show that geomagnetic latitude has only very small effects on the shape of the spectrum. It depends slightly on atmospheric depth, as at  $d_o$  the detectable particle flux can be regarded as the tails of the high energetic cascades, see sec. 3.1. A lower cutoff rigidity means a higher contribution of low energetic particles to the primary spectrum and a higher altitude means a different ratio of proton and neutron fluxes, which each have different interaction lengths [32]<sup>[a]</sup>.

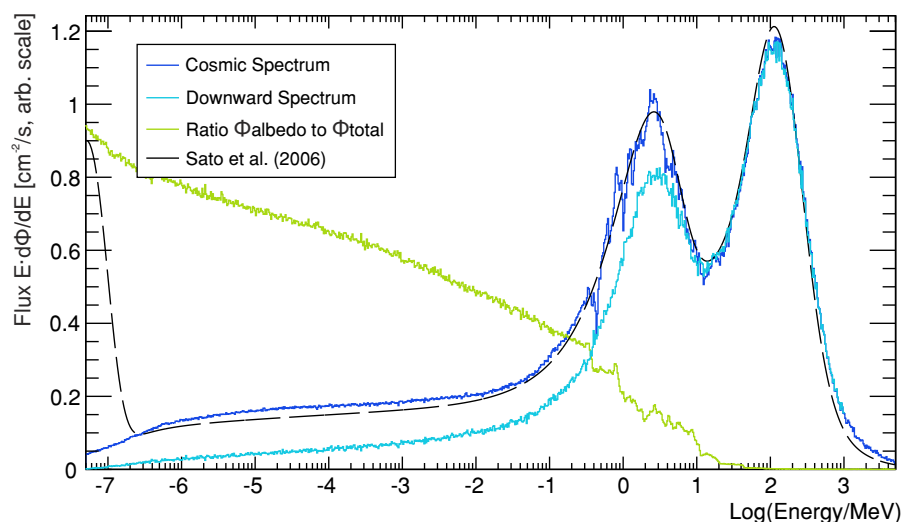


Figure 58: Cosmic-ray neutron spectra starting from the analytical angular integrated spectrum [66] (black) generating the downward flux only spectrum (cyan) by subtracting the albedo from the total spectrum (blue). The ratio (green) can be calculated independently over any, in this case water, body. Neutron flux given in units of lethargy (98).

[a] At sea level the hadronic flux can be estimated to be composed of 94% neutrons, 4% pions and 2% protons. Therefore, the overall-nucleon flux is dominated by neutrons. Their attenuation length ranges from  $140 \text{ g/cm}^2$  at evaporation energies to  $160 \text{ g/cm}^2$  in the GeV range. The high-energy proton attenuation length, however, is much lower with  $110 \text{ g/cm}^2$  due to electromagnetic interactions in addition to the hadronic channels. Myons, as mainly electromagnetically interacting minimum ionizing particles, in comparison are much more penetrating with  $520 \text{ g/cm}^2$ . This leads to a dynamic composition of the residual particles of atmospheric cascades and especially in regard to the above-ground neutron flux.

As the MeV-and-below-neutron spectra  $\Phi$  generally consist of an incoming  $\Phi_{\text{inc}}$  as well as a backscattered component  $\Phi_{\text{a}}$ , an incident spectrum is obtained by two steps:

1. for the given spectrum a response spectrum is calculated over pure water,
2. the resulting backscattered spectrum is subtracted from the original spectrum.

$$I_{\text{inc}} = \Phi - \Phi_{\text{a}} = \Phi (1 - r) \quad (141)$$

with the ratio being defined as  $r = \Phi_{\text{a}}/\Phi$ . This recalculated spectrum then contains only incident neutrons and can be used as the source of incoming radiation for any surface condition. Fig. 58 shows the result of this calculation. From the response of a pure water body a factor for each energy bin is obtained which is used to generate the downward-facing part from the analytical spectrum of [66]. This energy distribution can be used to arrive again at the full spectrum in a simulation model. For epithermal and fast neutrons the flux is considered distributed in  $2\pi$ . An exception to this otherwise isotropic distribution are emission angles of high-energy neutrons above 10 MeV, which are highly collimated along the downward facing direction (nadir angle  $\theta$ ). According to observations and simulations by Nesterenok [241] the non-uniformity of the angular spectrum  $J(\theta)$  is given by<sup>[b]</sup>:

$$J(\theta) = e^{-2.5 (1 - \cos \theta)}. \quad (142)$$

This strategy combines a universal and validated source spectrum for cosmic neutrons with a high computational efficiency. As the location of the source is commonly traded against computational effort, whereas the initial energy spectrum is bonded to a variety of uncertainties, the modeling presented here can entirely focus on the description of the air-ground interface. A popular approach is to emit secondary cosmic-ray neutrons at approximately 8 km altitude and to perform a cascaded propagation through the atmosphere [224, 227, 243]. This strategy and related simplifications come with several drawbacks:

- Cross-sections of high-energy neutrons exhibit uncertainties of up to 50 % depending on element and type of reaction, though there has been progress in the last two decades. As a consequence, inconsistencies are apparent throughout different codes for galactic and atmospheric cosmic-ray transport [244–246].
- Measurements of cosmic-ray energy spectra are additionally accompanied by observational uncertainties. Comparative studies of Monte Carlo codes show differences of up to 20 % for calculating sensitivities of the neutron response to experimental devices [247–249] and as well for the spectrum unfolding technique [250].
- The exclusive neutron source at the top of the modeled atmosphere inadvertently neglects neutron generation throughout the atmosphere by other secondary particles like protons, pions and muons.
- Atmospheric water vapor is often ignored, although hydrogen is the main moderator for neutrons<sup>[c]</sup>.
- The large difference in scale of the domain requires high computational effort to reach sufficient statistics.

[b] The factor of 2.4 for (142) originally published in [241] for atmospheric depths of 1000 g/cm<sup>2</sup> has been corrected to 2.5 according to [242]. As a comparison: the angular distribution over all energies in [159] scales by a factor of 1.9.

[c] However, the analytical spectrum by Sato [61, 66, 251] used in this work also has this shortcoming.

Models which rely on particle propagation through the upper atmosphere incorporate a high complexity and vulnerability to such uncertainties.

In the attempt to reduce computational effort, other studies identified the high-energy component of the cosmic-ray neutron spectrum as the precursor for the generation of fast neutrons in the soil [252, 253]. Since the attenuation process of high-energy neutrons in the ground is known, it seems likely that an artificial source in the soil is sufficient to mimic the production of evaporation neutrons. However, some drawbacks of this method are important to note:

- Attenuation of high-energy neutrons in the soil follows an exponential decrease that is dependent on soil type and location on Earth.
- There is no verified energy spectrum for neutrons in the soil.
- Evaporation neutrons are a significant part, but do not make up the spectrum as a whole, see Fig. 58. The incoming energy spectrum from the atmosphere exhibits low-energy components and particularly neutrons which already evaporated in the air.

Considering only evaporation neutrons in the soil can be an approach, especially for dry conditions, which tends to overestimate average neutron energies, as incident low-energy neutrons from the top are neglected, and thus also overestimates the footprint size. Moreover, the deduced footprint appears to be insensitive to soil moisture, because its influence on neutron moderation is underestimated. Here, a different approach is applied, which aims to combine the advantages as well as avoid the drawbacks of both strategies mentioned above. To minimize the uncertainties of the propagated energy spectrum, this study focuses on the domain close to the surface by using validated results from independent atmospheric simulations as model input.

### 9.1.2 | EXPERIMENTAL VERIFICATION

Since the footprint definition is based on a radial symmetry, direct empirical evidence is difficult to achieve with natural structures. However, approaching water surfaces and transiting the coast line has been a common procedure to determine the range of detected neutrons. For example, [254] moved the detector over a lake and interprets that the signal strength is hardly sensitive to neutrons from the land side at distances greater than 200 m. In the last years, many experiments with CRNS detectors have been performed across a water-land boundary. Data from Oceanside Pier (California, US) indicate that the sensitive distance is on the order of (100-200) m at sea level. With URANOS attempts have been made to reproduce these transect experiments by moving a 4 m square-shaped detector over pure water and land with exemplary soil moistures from 1 % to 30 % and fixed air humidity  $h = 10 \text{ g/m}^3$ . Figure 59 illustrates the simulations and the two experiments mentioned above. The simulated signal strengths clearly correspond to the measurements and give an indication of the soil water content which was unknown at the time of the experiments.

The signal gradient is asymmetric over water (Fig. 59 left) and land (Fig. 59 right), which agrees with results from [243], who investigated the influence of large wet structures on the signal strength. However, direct observables for neutron transport cannot be identified in the experiment as transect experiments do not give a direct measure of the footprint radius under conditions where the instrument is usually applied. These effects can be explained by (1) the overestimation of dry over wet regions in the signal, as a consequence of the non-linear relation:  $\theta \mapsto N$ , (2) the effective removal of traveling neutrons due to the presence of a water body on their way to the detector, and (3) the non-radial geometry of the experiment. However, the presented data provide

evidence for the valid performance of the URANOS model.

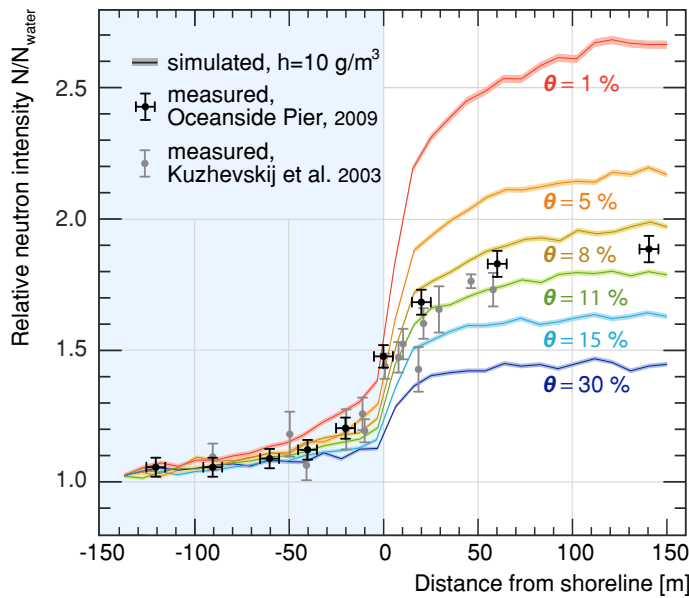
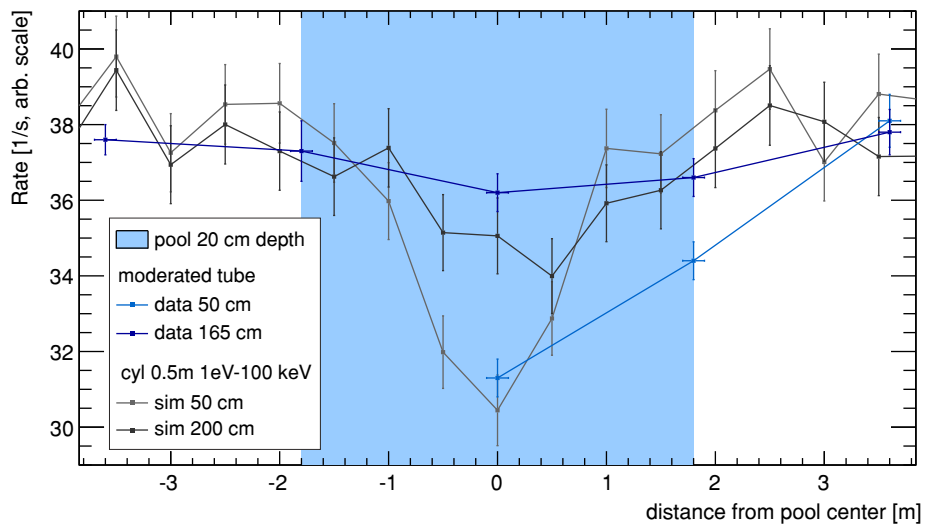


Figure 59: Coastal transect experiments simulated with a 4 m square-shaped detector every  $\pm 10$  m from the coast line. Relative neutron counts show good agreement with measurements across a water-land boundary at the Oceanside Pier (US) as well as tests at Lake Seliger (RU) [254]. Air humidity  $h$  and soil moisture  $\theta$  of the experiments were unknown. [KS2015]

In order to study the small-scale effects, which, as seen later, are predicted by URANOS, experiments have been carried out by M. Zreda with a detector over a pool. In a series

Figure 60: Swimming pool transect experiments by M. Zreda and accordingly simulated setup with virtual cylindrical detectors of 0.25 m radius. Furthermore, baseline measurements were taken in order to normalize simulation and experimental data outside the range shown in the plot.



of two transects at heights of 50 cm and 165 cm over a pool of 0.9 m radius filled with 20 cm of water. The experiment was carried out in a dry region of Arizona (US), where, using TDR probes, in the vicinity of the experiment  $\theta = 7\%$  was found and 9% soil moisture was found in 20 m distance around a building structure. A rover-type of CRNS detector was used, see sec. 7.2.1, which has a significant spatial extension of 1.3 m length compared to the pool itself. For the simulations the soil moisture was set to 7%, 6.5 g/m<sup>3</sup> air humidity and 920 mBar air pressure. The simulated detector entities were cylinders of radius 0.25 m and 0.5 m height, superimposed to the air layer, 100% efficiency<sup>[d]</sup> and an energy range of 1 eV to 100 keV at heights of 0.5 m to 1 m and 2 m to 2.5 m. Experiment and simulation agree remarkably well in this case where the signal domain is tiny compared to the overall footprint with an areal contribution of  $10^{-5}$  to  $10^{-6}$ . The slightly stronger signal in the simulations can be attributed to

[d] yet non-absorbing, otherwise the simulated detectors would influence each other.

the slightly larger water body and to possible contributions of lattice water and soil moisture gradients in the order of 2‰<sub>Vol</sub>.

### 9.1.3 | A CLOSER LOOK AT THE AIR-GROUND INTERFACE

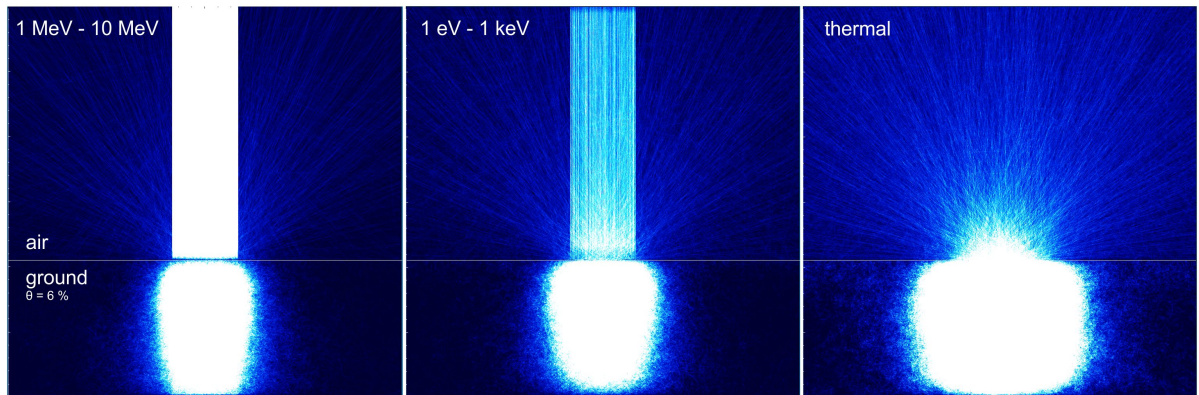


Figure 61: Flux calculation of an air-ground interface in which neutrons are artificially released centered straight down but with a CR spectrum according to Fig. 58 based on (67). The simulated neutron tracks from evaporation (MeV) to absorption (thermal) of  $80 \cdot 10^4$  histories are displayed in a domain of  $3 \text{ m} \times 3 \text{ m} \times 3 \text{ m}$ .

In air the mean free path for neutrons is approximately 1000 times larger than in the soil, see also Fig. 30. In an artificial scenario aiming to visualize the transport at the interface, a flux column is released onto the ground. A rather dry condition is chosen in order to show a more spatially extended distribution. Fig. 61 shows the tracks of all neutrons in the domain in three different energy regimes. Most high-energy neutrons entering the soil are scattered in forward direction, therefore, the possibility of leaving the ground is considerably low - except originating from evaporation processes, that emit secondary particles nearly isotropically. However, only neutrons within the top few dozen centimeters below the interface border exhibit a significant probability for leaving. In general, this also leads to slant soil emission angles being suppressed. Epithermal neutrons below 1 MeV behave rather diffusively until they are moderated to thermal energies. As a first order approach, one can indeed expect neutrons to behave as a diffusive gas, as it was formulated by [255], and applied to a footprint estimate by [253] besides the modeling. But since every collision results in an energy loss for the neutrons, their mean free path between collisions changes and pure diffusion theory loses validity. The Fermi age theory, e.g. applied in [256], accounts for these energy losses in a diffusive system, but analytical solutions exist only for mono-energetic particles and are not feasible for the cosmic-ray neutron spectrum exposed to a wide range of environmental conditions with different cross sections.

The cosmic-ray spectrum is partly also made up of neutrons slowed down in air, which have a higher probability of being emitted back into the air<sup>[e]</sup>. For thermalized neutrons the soil can be regarded as a source. It can be explained by the fact that the moderation due to the presence of hydrogen is effective and no isotope having a large capture cross section is present, contrary to the case of air, in which argon and especially nitrogen are comparably strong absorbers.

[e] In this scenario the emitted flux is partially suppressed as all particles are released straightly downwards, which means that by collisions with hydrogen at least two scatterings are required to change the direction along the z-axis. In a more realistic simulation with rather slant impact angles onto the ground a scattering reaction in forward direction can already lead to leaving the soil.

## 9.1.4 | MODEL SETUP

### 9.1.4.1 NEUTRON SOURCE AND DETECTOR

Neutrons are released from a volume source with randomly distributed origins from 2 m to 42 m above the surface. The amount of initial particles per run was chosen according to statistical errors -  $10^7$  histories are a reasonable trade-off between computational effort and precision for typical calculations presented here<sup>[f]</sup>. The simulations for the footprint analysis, which will be presented in the following, do not make use of the later implemented high energy cascade transport model.

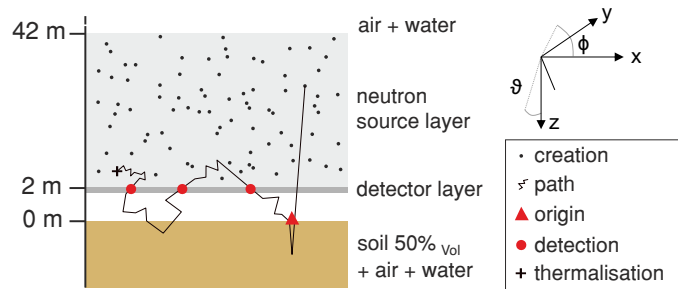


Figure 62: Setup of the simulation containing a 40 m thick neutron source layer in the atmosphere and a thin detector layer at 2 m above ground. A particle is counted as an albedo neutron if it had preceding contact with the soil. [KS2015]

Neutrons are recorded individually in an horizontally infinite detector layer, see also sec. 6.5.1. Any neutron that experienced interaction with the soil is counted as it passes the layer. The infinite plane detector overlays the atmosphere by means of a 25 cm high sheet at a vertical position of (175-200) cm, a usual height for mounting cosmic-ray probes. The detector layer is crossed by the neutrons and thus maps spatially the neutron density<sup>[g]</sup>. For the effective energy range to which the detector is sensitive, practical considerations by [253] and theoretical by for example [257], the detection energy is set to a window from 10 eV to  $10^4$  eV. The detection efficiency of moderated helium-3 detectors is nearly constant in that energy regime [258], which is why signal weighting for different energies is not necessary. However, common cosmic-ray neutron detectors, see sec. 7.2.1, are contaminated by approximately (10-20) % thermal neutrons [238]. It is not intended to account for this issue here, as this study aims to investigate characteristics for a detector ideally tailored to the needs of environmental water sensing.

### 9.1.4.2 AIR, SOIL AND WATER

The modeled pure air medium consists of 78 %<sub>vol</sub> nitrogen, 21 %<sub>vol</sub> oxygen and 1 %<sub>vol</sub> argon usually at a pressure of 1020 mbar. The soil extends to a depth of 3 m and the air to 1000 m. Both, soil and air are represented by planes of infinite extension, which can have subdomains, either to create a density profile in depth or to add specific entities like water or a detector. The soil consists of 50 %<sub>vol</sub> solids and a scalable amount of H<sub>2</sub>O. The solid domain is comprised of 75 %<sub>vol</sub> SiO<sub>2</sub> and 25 %<sub>vol</sub> Al<sub>2</sub>O<sub>3</sub> at a compound

[f] At the time of investigating the footprint such a calculation, depending on the soil moisture, took around 4 h. Due to further performance improvements URANOS meanwhile runs in such a setup approximately 250 neutrons per core per GHz per second, which means  $10^7$  histories can be tracked in around 40 min.

[g] Multiple counts of a single neutron in the detector layer account for the measured density equivalent for a single count per volume detector. This relation holds if (1) the dimension of the absorbing detector medium stays below typical scale lengths of neutron interactions (10 m-100 m), and (2) particles do not scatter multiple times in that volume. That is very unlikely for non-thermal neutrons and furthermore does not factorize in the count statistics.

Caveat: Typically Monte Carlo simulations like MCNP score particle flux as track length per volume. In the case presented here with no preferred detector orientation and infinite layer geometries this definition is at least unhandy.

density of  $2.86 \text{ g/cm}^3$ . Thus, the total densities vary from  $1.43 \text{ g/cm}^3$  to  $1.93 \text{ g/cm}^3$  for  $0\%_{\text{vol}}$  and  $50\%_{\text{vol}}$  soil moisture, respectively. Further chemical constituents regarding rock types are not significant<sup>[h]</sup> for the characteristics in the epithermal regime [218, 259]. Further material properties can be found in appendix B.1.3, however, the amount of chemically bound water in rocks lies in the order of a few percent, therefore  $0\%$  soil moisture is a case mainly of theoretical interest.

### 9.1.5 | SOIL MOISTURE AND ABOVE-GROUND NEUTRON DENSITY

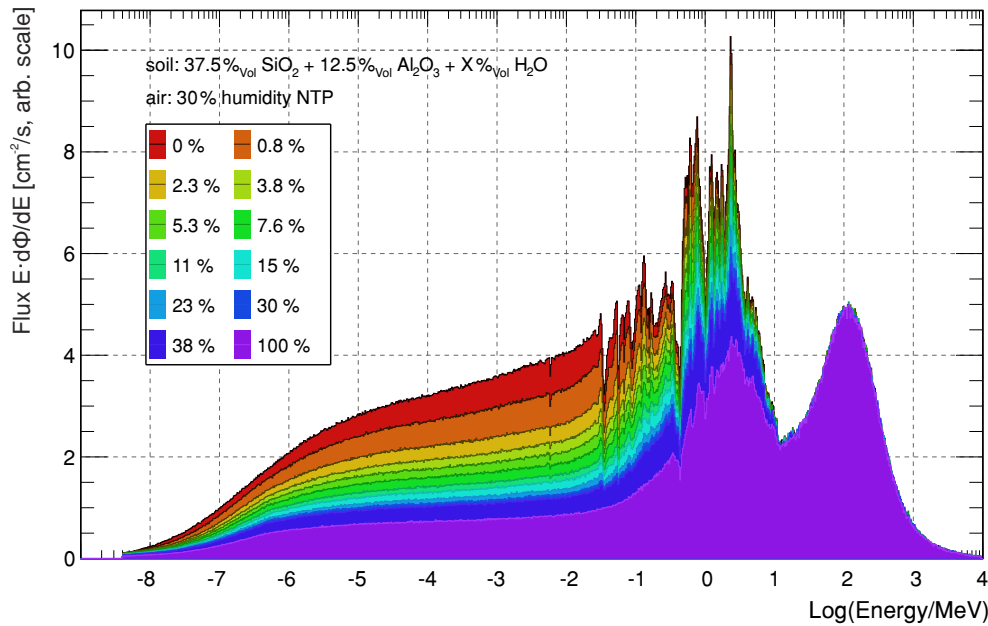


Figure 63: Neutron spectrum without thermal transport in a height of 2 m above the ground for different volumetric soil moisture conditions and a water body.

The response of the ground to the incoming flux of cosmic-ray neutrons lead to several interesting features in the resulting energy spectrum. Fig. 63 shows the efficient reduction of neutron intensity by soil moisture in the relevant energy range of the CRNS method. In general, the neutron density appears to be very sensitive to small amounts of hydrogen in the soil (and air).

The domain below 1 MeV is governed by elastic scattering, the relative density in this regime depends on how effectively neutrons are slowed down. Tab. 11 lists the stopping power, see also sec. 1.4.1, of some elements. It summarizes that isotopes heavier than hydrogen require an order of magnitude higher amount of collisions to reach thermal energies. For the effective moderating ratio the macroscopic cross section also has to be taken into account. Fig. 63 shows, that the relative neutron density difference between  $0\%$  and  $1\%$  soil moisture is large compared to any subsequent addition of further hydrogen. The change in above-ground flux from  $0\%$  to  $5\%$  is comparable to the change from  $5\%$  to  $50\%$  soil moisture. One can also observe that in the MeV-regime the spectrum above a water body reflects mainly the features of the cross section of oxygen, whereas for dry cases the silicon and nitrogen components become dominant. Yet, the details of the structure of the evaporation peak have a negligible influence for the method of soil moisture sensing.

This behavior can partly be related to the higher amount of neutrons being emitted into the air and partly to the transport within the system itself. Fig. 64 shows the flux spectrum emitted from the soil, e.g. neutrons which are either generated within the ground or reflected from it. One can observe a similar relation regarding soil moisture

[h] In rare cases larger amounts of heavier elements like iron can be present in rocks, which can slightly increase the amount of evaporation neutrons.

Figure 64: Neutron spectrum emitted from the soil without thermal transport in a height of 2 m above the ground for different soil moisture conditions and a water body.

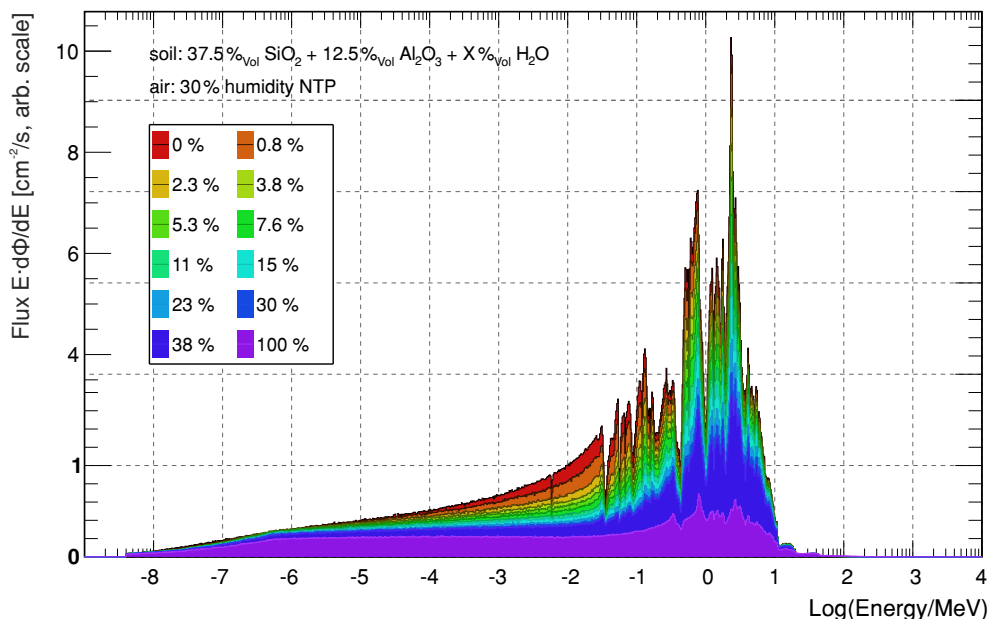


Table 11: Slowing down of neutrons by interaction with different isotopes from 2 MeV to thermal and to an exemplary energy relevant for CRNS. Calculations according to (31) and (32).

Element	Mass [u]	log. energy decrement $\xi$	avg. no. collisions $n_{col}$	
			to thermal	to 100 eV
H	1	1	18	10
H <sub>2</sub> O	-	0.92	20	11
N	14	0.136	135	73
O	16	0.12	153	82
Al	27	0.0723	255	137
Si	28	0.0698	264	142
Fe	56	0.0353	522	280

changes as for the total spectrum, Fig. 63, which extends the trend to lower energies. In case of the total absence of hydrogen the system behaves nearly like a resonator with a small damping constant - neutrons are scattering within a domain which rather acts as a reflector. Therefore, the presence of a small amount of hydrogen already leads to a smooth scaling of the system.

Exemplarily also the effect of air humidity is presented in Fig. 65 for the scaling of the above-ground neutron flux for rather dry conditions. In temperate zones typically humidities around 10 g/m<sup>3</sup> can be expected and 33 g/m<sup>3</sup> would correspond to a rain forest climate. For hydrogen in air the following observations can be made: The intensity scaling can be found in the sub-MeV region due to the fact, that contrary to soil moisture it does not significantly change the direct albedo flux<sup>[i]</sup>. The scaling of the total neutron flux as a function of water vapor shows a nearly linear behavior, yet slightly more sensitive for low air humidities. However, the relative change in intensity also depends on the soil moisture itself. In the example of 4% soil moisture we find a 15% change in the epithermal regime for the given setups. This scaling decreases with comparably larger amounts of water in the soil.

As seen from the discussion above and Fig. 63 the above-ground flux scales by a hyperbolic law, as also already indicated by (137) from [216]. This description is also underlined by the results from this work. Fig. 66 provides a comparison of neutron

[i] As the spectrum is released in the vicinity of the ground interface effects of atmospheric water vapor, which lead to a premoderation of the spectrum and an additional attenuation due to the increased area density, are neglected here.



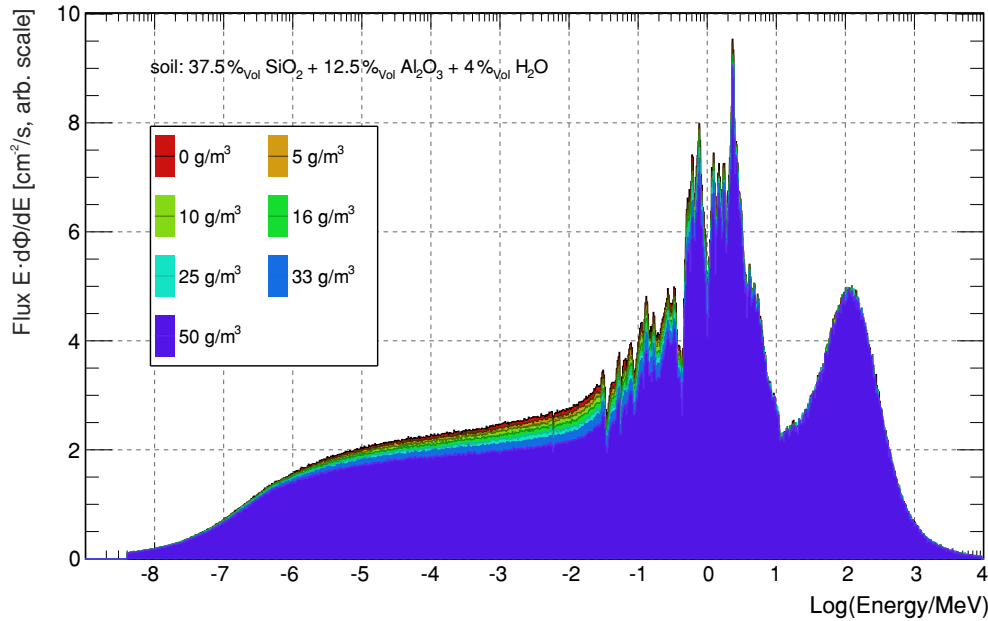


Figure 65: Neutron spectrum without thermal transport in a height of 2 m above the ground for different air humidity configurations.

densities as a function of soil moisture normalized to (137). For URANOS settings with and without the high-energy transport model are presented, whereas the latter propagates the particles above 20 MeV with an interaction-balanced model yielding typical attenuation lengths for the high-energy regime. In case this model is not used, the flux into ground is lower on average, which leads to a smaller amount of evaporation neutrons being emitted into the air. However, there is no qualitative difference between both, which shows that the hyperbolic shape is entirely determined by the physics below 1 MeV. Results from MCNPX, see sec. 5.2.1, are presented in comparison, scaled to match the porosity. The slope appears to be slightly higher, yet both simulations agree remarkably well given the complexity of the underlying system. However, the empirical results from [216] are not supported by any modeling. As seen from other experiments carried out afterwards and for example presented in sec. 9.1.2, simulation models can provide a consistent picture of measured above-ground densities.

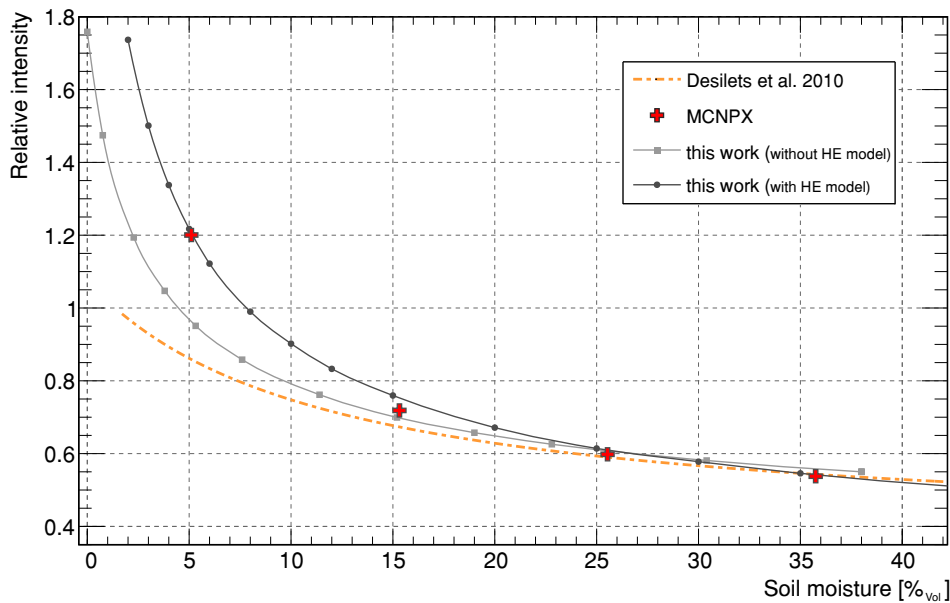
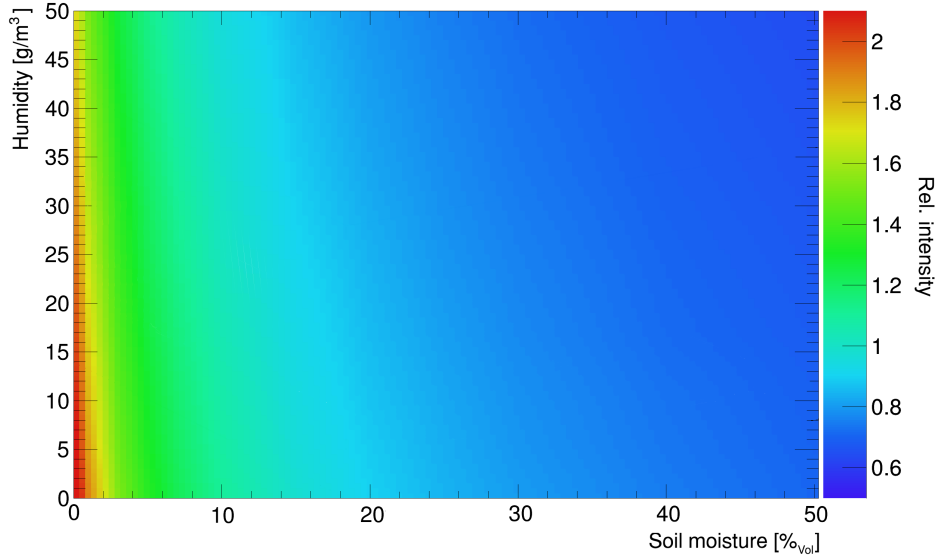


Figure 66: Above-ground neutron density as function of soil moisture, scored in the interval 1 eV-10 keV (with and without high energy particle transport) at  $h = 3 \text{ g/m}^3$  in comparison to MCNPX calculations ( $h = 0 \text{ g/m}^3$ ) and to the commonly used equation (137).

As already seen from the exemplary spectra of Fig. 65 the above-ground neutron intensity also depends on the water concentration in the air. The results from the analysis of the intensity scaling, see Fig. 67, are the following: The general response at

a fixed air humidity can be described by a hyperbolic expression. In first order humidity can be corrected linearly as proposed by [227], however, at least a cubic dependency correction has to be applied in addition. Furthermore, the sensitivity to water vapor also depends on the soil moisture itself.

Figure 67: Dependency of the above-ground neutron density in the energy interval 100 eV-10 keV as a function of volumetric soil moisture and air humidity. The white grid lines show the fitted function (143).



A function, which has been found to describe the relative intensity  $I(\theta, h)$  with the features mentioned above is the following:

$$I(\theta, h) = \left( k_0 \frac{1 - k_5 h}{\theta + k_2} + k_1 (1 + k_6) \exp(-k_3 \theta) + k_4 \right) \cdot (1 - k_7 h). \quad (143)$$

The parameters  $k_i^{[j]}$  are evaluated as summarized in tab. 12.

$k_0$	$k_1$	$k_2$	$k_3$	$k_4$	$k_5$	$k_6$	$k_7$
0.05774	0.217	0.03967	1.539	0.4964	0.0044	0.0026	0.00162

Table 12: Numerical values for the parameters of the intensity function (143).

### 9.1.6 | TRACKING COSMIC-RAY NEUTRONS IN SOIL AND AIR

The observed intensity scaling depending on different amounts of environmental water can be linked to the number of scatterings a neutron undertakes in such a system. Even for very dry conditions hydrogen contributes to at least 10% of the interactions as can be seen in Fig. 68. Oxygen is as well present in air ( $O_2$  molecules) as in water as in rocks. The contribution of nitrogen means significant transport via the atmosphere. Although in this chart ground and air are not scored independently, it can already be concluded from the relative share of aluminum and silicon atoms, that within the soil water is the main scattering partner, whereas in air nitrogen plays an important role. Therefore, soil tends to lose its reflection capability with increasing hydrogen content, whereas air, even in the case of 10 g/m<sup>3</sup> humidity, acts as a transport medium.

In order to unfold the picture of Fig. 68 one can analyze the individual histories of the neutrons in the system. Fig. 69 shows for the conditions presented before the elastic and inelastic scattering distributions per neutron. Important for the interpretation is the peak for a large amount of scatterings. These neutrons have potentially a long integrated travel distance and probed the soil many times and hence develop the

[j] With  $k_2$  in [m<sup>3</sup>/m<sup>3</sup>],  $k_5$  and  $k_7$  in [m<sup>3</sup>/g].

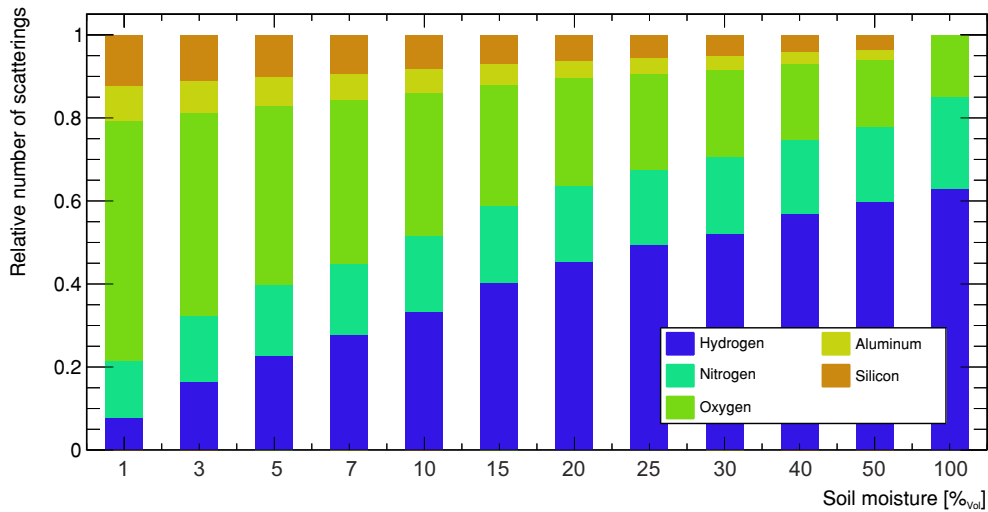


Figure 68: Relative distribution of scattering interactions for various volumetric soil moisture conditions and an air humidity of  $h = 10 \text{ g/m}^3$ .

characteristic of the system. At the lower end of the distribution histories of neutrons can be found, which directly leave the system, mainly downwards. For typical soil moisture conditions an antiproportional relation to the mean number of interactions can be observed. For extremely dry conditions the system changes towards an extremal behavior with neutrons, which never undergo any interaction with hydrogen as can be seen from the second peak of the 0% distribution. Another interesting observation is the long tail in case of extremely wet conditions. It corresponds to neutrons which are transported mainly over the air when the reflection probability for interface crossings becomes considerably low.

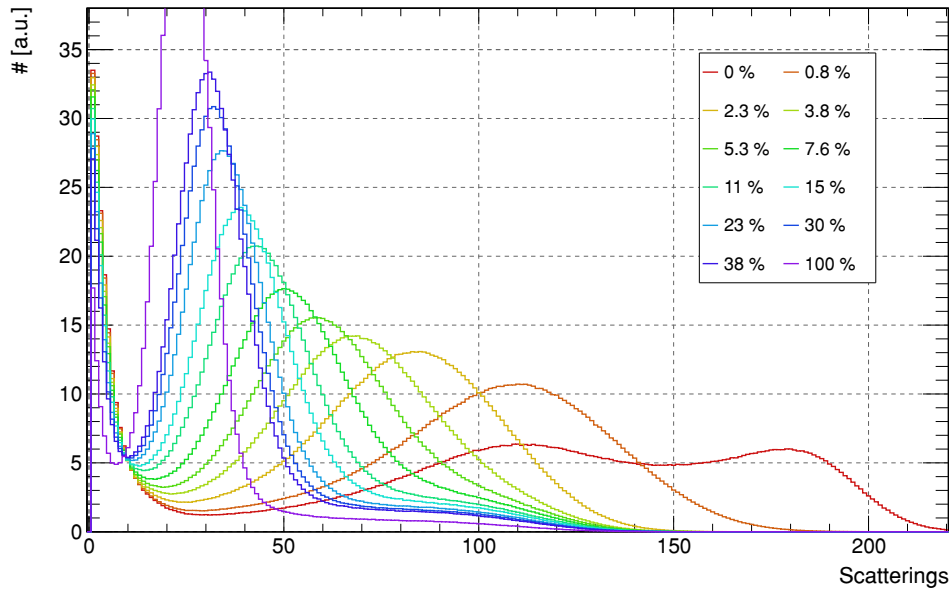


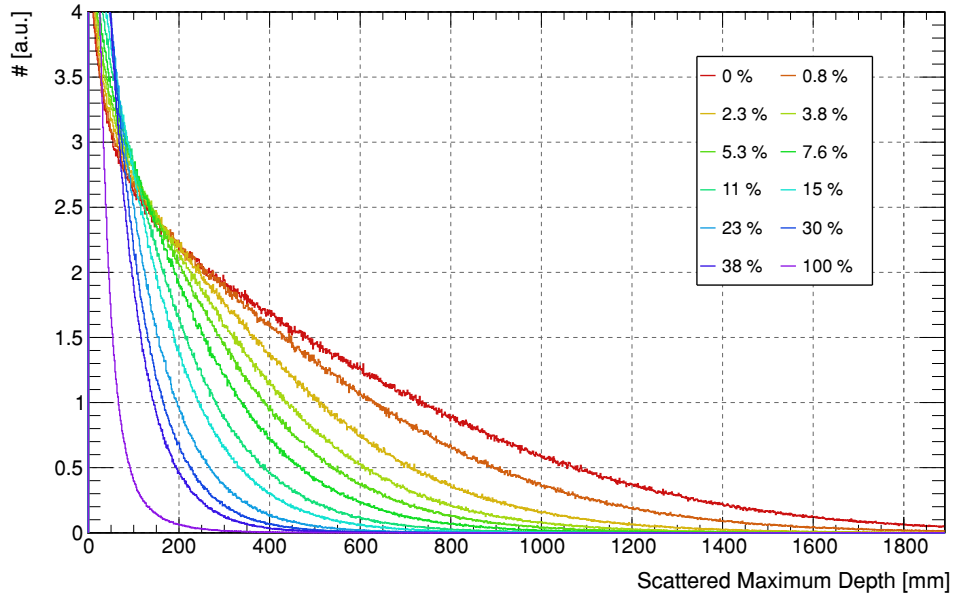
Figure 69: Average amount of scatterings per neutron for various soil moisture conditions.

For using the environmental neutron density as a proxy for soil moisture estimation the penetration depth is an important quantity for the probe depth. Yet, most neutrons are scattering within the soil without leaving it, see for example Fig. 61. In the further calculations of the characteristics of the air-ground interface the following definition is made:

- incoming radiation: no interaction with the soil,
- albedo neutrons: at least one interaction in the soil,

- direct albedo radiation: only one interface crossing. The majority of these neutrons are 'geometrically' transported to the sensor without further (diffusive) scattering in the air.

Figure 70: Maximum scattering depth of neutrons which reach the surface for various volumetric soil moisture conditions and  $h = 10 \text{ g/m}^3$ .



It is important to note that probing the soil and its water content does not necessarily mean that a neutron had scattered off any hydrogen atom. Indeed, compared to the dry case any addition of soil moisture reduces the above-ground density, not only by slowing down neutrons faster, but also by reducing the escape probability once entered into the soil.

Fig. 70 shows the distribution of the maximum probe depth, e.g. the most deep scattering centers or evaporation origins. For dry conditions neutrons can probe the soil beyond depths of 1 m and for a pure water body information below 10 cm can hardly be obtained. To the distribution of the scattering locations a similar scaling with soil moisture like in the cases before can be attributes, however, the relation is not as strongly dependent on the water content here. It can be explained by the fact that this observable quantifies the extreme values of the ensemble.

## 9.2 | COSMIC-RAY NEUTRON TRANSPORT ANALYSIS

### 9.2.1 | THEORETICAL DESCRIPTION BY NEUTRON TRANSPORT EQUATIONS

Considering a point source in an infinite medium the integral version of the transport equation (9) reduces to

$$\Phi(r) = \underbrace{Q \frac{e^{-\Sigma_t r}}{4\pi r^2}}_{\text{transient}:=\Phi_{tr}} + \underbrace{\int \Sigma_s \Phi(r') \frac{e^{-\Sigma_t |r-r'|}}{4\pi (r-r')^2} dV'}_{\text{diffusive transport}:=\Phi_{dt}}, \quad (144)$$

with as before  $\Sigma_t$  being the total cross section and  $\Sigma_s$  the scattering cross section for changes from  $E \rightarrow E'$ . The first term describes the direct/'geometric' transport without any collision from a source of strength  $Q$  to a surface proportional to  $r^2$ . At

larger distances the integration of the second term leads to the asymptotic solution<sup>[k]</sup> of

$$\Phi_{\text{dt}}(r) \approx \frac{e^{-\kappa r}}{r}, \quad (145)$$

with  $\kappa$  being a function of the ratio of the cross sections. It can be approximated in systems of weak absorption ( $\Sigma_a \ll \Sigma_s$ , in other words  $\Sigma_s \approx \Sigma_t$ ) by<sup>[l]</sup>

$$\kappa^2 = 3\Sigma_a\Sigma_t. \quad (146)$$

In general we are facing terms that have to fulfill the diffusion equation, which can be described by a transport equation for the neutron balance in a specific volume as

$$\text{div } \Phi + \Sigma_a \Phi = S. \quad (147)$$

Hence, in order to describe a plane or a volume source,  $\Phi$  has to be described by terms for which the integration over the total volume in spherical coordinates  $dV = r^2 \sin \vartheta d\vartheta d\phi dr$  does converge. Therefore, terms in  $\Phi$  involving  $\exp(-r)/r^n$  fulfill the norm  $\|\cdot\|_{\mathcal{L}^1}$  for  $n \leq 2$ . In the case of (144) with  $\Phi \propto \exp(-r)/r^2$  and  $\Phi \propto \exp(-r)/r$  this is satisfied.

In general also solutions in the form of

$$\Phi(r) = \sum_i S_i \frac{e^{-r/L_1^{(i)}}}{r^{1+e^{-r/a_2^{(i)}}}} \quad (148)$$

can be allowed with individual parameters describing a diffusion length  $L_1^{(i)}$  and absorption-to-scattering ratios  $a_1^{(i)}$  and overall source contributions  $S_i$  (for example for different energies).

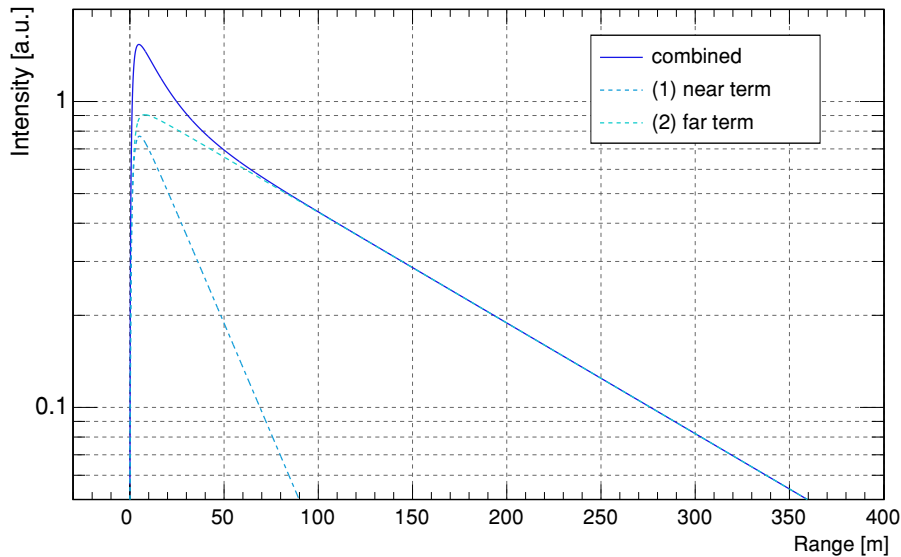


Figure 71: Theoretical neutron flux distribution for a diffusive point source with two energies according to (148). Term (1) with  $L_1 = 15$  m models a short range low energy distribution and term (2) with  $L_2 = 120$  m dominates the far field.

In general for a simple diffusion approach the resulting transport equation can characterize  $\Phi$  by a sum of exponential functions. Such is exemplarily plotted in Fig. 71 with two terms, one describing a long-range transport from high energy neutrons and a sec-

[k] The derivation can be found in [255].

[l] The derivation can be found in [23].

ond describing the transient near-field contributions. For a more complex configuration with a two-medium-interface, a spectral range for the source emission energies and for the detector acceptance energy, and an exponentially described volume source there is no simple general solution using Fermi-Age transport theory, nevertheless the exponential range dependence of the footprint can be motivated by the ansatz presented here.

### 9.2.2 | FOOTPRINT DEFINITION

The footprint of a geophysical instrument generally covers the area in which the medium of interest is probed and the carrier of such information is detected. The scenario of a centrally located sensor which detects neutrons isotropically exhibits a lateral symmetry and thus leads to the assumption of a circular footprint area,  $A = \pi r^2$ . Here, the travel distance  $r$  is defined as the Euclidian<sup>[m]</sup> distance between the point of detection and the point of the neutron's first contact with the ground or its generation. Since the observable is a result of multiple interactions,  $r$  depends on the neutron's initial energy and number of collisions and it can cover values between 0 m and  $10^3$  m. Thus, a quantile definition is needed to find a distance  $R$  within which most of the detected neutrons have probed the ground. In a simple diffusion model of a point source one can assume an exponential drop of intensity with travel distance, therefore [252] and [253] legitimate the use of two  $e$ -folding lengths, i.e. the 86 % quantile  $Q_{86}$ , in order to define the footprint radius.

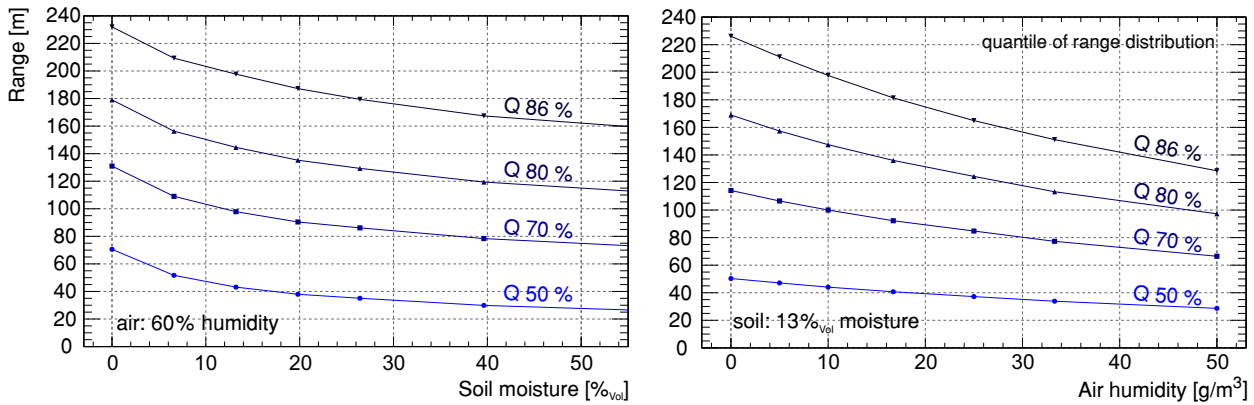


Figure 72: Travel distance of neutrons, exemplarily shown for four different quantiles  $Q$ , in the case of varying soil moisture (left) and varying air humidity (right).

Although the calculated response does not exhibit a simple exponential shape, any other quantile would be an arbitrary choice as well. A careful interpretation of this value is recommended, however, as a high quantile value will be biased towards long-range neutrons, see Fig. 72 and Fig. 73. Higher quantiles will also be biased towards the influence of air humidity, which plays an increasing role for large transport distances within the atmosphere. Nevertheless, going along with the 86 % quantile, the according footprint radius is denoted by  $R_{86}$  and the footprint area as  $A = \pi R_{86}^2$ . The number of neutrons  $N_R$  that have originated within a distance  $R$  from the sensor is given by

$$N_R = \int_0^R W_r dr. \quad (149)$$

[m] Eukleídēs, 300 BC, Ancient Greek.

In order to find the distance within which 86 % of the detected neutrons originate, the following equation is solved for  $R_{86}$  numerically:

$$\int_0^{R_{86}} W_r dr = 0.86 \int_0^{\infty} W_r dr. \quad (150)$$

In analogy the penetration depth  $D_{86}$  in the soil is defined as the integral of a depth weighting function  $W_d$  which is expected to also decrease with distance  $r$  to the sensor. This definition only indirectly takes into account how often a neutron has probed the soil, therefore, the applicability is restricted to cases of nearly homogeneous soil moisture conditions - inhomogeneous domains will be discussed later. However, it can already be concluded, that

- the footprint significantly depends on the environmental water content and
- compared to soil moisture, the influence of air humidity tends to be seen mainly in the higher quantiles, which represent the tails of the range distribution.

The latter can be seen especially in the comparison of both influence factors displayed in Fig. 73. Due to different transport paths around the interface soil water in the domain affects the travel distance distribution in a much more uniform way as air humidity. Long transport paths, where the macroscopic cross section of the water in the air plays an increasing role, manifest themselves in the higher quantiles of the range distribution.

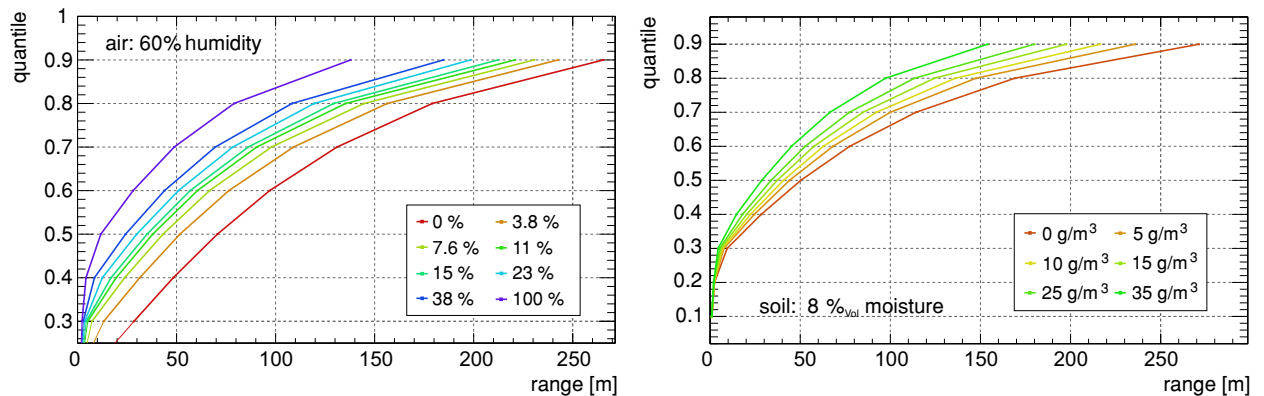


Figure 73: Travel distribution function of neutrons expressed by their quantiles in the case of varying soil moisture (left) and varying air humidity (right).

The decrease of travel distance by humidity shows a nearly linear effect on the quantiles, whereas for soil moisture a similar non-linear behavior, with 0 %<sub>Vol</sub> marking again a remarkable outlier, can be observed like before. The consequence in general is, that the range distribution is a function of different character in both variables. Another important finding, which is not shown here<sup>[n]</sup>, is, that the influence of air humidity for example decreases for wet conditions and the scaling of soil moisture under dry conditions is larger for dry conditions than for humid air. Both variables are correlated in the range distribution. It also has been found that the effect of air pressure is nearly not correlated with both variables and that biomass, as far as it is located well below the instrument, can be budgeted with the soil water content. This means, that the range distribution is also nearly independent of small height changes of the sensor, except for purely geometrical effects.

[n] In total 13 different soil moisture conditions were simulated for 8 different humidity conditions, which are 104 range distributions for the base data set.

The range distributions can be fitted very well in a frame of exponential functions by defining a near-field term below 50 m and a far-field term above. This approach is motivated by simple models of diffusion theory explained in sec. 9.2.1. The peak at  $r < 10$  m accounts for neutrons that directly emerge from the ground and have a high probability to be detected even though most of them come from the lower part of the neutron energy spectrum. The region up to  $r < 50$  m describes the average mean free path of most of the environmental neutrons in humid air. For distances between 50 m and 200 m neutrons interact with the soil multiple times until they are detected, which in turn means that with increasing  $r$ , average neutron energies quickly become insufficient in order to arrive at the detector before thermalization. From about 200 m on, detected neutrons are dominated by the higher energetic part of the spectrum, which appear to be higher in flux rates and are able to probe the soil very far from the detector.

The entire range distribution function is found to be

$$I_o(h, \theta) W_r(h, \theta) = I_o \cdot \begin{cases} (F_1 e^{-F_2 r^*} + F_3 e^{-F_4 r^*}) (1 - e^{-F_6 r^*}), & 0 \text{ m} < r \leq 1 \text{ m} \\ F_1 e^{-F_2 r^*} + F_3 e^{-F_4 r^*}, & 1 \text{ m} < r \leq 50 \text{ m} \\ F_5 e^{-F_6 r^*} + F_7 e^{-F_8 r^*}, & 50 \text{ m} < r < 600 \text{ m} \end{cases} \quad (151)$$

with  $I_o$  representing the overall intensity and  $W_r$  denoting the radial weighting function. The parameters  $F_i$  represent either signal contributions or attenuation coefficients for a rescaled distance  $r^*(r, p, \theta)$ , which can be considered as an unmodified distance  $r$  for standard environmental conditions. Each above defined interval contains one function modeling the main functional contributor, i.e. the soil moisture dependency, and one reflecting the second order correction. In order to account for the effect of the detector layer being positioned at a height of 2 m, for ranges below 1 m a purely geometrical factor is added.

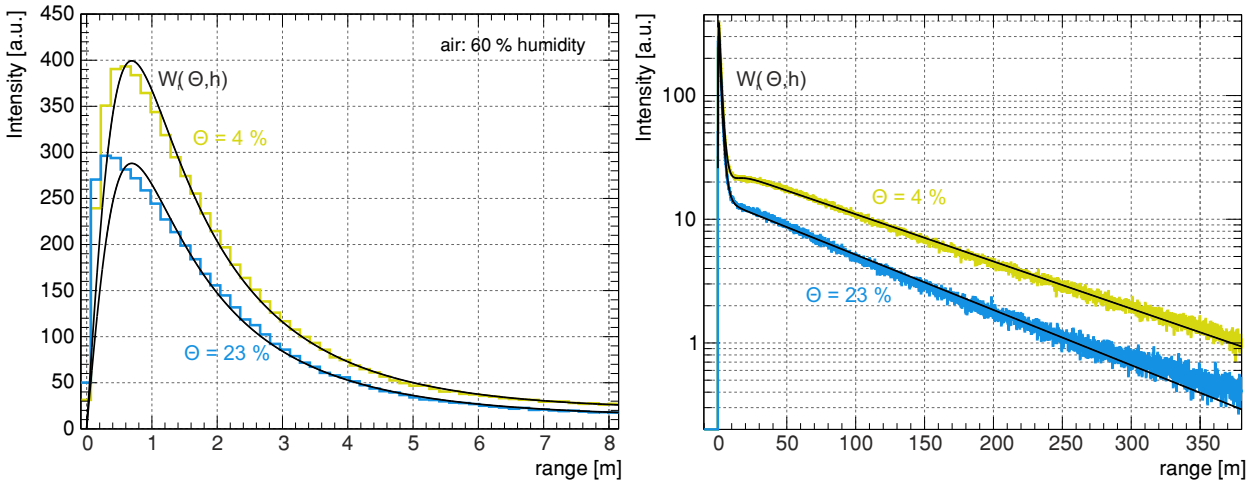


Figure 74: Test of the modeled function (162) with the parameter fits from tab. 16 in comparison to the simulated range distribution set in the near-field regime with focus on the first peak (left) and the far-field (right).

Finding a suitable analytic expression for the range distributions under typical environmental conditions is a question of multi-variate modeling. Therefore, all range distributions have been fitted by  $I_o \cdot W_r$  (151) and parametrized as functions of soil moisture and air humidity. At around 50 m the analytical description starts to deviate from the data. For this reason the value of 50 m has been chosen as a delimiter for both



regimes. Although the above described functional dependency of  $W_r$  has mainly been motivated from the far-field transport theory, the agreement in the near-field with the model data is also very good. Therefore, one function with different sets of parameters can characterize the entire problem.

As shown in Fig. 74 for two exemplary cases, there is a very good agreement between the proposed model (162) and the simulated range distribution. The analytical description is able to represent the first steep rise as well as the nearly exponential curve in the far-field. Also the small plateau in the near-field regime for dry conditions at approximately 20 m can be reproduced. As mentioned before, the fit model offers the best approximation for average moisture conditions in the range (7-40) % for which the error from integrally evaluating  $Q_{86}$  stays well below 5 m. For more extreme conditions there are notable deviations, especially for very dry soils. For this reason the limit of this model is set to 2 %<sub>Vol</sub> soil moisture. Furthermore, the model has been evaluated for a sensor height of 2 m. As the sensor height has a significant influence on the range distribution for  $r < 2$  m, where geometric transport dominates, deviations in that regime are anticipated and acceptable. Finally it should be noted, that the calculations only apply to cases of homogeneous environmental conditions. In domains with very inhomogeneous structures a significant deviation of the signal from the model can be observed. This will be discussed later, however, small inhomogeneities as can be found for natural soil moisture distribution patterns can still be covered.

#### 9.2.4 | ANALYTICAL DESCRIPTION OF THE PENETRATION DEPTH

The footprint covers an entire support volume, spatially extended into the ground. The comparably high thickness of the probed soil is an important advantage of the CRNS method compared to most remote-sensing products. Cosmic-ray neutrons can penetrate the first decimeters of the soil with nearly no interaction, whereas electromagnetic signals interact within the upper (0-5) cm. [259] showed that the effective representation of the penetration depth,  $z^*(\theta)$ , is a reciprocal function of soil moisture, but made no clear statement how it varies with the distance from the probe.

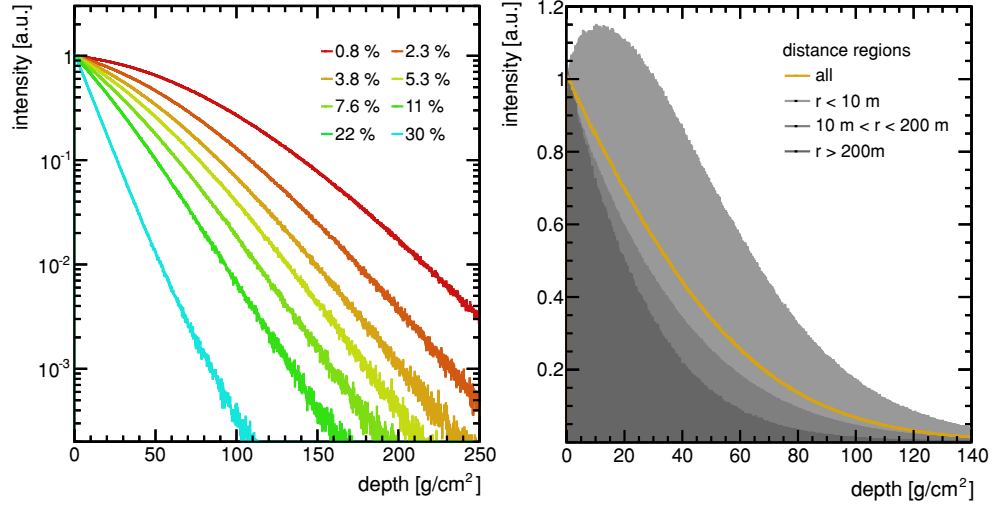
In URANOS the vertical positions, where neutrons probed the soil, were logged with their interaction coordinates. It has to be pointed out, that this procedure is different from scoring in air. In the atmosphere particle tracks at the (virtual) position of the detector have to be tracked. In the ground not the tracks itself, but the interactions, i.e. scattering centers, are relevant for the measurement process. Above  $\theta \approx 10$  %, the penetration depth of neutrons appears to decrease exponentially. This behavior can be expected from a simple mono-energetic attenuation law approach, and has also been found by [252]. A simple analytical description of the vertical weighting function was found for  $\theta \geq 10$  %:

$$W_d(r, \theta) \sim e^{-2d/D_{86}(r, \theta)}. \quad (152)$$

The relation can be used to obtain a properly averaged mean value of point measurements when compared to the cosmic-ray derived estimates. Of course, due to a much higher energy loss within the soil, the probe depth is lower for wet conditions. However, the penetration depth varies within the footprint of the sensor. Neutrons, which emerged from the soil in the direct vicinity of the instrument, can originate from or be scattered off locations more deep within the soil. The reason for this observation is simple, namely because neutrons leave the soil with a broad energy spectrum, see also Fig. 64.

Transport in the soil-air interface inevitably goes along with subsequent energy loss. Therefore, neutrons emitted from distant locations tend to have a higher emission

Figure 75: Penetration depth distribution characterization in the ground at a humidity of  $h = 10 \text{ g/m}^3$ . Scattering center distribution (left) for different soil moistures and (right) mean scattering center distributions for different impact distance ranges to the sensor for 7%<sub>vol</sub> soil moisture.



energy as more collisions are necessary to reach the sensor. On the other this also requires less energy loss in the soil and therefore a rather shallow origin. With different soil moistures the balance of energies within the emission band changes as the transport efficiencies in the domain vary in parallel. This leads to fact that the mean depth distribution varies more for wet conditions in terms of percentage than for dry soils. The numerical determination of the penetration depth  $D_{86}$ , however, is certainly valid for any soil moisture condition:

$$D_{86} = \frac{\text{g/cm}^2}{\rho_{\text{bulk}}} \left( p_0 + p_1 \left( p_2 + e^{-p_3 r^*} \right) \frac{p_4 + \theta}{p_5 + \theta} \right), \quad \text{adapted distance } r^*. \quad (153)$$

The quantity denotes up to which depth 86 % of the detected neutrons had contact with constituents of the soil. Numerical parameters are provided in tab. 17 in appendix B.2.2.

#### 9.2.5 | PRESSURE DEPENDENCY

The footprint can also expand with decreasing air pressure, e.g. increasing altitude of the sensor location. The lower air density allows neutrons to cover longer distances between collisions. For example, the footprint can be 20 % larger at a  $\approx 2000 \text{ m}$  altitude ( $\approx 800 \text{ mbar}$ ) compared to sea level. Although a reciprocal fit is a reasonable estimate [253], the results presented in Fig. 76 indicate an exponential dependence on  $p$  due to the presence of hydrogen:

$$f_p = \frac{0.5}{0.86 - \exp(-p/p_0)} \approx \frac{p_0}{p}. \quad (154)$$

However, differences between the two models appear to be insignificant. Yet, the footprint weighting function can be consistently scaled by the pressure correction function (154) in the far-field for typical soil moisture conditions and sensor altitudes.

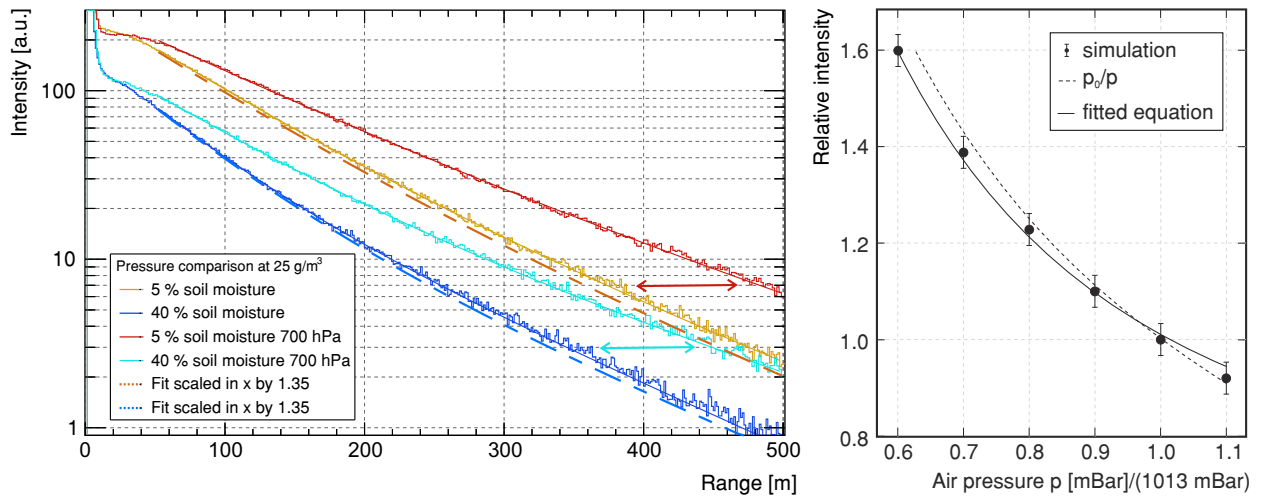


Figure 76: Pressure dependency of the range distribution for two exemplary soil moisture and air pressure conditions (left). The 1013 mb distributions are fitted by the far-field term of (151), if that function is then rescaled by a common factor, it matches the corresponding range distribution of the designated pressure. This model for the pressure dependency is depicted in the right panel.

### 9.2.6 | HEIGHT DEPENDENCY

Stationary sensors are typically placed in heights of approximately 2 m as well as roving constrains the elevation by the use of vehicles. These requirements justify the emphasis of this study to that common setup distance to the ground. However, measurements of the environmental flux at larger heights have been carried out as early as 1966 [260] using an antenna tower or [65] performing airborne surveys. With large-scale soil moisture measurement campaigns on terrains, which cannot easily be accessed by roving, airborne measurements are discussed as a feasible solution. As discussed in the previous sec. 9.2.1 the near-field is dominated by geometrical transport of neutrons from the direct vicinity of the instrument.

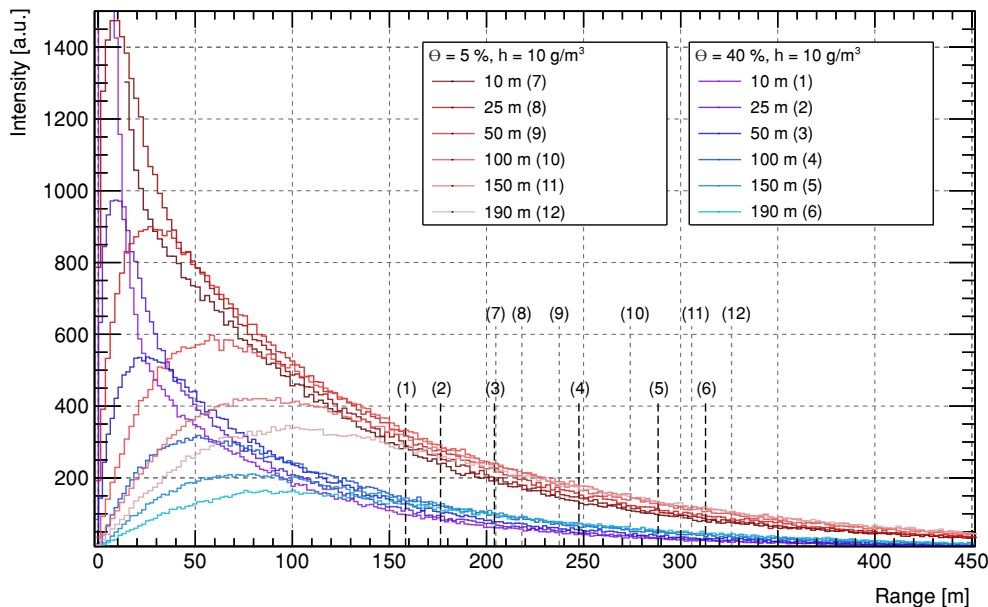


Figure 77: Height dependency of the range distribution for two soil moisture settings and elevations up to 200 m. It is clearly visible how the near-field is dominated by geometric transport, whereas the far-field consistently remains nearly unchanged. Lines and numbers indicate  $Q_{8\%}$  for each respective distribution, see also tab. 13.

Elevating the sensor by several tens of meters already increases the footprint substantially. Fig. 77 shows simulations, where the detector layer has been placed at heights up to 200 m. Two conclusions can be drawn from the depicted range distributions:

The dominant near-field peak, see also Fig. 93, smooths out and its peak drifts to higher range values, so that the overall footprint increases substantially. Furthermore, although the near-field entirely changes in the range distribution, the far-field is barely affected. As the latter is dominated by transport over the atmosphere, less than ground interaction, that result can be expected.

The following tab. 13 provides a characterization of the height dependent footprint increase.

Table 13: Elevated Footprint: Range quantiles  $Q_{86}$  depending on soil moisture and sensor height above ground. Conservatively, an error of 2 m can be assumed.

moisture [% <sub>Vol</sub> ]	$Q_{86}$ [m] at elevation					
	10 m	25 m	50 m	100 m	150 m	190 m
5	227	241	263	303	338	360
10	213	230	255	299	336	360
20	196	214	242	290	329	355
40	176	196	227	275	320	347

One can conclude, that the footprint can easily be expanded by a factor of 1.5 by elevating the sensor by 100 m and more.

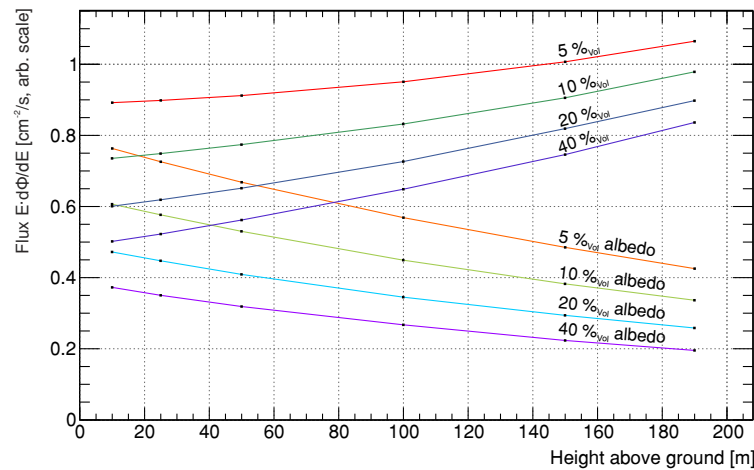


Figure 78: Height dependence of the measured neutron density. The total flux increases with increasing elevation. However, the fraction of the reflected component (albedo), which carries information about the soil moisture, decreases.

The flux of particles from atmospheric showers follows an exponential law as a function of altitude, e.g. Fig. 12 in sec. 3.1. Yet, with increasing distance to the ground, the albedo neutron component, which carries information about soil moisture, decreases. This can be seen in Fig. 78, which depicts the total flux and the fraction of albedo neutrons for different heights. These simulations also agree well with data from M. Zreda from a vertical profile measured using a helicopter (2009, unpublished). It can be concluded, that airborne measurements are feasible up to heights of 200 m above ground, but should be limited to approximately 100 m, where the signal fraction is in the order of 0.5, whereas approaching 0.25 at the largest altitude studied here.

### 9.3 | RESULTS

The systematic analysis and modeling of the soil-air interface, see previous sec. 9.2.3, allows now to characterize the neutron transport problem for CRNS for any soil moisture and air humidity condition. In the following the consequent use of the footprint weighting function (151) provides various quantitative results, which have already significantly improved the interpretation of CRNS data from field campaigns.

9.3.1 | INTENSITY RELATION

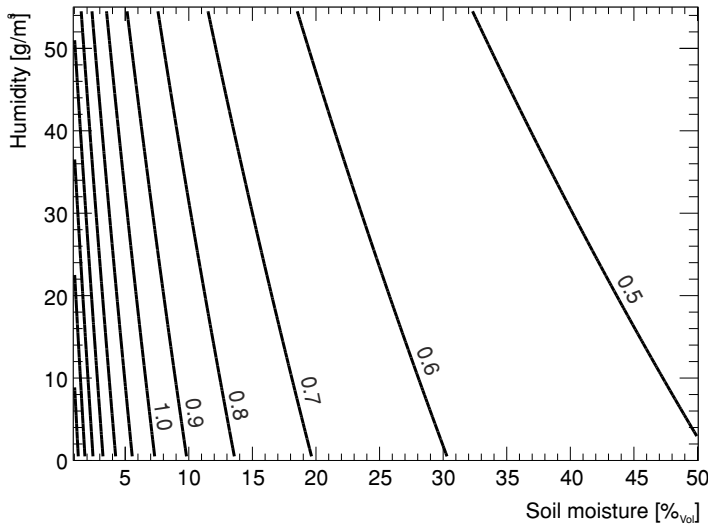


Figure 79: Dependency of the above-ground neutron density in the energy interval 100 eV-10 keV as a function of soil moisture and air humidity evaluated from (143).

The relative change of intensity generally follows a hyperbolic  $\theta$ -dependency, yet, this relation is as well a function of the actual soil water content. One observes a 0.33 % change at 4% soil moisture per 1 g/m<sup>3</sup> water vapor in the range  $h = 10$  g/m<sup>3</sup> to  $h = 30$  g/m<sup>3</sup> and a 0.16 % change at  $\theta = 15$  %. In cases of wet soils the fraction of hydrogen in the air at the same absolute humidity is lower. Therefore, slowing down predominantly takes place in the ground. Both values are lower than the static 0.54 % per 1 g/m<sup>3</sup> water vapor change from [227]. However, compared to the reference, this work utilizes a cosmic-ray neutron spectrum released directly from above the surface. This fact reduces the possible effect of premoderation by water vapor in the atmosphere as mainly the accumulated travel distance by neutron transport after soil contact can be considered here. Therefore, it is possible that the water column prior to the interface crossing can account for an additional reduction of the flux. However, the above-ground neutron density is a function of soil moisture and air humidity. Due to the pending analysis of the premoderation in air, the results of Fig. 79 can be considered as preliminary.

9.3.2 | PENETRATION DEPTH SCALING

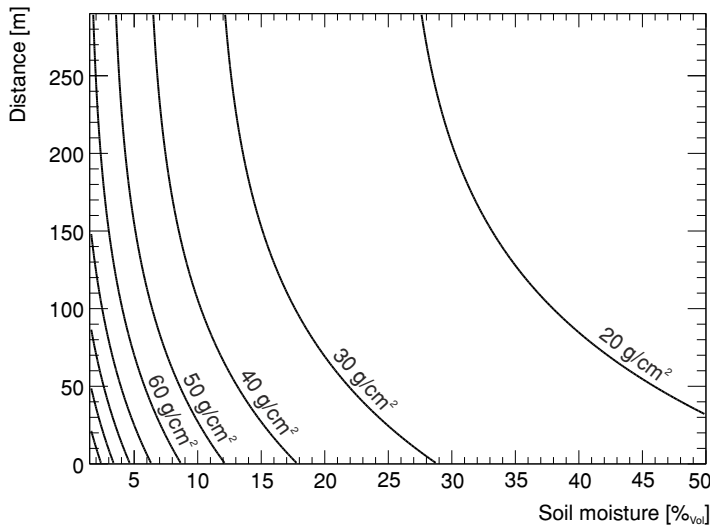


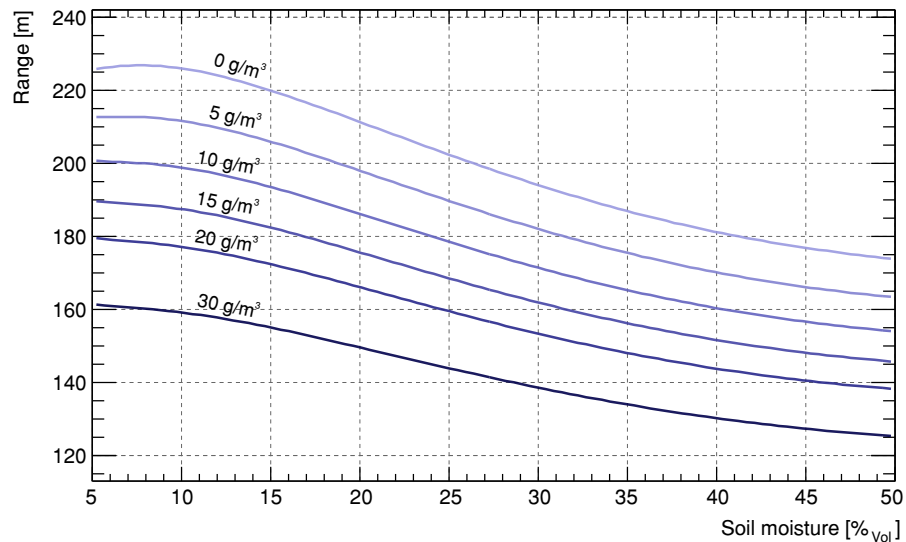
Figure 80: Dependency of the penetration depth  $D_{86}$  according to (153) on the radial impact distance  $r$  to the sensor for a range of soil water contents  $\theta$ . Contour lines show  $D_{86}$  in intervals of 10 g/cm<sup>2</sup>. An exemplary humidity  $h = 10$  g/m<sup>3</sup> and soil composition according to sec. 9.1.4.2 is considered.

The average probe depth is typically a result of many interactions in the ground and nearly follows an exponential law with a soil moisture depending attenuation coefficient. However, this value also depends on the distance, where the neutron entered the soil in the first place. Fig. 80 shows the penetration depths  $D_{86}(r, \theta)$  as a function of radial distance  $r$  from the sensor for exemplary soil moisture values  $\theta$ . For dry soil  $D_{86}(r, \theta \approx 1\%)$  ranges from 83 cm right below the sensor to 46 cm at  $r = 300$  m distance. At most, the penetration depth varies between 15 cm and 83 cm below the sensor for wet and dry soil, respectively. This is in close agreement with depths of (12-76) cm given by [252]. The reported values are rather confirmed than contradicted by URANOS, because they stemmed from experiences and various studies in the research field of cosmogenic nuclide production and are thus independent of the mentioned model approach. On average over the first tens of meters distance, the functional dependency on  $\theta$ , see (153), is relatively similar to the reciprocal model for the *effective sensor depth*  $z^*(\theta)$  from [259]. Their model was constrained on the limits introduced by [252] and validated with measurements and hydrodynamic simulations. Further evidence for the correct performance of the URANOS model provides the comparison with measurement depths of (50-100) cm on the Moon or Mars missions, where cosmic-ray neutrons penetrate dry ground of similar chemical composition [261, 262].

### 9.3.3 | FOOTPRINT

The response to soil moisture variations is significant for humid climates between (15-50) % $_{Vol}$  as well as for very dry conditions  $< 3\%_{Vol}$ . Previous studies underestimated the role of soil moisture for the footprint due to the choice of a modeled neutron source below the surface. This detail is the major cause for the discrepancy to findings from [253], who stated, that the footprint remains mainly unchanged for typical soil moisture conditions.

Figure 81: Dependency of the radial distance quantile  $Q_{86}$  according to (151) for a range of soil water contents  $\theta$ . Contour lines show  $Q_{86}$  for different humidities.



The footprint itself is a function of soil moisture. This effect can be attributed to the different initial energies from the soil emission spectra and more importantly to the transport efficiency of the interface. Neutrons cross the air-ground boundary on average three times before they reach the sensor. With increasing soil moisture the probability of leaving after re-entry decreases. Hydrogen contributes to this behavior in two ways: The energy loss is much higher compared to any other element, which significantly decreases the average travel distance, and in elastic collisions backward-scattering is highly suppressed, which requires at least two collision with hydrogen for a neutron to

be emitted back into the air contrary to other elements that allow direct backscattering. For  $\theta = 5\%$  to  $\theta = 12\%$  the footprint radius is not significantly influenced. Beyond that a decrease of 10 m for every 5% of soil moisture can be observed, see also Fig. 81.

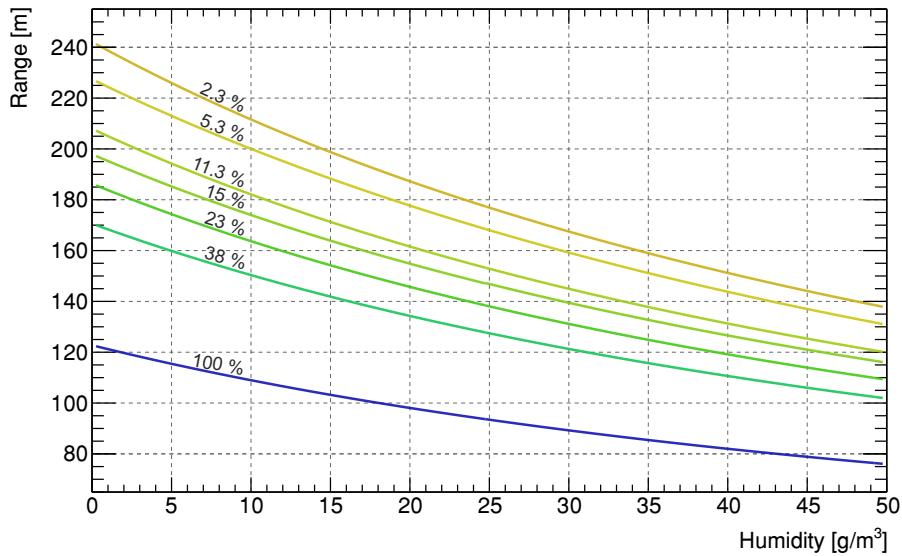


Figure 82: Dependency of the radial distance quantile  $Q_{86}$  according to (151) for a range of soil water contents  $\theta$ . Contour lines show  $Q_{86}$  for different humidities.

Moreover, the response to variations of absolute humidity features a 10 m decrease of the footprint radius for every change of (4-6)  $\text{g}/\text{m}^3$  water vapor, see Fig. 82. [218] refers to  $\approx 10\%$  reduction of the footprint from dry to saturated air, which can easily span  $\approx 25 \text{ g}/\text{m}^3$ . This change corresponds to a 20% change in footprint radius calculated with URANOS. However, [253] investigated the influence of humidity in further detail and found a 10 m decrease for every change of  $\approx 6 \text{ g}/\text{m}^3$  humidity from MCNPX simulations with dry soil. This value is consistent with results from URANOS, whereas the slightly higher gradient is a consequence of the different energy spectra used in the models. In summary, the contour plot Fig. 83 shows that the footprint radius ranges from 220 m to 130 m between arid and tropical climate, respectively.

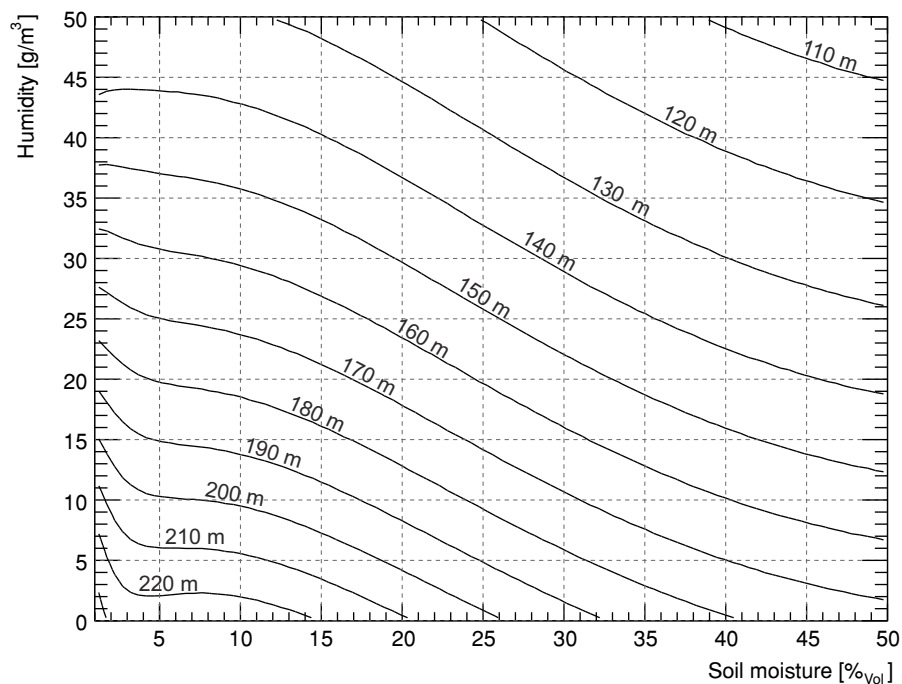


Figure 83: Dependency of the radial distance quantile  $Q_{86}$  according to (151) for a range of soil water contents  $\theta$ . Contour lines show  $Q_{86}$  for different humidities.

The decrease of the footprint with increasing soil moisture does not necessarily imply that the area-average estimate is less representative. According to [263], the spatial

variability of soil moisture tends to be low for rather wet soils. In this context, the effective representativeness of the CRNS method appears to be almost unchanged. Conservatively, a total error of  $\Delta R_{86} = (4-6) \%$  can be assumed, which scales from wet to dry conditions. A detailed error budget is listed in appendix B.2.3.

### 9.3.4 | WHERE DO NEUTRONS COME FROM?

CRNS sensors are sometimes placed close to roads, trees or rivers. Mobile rover surveys inevitably pass alongside forests, lakes or fields of different land use. In most of these cases an isotropic footprint cannot be expected, because large structures of different hydrogen content vary the transport paths towards the sensor.

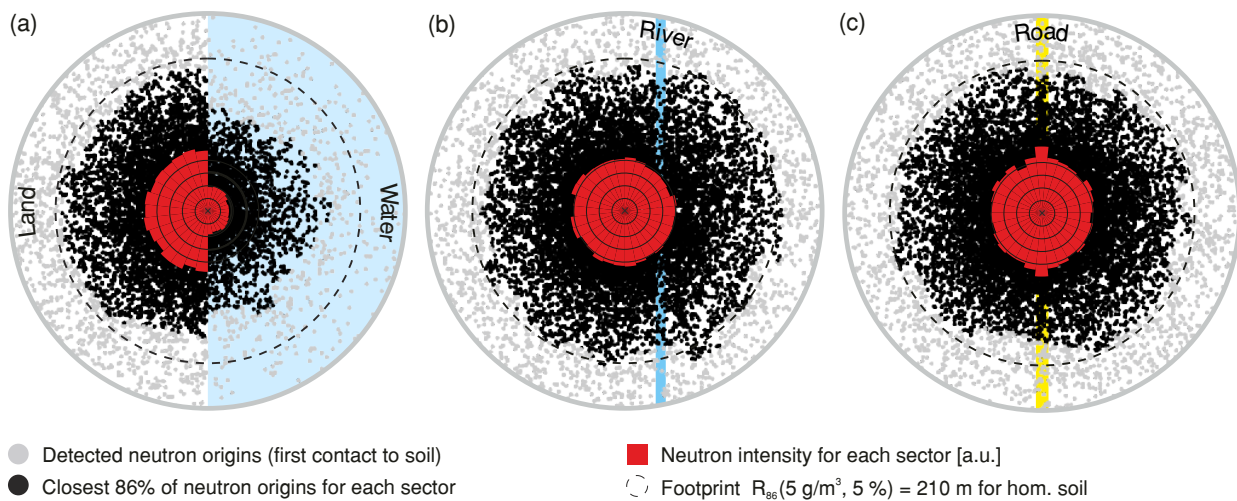


Figure 84: Anisotropy of detected neutron origins (black) and neutron intensity (red) determined for every 12° sector of a circle around a centered detector. The displayed extent is 270 m in radius, whereas the dashed line represents the isotropic footprint. The three exemplary cases illustrate bare soil (white) with (a) a coast line to water (blue), (b) a 10 m river at 50 m distance and (c) a 10 m concrete road (yellow). [KS2015]

In order to quantify the anisotropy of detected neutrons, exemplary cases where such scenarios are extreme have been simulated. In Fig. 84 the vicinity of a centered detector is shown and the isotropic footprint  $R_{86}(h = 5 \text{ g/m}^3, \theta = 5 \%) = 210 \text{ m}$  is indicated (dashed line). Dots illustrate the origin of detected neutrons, where the closest 86 % of total neutrons are emphasized (black) in each direction. The area is discretized into 12° sectors in order to quantify range (black dots) and intensity (red).

In a coast line setup, Fig. 84a, the density of the origins (dots) and neutron intensity (sectors) appear to be much smaller in the ponded area. The range of neutrons decreases by up to (30-40) % although neutrons still manage to travel long distances over water. Their contribution to the count rate sharply drops to about 40 % at the interface. In Fig. 84b the detector is placed 50 m away from a 10 m wide river. This setup can especially be found for irrigated land-use. The neutron origins clearly show that the river hardly contributes to the signal because most neutrons lose too much energy after probing water, see also point density and neutron intensity for water, Fig. 84a. This is also visible in the respective intensity which shows a slight asymmetry towards the dry side. However, the setup reveals a slightly wider footprint in the direction to the river, as a consequence of the intensity gap.

A detector carried on a dry, concrete road, see Fig. 84c, is the typical setup for rover applications. The sensor detects about (10-20) % more neutrons from the road than from other directions. However, the decrease of the footprint along the road due to



short-range dominated contribution is small. The effect of the road is especially studied in the following sec. 9.3.5.

### 9.3.5 | INHOMOGENEOUS TERRAIN: ROADS

*Part of the results about mobile measurements on roads presented in this chapter have been published in [SK2018].*

Cultivated fields, forests, mountainous terrain, and private land are often not accessible by vehicles. Hence, the CRNS rover is usually moved along existing roads, streets, and pathways in a site. This strategy is also practical when the rover is used to cover large areas at the regional scale in a short period of time. However, the neutron simulations presented here showed that the stationary CRNS detector is particularly sensitive to the first few meters around the sensor. This feature could be verified by moving stationary CRNS probes over highly inhomogeneous domains, see also for example Fig. 60 in sec. 9.1.2. The effect of dry structures in the footprint was introduced for the first time by [243] and was also observed by [219] and [SK2017b] on rover surveys through urban areas. [217] sensed soil moisture of agricultural fields by roving on paved and gravel roads, and speculated that the road material could have introduced a dry bias to their measurements. It is therefore critical to quantify such an effect, not only for the advancement of the CRNS roving method, but also for its application.

The radial sensitivity of a CRNS detector is strongly influenced by the first few meters around the sensor, see also Fig. 74. As a result of this local sensitivity, the CRNS measurement is biased significantly when the moisture conditions present in the road differ substantially from the actual field of interest. The footprint analysis as presented before, however, has been developed for homogeneous soil moisture conditions, especially the radial weighting function strictly only applies to domains of low variations in  $\theta$ . One can already derive an estimation using the radial weighting function  $W_r$  (151) in order to calculate a road bias  $N_b(x_c, w, \theta_{\text{field}})$

$$\begin{aligned}
 N_b = & \left( \int_{-\infty}^{\infty} \int_{x_c-w/2}^{x_c+w/2} W_r(\sqrt{x^2+y^2}, \theta_{\text{road}}) dx dy \right. \\
 & + \int_{-\infty}^{\infty} \int_{-\infty}^{x_c-w/2} W_r(\sqrt{x^2+y^2}, \theta_{\text{field}}) dx dy + \int_{-\infty}^{\infty} \int_{x_c+w/2}^{\infty} W_r(\sqrt{x^2+y^2}, \theta_{\text{field}}) dx dy \\
 & \left. \cdot \left( \int_{-\infty}^{\infty} \int_{-\infty}^{\infty} W_r(\sqrt{x^2+y^2}, \theta_{\text{field}}) dx dy \right)^{-1} \right), \tag{155}
 \end{aligned}$$

with road width  $w$  and distance to the road center  $x_c$ . One observes already quite at some distance to the road that the intensity is enhanced compared to the field-only domain due to the significant geometric contribution. As soon as the sensor is located above or next to the road, depending on material and width a local enhancement in neutron density would create the impression of a false low water content. It can be expected that a potential 'road effect' is larger when differences between road moisture and surrounding field water content are larger. However, the integral approach cannot entirely take into account the inhomogeneous configuration as it disentangles both domains as there is no correction for the transport  $\theta_i \rightarrow \theta_j$ . (155) slightly overestimates the road contribution and leads a relative bias below a factor of 1, if  $\theta_{\text{road}} < \theta_{\text{field}}$ . The latter can be seen in the lowest curve of Fig. 85 with the integral values for the 7 m-asphalt road with an effective  $\theta_{\text{road}} = 12\%$  within a field of 10% soil moisture.

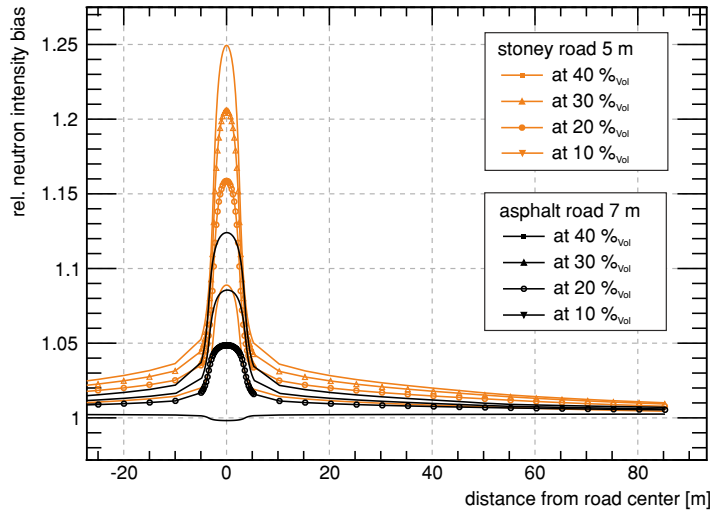
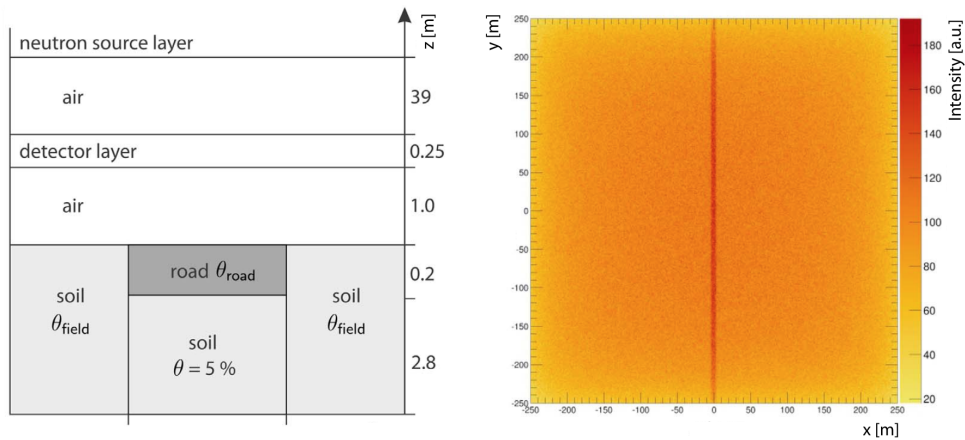


Figure 85: Road bias  $N_b$ , evaluated by (155) using the radial weighting function (151). The sensor is located at a distance  $x_c$  from the road center, here two examples of stone and asphalt pavements. The influence of the road leads to a relative flux change compared to the one expected from a domain with  $\theta_{\text{field}}$  alone.

The application of roving on roads has been taken as an example of inhomogeneous terrain, which is in the following further studied using URANOS. In order to The road is modeled as a 20 cm deep layer of either stone or asphalt, while the soil below was set to 5 % volumetric water content. Following the compendium of material composition data [147], asphalt pavement is modeled as a mixture of O, H, C, and Si, with an effective density of 2.58 g/cm<sup>3</sup>, which corresponds to a soil water equivalent of  $\theta_{\text{road}} \approx 12\%$ . Stone/gravel is a mixture of Si, O, and Al, plus 3 % volumetric water content at a total density of 1.4 g/cm<sup>3</sup>. The wetness of the surrounding soil,  $\theta_{\text{field}}$ , has been set homogeneously to 10 %, 20 %, 30 %, and 40 % volumetric water content. The neutron response to roads was simulated for road widths of 3 m, 5 m, and 7 m.

Figure 86: (left) Schematic of the model setup used by URANOS to simulate the response of cosmic-ray neutrons to ground materials. (right) Exemplary URANOS model output showing a birds-eye view of the neutron density in the horizontal detector layer for a 5 m stoney road and 50 % field soil moisture. [SK2018]



The result from the simulation confirms that the bias increases with increasing field soil moisture, increasing road width and decreasing road moisture. Fig. 87 plots the simulated road bias over distance from the road center, showing that the bias is a short-range effect that decreases a few meters away from the road, so that almost no measurable effect can be expected. Yet, there are two differences in the particle-tracking solution compared to the integral approach (155). The road bias is slightly emphasized for the asphalt road and a few percent lower for the stone road. Furthermore, the long-range enhancement tails at distances far from the road center appear slightly weaker. The quantitative differences between both approaches might not be relevant in practice compared to other sources of errors. It may be not feasible to estimate the hydrogen concentration of the road precisely, therefore, biases which correspond to effective soil moisture changes of the road in the order of 2 % can be expected. From this point of view the analytical approach can already provide a reasonably good estimation for the 'road effect'.

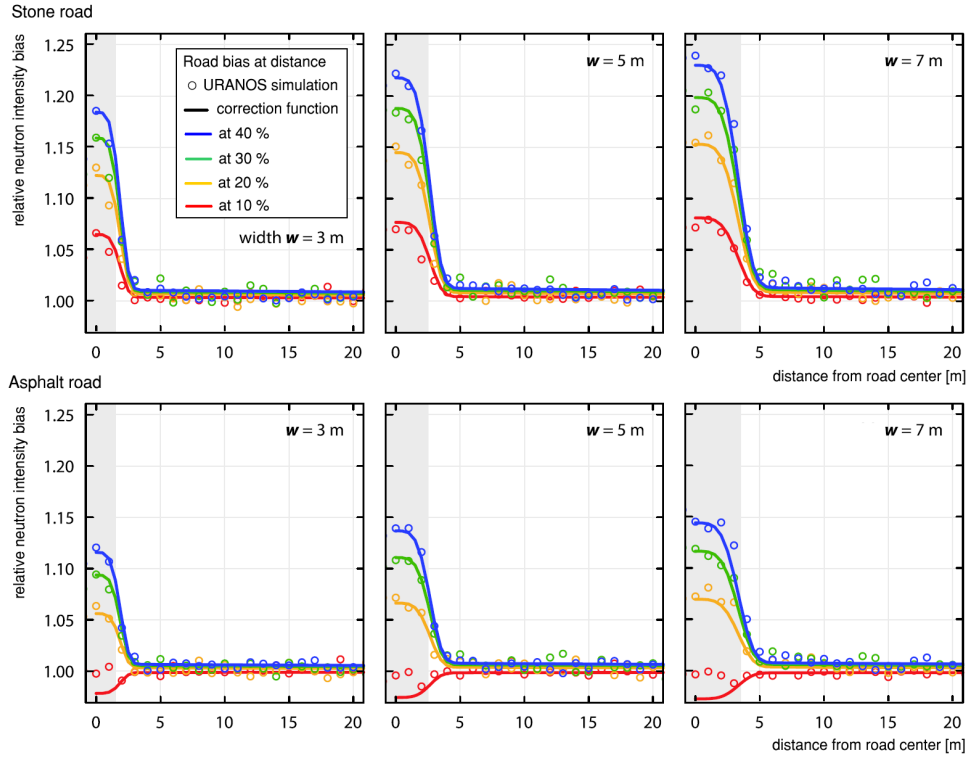


Figure 87: URANOS simulations (circles) and fitted correction functions representing the neutron bias at different distances  $x_c$  from the road center ( $x_c = 0$  m) for various road widths  $w$  (geometry shaded), field soil moisture (color), and (top) stone road material with an effective water content of  $\theta_{Vol} = 3\%$  and (bottom) asphalt road material with  $\theta_{Vol} = 12\%$ . Field conditions that are dryer than the road moisture (lower panel, red curve) cannot be represented by the analytical approach. [SK2018]

Using the results from the simulations, a correction approach was developed with M. Schrön, which would allow to correct measurements of roving campaigns. The correction function  $C_{road}$ , which relates the measured neutron density  $N_{Corr}$  in the field to the flux bias from the road  $N_{road}$  as  $N_{Corr} = N_{road}/C_{road}$  should include an exponential dependency on the road width and road center distance due to the geometric contribution from the weighting function and a hyperbolic contribution from the domain water differences. In detail it is discussed in appendix B.2.4.

The function describes the simulation results, see Fig. 87, for different distances  $x_c$  from the road center and for different  $\theta_{field}$ ,  $\theta_{road}$  and widths  $w$ . However, the validity of this analytical approach is limited to road widths below approximately 7 m, as for wider roads the neutron density saturates around the center at a peak value (not shown, but it can partly be already seen in the example of Fig. 87, lower right panel). Furthermore, this function is limited to effective values for  $\theta_{road}$  between 1% and 16% and requires a prior knowledge about the field moisture conditions.

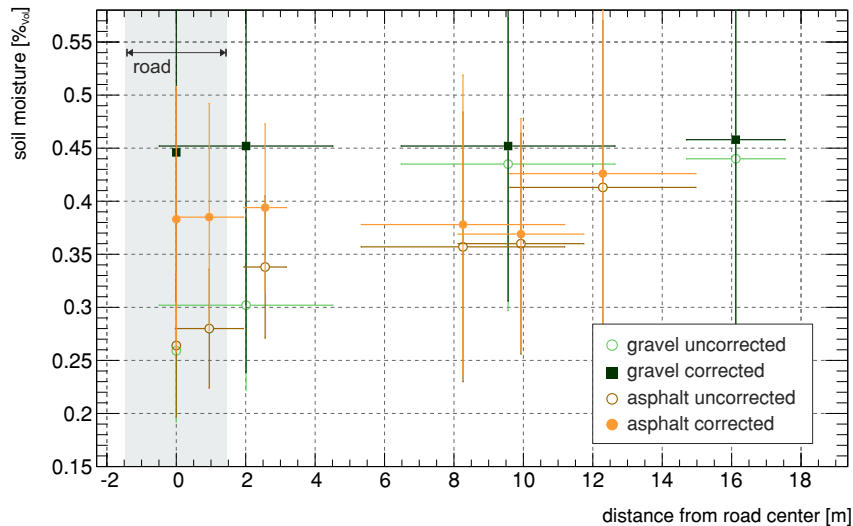


Figure 88: Roving measurements along an asphalt and a stone road. After application of the road correction function (163), measurements converge to similar values for all distances. Error bars are mainly due to the heterogeneity of the environmental water along the 400 m track length, i.e. account for the signal variance. [SK2018]

This function has extensively been applied in the study of [SK2018]. Here, exemplarily the correction of the data set of R. Rosolem and M. Schrön collected in the Lambourn catchment in South England (51°32'N, 1°29'W) is shown. The general objective of these experiments was to clarify whether the road correction function and the underlying simulations can be used to transfer the apparent soil moisture patterns seen from the road to values that were taken in the actual field. The loamy clay soil has an average bulk density of  $\rho_{bd} = 1.25 \text{ g/cm}^3$  and a water equivalent of additional hydrogen pools has been determined to be  $\theta_{\text{Offset}} = 4\%$  with insignificant differences between the fields. The road network consists of a paved major road ( $w = 3 \text{ m}$ ) made of an asphalt/stone mixture with an estimated moisture equivalent of 11%. The main side roads are made of a gravel/stone mixture with an estimated moisture equivalent of 7%, mostly around 2.3 m wide, while the southern road is 4.5 m wide. Many non-sealed tracks ( $w = 3 \text{ m}$ ) follow the borders between fields which partly consist of sand, grass, and organic material, such that their average moisture equivalent was estimated to 12%.

In the experiment a rover-type of cosmic-ray neutron detector, see sec. 7.2.1 and 8.1 was driven along a 400 m track in various distances from a gravel/stone road and an asphalt road. Upon application of the road correction function, see Fig. 88, measurements converge to similar values for all distances (right) and could also reveal different soil moisture conditions for the northern and southern fields (not shown). The overall result provides strong evidence that the analytical correction function properly represents the road bias at different distances and for different materials.

Part V

SUMMARY AND CONCLUSION

## CONCLUSION

---

This work is split into three parts which align in one development line. In order to precisely understand the physics of the CASCADE thermal neutron detector, the Ultra Rapid Neutron-Only Simulation (URANOS) has been created. This tool turned out to be feasible to solve another problem of a novel method of soil moisture determination in environmental physics. It was able to correctly solve the neutron transport problem in the soil-air interface and laid the foundation to a detailed understanding of the measured response to different hydrogen pools.

### THE URANOS NEUTRON MONTE CARLO TRANSPORT CODE

By a radical reset an entire neutron transport Monte Carlo has been built from scratch. It is the first of its kind natively written in C++ and based on a voxel engine. Neutrons interact with volumes rather than with surfaces, which makes compared to polygons the three-dimensional pixel to a geometry definition more close to the physical interaction. The computational framework could be slimmed down at decisive bottlenecks. The software mainly treats the propagation of neutrons as for example abandoning the complex gamma emissions, which come along with excited nuclei, are neither relevant for the CASCADE detector nor for the method of Cosmic-Ray Neutron Sensing. Further expenses could be avoided by not taking into account heat production, which for example changes the environment and the material cross sections, as from a neutron point of view the relevant systems here are entirely static.

The original motivation, however, which has been realized, was to merge all relevant parts from the initial beam to the signal generation into a detector simulation in order to study its performance in the highly demanding field of Spin Echo spectroscopy. Therefore it is necessary to simulate neutron interactions for the host instrument until being scattered or converted in the detector. The charged ion physics has to be incorporated, as well in the converter layer as in the detector gas. The ionization tracklet has to be projected through several stages of gas amplification while diffusing and drifting onto the nested readout structure of the detector, where multi-channel amplifiers with a specific threshold have to be triggered in order to generate a timestamp for a signal. Additionally, from the instrument upstream the neutron spin state has to be taken into account, as finally the detector response is analyzed in terms of the measured polarization.

Along with the language change, which makes it attractive as an open source project, an intuitive graphical user interface has been created, which has already attracted users without an extensive informatics background. Using URANOS allowed them to directly address their research question instead of training oneself for several weeks in the usage of sophisticated tools, which technically aim to calculate reactor criticality setups. Apart from the examples of the author presented in this work URANOS has successfully been employed in the study of the detector response of radiation portal monitors, in the development of novel neutron detectors for CRNS, in the calibration of an incoming cosmic radiation neutron detector and in the study of drip irrigation in agriculture. Most recently URANOS could impressively be used to study the feasibility of CRNS for measuring the integral snow water equivalent in the Alps. The data from a 3D laser scanner could directly be used to extrude the corresponding complex snow voxel landscape, allowing to calculate responses of the sensor during the different accumulation and melt-out phases.

## COSMIC-RAY NEUTRON SENSING

This work presents the most extensive study of neutron transport in the soil-air interface with specifically focusing on the dependency on hydrogen pools. To precisely understand the system this work heavily relies on Monte Carlo simulations, which allow to analyze the relevant observables with their influence factors. The so obtained data sets were parametrized by analytical functions, which describe the system without the further necessity to repeat a series of case studies.

The spatial distribution of neutrons can often be simplified in terms of thermodynamic models, however, it is very sensitive to initial energies and even to small amounts of hydrogen. As a consequence, the complexity of environmental neutron transport seems to impede any attempt to simplify the problem. Therefore, the need arose for revisiting neutron transport models and for addressing some of the open questions regarding the radial sensitivity, humid climate or terrain structures. As this study shows, the description of the footprint and neutron intensity is nontrivial to an exceptional degree.

Initially, the response functions of cosmic-ray neutron sensors were analyzed in terms of energy-dependent detection efficiency and angular sensitivity. The investigated detectors, which are specific models for hydrological research, comprise vertical (CRS1000) and horizontal configurations (Rover), each moderated by one inch of polyethylene and equipped with either  $^{10}\text{BF}_3$  or  $^3\text{He}$  proportional counters. The results show, that the energy window of highest response ranges from 0.1 eV to  $10^6$  eV. Hence, the typically used range of  $(10^2\text{-}10^4)$  eV provides a reasonable basis for CRNS investigations, yet, a significant fraction of neutrons are contributing to the signal of the sensor below and above this range.

The important result from this study for CRNS is, that the response to soil moisture varies significantly for humid climates between  $(10\text{-}40)\%_{\text{vol}}$  as well as for very dry conditions  $<3\%_{\text{vol}}$ . Previous studies underestimated the role of soil moisture for the footprint due to the choice of a modeled neutron source below the surface. This detail is the major cause for the discrepancy to findings from [253]. The footprint is defined by the radius of the 86 % quantile of the range distribution function of neutrons probing a soil of homogeneous moisture content. It has been found to range from approximately 160 m over a water body to 210 m over dry soil with a total error of about (4-6) %. The circular shape of the footprint remains isotropic for most field applications, like hilly terrain, nearby rivers or heterogeneous land. However, large water bodies or forests nearby can reduce range and intensity of detected neutrons from that direction.

The response to variations of absolute humidity features a 10 m decrease of the footprint radius for every change of  $(4\text{-}6)\text{ g/m}^3$  water vapor, which can easily span  $\approx 25\text{ g/m}^3$ . This change corresponds to a 20 % change in footprint radius calculated with URANOS. The penetration depth  $D_{86}(r, \theta)$  of detected neutrons directly below the sensor ranges from 15 cm to 83 cm depending on soil moisture. An exponential decrease with depth is a good estimate for the sensor's vertical sensitivity, whereas the depth in turn shrinks significantly with radial distance to the sensor.

The function  $W_r$  lays the basis for a refinement of the commonly applied sampling strategy, which assigned weights according to a static exponential radial function. In contrast, the present work shows that (1) the first tens of meters provide a dominant contribution to the signal in a rather non-exponential relation, and (2) the shape of the weighting function changes temporally as it is affected by variable moisture conditions. Subsequently, data can be weighted with  $W_r(h, \theta)$  in an iterative procedure.

The revised footprint function could fundamentally improve the reliability of the CRNS method. Many deviations from the expected soil water response, which had been found in previous studies, can now be explained. Therefore, results from this work have quickly been adopted by the community and are meanwhile the basis for inter-

preting CRNS measurements. The improved understanding also allows to correct for systematic biases as have been found for the so-called „road effect“. This specifically high near-field sensitivity plays an important role for mobile measurements. The variability of the road width and material significantly influences the measurements and can now be corrected for analytically.



Part VI

APPENDIX



## LITERATURE AND REFERENCES

## A.1 | JOURNAL PUBLICATIONS

M. KÖHLI, F. ALLMENDINGER, et al. “Efficiency and spatial resolution of the CASCADE thermal neutron detector.” In: *Nuclear Instruments and Methods in Physics Research Section A: Accelerators, Spectrometers, Detectors and Associated Equipment* **828** (Aug. 2016), pp. 242–249.

DOI: [10.1016/j.nima.2016.05.014](https://doi.org/10.1016/j.nima.2016.05.014)

M. KÖHLI, M. KLEIN, et al. “CASCADE - a multi-layer Boron-10 neutron detection system.” In: *Journal of Physics: Conference Series* **746**(1) (Sept. 2016), p. 012003.

DOI: [10.1088/1742-6596/746/1/012003](https://doi.org/10.1088/1742-6596/746/1/012003)

M. KÖHLI, M. SCHRÖN, et al. “Footprint characteristics revised for field-scale soil moisture monitoring with cosmic-ray neutrons.” In: *Water Resources Research* **51**(7) (July 2015), pp. 5772–5790.

DOI: [10.1002/2015WR017169](https://doi.org/10.1002/2015WR017169)

M. HENSKE, M. KLEIN, et al. “The  $^{10}\text{B}$  based Jalousie neutron detector: An alternative for  $^3\text{He}$  filled position sensitive counter tubes.” In: *Nuclear Instruments and Methods in Physics Research Section A: Accelerators, Spectrometers, Detectors and Associated Equipment* **686** (Sept. 2012), pp. 151–155.

DOI: [10.1016/j.nima.2012.05.075](https://doi.org/10.1016/j.nima.2012.05.075)

G. MODZEL, M. HENSKE, et al. “Absolute efficiency measurements with the  $^{10}\text{B}$  based Jalousie detector.” In: *Nuclear Instruments and Methods in Physics Research Section A: Accelerators, Spectrometers, Detectors and Associated Equipment* **743** (Apr. 2014), pp. 90–95.

DOI: [10.1016/j.nima.2014.01.007](https://doi.org/10.1016/j.nima.2014.01.007)

M. SCHRÖN, S. ZACHARIAS, et al. “Monitoring Environmental Water with Ground Albedo Neutrons and Correction for Incoming Cosmic Rays with Neutron Monitor Data.” In: *PoS Proceedings of Science* **231** (Aug. 2015). The 34<sup>th</sup> International Cosmic Ray Conference, pp. 101–104.

DOI: [10.1063/1.2825756](https://doi.org/10.1063/1.2825756)

M. SCHRÖN, M. KÖHLI, et al. “Improving Calibration and Validation of Cosmic-Ray Neutron Sensors in the Light of Spatial Sensitivity.” In: *Hydrology and Earth System Sciences* **21**(10) (Oct. 2017), pp. 5009–5030.

DOI: [10.5194/hess-21-5009-2017](https://doi.org/10.5194/hess-21-5009-2017)

M. SCHRÖN, S. ZACHARIAS, et al. “Intercomparison of Cosmic-Ray Neutron Sensors and Water Balance Monitoring in an Urban Environment.” In: *Geoscientific Instrumentation, Methods and Data Systems Discussions* **2017** (2017), pp. 1–24.

DOI: [10.5194/gi-2017-34](https://doi.org/10.5194/gi-2017-34)

M. SCHRÖN, R. ROSOLEM, et al. “Cosmic-ray Neutron Rover Surveys of Field Soil Moisture and the Influence of Roads.” In: *Water Resources Research* **54**(9) (May 2018), pp. 6441–6459.

DOI: [10.1029/2017WR021719](https://doi.org/10.1029/2017WR021719)

M. KÖHLI, M. SCHRÖN, and U. SCHMIDT. “Response functions for detectors in cosmic ray neutron sensing.” In: *Nuclear Instruments and Methods in Physics Research Section A: Accelerators, Spectrometers, Detectors and Associated Equipment* **902** (Sept. 2018), pp. 184–189.

DOI: [10.1016/j.nima.2018.06.052](https://doi.org/10.1016/j.nima.2018.06.052)

- M. KÖHLI. *Das CASCADE-Projekt: Neutronendetektion mittels Bor-10 als Alternative zu Helium-3*. 76<sup>th</sup> DPG Annual Conference. HK 42.2. Mainz, Germany, Mar. 2012
- M. KÖHLI. *Probing soil moisture by cosmic-ray induced Neutron Showers*. 78<sup>th</sup> DPG Annual Conference. UP 7.3. Berlin, Germany, Mar. 2014
- M. KÖHLI. *Monte-Carlo Simulations on the Detector Sensitivity to Cosmic-Ray induced Neutron Showers*. 4<sup>th</sup> COSMOS Workshop. Leipzig, Germany, May 2014
- M. KÖHLI. *The CASCADE Project - a perspective for solid state detectors*. International Workshop on Position Sensitive Neutron Detectors. Jülich, Germany, June 2014
- M. KÖHLI. *Probing nano and macro scales: solid state detectors and cosmic neutron soil moisture determination*. 9<sup>th</sup> Annual PNN and Well Logging Conference. Klingenbach, Austria, Sept. 2014
- M. KÖHLI. *CASCADE - eine alternative Perspektive für Festkörper-Neutronendetektoren*. Deutsche Tagung für Forschung mit Synchrotronstrahlung, Neutronen und Ionenstrahlen an Großgeräten 2014. Bonn, Germany, Sept. 2014
- M. KÖHLI. *Soil moisture sensing by cosmic-ray induced neutron showers*. 79<sup>th</sup> DPG Annual Conference. UP 16.2. Heidelberg, Germany, Mar. 2015
- M. KÖHLI. *The CASCADE Detector - high-resolution neutron detection by solid  $^{10}\text{B}$  layers*. Design and Engineering of Neutron Instruments Meeting (DENIM). Budapest, Hungary, Sept. 2015
- M. KÖHLI. *The CASCADE Project - a multi-layer  $^{10}\text{B}$  neutron detection system*. European Conference on Neutron Scattering (ECNS). Zaragossa, Spain, Sept. 2015
- M. KÖHLI. *On the Phase Front of Neutron Detection*. Neutronen in der Forschung und Industrie. München, Germany, Nov. 2015
- M. KÖHLI. *The method of soil moisture sensing by cosmic-ray neutrons*. 80<sup>th</sup> DPG Annual Conference. UP 15.1. Regensburg, Germany, Mar. 2016
- M. KÖHLI. *The CASCADE Project - On the Phase Front of Neutron Detection*. 80<sup>th</sup> DPG Annual Conference. HK 70.6. Darmstadt, Germany, Mar. 2016
- M. KÖHLI. *Neutron Transport Modelling with URANOS and Footprint Sensitivity - Making Neutrons great again*. 5<sup>th</sup> International COSMOS Workshop. Copenhagen, Denmark, Aug. 2016
- M. KÖHLI. *Soil moisture sensing by detection of cosmic-ray neutrons*. 2<sup>nd</sup> ATTRACT TWD Symposium in Detection and Imaging. Strasbourg, France, Nov. 2016
- M. KÖHLI. *Soil Moisture Measurement at the hectometer scale with cosmic-ray neutrons*. 81<sup>th</sup> DPG Annual Conference. UP 4.2. Bremen, Germany, Mar. 2017
- M. KÖHLI. *High Spatial Resolution in Thermal Neutron Detection: CASCADE*. 81<sup>th</sup> DPG Annual Conference. HK 7.2. Darmstadt, Germany, Mar. 2017
- M. KÖHLI. *Soil moisture measurement at the hectometer scale using CRNS for mobile applications*. 82<sup>th</sup> DPG Annual Conference. UP 8.2. Erlangen, Germany, Mar. 2018
- M. KÖHLI. *URANOS - The Cosmic Ray Monte Carlo tool*. EGU General Assembly. GI 2.7. Vienna, Austria, Apr. 2018

- [1] M. TANABASHI et al. “Review of Particle Physics.” In: *Physical Review D* **98** (Sept. 2018), p. 030001. DOI: [10.1103/PhysRevD.98.030001](https://doi.org/10.1103/PhysRevD.98.030001).
- [2] M. BATTAGLIA et al. *The CKM matrix and the unitarity triangle*. Oct. 2003. DOI: [10.5170/CERN-2003-002-corr](https://doi.org/10.5170/CERN-2003-002-corr). arXiv: [0304132v2](https://arxiv.org/abs/hep-ph/0304132v2) [hep-ph]. URL: <https://arxiv.org/abs/hep-ph/0304132v2>.
- [3] CKMFITTER GROUP (J. CHARLES ET AL.) “CP violation and the CKM matrix: assessing the impact of the asymmetric B factories.” In: *The European Physical Journal C - Particles and Fields* **41** (May 2005). updated results and plots available at: <http://ckmfitter.in2p3.fr>, pp. 1–131. DOI: [10.1140/epjc/s2005-02169-1](https://doi.org/10.1140/epjc/s2005-02169-1).
- [4] B. MÄRKISCH. *Experimental Status of  $V_{ud}$  from Neutron Decay*. July 2011. arXiv: [1107.3422](https://arxiv.org/abs/1107.3422) [nucl-ex]. URL: <https://arxiv.org/abs/1107.3422>.
- [5] J.C. HARDY and I.S. TOWNER. “Superallowed  $o^+ \rightarrow o^+$  nuclear  $\beta$  decays: 2014 critical survey, with precise results for  $V_{ud}$  and CKM unitarity.” In: *Physical Review C* **91** (Feb. 2015), p. 025501. DOI: [10.1103/PhysRevC.91.025501](https://doi.org/10.1103/PhysRevC.91.025501).
- [6] S. DAR. *The Neutron EDM in the SM: A Review*. Aug. 2000. arXiv: [hep-ph/0008248](https://arxiv.org/abs/hep-ph/0008248) [hep-ph]. URL: <https://arxiv.org/abs/hep-ph/0008248>.
- [7] J.D. JACKSON. “The Nature of Intrinsic Magnetic Dipole Moments.” In: *CERN Lectures* **77** (Sept. 1977).
- [8] S. PAUL. “The puzzle of neutron lifetime.” In: *Nuclear Instruments and Methods in Physics Research Section A: Accelerators, Spectrometers, Detectors and Associated Equipment* **611**(2) (Dec. 2009). Particle Physics with Slow Neutrons, pp. 157–166. DOI: [10.1016/j.nima.2009.07.095](https://doi.org/10.1016/j.nima.2009.07.095).
- [9] N. FEATHER. “A History of Neutrons and Nuclei. Part 1.” In: *Contemporary Physics* **1**(3) (1960), pp. 191–203. DOI: [10.1080/00107516008202611](https://doi.org/10.1080/00107516008202611).
- [10] W. SUTHERLAND. “XX. Cathode, Lenard, and Röntgen rays.” In: *Philosophical Magazine Series 5* **47**(286) (1899), pp. 269–284. DOI: [10.1080/14786449908621259](https://doi.org/10.1080/14786449908621259).
- [11] E. RUTHERFORD. “Scattering of  $\alpha$  and  $\beta$  Particles by Matter.” In: *Philosophical Magazine Series 6* **21**(286) (Apr. 1911), pp. 669–688. DOI: [10.1080/14786440508637080](https://doi.org/10.1080/14786440508637080).
- [12] E. RUTHERFORD. “Bakerian Lecture. Nuclear Constitution of Atoms.” In: *Proceedings of the Royal Society of London A: Mathematical, Physical and Engineering Sciences* **97**(686) (July 1920), pp. 374–400. DOI: [10.1098/rspa.1920.0040](https://doi.org/10.1098/rspa.1920.0040).
- [13] E. RUTHERFORD. *Radio-activity*. 1<sup>st</sup> Edition. Cambridge University Press, Feb. 1904. 399 pp. URL: <https://link.springer.com/article/10.1007/BF01390908>.
- [14] W. BOTHE and H. BECKER. “Künstliche Erregung von Kern- $\gamma$ -Strahlen.” In: *Zeitschrift für Physik* **66**(5) (May 1930), pp. 289–306. DOI: [10.1007/BF01390908](https://doi.org/10.1007/BF01390908).
- [15] I. CURIE and F. JOLIOT. “Émission de protons de grande vitesse par les substances hydrogénées sous l’influence des rayons gamma très pénétrants.” In: *Comptes rendus hebdomadaires des séances de l’Académie des Sciences* **194** (Jan. 1932), pp. 273–275. URL: <https://gallica.bnf.fr/ark:/12148/bpt6k31473/f273.image.r=>.
- [16] E. AMALDI. *Ettore Majorana, Man and Scientist: Commemoration Speech*. Academic Press, 1966.
- [17] J. CHADWICK. “Possible Existence of a Neutron.” In: *Nature* **129**(3252) (Feb. 1932), p. 312. DOI: [10.1038/129312a0](https://doi.org/10.1038/129312a0).
- [18] D.D. IWANENKO. “The Neutron Hypothesis.” In: *Nature* **129**(3265) (May 1932), p. 798. DOI: [10.1038/129798d0](https://doi.org/10.1038/129798d0).

- [19] J. CHADWICK. “The Existence of a Neutron.” In: *Proceedings of the Royal Society of London Series A* **136** (June 1932), pp. 692–708.  
DOI: [10.1098/rspa.1932.0112](https://doi.org/10.1098/rspa.1932.0112).
- [20] W. HEISENBERG. “Über den Bau der Atomkerne. I.” In: *Zeitschrift für Physik* **77**(1) (Jan. 1932), pp. 1–11.  
DOI: [10.1007/BF01342433](https://doi.org/10.1007/BF01342433).
- [21] H. BECKER and W. BOTHE. “Die in Bor und Beryllium erregten  $\gamma$ -Strahlen.” In: *Zeitschrift für Physik* **76**(7) (July 1932), pp. 421–438.  
DOI: [10.1007/BF01336726](https://doi.org/10.1007/BF01336726).
- [22] L.M. MOTT-SMITH and G.L. LOCHER. “A New Experiment Bearing on Cosmic-ray Phenomena.” In: *Physical Review* **38** (Oct. 1931), pp. 1399–1408.  
DOI: [10.1103/PhysRev.38.1399](https://doi.org/10.1103/PhysRev.38.1399).
- [23] K.H. BECKURTS and K.W. WIRTZ. *Neutron Physics*. Berlin, Heidelberg: Springer Berlin Heidelberg, 1964. 439 pp. ISBN: 978-3-642-87616-5.  
DOI: [10.1007/978-3-642-87614-1](https://doi.org/10.1007/978-3-642-87614-1).
- [24] E. AMALDI. “The Production and Slowing Down of Neutrons.” In: *Neutrons and Related Gamma Ray Problems / Neutronen und Verwandte Gammastrahlprobleme*. 1<sup>st</sup> Edition. Berlin, Heidelberg: Springer Berlin Heidelberg, Jan. 1959, pp. 1–659. ISBN: 978-3-642-45922-1.  
DOI: [10.1007/978-3-642-45920-7](https://doi.org/10.1007/978-3-642-45920-7).
- [25] M. BERGER, J.S. COURSEY, M.A. ZUCKER, and J. CHANG. *NIST XCOM: Stopping-Power and Range Tables for Electrons, Protons, and Helium Ions*. Website. <https://www.nist.gov/pml/stopping-power-range-tables-electrons-protons-and-helium-ions>; (01.03.2019). 2017.  
DOI: [10.18434/T4NC7P](https://doi.org/10.18434/T4NC7P).
- [26] C. GRUPEN and B.A. SCHWARZ. *Particle Detectors*. 2nd ed. Cambridge University Press, Mar. 2008. 676 pp. ISBN: 978-0-521-84006-4.  
URL: [www.cambridge.org/9780521840064](http://www.cambridge.org/9780521840064).
- [27] F. SAULI. “Principles of operation of multiwire proportional and drift chambers.” In: *CERN Academic Training Lecture*. CERN, Geneva, 1975 - 1976. CERN. Geneva: CERN, Sept. 1977.  
DOI: [10.5170/CERN-1977-009](https://doi.org/10.5170/CERN-1977-009).
- [28] W.R. LEO. *Techniques for Nuclear and Particle Physics Experiments*. 2<sup>nd</sup> ed. Berlin Heidelberg: Springer, 1994. 377 pp. ISBN: 978-3-540-57280-0.  
DOI: [10.1007/978-3-642-57920-2](https://doi.org/10.1007/978-3-642-57920-2).
- [29] T. DOKE, N. ISHIDA, and M. KASE. “Fano factors in rare gases and their mixtures.” In: *Nuclear Instruments and Methods in Physics Research Section B: Beam Interactions with Materials and Atoms* **63**(4) (Mar. 1992), pp. 373–376.  
DOI: [10.1016/0168-583X\(92\)95207-8](https://doi.org/10.1016/0168-583X(92)95207-8).
- [30] M. HAUSCHILD. *MediPix Simulations, gas properties and GEMs*. Website. <http://hausch.home.cern.ch/hausch/MediPix.html>; (01.03.2019). 2006.
- [31] F. GAUTHIER-LAFAYE. “2 billion year old natural analogs for nuclear waste disposal: the natural nuclear fission reactors in Gabon (Africa).” In: *Comptes Rendus Physique* **3**(7) (Sept. 2002), pp. 839–849.  
DOI: [10.1016/S1631-0705\(02\)01351-8](https://doi.org/10.1016/S1631-0705(02)01351-8).
- [32] J.F. ZIEGLER. “Terrestrial cosmic rays.” In: *IBM Journal of Research and Development* **40**(1) (Jan. 1996), pp. 19–39.  
DOI: [10.1147/rd.401.0019](https://doi.org/10.1147/rd.401.0019).
- [33] B.C. LACKI, T.A. THOMPSON, and E. QUATAERT. “The Physics of the Far-infrared-Radio Correlation. I. Calorimetry, Conspiracy, and Implications.” In: *The Astrophysical Journal* **717**(1) (June 2010), p. 1.  
DOI: [10.1088/0004-637X/717/1/1](https://doi.org/10.1088/0004-637X/717/1/1).
- [34] C. CAPRINI and P.G. FERREIRA. “Constraints on the electrical charge asymmetry of the universe.” In: *Journal of Cosmology and Astroparticle Physics* **2005**(02) (Feb. 2005), pp. 006–006.  
DOI: [10.1088/1475-7516/2005/02/006](https://doi.org/10.1088/1475-7516/2005/02/006).

- [35] C.L. SARAZIN and R. LIEU. “Extreme-Ultraviolet Emission from Clusters of Galaxies: Inverse Compton Radiation from a Relic Population of Cosmic-Ray Electrons?” In: *The Astrophysical Journal Letters* **494**(2) (Feb. 1998), p. L177.  
DOI: [10.1086/311196](https://doi.org/10.1086/311196).
- [36] R.M. BALTRUSAITIS, R. CADY, et al. “The Utah Fly’s Eye detector.” In: *Nuclear Instruments and Methods in Physics Research Section A: Accelerators, Spectrometers, Detectors and Associated Equipment* **240**(2) (Oct. 1985), pp. 410–428.  
DOI: [10.1016/0168-9002\(85\)90658-8](https://doi.org/10.1016/0168-9002(85)90658-8).
- [37] T.K. GAISSER. “The Cosmic-ray Spectrum: from the knee to the ankle.” In: *Journal of Physics: Conference Series* **47**(1) (Mar. 2006), pp. 15–20.  
DOI: [10.1088/1742-6596/47/1/002](https://doi.org/10.1088/1742-6596/47/1/002).
- [38] B.W. CARROLL and D.A. OSTLIE. *An Introduction to Modern Astrophysics*. Ed. by San Francisco ADDISON-WESLEY. 2<sup>nd</sup>. Pearson Education, July 2006. 1400 pp. ISBN: 978-0805304022.  
DOI: [10.1017/9781108380980](https://doi.org/10.1017/9781108380980).
- [39] A.M. BYKOV, D.C. ELLISON, A. MARCOWITH, and S.M. OSIPOV. “Cosmic Ray Production in Supernovae.” In: *Space Science Reviews* **214**(1) (Jan. 2018), p. 41.  
DOI: [10.1007/s11214-018-0479-4](https://doi.org/10.1007/s11214-018-0479-4).
- [40] L. MERTEN, C. BUSTARD, E.G. ZWEIBEL, and J.B. TJUS. “The Propagation of Cosmic Rays from the Galactic Wind Termination Shock: Back to the Galaxy?” In: *The Astrophysical Journal* **859**(1) (May 2018), p. 63.  
DOI: [10.3847/1538-4357/aabfdd](https://doi.org/10.3847/1538-4357/aabfdd).
- [41] V.N. ZIRAKASHVILI and H.J. VÖLK. “Cosmic ray reacceleration on the galactic wind termination shock.” In: *Advances in Space Research* **37**(10) (Aug. 2006). Astrophysics, pp. 1923–1927.  
DOI: [10.1016/j.asr.2005.06.013](https://doi.org/10.1016/j.asr.2005.06.013).
- [42] F.C. MICHEL. “Cosmic-ray acceleration by pulsars.” In: *Advances in Space Research* **4**(2) (1984), pp. 387–391.  
DOI: [10.1016/0273-1177\(84\)90336-3](https://doi.org/10.1016/0273-1177(84)90336-3).
- [43] R. BLANDFORD, P. SIMEON, and Y. YUAN. “Cosmic Ray Origins: An Introduction.” In: *Nuclear Physics B - Proceedings Supplements* **256-257** (Dec. 2014). Cosmic Ray Origin - Beyond the Standard Models, pp. 9–22.  
DOI: [10.1016/j.nuclphysbps.2014.10.002](https://doi.org/10.1016/j.nuclphysbps.2014.10.002).
- [44] J. BEER, S.M. TOBIAS, and N.O. WEISS. “On long-term modulation of the Sun’s magnetic cycle.” In: *Monthly Notices of the Royal Astronomical Society* **473**(2) (Jan. 2018), pp. 1596–1602.  
DOI: [10.1093/mnras/stx2337](https://doi.org/10.1093/mnras/stx2337).
- [45] K. KUDELA, H. MAVROMICHALAKI, A. PAPAIOANNOU, and M. GERONTIDOU. “On Mid-Term Periodicities in Cosmic Rays.” In: *Solar Physics* **266**(1) (Sept. 2010), pp. 173–180.  
DOI: [10.1007/s11207-010-9598-0](https://doi.org/10.1007/s11207-010-9598-0).
- [46] K.G. MCCrackEN, H. MORAAL, and M.A. SHEA. “The high-energy impulsive ground-level enhancement.” In: *The Astrophysical Journal* **761**(2) (Nov. 2012), p. 101.  
DOI: [10.1088/0004-637X/761/2/101](https://doi.org/10.1088/0004-637X/761/2/101).
- [47] H.V. CANE. “Coronal Mass Ejections and Forbush Decreases.” In: *Space Science Reviews* **93**(1) (July 2000), pp. 55–77.  
DOI: [10.1023/A:1026532125747](https://doi.org/10.1023/A:1026532125747).
- [48] S.R. THOMAS, M.J. OWENS, and M. LOCKWOOD. “The 22-Year Hale Cycle in Cosmic Ray Flux - Evidence for Direct Heliospheric Modulation.” In: *Solar Physics* **289**(1) (Jan. 2014), pp. 407–421.  
DOI: [10.1007/s11207-013-0341-5](https://doi.org/10.1007/s11207-013-0341-5).
- [49] M.A. SHEA and D.F. SMART. “Geomagnetic cutoff rigidities and geomagnetic coordinates appropriate for the Carrington flare Epoch.” In: *Advances in Space Research* **38**(2) (Sept. 2006). The Great Historical Geomagnetic Storm of 1859: A Modern Look, pp. 209–214.  
DOI: [10.1016/j.asr.2005.03.156](https://doi.org/10.1016/j.asr.2005.03.156).

- [50] M. ANDREASEN, K.H. JENSEN, D. DESILETS, T.E. FRANZ, M. ZREDA, H.R. BOGENA, and M.C. LOOMS. “Status and Perspectives on the Cosmic-Ray Neutron Method for Soil Moisture Estimation and Other Environmental Science Applications.” In: *Vadose Zone Journal* **16**(8) (Aug. 2017), pp. 1–11. DOI: [10.2136/vzj2017.04.0086](https://doi.org/10.2136/vzj2017.04.0086).
- [51] L.I. DORMAN, S.G. FEDCHENKO, L.V. GRANITSKY, and G.A. RISHE. “Coupling and barometer coefficients for measurements of cosmic ray variations at altitudes of 260-400 mb.” In: *Acta Physica* **2** (Jan. 1970). Supplement to Volume 29, pp. 233–236. URL: <http://adsabs.harvard.edu/full/1970ICRC....2..233D>.
- [52] C.W. FABJAN and F. GIANOTTI. “Calorimetry for particle physics.” In: *Reviews of Modern Physics* **75** (Oct. 2003), pp. 1243–1286. DOI: [10.1103/RevModPhys.75.1243](https://doi.org/10.1103/RevModPhys.75.1243).
- [53] C. LEROY and R.-G. RANCOITA. “Physics of cascading shower generation and propagation in matter: principles of high-energy, ultrahigh-energy and compensating calorimetry.” In: *Reports on Progress in Physics* **63**(4) (Apr. 2000), pp. 505–606. DOI: [10.1088/0034-4885/63/4/202](https://doi.org/10.1088/0034-4885/63/4/202).
- [54] B.B. ROSSI. *High-energy Particles*. Prentice-Hall physics series. New York, 1952. 569 pp. ISBN: 978-0133873245.
- [55] R. ULRICH, R. ENGEL, and M. UNGER. “Hadronic multiparticle production at ultrahigh energies and extensive air showers.” In: *Physical Review D* **83** (Mar. 2011), p. 054026. DOI: [10.1103/PhysRevD.83.054026](https://doi.org/10.1103/PhysRevD.83.054026).
- [56] A. CAPELLA, U. SUKHATME, C.-I. TAN, and J. TRAN THANH VAN. “Dual parton model.” In: *Physics Reports* **236**(4) (Jan. 1994), pp. 225–329. DOI: [10.1016/0370-1573\(94\)90064-7](https://doi.org/10.1016/0370-1573(94)90064-7).
- [57] S.D. ELLIS and M.B. KISLINGER. “Implications of parton-model concepts for large-transverse-momentum production of hadrons.” In: *Physical Review D* **9** (Apr. 1974), pp. 2027–2051. DOI: [10.1103/PhysRevD.9.2027](https://doi.org/10.1103/PhysRevD.9.2027).
- [58] S. MOLLERACH and E. ROULET. “Progress in high-energy cosmic ray physics.” In: *Progress in Particle and Nuclear Physics* **98** (Jan. 2018), pp. 85–118. DOI: [10.1016/j.ppnp.2017.10.002](https://doi.org/10.1016/j.ppnp.2017.10.002).
- [59] D. HECK, J. KNAPP, J.N. CAPDEVIELLE, G. SCHATZ, and T. THOUW. *CORSIKA: A Monte Carlo code to simulate extensive air showers*. Tech. rep. FZKA 6019. Forschungszentrum Karlsruhe, 1998. 98 pp. URL: <http://digbib.ubka.uni-karlsruhe.de/volltexte/fzk/6019/6019.pdf>.
- [60] G. PFOTZER. “Dreifachkoinzidenzen der Ultrastrahlung aus vertikaler Richtung in der Stratosphäre.” In: *Zeitschrift für Physik* **102**(1–2) (Jan. 1936), pp. 41–58. DOI: [10.1007/BF01336830](https://doi.org/10.1007/BF01336830).
- [61] T. SATO. “Analytical Model for Estimating Terrestrial Cosmic Ray Fluxes Nearly Anytime and Anywhere in the World: Extension of PARMA/EXPACS.” In: *PLOS ONE* **10**(12) (Dec. 2015), pp. 1–33. DOI: [10.1371/journal.pone.0144679](https://doi.org/10.1371/journal.pone.0144679).
- [62] K.K. GUDIMA, S.G. MASHNIK, and V.D. TONEEV. “Cascade-exciton model of nuclear reactions.” In: *Nuclear Physics A* **401**(2) (June 1983), pp. 329–361. DOI: [10.1016/0375-9474\(83\)90532-8](https://doi.org/10.1016/0375-9474(83)90532-8).
- [63] E.T. JURNEY, J.W. STARNER, J.E. LYNN, and S. RAMAN. “Thermal-neutron capture by  $^{14}\text{N}$ .” In: *Physical Review C* **56** (July 1997), pp. 118–134. DOI: [10.1103/PhysRevC.56.118](https://doi.org/10.1103/PhysRevC.56.118).
- [64] R.E. TAYLOR. “Radiocarbon dating: The continuing revolution.” In: *Evolutionary Anthropology: Issues, News, and Reviews* **4**(5) (June 1995), pp. 169–181. DOI: [10.1002/evan.1360040507](https://doi.org/10.1002/evan.1360040507).
- [65] P. GOLDHAGEN, J.M. CLEM, and J.W. WILSON. “The energy spectrum of cosmic-ray induced neutrons measured on an airplane over a wide range of altitude and latitude.” In: *Radiation Protection Dosimetry* **110**(1–4) (Aug. 2004), pp. 387–392. DOI: [10.1093/rpd/nch216](https://doi.org/10.1093/rpd/nch216).



- [66] T. SATO and K. NIITA. “Analytical Functions to Predict Cosmic-Ray Neutron Spectra in the Atmosphere.” In: *Radiation Research* **166**(3) (Sept. 2006), pp. 544–555.  
DOI: [10.1667/RR0610.1](https://doi.org/10.1667/RR0610.1).
- [67] T. SATO, H. YASUDA, K. NIITA, A. ENDO, and L. SIHVER. “Development of PARMA: PHITS-based Analytical Radiation Model in the Atmosphere.” In: *Radiation Research* **170**(2) (Aug. 2008), pp. 244–259.  
DOI: [10.1667/RR1094.1](https://doi.org/10.1667/RR1094.1).
- [68] H. IWASE, K. NIITA, and T. NAKAMURA. “Development of General-Purpose Particle and Heavy Ion Transport Monte Carlo Code.” In: *Journal of Nuclear Science and Technology* **39**(11) (Aug. 2002), pp. 1142–1151.  
DOI: [10.1080/18811248.2002.9715305](https://doi.org/10.1080/18811248.2002.9715305).
- [69] M.S. GORDON, P. GOLDHAGEN, K.P. RODBELL, T.H. ZABEL, H.H.K. TANG, J.M. CLEM, and P. BAILEY. “Measurement of the flux and energy spectrum of cosmic-ray induced neutrons on the ground.” In: *IEEE Transactions on Nuclear Science* **51**(6) (Dec. 2004), pp. 3427–3434.  
DOI: [10.1109/TNS.2004.839134](https://doi.org/10.1109/TNS.2004.839134).
- [70] R.M. BRUGGER. “We need more intense thermal-neutron beams.” In: *Physics Today* **21**(12) (Dec. 1968), pp. 23–30.  
DOI: [10.1063/1.3034644](https://doi.org/10.1063/1.3034644).
- [71] J.M. CARPENTER and W.B. YELON. “2. Neutron Sources.” In: *Neutron Scattering*. Ed. by K. SKÖLD and D.L. PRICE. Vol. 23. Methods in Experimental Physics. Academic Press, 1986, pp. 99–196.  
DOI: [10.1016/S0076-695X\(08\)60555-4](https://doi.org/10.1016/S0076-695X(08)60555-4).
- [72] K.H. ANDERSEN and C.J. CARLILE. “A Proposal for a Next Generation European Neutron Source.” In: *Journal of Physics: Conference Series* **746**(1) (Oct. 2016), p. 012030.  
DOI: [10.1088/1742-6596/746/1/012030](https://doi.org/10.1088/1742-6596/746/1/012030).
- [73] G.E. MOORE. “Cramming more components onto integrated circuits.” In: *Electronics* **38**(8) (Apr. 1965). URL for IEEE reprint 2006, pp. 114–118.  
URL: <https://ieeexplore.ieee.org/document/4785860/>.
- [74] M.S. LIVINGSTON. *High-energy accelerators*. Interscience tracts on physics and astronomy. New York, U.S.A.: Interscience Publishers, May 1954. 157 pp.
- [75] M. TIGNER. “Does Accelerator-Based Particle Physics Have a Future?” In: *Physics Today* **54**(1) (Jan. 2001), pp. 36–40.  
DOI: [10.1063/1.1349610](https://doi.org/10.1063/1.1349610).
- [76] THE EUROPEAN NEUTRON SCATTERING ASSOCIATION (ENSA). (accessed 26.08.2016). 2016. URL: <http://www.neutrons-ensa.eu>.
- [77] M. ARAI and K. CRAWFORD. “Neutron Imaging and Applications: A Reference for the Imaging Community.” In: *Neutron Scattering Applications and Techniques*. Ed. by I.S. ANDERSON, R.L. MCGREEVY, and H.Z. BILHEUX. Springer USA, 2009. Chap. Neutron Sources and Facilities, pp. 13–30. ISBN: 9780387786933.  
DOI: [10.1007/978-0-387-78693-3](https://doi.org/10.1007/978-0-387-78693-3).
- [78] INTERNATIONAL ATOMIC ENERGY AGENCY. *Research Reactors*. (accessed 10.03.2019). June 2016. URL: <https://nucleus.iaea.org/RRDB/RR/ReactorSearch.aspx>.
- [79] A. RÖHRMOSER. “Core model of new German neutron source FRM II.” In: *Nuclear Engineering and Design* **240**(6) (2010), pp. 1417–1432.  
DOI: [10.1016/j.nucengdes.2010.02.011](https://doi.org/10.1016/j.nucengdes.2010.02.011).
- [80] K. BÖNING, W. GLÄSER, and A. RÖHRMOSER. “Physics of the Munich compact core design.” In: *Proceedings of the 1988 International Meeting on Reduced Enrichment for Research and Test Reactors*. Vol. 25. 17. ANL/RERTR/TM-13. July 1993, pp. 393–403.  
DOI: [10.1109/NSSMIC.2007.4436548](https://doi.org/10.1109/NSSMIC.2007.4436548).
- [81] T. BÜCHERL and S. SÖLLRADL. “NECTAR: Radiography and tomography station using fission neutrons.” In: *Journal of large-scale Research Facilities* **1**(A19) (June 2015).  
DOI: [10.17815/jlsrf-1-45](https://doi.org/10.17815/jlsrf-1-45).

- [82] C. FRANZ and T. SCHRÖDER. “RESEDA: Resonance spin echo spectrometer.” In: *Journal of large-scale Research Facilities* **1**(A14) (June 2015).  
DOI: [10.17815/jlsrf-1-37](https://doi.org/10.17815/jlsrf-1-37).
- [83] R. GEORGI and K. SEEMANN. “MIRA: Dual wavelength band instrument.” In: *Journal of large-scale Research Facilities* **1**(A3) (June 2015).  
DOI: [10.17815/jlsrf-1-21](https://doi.org/10.17815/jlsrf-1-21).
- [84] M. MEVEN and A. SAZONOV. “HEiDi: Single crystal diffractometer at hot source.” In: *Journal of large-scale Research Facilities* **1**(A7) (June 2015).  
DOI: [10.17815/jlsrf-1-20](https://doi.org/10.17815/jlsrf-1-20).
- [85] F. GRÜNAUER. “Design, optimization, and implementation of the new neutron radiography facility at FRM-II.” PhD thesis. Institut E21, Technische Universität München, Sept. 2005. 199 pp.  
URL: [https://www.physi.uni-heidelberg.de/Publications/phd\\_haeusler.pdf](https://www.physi.uni-heidelberg.de/Publications/phd_haeusler.pdf).
- [86] S. Ulam N. METROPOLIS. “The Monte Carlo Method.” In: *Journal of the American Statistical Association* **44**(247) (Sept. 1949), pp. 335–341.  
DOI: [10.2307/2280232](https://doi.org/10.2307/2280232).
- [87] F. COCCETTI. “The Fermiac or Fermi’s Trolley.” In: *Il Nuovo Cimento C* **39**(2) (Sept. 2016).  
DOI: [10.1393/ncc/i2016-16296-7](https://doi.org/10.1393/ncc/i2016-16296-7).
- [88] N. METROPOLIS. “The Beginning of the Monte Carlo Method.” In: *Los Alamos Science* **15** (1987). Special Issue, Stanislaw Ulam 1909-1984, pp. 125–130.  
URL: <https://permlink.lanl.gov/object/tr?what=info:lanl-repo/lareport/LA-UR-88-9067>.
- [89] A. BURKS, H.D. HUSKEY, C. CHU, J.A. CUMMINGS, J.H. DAVIS, T.K. SHARPLESS, and R.F. SHAW. *Report on the ENIAC (Electronic Numerical Integrator and Computer)*. Technical Report. Moore School of Electrical Engineering. The University of Pennsylvania, June 1946. 786 pp.  
URL: <https://www.dtic.mil/get-tr-doc/pdf?AD=ADA622372>.
- [90] T. HAIGH, M. PRIESTLEY, and C. ROPE. “Los Alamos Bets on ENIAC: Nuclear Monte Carlo Simulations, 1947-1948.” In: *IEEE Annals of the History of Computing* **36**(3) (July 2014), pp. 42–63.  
DOI: [10.1109/MAHC.2014.40](https://doi.org/10.1109/MAHC.2014.40).
- [91] M. MATSUMOTO and T. NISHIMURA. “Mersenne Twister: A 623-dimensionally Equidistributed Uniform Pseudo-random Number Generator.” In: *ACM Transactions on Modeling and Computer Simulation* **8**(1) (Jan. 1998), pp. 3–30.  
DOI: [10.1145/272991.272995](https://doi.org/10.1145/272991.272995).
- [92] D.E. KNUTH. *The Art of Computer Programming, Volume 2 (3<sup>rd</sup> Ed.): Seminumerical Algorithms*. Boston, MA, USA: Addison-Wesley Longman Publishing Co., Inc., Nov. 1997. 106 pp. ISBN: 0-201-89684-2.
- [93] E.M. GELBARD. *Epithermal scattering in VIM*. Tech. rep. FRA-TM-123. Argonne National Laboratory, 1979.
- [94] P.K. ROMANO and B. FORGET. “The OpenMC Monte Carlo particle transport code.” In: *Annals of Nuclear Energy* **51** (Jan. 2013), pp. 274–281.  
DOI: [10.1016/j.anucene.2012.06.040](https://doi.org/10.1016/j.anucene.2012.06.040).
- [95] J.A. WALSH, B. FORGET, and K.S. SMITH. “Accelerated sampling of the free gas resonance elastic scattering kernel.” In: *Annals of Nuclear Energy* **69** (July 2014), pp. 116–124.  
DOI: [10.1016/j.anucene.2014.01.017](https://doi.org/10.1016/j.anucene.2014.01.017).
- [96] N. OTUKA, E. DUPONT, et al. “Towards a More Complete and Accurate Experimental Nuclear Reaction Data Library (EXFOR): International Collaboration Between Nuclear Reaction Data Centres (NRDC).” In: *Nuclear Data Sheets* **120** (June 2014), pp. 272–276.  
DOI: [10.1016/j.nds.2014.07.065](https://doi.org/10.1016/j.nds.2014.07.065).
- [97] M.B. CHADWICK, M. HERMAN, et al. “ENDF/B-VII.1 Nuclear Data for Science and Technology: Cross Sections, Covariances, Fission Product Yields and Decay Data.” In: *Nuclear Data Sheets* **112**(12) (Dec. 2011). Special Issue on ENDF/B-VII.1 Library, pp. 2887–2996.  
DOI: [10.1016/j.nds.2011.11.002](https://doi.org/10.1016/j.nds.2011.11.002).

- [98] K. SHIBATA, O. IWAMOTO, et al. “JENDL-4.0: A New Library for Nuclear Science and Engineering.” In: *Journal of Nuclear Science and Technology* **48**(1) (Sept. 2011), pp. 1–30.  
DOI: [10.1080/18811248.2011.9711675](https://doi.org/10.1080/18811248.2011.9711675).
- [99] A. TRKOV, M. HERMAN, and D.A. BROWN. *ENDF-6 Formats Manual*. Report. Data Formats and Procedures for the Evaluated Nuclear Data Files ENDF/B-VI and ENDF/B-VII. National Nuclear Data Center. Brookhaven National Laboratory, Oct. 2012. 396 pp.  
URL: <https://www-nds.iaea.org/public/endl/endl-manual.pdf>.
- [100] R. SEDGEWICK. *Algorithms in C*. Boston, USA: Addison-Wesley Longman Publishing Co., Inc., Dec. 1990. 672 pp. ISBN: 0-201-51425-7.
- [101] J.F. BRIESMEISTER et al. “MCNP-A general Monte Carlo N-particle transport code.” In: *Version 4C, LA-13709-M* (Dec. 2000).  
URL: <https://permalink.lanl.gov/object/tr?what=info:lanl-repo/lareport/LA-13709-M>.
- [102] SUN PROGRAMMERS GROUP. *Fortran 77 Reference Manual*. Tech. rep. Version 1.0. Mar. 1995. 513 pp.  
URL: [http://wwwcdf.pd.infn.it/localdoc/f77\\_sun.pdf](http://wwwcdf.pd.infn.it/localdoc/f77_sun.pdf).
- [103] X-5 MONTE CARLO TEAM. “MCNP-A general Monte Carlo N-particle transport code, Version 5.” In: *LA-UR-03-1987* (Apr. 2003). Volume I: Overview and Theory.  
URL: [https://laws.lanl.gov/vhosts/mcnp.lanl.gov/pdf\\_files/la-ur-03-1987.pdf](https://laws.lanl.gov/vhosts/mcnp.lanl.gov/pdf_files/la-ur-03-1987.pdf).
- [104] L.S. WATERS, G.W. MCKINNEY, J.W. DURKEE, M.L. FENSIN, J.S. HENDRICKS, M.R. JAMES, R.C. JOHNS, and D.B. PELOWITZ. “The MCNPX Monte Carlo Radiation Transport Code.” In: *AIP Conference Proceedings* **896**(1) (Mar. 2007), pp. 81–90.  
DOI: [10.1063/1.2720459](https://doi.org/10.1063/1.2720459).
- [105] SUN PROGRAMMERS GROUP. *Fortran 90 User’s Guide*. Tech. rep. Version 1.0. Mar. 1995.  
URL: <http://smdc.sinp.msu.ru/doc/Fortran90UsersGuide.pdf>.
- [106] R.E. PRAEL and H. LICHTENSTEIN. “User Guide to LCS: The LAHET Code System.” In: *LA-UR-89-3014* (Sept. 1989).  
URL: <https://permalink.lanl.gov/object/tr?what=info:lanl-repo/lareport/LA-UR-89-3014>.
- [107] K.K. GUDIMA, S.G. MASHNIK, and A.J. SIERK. “User Manual for the Code LAQGSM.” In: *LA-UR-01-6804* (Dec. 2001).  
URL: <https://permalink.lanl.gov/object/tr?what=info:lanl-repo/lareport/LA-UR-01-6804>.
- [108] T. GOORLEY, M. JAMES, et al. “Initial MCNP6 Release Overview.” In: *Nuclear Technology* **180**(3) (Aug. 2012), pp. 298–315.  
DOI: [10.13182/NT11-135](https://doi.org/10.13182/NT11-135).
- [109] G.W. MCKINNEY, H. ARMSTRONG, M.R. JAMES, J. CLEM, and P. GOLDHAGEN. “MCNP6 Cosmic-Source Option.” In: *LA-UR-12-22318* (June 2012).  
URL: <https://permalink.lanl.gov/object/tr?what=info:lanl-repo/lareport/LA-UR-12-22318>.
- [110] G.W. MCKINNEY. “MCNP6 Cosmic and Terrestrial Background Particle Fluxes.” In: *LA-UR-13-24293* (June 2013). Release 3.  
URL: [https://mcnp.lanl.gov/pdf\\_files/la-ur-13-24293.pdf](https://mcnp.lanl.gov/pdf_files/la-ur-13-24293.pdf).
- [111] K. NIITA, H. TAKADA, S. MEIGO, and Y. IKEDA. “High-energy particle transport code NMTC/JAM.” In: *Nuclear Instruments and Methods in Physics Research Section B: Beam Interactions with Materials and Atoms* **184**(3) (Nov. 2001), pp. 406–420.  
DOI: [10.1016/S0168-583X\(01\)00784-4](https://doi.org/10.1016/S0168-583X(01)00784-4).
- [112] A.T. NELMS. *Energy loss and range of electrons and positrons*. National Bureau of Standards Circular 577 and Suppl. July 1956, pp. 1–30.  
URL: <https://catalog.hathitrust.org/Record/007291096>.
- [113] K. NIITA. “QMD and JAM Calculations for High Energy Nucleon-Nucleus Collisions.” In: *Journal of Nuclear Science and Technology* **39** (Aug. 2002). sup2, pp. 714–719.  
DOI: [10.1080/00223131.2002.10875198](https://doi.org/10.1080/00223131.2002.10875198).

- [114] O. IWAMOTO, N. IWAMOTO, S. KUNIEDA, F. MINATO, and K. SHIBATA. “The CCONE Code System and its Application to Nuclear Data Evaluation for Fission and Other Reactions.” In: *Nuclear Data Sheets* **131** (Jan. 2016). Special Issue on Nuclear Reaction Data, pp. 259–288.  
DOI: [10.1016/j.nds.2015.12.004](https://doi.org/10.1016/j.nds.2015.12.004).
- [115] A. BOUDARD, J. CUGNON, J.-C. DAVID, S. LERAY, and D. MANCUSI. “New potentialities of the Liège intranuclear cascade model for reactions induced by nucleons and light charged particles.” In: *Physical Review C* **87** (Jan. 2013), p. 014606.  
DOI: [10.1103/PhysRevC.87.014606](https://doi.org/10.1103/PhysRevC.87.014606).
- [116] G. BATTISTONI, T. BOEHLER, et al. “Overview of the FLUKA code.” In: *Annals of Nuclear Energy* **82** (Aug. 2015). Joint International Conference on Supercomputing in Nuclear Applications and Monte Carlo 2013, pp. 10–18.  
DOI: [10.1016/j.anucene.2014.11.007](https://doi.org/10.1016/j.anucene.2014.11.007).
- [117] M.B. EMMETT. “The MORSE Monte Carlo Transport Code System.” In: *ORNL-4972/R2* (Feb. 1975).  
URL: [https://inis.iaea.org/collection/NCLCollectionStore/\\_Public/16/029/16029296.pdf](https://inis.iaea.org/collection/NCLCollectionStore/_Public/16/029/16029296.pdf).
- [118] S. AGOSTINELLI, ET AL. “GEANT4 - a simulation toolkit.” In: *Nuclear Instruments and Methods in Physics Research Section A: Accelerators, Spectrometers, Detectors and Associated Equipment* **506**(3) (July 2003), pp. 250–303.  
DOI: [10.1016/S0168-9002\(03\)01368-8](https://doi.org/10.1016/S0168-9002(03)01368-8).
- [119] A.N. SOLOVYEV, V.V. FEDOROV, V.I. KHARLOV, and U.A. STEPANOVA. “Comparative analysis of MCNPX and GEANT4 codes for fast-neutron radiation treatment planning.” In: *Nuclear Energy and Technology* **1**(1) (Sept. 2015), pp. 14–19.  
DOI: [10.1016/j.nucet.2015.11.004](https://doi.org/10.1016/j.nucet.2015.11.004).
- [120] B.M. VAN DER ENDE, J. ATANACKOVIC, A. ERLANDSON, and G. BENTOUMI. “Use of GEANT4 vs. MCNPX for the characterization of a boron-lined neutron detector.” In: *Nuclear Instruments and Methods in Physics Research Section A: Accelerators, Spectrometers, Detectors and Associated Equipment* **820** (June 2016), pp. 40–47.  
DOI: [10.1016/j.nima.2016.02.082](https://doi.org/10.1016/j.nima.2016.02.082).
- [121] L.B. LEVITT and R.C. LEWIS. *VIM-1, A Non-multigroup Monte Carlo Code for Analysis of Fast Critical Assemblies*. AI-AEC-12951. Jan. 1970. 94 pp.  
DOI: [10.2172/4615237](https://doi.org/10.2172/4615237).
- [122] E. BRUN, F. DAMIAN, et al. “TRIPOLI-4, CEA, EDF and AREVA reference Monte Carlo code.” In: *Annals of Nuclear Energy* **82** (Aug. 2015). Joint International Conference on Supercomputing in Nuclear Applications and Monte Carlo 2013, pp. 151–160.  
DOI: [10.1016/j.anucene.2014.07.053](https://doi.org/10.1016/j.anucene.2014.07.053).
- [123] D.E. CULLEN. “TART 2005 A Coupled Neutron-Photon 3-D, Combinatorial Geometry Time Dependent Monte Carlo Transport Code.” In: *UCRL-SM-218009* (Nov. 2005).  
URL: <https://e-reports-ext.llnl.gov/pdf/329012.pdf>.
- [124] R.J. PROCASSINI, D.E. CULLEN, G.M. GREENMAN, and C.A. HAGMANN. “Verification and Validation of MERCURY: A Modern, Monte Carlo Particle Transport Code.” In: *Proceedings of the Monte Carlo 2005 Conference, Chattanooga*. UCRL-CONF-208667. Dec. 2004.  
URL: <https://e-reports-ext.llnl.gov/pdf/314728.pdf>.
- [125] Y.Z. KANDIEV, E.A. KASHAEVA, et al. “PRIZMA status.” In: *Annals of Nuclear Energy* **82** (Aug. 2015). Joint International Conference on Supercomputing in Nuclear Applications and Monte Carlo 2013, pp. 116–120.  
DOI: [10.1016/j.anucene.2014.09.006](https://doi.org/10.1016/j.anucene.2014.09.006).
- [126] T.M. PANDYA, S.R. JOHNSON, G.G. DAVIDSON, T.M. EVANS, and S.P. HAMILTON. “Shift: A massively parallel Monte Carlo radiation transport package.” In: *Proceedings of the ANS MC2015 - Joint International Conference on Mathematics and Computation*. Apr. 2015, pp. 19–23.  
URL: <https://www.casl.gov/sites/default/files/docs/CASL-U-2015-0170-000.pdf>.

- [127] J. LEPPÄNEN, M. PUSA, T. VIITANEN, V. VALTAVIRTA, and T. KALTIAISENAHO. “The Serpent Monte Carlo code: Status, development and applications in 2013.” In: *Annals of Nuclear Energy* **82** (Aug. 2015). Joint International Conference on Supercomputing in Nuclear Applications and Monte Carlo 2013, pp. 142–150.  
DOI: [10.1016/j.anucene.2014.08.024](https://doi.org/10.1016/j.anucene.2014.08.024).
- [128] E. WOODCOCK, T. MURPHY, P.J. HEMMINGS, and T.C. LONGWORTH. “Techniques used in the GEM code for Monte Carlo neutronics calculations in reactors and other systems of complex geometry.” In: *Proc. Conf. Applications of Computing Methods to Reactor Problems*. Vol. 557. May 1965, pp. 557–579.  
URL: <https://yiningkarlli.com/projects/specdecomptracking/references/Woodcock1965.pdf>.
- [129] K. WANG, Z. LI, D. SHE, J. LIANG, Q. XU, Y. QIU, J. YU, J. SUN, X. FAN, and G. YU. “RMC - A Monte Carlo code for reactor core analysis.” In: *Annals of Nuclear Energy* **82** (Aug. 2015). Joint International Conference on Supercomputing in Nuclear Applications and Monte Carlo 2013, pp. 121–129.  
DOI: [10.1016/j.anucene.2014.08.048](https://doi.org/10.1016/j.anucene.2014.08.048).
- [130] B. COCHET, A. JINAPHANH, L. HEULERS, and O. JACQUET. “Capabilities overview of the MORET 5 Monte Carlo code.” In: *Annals of Nuclear Energy* **82** (Aug. 2015). Joint International Conference on Supercomputing in Nuclear Applications and Monte Carlo 2013, pp. 74–84.  
DOI: [10.1016/j.anucene.2014.08.022](https://doi.org/10.1016/j.anucene.2014.08.022).
- [131] N. SMITH, T. SHUTTLEWORTH, M. GRIMSTONE, L. HUTTON, M. ARMISHAW, A. BIRD, N. FRANCE, and S. CONNOLLY. “The Current Status and Future Plans for the Monte Carlo Codes MONK and MCBEND.” In: *Advanced Monte Carlo for Radiation Physics, Particle Transport Simulation and Applications: Proceedings of the Monte Carlo 2000 Conference, Lisbon*. Berlin, Heidelberg: Springer, 2001, pp. 637–642. ISBN: 978-3-642-18211-2.  
DOI: [10.1007/978-3-642-18211-2\\_102](https://doi.org/10.1007/978-3-642-18211-2_102).
- [132] G. ARNECKE, H. BORGWALDT, V. BRANDL, and M. LALOVIC. “KAMCCO, ein reaktorphysikalischer Monte Carlo Neutronentransportcode.” In: *KFK 2190* (June 1976). Joint International Conference on Supercomputing in Nuclear Applications and Monte Carlo 2013.  
URL: <https://publikationen.bibliothek.kit.edu/270009404/3811483>.
- [133] W. MARTH. *The history of the construction and operation of the KNK II German Fast Breeder Power Plant*. Tech. rep. KFK-5155. IAEA INIS, Sept. 1993. 181 pp.  
URL: <https://publikationen.bibliothek.kit.edu/270038327/3813557>.
- [134] G. VAN ROSSUM. *The Python Language Reference Manual*. Tech. rep. Version 3.5.4. Aug. 2017.  
URL: <https://docs.python.org/3/library/>.
- [135] JUPYTER TEAM. *Jupyter Documentation*. Tech. rep. Version 4.1.1. Sept. 2017.  
URL: <https://media.readthedocs.org/pdf/jupyter/latest/jupyter.pdf>.
- [136] *Programming Languages - C++*. Standard. Geneva, CH: International Organization for Standardization, May 2013. 1374 pp.  
URL: <http://www.open-std.org/jtc1/sc22/wg21/docs/papers/2013/n3690.pdf>.
- [137] R. BRUN and F. RADEMAKERS. “ROOT - An Object Oriented Data Analysis Framework.” In: *Proceedings of AIHENP’96 Workshop, Lausanne*. Vol. 389. see also <https://root.cern.ch/>. May 1997, pp. 81–86.  
DOI: [10.1016/S0168-9002\(97\)00048-X](https://doi.org/10.1016/S0168-9002(97)00048-X).
- [138] THE QT COMPANY LTD. *The Qt Framework*. Jan. 2018. URL: <https://www.qt.io/qt-for-application-development/>.
- [139] M. GALASSI et al. *GNU Scientific Library: reference manual for GSL version 2.3*. Free Software Foundation, Dec. 2016.  
URL: <https://www.gnu.org/software/gsl/manual/gsl-ref.pdf>.
- [140] A. HÉBERT. “Multigroup Neutron Transport and Diffusion Computations.” In: *Handbook of Nuclear Engineering*. Ed. by D.G. CACUCI. Boston: Springer US, Aug. 2010, pp. 751–911. ISBN: 978-0-387-98149-9.  
DOI: [10.1007/978-0-387-98149-9\\_8](https://doi.org/10.1007/978-0-387-98149-9_8).

- [141] A.J. KONING, E. BAUGE, et al. “Status of the JEFF Nuclear Data Library.” In: *Journal of the Korean Physical Society* **59**(2) (Aug. 2011), pp. 1057–1062.  
DOI: [10.3938/jkps.59.1057](https://doi.org/10.3938/jkps.59.1057).
- [142] T. KITTELMANN and M. BOIN. “Polycrystalline neutron scattering for Geant4: NXSG4.” In: *Computer Physics Communications* **189** (Apr. 2015), pp. 114–118.  
DOI: [10.1016/j.cpc.2014.11.009](https://doi.org/10.1016/j.cpc.2014.11.009).
- [143] S.D. ROTH. “Ray casting for modeling solids.” In: *Computer Graphics and Image Processing* **18**(2) (Feb. 1982), pp. 109–144.  
DOI: [10.1016/0146-664X\(82\)90169-1](https://doi.org/10.1016/0146-664X(82)90169-1).
- [144] E. MAIRE and P.J. WITHERS. “Quantitative X-ray tomography.” In: *International Materials Reviews* **59**(1) (Dec. 2013), pp. 1–43.  
DOI: [10.1179/1743280413Y.0000000023](https://doi.org/10.1179/1743280413Y.0000000023).
- [145] V. CNUUDE and M.N. BOONE. “High-resolution X-ray computed tomography in geosciences: A review of the current technology and applications.” In: *Earth-Science Reviews* **123** (Aug. 2013), pp. 1–17.  
DOI: [10.1016/j.earsci.2013.04.003](https://doi.org/10.1016/j.earsci.2013.04.003).
- [146] L.W. GOLDMAN. “Principles of CT and CT Technology.” In: *Journal of Nuclear Medicine Technology* **35**(3) (Sept. 2007), pp. 115–128.  
DOI: [10.2967/jnmt.107.042978](https://doi.org/10.2967/jnmt.107.042978).
- [147] R.J. MCCONN JR, C.J. GESH, R.T. PAGH, R.A. RUCKER, and R.G. WILLIAMS III. *Compendium of Material Composition Data for Radiation Transport Modeling*. Tech. rep. PNNL-15870 Rev. 1. Richland, Washington 99352: Pacific Northwest National Laboratory, Mar. 2011. 375 pp.  
URL: [https://www.pnnl.gov/main/publications/external/technical\\_reports/pnnl-15870rev1.pdf](https://www.pnnl.gov/main/publications/external/technical_reports/pnnl-15870rev1.pdf).
- [148] *Information technology - ISO 7-bit coded character set for information interchange*. Standard. Geneva, CH: International Organization for Standardization, Dec. 1991. 15 pp.  
URL: <https://www.iso.org/standard/4777.html>.
- [149] *Information technology - Computer graphics and image processing – Portable Network Graphics (PNG)*. Standard. Geneva, CH: International Organization for Standardization, Mar. 2004. 80 pp.  
URL: <https://www.iso.org/standard/29581.html>.
- [150] *Reference neutron radiations - Part 1*. Standard. Geneva, CH: International Organization for Standardization, Feb. 2001. 24 pp.  
URL: <https://www.iso.org/standard/25666.html>.
- [151] V. WEISSKOPF. “Statistics and Nuclear Reactions.” In: *Physical Review* **52** (Aug. 1937), pp. 295–303.  
DOI: [10.1103/PhysRev.52.295](https://doi.org/10.1103/PhysRev.52.295).
- [152] J. TERRELL. “Fission Neutron Spectra and Nuclear Temperatures.” In: *Physical Review* **113** (Jan. 1959), pp. 527–541.  
DOI: [10.1103/PhysRev.113.527](https://doi.org/10.1103/PhysRev.113.527).
- [153] M.R. IYER and A.K. GANGULY. “Neutron Evaporation and Energy Distribution in Individual Fission Fragments.” In: *Physical Review C* **5** (Apr. 1972), pp. 1410–1421.  
DOI: [10.1103/PhysRevC.5.1410](https://doi.org/10.1103/PhysRevC.5.1410).
- [154] B.E. WATT. “Energy Spectrum of Neutrons from Thermal Fission of  $^{235}\text{U}$ .” In: *Physical Review* **87** (Sept. 1952), pp. 1037–1041.  
DOI: [10.1103/PhysRev.87.1037](https://doi.org/10.1103/PhysRev.87.1037).
- [155] A.B. SMITH, P.R. FIELDS, and J.H. ROBERTS. “Spontaneous Fission Neutron Spectrum of  $^{252}\text{Cf}$ .” In: *Physical Review* **108** (Oct. 1957), pp. 411–413.  
DOI: [10.1103/PhysRev.108.411](https://doi.org/10.1103/PhysRev.108.411).
- [156] J. CUGNON, C. VOLANT, and S. VUILLIER. “Nucleon and deuteron induced spallation reactions.” In: *Nuclear Physics A* **625**(4) (Nov. 1997), pp. 729–757.  
DOI: [10.1016/S0375-9474\(97\)00602-7](https://doi.org/10.1016/S0375-9474(97)00602-7).

- [157] T. KAWANO, P. TALOU, I. STETCU, and M.B. CHADWICK. “Statistical and evaporation models for the neutron emission energy spectrum in the center-of-mass system from fission fragments.” In: *Nuclear Physics A* **913**(Supplement C) (Sept. 2013), pp. 51–70.  
DOI: [10.1016/j.nuclphysa.2013.05.020](https://doi.org/10.1016/j.nuclphysa.2013.05.020).
- [158] R.L. BRAMBLETT and T.W. BONNER. “Neutron evaporation spectra from (p, n) reactions.” In: *Nuclear Physics* **20**(Supplement C) (Nov. 1960), pp. 395–407.  
DOI: [10.1016/0029-5582\(60\)90182-6](https://doi.org/10.1016/0029-5582(60)90182-6).
- [159] T. SATO. “Analytical Model for Estimating the Zenith Angle Dependence of Terrestrial Cosmic Ray Fluxes.” In: *PLoS ONE* **11**(8) (Aug. 2016), pp. 1–22.  
DOI: [10.1371/journal.pone.0160390](https://doi.org/10.1371/journal.pone.0160390).
- [K2016] M. KÖHLI, F. ALLMENDINGER, W. HÄUSSLER, T. SCHRÖDER, M. KLEIN, M. MEVEN, and U. SCHMIDT. “Efficiency and spatial resolution of the CASCADE thermal neutron detector.” In: *Nuclear Instruments and Methods in Physics Research Section A: Accelerators, Spectrometers, Detectors and Associated Equipment* **828** (Aug. 2016), pp. 242–249.  
DOI: [10.1016/j.nima.2016.05.014](https://doi.org/10.1016/j.nima.2016.05.014).
- [160] J.F. ZIEGLER, M.D. ZIEGLER, and J.P. BIRSACK. “SRIM - The stopping and range of ions in matter (2010).” In: *Nuclear Instruments and Methods in Physics Research Section B: Beam Interactions with Materials and Atoms* **268**(11-12) (June 2010). 19<sup>th</sup> International Conference on Ion Beam Analysis, pp. 1818–1823.  
DOI: [10.1016/j.nimb.2010.02.091](https://doi.org/10.1016/j.nimb.2010.02.091).
- [161] K. NIKOLOPOULOS, P. BHATTACHARYA, V. CHERNYATIN, and R. VEENHOF. “Electron transparency of a Micromegas mesh.” In: *Journal of Instrumentation* **6**(06) (June 2011), P06011.  
DOI: [10.1088/1748-0221/6/06/P06011](https://doi.org/10.1088/1748-0221/6/06/P06011).
- [162] X. LLOPART, R. BALLABRIGA, M. CAMPBELL, L. TLUSTOS, and W. WONG. “Timepix, a 65k programmable pixel readout chip for arrival time, energy and/or photon counting measurements.” In: *Nuclear Instruments and Methods in Physics Research Section A: Accelerators, Spectrometers, Detectors and Associated Equipment* **581**(1–2) (Oct. 2007). VCI 2007, Proceedings of the 11<sup>th</sup> International Vienna Conference on Instrumentation, pp. 485–494.  
DOI: [10.1016/j.nima.2007.08.079](https://doi.org/10.1016/j.nima.2007.08.079).
- [163] R.S. CASWELL, R.F. GABBARD, D.W. PADGETT, and W.P. DOERING. “Attenuation of 14.1-Mev Neutrons in Water.” In: *Nuclear Science and Engineering* **2**(2) (Apr. 1957), pp. 143–159.  
DOI: [10.13182/NSE57-A25383](https://doi.org/10.13182/NSE57-A25383).
- [164] N.E. HERTEL and J.W. DAVIDSON. “The response of Bonner Spheres to neutrons from thermal energies to 17.3 MeV.” In: *Nuclear Instruments and Methods in Physics Research Section A: Accelerators, Spectrometers, Detectors and Associated Equipment* **238**(2) (Aug. 1985), pp. 509–516.  
DOI: [10.1016/0168-9002\(85\)90494-2](https://doi.org/10.1016/0168-9002(85)90494-2).
- [165] V. VYLET and A. KUMAR. “Energy response of Bonner Spheres to neutrons in parallel beam and point source geometries.” In: *Nuclear Instruments and Methods in Physics Research Section A: Accelerators, Spectrometers, Detectors and Associated Equipment* **271**(3) (Sept. 1988), pp. 607–610.  
DOI: [10.1016/0168-9002\(88\)90329-4](https://doi.org/10.1016/0168-9002(88)90329-4).
- [166] V. MARES and H. SCHRAUBE. “Evaluation of the response matrix of a Bonner Sphere Spectrometer with LiI detector from thermal energy to 100 MeV.” In: *Nuclear Instruments and Methods in Physics Research Section A: Accelerators, Spectrometers, Detectors and Associated Equipment* **337**(2) (Jan. 1994), pp. 461–473.  
DOI: [10.1016/0168-9002\(94\)91116-9](https://doi.org/10.1016/0168-9002(94)91116-9).
- [167] S. GARNY, V. MARES, and W. RÜHM. “Response functions of a Bonner Sphere Spectrometer calculated with GEANT4.” In: *Nuclear Instruments and Methods in Physics Research Section A: Accelerators, Spectrometers, Detectors and Associated Equipment* **604**(3) (June 2009), pp. 612–617.  
DOI: [10.1016/j.nima.2009.02.044](https://doi.org/10.1016/j.nima.2009.02.044).
- [168] A.W. DECKER, S.R. MCHALE, M.P. SHANNON, J.A. CLINTON, and J.W. MCCLORY. “Novel Bonner Sphere Spectrometer Response Functions Using MCNP6.” In: *IEEE Transactions on Nuclear Science* **62**(4) (Aug. 2015), pp. 1689–1694.  
DOI: [10.1109/TNS.2015.2416652](https://doi.org/10.1109/TNS.2015.2416652).

- [169] E.A. BURGETT, N.E. HERTEL, and R.M. HOWELL. “Energy Response and Angular Dependence of a Bonner Sphere Extension.” In: *IEEE Transactions on Nuclear Science* **56**(3) (June 2009), pp. 1325–1328.  
DOI: [10.1109/TNS.2009.2019272](https://doi.org/10.1109/TNS.2009.2019272).
- [170] V. MARES, G. SCHRAUBE, and H. SCHRAUBE. “Calculated neutron response of a Bonner Sphere Spectrometer with  $^3\text{He}$  counter.” In: *Nuclear Instruments and Methods in Physics Research Section A: Accelerators, Spectrometers, Detectors and Associated Equipment* **307**(2) (Oct. 1991), pp. 398–412.  
DOI: [10.1016/0168-9002\(91\)90210-H](https://doi.org/10.1016/0168-9002(91)90210-H).
- [171] M. YAMASHITA, L.D. STEPHENS, and H.W. PATTERSON. “Cosmic-ray-produced neutrons at ground level: Neutron production rate and flux distribution.” In: *Journal of Geophysical Research* **71**(16) (Aug. 1966), pp. 3817–3834.  
DOI: [10.1029/JZ071i016p03817](https://doi.org/10.1029/JZ071i016p03817).
- [172] J. SWEEZY, N. HERTEL, and K. VEINOT. “BUMS - Bonner Sphere Unfolding Made Simple: an HTML based multisphere neutron spectrometer unfolding package.” In: *Nuclear Instruments and Methods in Physics Research Section A: Accelerators, Spectrometers, Detectors and Associated Equipment* **476**(1) (Jan. 2002). International Workshop on Neutron Field Spectrometry in Science, Technology and Radiation Protection, pp. 263–269.  
DOI: [10.1016/S0168-9002\(01\)01466-8](https://doi.org/10.1016/S0168-9002(01)01466-8).
- [173] D.J. THOMAS and A.V. ALEVRA. “Bonner Sphere Spectrometers - a critical review.” In: *Nuclear Instruments and Methods in Physics Research Section A: Accelerators, Spectrometers, Detectors and Associated Equipment* **476**(1) (Jan. 2002). International Workshop on Neutron Field Spectrometry in Science, Technology and Radiation Protection, pp. 12–20.  
DOI: [10.1016/S0168-9002\(01\)01379-1](https://doi.org/10.1016/S0168-9002(01)01379-1).
- [174] H. SCHRAUBE, J. JAKES, A. SANNIKOV, E. WEITZENEGGER, S. ROESLER, and W. HEINRICH. “The Cosmic Ray Induced Neutron Spectrum at the Summit of the Zugspitze (2963 m).” In: *Radiation Protection Dosimetry* **70**(1-4) (Apr. 1997), pp. 405–408.  
DOI: [10.1093/oxfordjournals.rpd.a031986](https://doi.org/10.1093/oxfordjournals.rpd.a031986).
- [175] W. RÜHM, V. MARES, C. PIOCH, G. SIMMER, and E. WEITZENEGGER. “Continuous measurement of secondary neutrons from cosmic radiation at mountain altitudes and close to the north pole - a discussion in terms of  $H^*(10)$ .” In: *Radiation Protection Dosimetry* **136**(4) (Aug. 2009), pp. 256–261.  
DOI: [10.1093/rpd/ncp161](https://doi.org/10.1093/rpd/ncp161).
- [176] H.W. BERTINI. “Low-Energy Intranuclear Cascade Calculation.” In: *Physical Review* **131** (Aug. 1963), pp. 1801–1821.  
DOI: [10.1103/PhysRev.131.1801](https://doi.org/10.1103/PhysRev.131.1801).
- [177] A. HEIKKINEN, N. STEPANOV, and J.P. WELLISCH. “Bertini intranuclear cascade implementation in GEANT4.” In: *eConf C0303241* (June 2003). Proceedings, 13<sup>th</sup> International Conference on Computing in High-Energy and Nuclear Physics (CHEP 2003): La Jolla, California, March 24-28, 2003, MOMT008.  
URL: <http://www.slac.stanford.edu/econf/C0303241/proc/papers/MOMT008.PDF>.
- [178] G. FOLGER, V.N. IVANCHENKO, and J.P. WELLISCH. “The Binary Cascade.” In: *The European Physical Journal A - Hadrons and Nuclei* **21**(3) (Aug. 2004), pp. 407–417.  
DOI: [10.1140/epja/i2003-10219-7](https://doi.org/10.1140/epja/i2003-10219-7).
- [179] G. HUBERT, C.A. FEDERICO, M.T. PAZIANOTTO, and O.L. GONÇALES. “Long and short-term atmospheric radiation analyses based on coupled measurements at high altitude remote stations and extensive air shower modeling.” In: *Astroparticle Physics* **74** (Feb. 2016), pp. 27–36.  
DOI: [10.1016/j.astropartphys.2015.09.005](https://doi.org/10.1016/j.astropartphys.2015.09.005).
- [180] M.T. PAZIANOTTO, M.A. CORTÉS-GIRALDO, C.A. FEDERICO, G. HUBERT, O.L. GONÇALEZ, J.M. QUE-SADA, and B.V. CARLSON. “Extensive air shower Monte Carlo modeling at the ground and aircraft flight altitude in the South Atlantic Magnetic Anomaly and comparison with neutron measurements.” In: *Astroparticle Physics* **88** (Feb. 2017), pp. 17–29.  
DOI: [10.1016/j.astropartphys.2016.12.004](https://doi.org/10.1016/j.astropartphys.2016.12.004).



- [181] P. GOLDHAGEN, M. REGINATTO, T. KNISS, J.W. WILSON, R.C. SINGLETERRY, I.W. JONES, and W. VAN STEVENINCK. “Measurement of the energy spectrum of cosmic-ray induced neutrons aboard an ER-2 high-altitude airplane.” In: *Nuclear Instruments and Methods in Physics Research Section A: Accelerators, Spectrometers, Detectors and Associated Equipment* **476**(1–2) (Jan. 2002), pp. 42–51. DOI: [10.1016/S0168-9002\(01\)01386-9](https://doi.org/10.1016/S0168-9002(01)01386-9).
- [182] C.A. FEDERICO, O.L. GONÇALEZ, E.S. FONSECA, I.M. MARTIN, and L.V.E. CALDAS. “Neutron spectra measurements in the south Atlantic anomaly region.” In: *Radiation Measurements* **45**(10) (Dec. 2010). Proceedings of the 11<sup>th</sup> Symposium on neutron and ion dosimetry, pp. 1526–1528. DOI: [10.1016/j.radmeas.2010.06.038](https://doi.org/10.1016/j.radmeas.2010.06.038).
- [183] M.T. PAZIANOTTO, M.A. CORTÉS-GIRALDO, C.A. FEDERICO, O.L. GONÇALEZ, J.M. QUESADA, and B.V. CARLSON. “Determination of the cosmic-ray-induced neutron flux and ambient dose equivalent at flight altitude.” In: *Journal of Physics: Conference Series* **630**(1) (Apr. 2015), p. 012022. DOI: [10.1088/1742-6596/630/1/012022](https://doi.org/10.1088/1742-6596/630/1/012022).
- [SK2017b] M. SCHRÖN, S. ZACHARIAS, et al. “Intercomparison of Cosmic-Ray Neutron Sensors and Water Balance Monitoring in an Urban Environment.” In: *Geoscientific Instrumentation, Methods and Data Systems Discussions* **2017** (2017), pp. 1–24. DOI: [10.5194/gi-2017-34](https://doi.org/10.5194/gi-2017-34).
- [184] P. KOCHER, D. GENKIN, D. GRUSS, W. HAAS, M. HAMBURG, M. LIPP, S. MANGARD, T. PRESCHER, M. SCHWARZ, and Y. YAROM. *Spectre Attacks: Exploiting Speculative Execution*. Aug. 2018. arXiv: [1801.01203](https://arxiv.org/abs/1801.01203) [cs]. URL: <https://arxiv.org/abs/1801.01203>.
- [185] P.U. VILLARD. “Sur la réflexion et la réfraction des rayons cathodiques et des rayons déviables du radium.” In: *Comptes rendus hebdomadaires des séances de l'Académie des Sciences* **130** (Jan. 1900), pp. 1010–1012. URL: <https://gallica.bnf.fr/ark:/12148/bpt6k3086n/f1010.image.r=>.
- [186] T. WULF. “Über die in der Atmosphäre vorhandene Strahlung von hoher Durchdringungsfähigkeit.” In: *Physikalische Zeitschrift* **10**(5) (Mar. 1909), pp. 152–157.
- [187] A. GOCKEL. “Messungen der durchdringenden Strahlung bei Ballonfahrten.” In: *Physikalische Zeitschrift* **12**(14) (July 1911), pp. 595–597.
- [188] V.F. HESS. “Über die Absorption der  $\gamma$ -Strahlung in der Atmosphäre.” In: *Physikalische Zeitschrift* **12**(22) (Nov. 1911), pp. 998–1001.
- [189] A.H. COMPTON. “A Geographic Study of Cosmic Rays.” In: *Physical Review* **43** (Mar. 1933), pp. 387–403. DOI: [10.1103/PhysRev.43.387](https://doi.org/10.1103/PhysRev.43.387).
- [190] T.H. JOHNSON. “The Azimuthal Asymmetry of the Cosmic Radiation.” In: *Physical Review* **43** (May 1933), pp. 834–835. DOI: [10.1103/PhysRev.43.834](https://doi.org/10.1103/PhysRev.43.834).
- [191] H.J. BHABHA and W. HEITLER. “The Passage of Fast Electrons and the Theory of Cosmic Showers.” In: *Proceedings of the Royal Society of London A: Mathematical, Physical and Engineering Sciences* **159**(898) (Apr. 1937), pp. 432–458. DOI: [10.1098/rspa.1937.0082](https://doi.org/10.1098/rspa.1937.0082).
- [192] S.E. FORBUSH. “World-wide cosmic ray variations, 1937–1952.” In: *Journal of Geophysical Research* **59**(4) (Dec. 1954), pp. 525–542. DOI: [10.1029/JZ059i004p00525](https://doi.org/10.1029/JZ059i004p00525).
- [193] W. BAADE and F. ZWICKY. “Remarks on Super-Novae and Cosmic Rays.” In: *Physical Review* **46** (July 1934), pp. 76–77. DOI: [10.1103/PhysRev.46.76.2](https://doi.org/10.1103/PhysRev.46.76.2).
- [194] V. COCCONI-TONGIORGI. “Neutrons in the Extensive Air Showers of the Cosmic Radiation.” In: *Physical Review* **75** (May 1949), pp. 1532–1540. DOI: [10.1103/PhysRev.75.1532](https://doi.org/10.1103/PhysRev.75.1532).
- [195] J.A. SIMPSON and R.B. URETZ. “On the Latitude Dependence of Nuclear Disintegrations and Neutrons at 30,000 Feet.” In: *Physical Review* **76** (Aug. 1949), pp. 569–570. DOI: [10.1103/PhysRev.76.569](https://doi.org/10.1103/PhysRev.76.569).

- [196] J.A. SIMPSON. “The Cosmic Ray Nucleonic Component: The Invention and Scientific Uses of the Neutron Monitor - (Keynote Lecture).” In: *Space Science Reviews* **93**(1) (July 2000), pp. 11–32. DOI: [10.1023/A:1026567706183](https://doi.org/10.1023/A:1026567706183).
- [197] H. VEREECKEN, J.A. HUISMAN, H. BOGENA, J. VANDERBORGHT, J.A. VRUGT, and J.W. HOPMANS. “On the value of soil moisture measurements in vadose zone hydrology: A review.” In: *Water Resources Research* **44**(4) (Apr. 2008), W00D06. DOI: [10.1029/2008WR006829](https://doi.org/10.1029/2008WR006829).
- [198] D.A. ROBINSON, C.S. CAMPBELL, J.W. HOPMANS, B.K. HORNBuckle, S.B. JONES, R. KNIGHT, F. OGDEN, J. SELKER, and O. WENDROTH. “Soil Moisture Measurement for Ecological and Hydrological Watershed-Scale Observatories: A Review.” In: *Vadose Zone Journal* **7**(1) (Feb. 2008), pp. 358–389. DOI: [10.2136/vzj2007.0143](https://doi.org/10.2136/vzj2007.0143).
- [199] J.D. RHOADES, P.A.C. RAATS, and R.J. PRATHER. “Effects of Liquid-phase Electrical Conductivity, Water Content, and Surface Conductivity on Bulk Soil Electrical Conductivity.” In: *Soil Science Society of America Journal* **40**(5) (Apr. 1976), pp. 651–655. DOI: [10.2136/sssaj1976.03615995004000050017x](https://doi.org/10.2136/sssaj1976.03615995004000050017x).
- [200] T.J. DEAN, J.P. BELL, and A.J.B. BATY. “Soil moisture measurement by an improved capacitance technique, Part I. Sensor design and performance.” In: *Journal of Hydrology* **93**(1) (Feb. 1987), pp. 67–78. DOI: [10.1016/0022-1694\(87\)90194-6](https://doi.org/10.1016/0022-1694(87)90194-6).
- [201] G.C. TOPP, J.L. DAVIS, and A.P. ANNAN. “Electromagnetic determination of soil water content: Measurements in coaxial transmission lines.” In: *Water Resources Research* **16**(3) (June 1980), pp. 574–582. DOI: [10.1029/WR016i003p00574](https://doi.org/10.1029/WR016i003p00574).
- [202] R. KNIGHT. “Ground Penetrating Radar for Environmental Applications.” In: *Annual Review of Earth and Planetary Sciences* **29**(1) (May 2001), pp. 229–255. DOI: [10.1146/annurev.earth.29.1.229](https://doi.org/10.1146/annurev.earth.29.1.229).
- [203] E. DE JONG, A.K. BALLANTYNE, D.R. CAMERON, and D.W.L. READ. “Measurement of Apparent Electrical Conductivity of Soils by an Electromagnetic Induction Probe to Aid Salinity Surveys.” In: *Soil Science Society of America Journal* **43**(4) (Mar. 1979), pp. 810–812. DOI: [10.2136/sssaj1979.03615995004300040040x](https://doi.org/10.2136/sssaj1979.03615995004300040040x).
- [204] B. MAJONE, F. VIANI, E. FILIPPI, A. BELLIN, A. MASSA, G. TOLLER, F. ROBOL, and M. SALUCCI. “Wireless Sensor Network Deployment for Monitoring Soil Moisture Dynamics at the Field Scale.” In: *Procedia Environmental Sciences* **19** (July 2013). Four Decades of Progress in Monitoring and Modeling of Processes in the Soil-Plant-Atmosphere System: Applications and Challenges, pp. 426–435. DOI: [10.1016/j.proenv.2013.06.049](https://doi.org/10.1016/j.proenv.2013.06.049).
- [205] C.A. LAYMON, W.L. CROSSON, T.J. JACKSON, A. MANU, and T.D. TSEGAYE. “Ground-based passive microwave remote sensing observations of soil moisture at S-band and L-band with insight into measurement accuracy.” In: *IEEE Transactions on Geoscience and Remote Sensing* **39**(9) (Sept. 2001), pp. 1844–1858. DOI: [10.1109/36.951075](https://doi.org/10.1109/36.951075).
- [206] J.R. EAGLEMAN and W.C. LIN. “Remote sensing of soil moisture by a 21-cm passive radiometer.” In: *Journal of Geophysical Research* **81**(21) (July 1976), pp. 3660–3666. DOI: [10.1029/JC081i021p03660](https://doi.org/10.1029/JC081i021p03660).
- [207] I. MANAKOS and S. LAVENDER. “Remote Sensing in Support of the Geo-information in Europe.” In: *Land Use and Land Cover Mapping in Europe: Practices & Trends*. Ed. by I. MANAKOS and M. BRAUN. Dordrecht: Springer Netherlands, Jan. 2014, pp. 3–10. ISBN: 978-94-007-7969-3. DOI: [10.1007/978-94-007-7969-3\\_1](https://doi.org/10.1007/978-94-007-7969-3_1).
- [208] D. GEUDTNER, R. TORRES, P. SNOEIJ, M. DAVIDSON, and B. ROMMEN. “Sentinel-1 System capabilities and applications.” In: *2014 IEEE Geoscience and Remote Sensing Symposium*. July 2014, pp. 1457–1460. DOI: [10.1109/IGARSS.2014.6946711](https://doi.org/10.1109/IGARSS.2014.6946711).

- [209] F.D. VAN DER MEER, H.M.A. VAN DER WERFF, and F.J.A. VAN RUITENBEEK. “Potential of ESA’s Sentinel-2 for geological applications.” In: *Remote Sensing of Environment* **148** (May 2014), pp. 124–133.  
DOI: [10.1016/j.rse.2014.03.022](https://doi.org/10.1016/j.rse.2014.03.022).
- [210] B. WOLTER and M. KRUS. “Moisture Measuring with Nuclear Magnetic Resonance (NMR).” In: *Electromagnetic Aquametry: Electromagnetic Wave Interaction with Water and Moist Substances*. Ed. by K. KUPFER. Berlin, Heidelberg: Springer Berlin Heidelberg, 2005, pp. 491–515. ISBN: 978-3-540-26491-0.  
DOI: [10.1007/3-540-26491-4\\_21](https://doi.org/10.1007/3-540-26491-4_21).
- [211] D.R. POOL and J.H. EYCHANER. “Measurements of Aquifer-Storage Change and Specific Yield Using Gravity Surveys.” In: *Ground Water* **33**(3) (Aug. 1995), pp. 425–432.  
DOI: [10.1111/j.1745-6584.1995.tb00299.x](https://doi.org/10.1111/j.1745-6584.1995.tb00299.x).
- [212] F. KOCH, F. SCHLENZ, M. PRASCH, F. APPEL, T. RUF, and W. MAUSER. “Soil Moisture Retrieval Based on GPS Signal Strength Attenuation.” In: *Water* **8**(7) (July 2016), pp. 1–22.  
DOI: [10.3390/w8070276](https://doi.org/10.3390/w8070276).
- [213] I.F. LONG and B.K. FRENCH. “Measurement of Soil Moisture in the Field by Neutron Moderation.” In: *Journal of Soil Science* **18**(1) (Mar. 1967), pp. 149–166.  
DOI: [10.1111/j.1365-2389.1967.tb01496.x](https://doi.org/10.1111/j.1365-2389.1967.tb01496.x).
- [214] M. QUINTA-FERREIRA, J.F. DIAS, and S. ALIJA. “False low water content in road field compaction control using nuclear gauges: a case study.” In: *Environmental Earth Sciences* **75**(14) (July 2016), p. 1114.  
DOI: [10.1007/s12665-016-5901-1](https://doi.org/10.1007/s12665-016-5901-1).
- [215] D.V. ELLIS and J.M. SINGER. “Basic Neutron Physics for Logging Applications.” In: *Well Logging for Earth Scientists*. Dordrecht: Springer Netherlands, 2007, pp. 325–349. ISBN: 978-1-4020-4602-5.  
DOI: [10.1007/978-1-4020-4602-5\\_13](https://doi.org/10.1007/978-1-4020-4602-5_13).
- [216] D. DESILETS, M. ZREDA, and T.P.A. FERRÉ. “Nature’s neutron probe: Land surface hydrology at an elusive scale with cosmic rays.” In: *Water Resources Research* **46**(11) (Nov. 2010), W11505.  
DOI: [10.1029/2009WR008726](https://doi.org/10.1029/2009WR008726).
- [217] T.E. FRANZ, T. WANG, W. AVERY, C. FINKENBINER, and L. BROCCA. “Combined analysis of soil moisture measurements from roving and fixed cosmic ray neutron probes for multiscale real-time monitoring.” In: *Geophysical Research Letters* **42**(9) (May 2015), pp. 3389–3396.  
DOI: [10.1002/2015gl063963](https://doi.org/10.1002/2015gl063963).
- [218] M. ZREDA, W.J. SHUTTLEWORTH, X. ZENG, C. ZWECK, D. DESILETS, T.E. FRANZ, and R. ROSOLEM. “COSMOS: The COsmic-ray Soil Moisture Observing System.” In: *Hydrology and Earth System Sciences* **16**(11) (Nov. 2012), pp. 4079–4099.  
DOI: [10.5194/hess-16-4079-2012](https://doi.org/10.5194/hess-16-4079-2012).
- [219] B. CHRISMAN and M. ZREDA. “Quantifying mesoscale soil moisture with the cosmic-ray rover.” In: *Hydrology and Earth System Sciences* **17**(12) (Dec. 2013), pp. 5097–5108.  
DOI: [10.5194/hess-17-5097-2013](https://doi.org/10.5194/hess-17-5097-2013).
- [KS2018] M. KÖHLI, M. SCHRÖN, and U. SCHMIDT. “Response functions for detectors in cosmic ray neutron sensing.” In: *Nuclear Instruments and Methods in Physics Research Section A: Accelerators, Spectrometers, Detectors and Associated Equipment* **902** (Sept. 2018), pp. 184–189.  
DOI: [10.1016/j.nima.2018.06.052](https://doi.org/10.1016/j.nima.2018.06.052).
- [220] H.R. BOGENA, J.A. HUISMAN, R. BAATZ, H.-J. HENDRICKS-FRANSSSEN, and H. VEREECKEN. “Accuracy of the cosmic-ray soil water content probe in humid forest ecosystems: The worst case scenario.” In: *Water Resources Research* **49**(9) (Sept. 2013), pp. 5778–5791.  
DOI: [10.1002/wrcr.20463](https://doi.org/10.1002/wrcr.20463).
- [221] M. SCHRÖN. “Cosmic-ray neutron sensing and its applications to soil and land surface hydrology.” PhD thesis. University of Potsdam, June 2017. 226 pp. ISBN: 978-3-8439-3139-7.  
URL: <https://nbn-resolving.org/urn:nbn:de:kobv:517-opus4-395433>.
- [222] D. DESILETS, M. ZREDA, and T. PRABU. “Extended scaling factors for in situ cosmogenic nuclides: new measurements at low latitude.” In: *Earth and Planetary Science Letters* **246**(3–4) (June 2006), pp. 265–276.  
DOI: [10.1016/j.epsl.2006.03.051](https://doi.org/10.1016/j.epsl.2006.03.051).

- [223] D. DESILETS and M. ZREDA. “On scaling cosmogenic nuclide production rates for altitude and latitude using cosmic-ray measurements.” In: *Earth and Planetary Science Letters* **193**(1–2) (Nov. 2001), pp. 213–225.  
DOI: [10.1016/S0012-821X\(01\)00477-0](https://doi.org/10.1016/S0012-821X(01)00477-0).
- [224] C. ZWECK, M. ZREDA, and D. DESILETS. “Snow shielding factors for cosmogenic nuclide dating inferred from Monte Carlo neutron transport simulations.” In: *Earth and Planetary Science Letters* **379** (Aug. 2013), pp. 64–71.  
DOI: [10.1016/j.epsl.2013.07.023](https://doi.org/10.1016/j.epsl.2013.07.023).
- [225] N. LIFTON, T. SATO, and T.J. DUNAI. “Scaling in situ cosmogenic nuclide production rates using analytical approximations to atmospheric cosmic-ray fluxes.” In: *Earth and Planetary Science Letters* **386**(0) (Jan. 2014), pp. 149–160.  
DOI: [10.1016/j.epsl.2013.10.052](https://doi.org/10.1016/j.epsl.2013.10.052).
- [226] J.F. ZIEGLER. “Terrestrial cosmic ray intensities.” In: *IBM Journal of Research and Development* **42**(1) (Jan. 1998), pp. 117–140.  
DOI: [10.1147/rd.421.0117](https://doi.org/10.1147/rd.421.0117).
- [227] R. ROSOLEM, W.J. SHUTTLEWORTH, M. ZREDA, T.E. FRANZ, X. ZENG, and S.A. KURC. “The Effect of Atmospheric Water Vapor on Neutron Count in the Cosmic-Ray Soil Moisture Observing System.” In: *Journal of Hydrometeorology* **14**(5) (Oct. 2013), pp. 1659–1671.  
DOI: [10.1175/JHM-D-12-0120.1](https://doi.org/10.1175/JHM-D-12-0120.1).
- [228] C.A. RIVERA VILLARREYES, G. BARONI, and S.E. OSWALD. “Integral quantification of seasonal soil moisture changes in farmland by cosmic-ray neutrons.” In: *Hydrology and Earth System Sciences* **15**(12) (Dec. 2011), pp. 3843–3859.  
DOI: [10.5194/hess-15-3843-2011](https://doi.org/10.5194/hess-15-3843-2011).
- [229] L. LV, T.E. FRANZ, D.A. ROBINSON, and S.B. JONES. “Measured and Modeled Soil Moisture Compared with Cosmic-Ray Neutron Probe Estimates in a Mixed Forest.” In: *Vadose Zone Journal* **13**(12) (Dec. 2014).  
DOI: [10.2136/vzj2014.06.0077](https://doi.org/10.2136/vzj2014.06.0077).
- [230] J. IWEMA, R. ROSOLEM, R. BAATZ, T. WAGENER, and H.R. BOGENA. “Investigating temporal field sampling strategies for site-specific calibration of three soil moisture–neutron intensity parameterisation methods.” In: *Hydrology and Earth System Sciences* **19**(7) (July 2015), pp. 3203–3216.  
DOI: [10.5194/hess-19-3203-2015](https://doi.org/10.5194/hess-19-3203-2015).
- [231] J.M. CLEM and L.I. DORMAN. “Neutron Monitor Response Functions.” In: *Space Science Review* **93**(1) (July 2000), pp. 335–359.  
DOI: [10.1023/A:1026508915269](https://doi.org/10.1023/A:1026508915269).
- [232] H. KRÜGER, H. MORAAL, J.W. BIEBER, J.M. CLEM, P.A. EVENSON, K.R. PYLE, M.L. DULDIG, and J.E. HUMBLE. “A calibration neutron monitor: Energy response and instrumental temperature sensitivity.” In: *Journal of Geophysical Research: Space Physics* **113**(A8) (Aug. 2008). A08101.  
DOI: [10.1029/2008JA013229](https://doi.org/10.1029/2008JA013229).
- [233] C. PIOCH, V. MARES, and W. RÜHM. “Influence of Bonner Sphere response functions above 20 MeV on unfolded neutron spectra and doses.” In: *Radiation Measurements* **45**(10) (May 2010), pp. 1263–1267.  
DOI: [10.1016/j.radmeas.2010.05.007](https://doi.org/10.1016/j.radmeas.2010.05.007).
- [234] J.C. WAGNER, D.E. PELOW, and S.W. MOSHER. “FW-CADIS Method for Global and Regional Variance Reduction of Monte Carlo Radiation Transport Calculations.” In: *Nuclear Science and Engineering* **176**(1) (Jan. 2014), pp. 37–57.  
DOI: [10.13182/NSE12-33](https://doi.org/10.13182/NSE12-33).
- [235] A. HAGHIGHAT and J.C. WAGNER. “Monte Carlo variance reduction with deterministic importance functions.” In: *Progress in Nuclear Energy* **42**(1) (Jan. 2003), pp. 25–53.  
DOI: [10.1016/S0149-1970\(02\)00002-1](https://doi.org/10.1016/S0149-1970(02)00002-1).
- [236] D. DESILETS. *CRS1000 and CRS1000/B User’s Guide*. Report. Cosmic-Ray Soil Moisture/Snow Sensing System. Hydroinnova. Albuquerque, USA, Apr. 2013. 48 pp.  
URL: [http://hydroinnova.com/\\_downloads/CRS-1000\\_complete.pdf](http://hydroinnova.com/_downloads/CRS-1000_complete.pdf).

- [237] D.S. MCGREGOR and J.K. SHULTIS. “Reporting detection efficiency for semiconductor neutron detectors: A need for a standard.” In: *Nuclear Instruments and Methods in Physics Research Section A: Accelerators, Spectrometers, Detectors and Associated Equipment* **632**(1) (Mar. 2011), pp. 167–174.  
DOI: [10.1016/j.nima.2010.12.084](https://doi.org/10.1016/j.nima.2010.12.084).
- [238] D. MCJANNET, T.E. FRANZ, A. HAWDON, D. BOADLE, B. BAKER, A. ALMEIDA, R. SILBERSTEIN, T. LAMBERT, and D. DESILETS. “Field testing of the universal calibration function for determination of soil moisture with cosmic-ray neutrons.” In: *Water Resources Research* **50**(6) (June 2014), pp. 5235–5248.  
DOI: [10.1002/2014WR015513](https://doi.org/10.1002/2014WR015513).
- [239] M. ANDREASEN, H. KARSTEN JENSEN, M. ZREDA, D. DESILETS, H. BOGENA, and C.M. LOOMS. “Modeling cosmic ray neutron field measurements.” In: *Water Resources Research* **52**(8) (2016), pp. 6451–6471.  
DOI: [10.1002/2015wr018236](https://doi.org/10.1002/2015wr018236).
- [240] P. SCHATTA, G. BARONI, S.E. OSWALD, J. SCHÖBER, C. FEY, C. KORMANN, M. HUTTENLAU, and S. ACHLEITNER. “Continuous monitoring of snowpack dynamics in alpine terrain by aboveground neutron sensing.” In: *Water Resources Research* **53**(5) (May 2017), pp. 3615–3634.  
DOI: [10.1002/2016WR020234](https://doi.org/10.1002/2016WR020234).
- [KS2015] M. KÖHLI, M. SCHRÖN, M. ZREDA, U. SCHMIDT, P. DIETRICH, and S. ZACHARIAS. “Footprint characteristics revised for field-scale soil moisture monitoring with cosmic-ray neutrons.” In: *Water Resources Research* **51**(7) (July 2015), pp. 5772–5790.  
DOI: [10.1002/2015WR017169](https://doi.org/10.1002/2015WR017169).
- [SK2017] M. SCHRÖN, M. KÖHLI, et al. “Improving Calibration and Validation of Cosmic-Ray Neutron Sensors in the Light of Spatial Sensitivity.” In: *Hydrology and Earth System Sciences* **21**(10) (Oct. 2017), pp. 5009–5030.  
DOI: [10.5194/hess-21-5009-2017](https://doi.org/10.5194/hess-21-5009-2017).
- [241] A. NESTERENOK. “Numerical calculations of cosmic ray cascade in the Earth’s atmosphere - Results for nucleon spectra.” In: *Nuclear Instruments and Methods in Physics Research B* **295** (Jan. 2013), pp. 99–106.  
DOI: [10.1016/j.nimb.2012.11.005](https://doi.org/10.1016/j.nimb.2012.11.005).
- [242] A. NESTERENOK. personal communication. 2013.
- [243] T.E. FRANZ, M. ZREDA, T.P.A. FERRÉ, and R. ROSELEM. “An assessment of the effect of horizontal soil moisture heterogeneity on the area-average measurement of cosmic-ray neutrons.” In: *Water Resources Research* **49**(10) (Oct. 2013), pp. 6450–6458.  
DOI: [10.1002/wrcr.20530](https://doi.org/10.1002/wrcr.20530).
- [244] Z.W. LIN, J.H. ADAMS JR., A.F. BARGHOUTY, S.D. RANDENIYA, R.K. TRIPATHI, J.W. WATTS, and P.P. YEPES. “Comparisons of several transport models in their predictions in typical space radiation environments.” In: *Advances in Space Research* **49**(4) (Feb. 2012), pp. 797–806.  
DOI: [10.1016/j.asr.2011.11.025](https://doi.org/10.1016/j.asr.2011.11.025).
- [245] F. LEI, A. HANDS, S. CLUCAS, C. DYER, and P. TRUSCOTT. “Improvements to and Validations of the QinetiQ Atmospheric Radiation Model (QARM).” In: *IEEE Transactions on Nuclear Science* **53**(4) (Aug. 2006), pp. 1851–1858.  
DOI: [10.1109/TNS.2006.880567](https://doi.org/10.1109/TNS.2006.880567).
- [246] R.J. SHEU and S.H. JIANG. “Cosmic-ray-induced neutron spectra and effective dose rates near air/ground and air/water interfaces in Taiwan.” In: *Health Physics* **84**(1) (Jan. 2003), pp. 92–99.  
DOI: [10.1097/00004032-200301000-00008](https://doi.org/10.1097/00004032-200301000-00008).
- [247] S. BARROS, V. MARES, R. BEDOGNI, M. REGINATTO, A. ESPOSITO, I. F. GONÇALVES, P. VAZ, and W. RÜHM. “Comparison of unfolding codes for neutron spectrometry with Bonner Spheres.” In: *Radiation Protection Dosimetry* **161**(1-4) (Jan. 2014), pp. 46–52.  
DOI: [10.1093/rpd/nct353](https://doi.org/10.1093/rpd/nct353).
- [248] K.-W. LEE, M.-C. YUAN, S.-H. JIANG, and R.-J. SHEU. “Comparing standard Bonner Spheres and high-sensitivity Bonner cylinders.” In: *Radiation Protection Dosimetry* **161**(1-4) (Dec. 2014), pp. 233–236.  
DOI: [10.1093/rpd/nct333](https://doi.org/10.1093/rpd/nct333).

- [249] D.J. THOMAS, N.P. HAWKES, L.N. JONES, P. KOLKOWSKI, and N.J. ROBERTS. “Characterization and utilization of a Bonner Sphere set based on gold activation foils.” In: *Radiation Protection Dosimetry* **126**(1–4) (May 2007), pp. 229–233.  
DOI: [10.1093/rpd/ncm047](https://doi.org/10.1093/rpd/ncm047).
- [250] W. RÜHM, V. MARES, C. PIOCH, S. AGOSTEO, A. ENDO, M. FERRARINI, I. RAKHNO, S. ROLLET, D. SATOH, and H. VINCKE. “Comparison of Bonner Sphere responses calculated by different Monte Carlo codes at energies between 1 MeV and 1 GeV - Potential impact on neutron dosimetry at energies higher than 20 MeV.” In: *Radiation Measurements* **67**(0) (May 2014), pp. 24–34.  
DOI: [10.1016/j.radmeas.2014.05.006](https://doi.org/10.1016/j.radmeas.2014.05.006).
- [251] T. SATO. “Analytical Model for Estimating the Zenith Angle Dependence of Terrestrial Cosmic Ray Fluxes.” In: *PLOS ONE* **11**(8) (Aug. 2016), pp. 1–22.  
DOI: [10.1371/journal.pone.0160390](https://doi.org/10.1371/journal.pone.0160390).
- [252] M. ZREDA, D. DESILETS, T.P.A. FERRÉ, and R.L. SCOTT. “Measuring soil moisture content non-invasively at intermediate spatial scale using cosmic-ray neutrons.” In: *Geophysical Research Letters* **35**(21) (Nov. 2008), p. L21402.  
DOI: [10.1029/2008GL035655](https://doi.org/10.1029/2008GL035655).
- [253] D. DESILETS and M. ZREDA. “Footprint diameter for a cosmic-ray soil moisture probe: Theory and Monte Carlo simulations.” In: *Water Resources Research* **49**(6) (June 2013), pp. 3566–3575.  
DOI: [10.1002/wrcr.20187](https://doi.org/10.1002/wrcr.20187).
- [254] B.M. KUZHEVSKIY, O.Y. NECHAEV, E.A. SIGAEVA, and V.A. ZAKHAROV. “Neutron flux variations near the Earth’s crust. A possible tectonic activity detection.” In: *Natural Hazards and Earth System Science* **3**(6) (Jan. 2003), pp. 637–645.  
DOI: [10.5194/nhess-3-637-2003](https://doi.org/10.5194/nhess-3-637-2003).
- [255] S. GLASSTONE and M.C. EDLUND. *The Elements of Nuclear Reactor Theory*. New Jersey and New York: D. Van Nostrand Company, Nov. 1952. 416 pp.  
URL: <https://babel.hathitrust.org/cgi/pt?id=mdp.39015026517386;view=1up;seq=1>.
- [256] L.M. BARKOV, V.K. MAKARIN, and K.N. MUKHIN. “Measurement of the slowing down of neutrons in the energy range 1.46–0.025 eV in water.” In: *Journal of Nuclear Energy (1954)* **4**(1) (Oct. 1957), pp. 94–102.  
DOI: [10.1016/0891-3919\(57\)90124-9](https://doi.org/10.1016/0891-3919(57)90124-9).
- [257] N.E. HERTEL and J.W. DAVIDSON. “The response of Bonner Spheres to neutrons from thermal energies to 17.3 MeV.” In: *Nuclear Instruments and Methods in Physics Research A* **238** (Aug. 1985), pp. 509–516.  
DOI: [10.1016/0168-9002\(85\)90494-2](https://doi.org/10.1016/0168-9002(85)90494-2).
- [258] R.T. KOUZES, E.R. SICILIANO, J.H. ELY, P.E. KELLER, and R.J. MCCONN. “Passive neutron detection for interdiction of nuclear material at borders.” In: *Nuclear Instruments and Methods in Physics Research Section A: Accelerators, Spectrometers, Detectors and Associated Equipment* **584**(2–3) (Jan. 2008), pp. 383–400.  
DOI: [10.1016/j.nima.2007.10.026](https://doi.org/10.1016/j.nima.2007.10.026).
- [259] T.E. FRANZ, M. ZREDA, T.P.A. FERRÉ, R. ROSOLEM, C. ZWECK, S. STILLMAN, X. ZENG, and W.J. SHUTTLEWORTH. “Measurement depth of the cosmic ray soil moisture probe affected by hydrogen from various sources.” In: *Water Resources Research* **48**(8) (Aug. 2012).  
DOI: [10.1029/2012WR011871](https://doi.org/10.1029/2012WR011871).
- [260] L.D. HENDRICK and R.D. EDGE. “Cosmic-Ray Neutrons near the Earth.” In: *Physical Review* **145** (May 1966), pp. 1023–1025.  
DOI: [10.1103/PhysRev.145.1023](https://doi.org/10.1103/PhysRev.145.1023).
- [261] R.C. ELPHIC, P. CHU, S. HAHN, M.R. JAMES, D.J. LAWRENCE, T.H. PRETTYMAN, J.B. JOHNSON, and R.K. PODGORNEY. “Surface and downhole prospecting tools for planetary exploration: tests of neutron and gamma ray probes.” In: *Astrobiology* **8**(3) (Aug. 2008), pp. 639–652.  
DOI: [10.1089/ast.2007.0163](https://doi.org/10.1089/ast.2007.0163).
- [262] G.W. MCKINNEY, D.J. LAWRENCE, T.H. PRETTYMAN, R.C. ELPHIC, W.C. FELDMAN, and J.J. HAGERTY. “MCNPX benchmark for cosmic ray interactions with the Moon.” In: *Journal of Geophysical Research: Planets* **111**(E6) (June 2006), E06004.  
DOI: [10.1029/2005JE002551](https://doi.org/10.1029/2005JE002551).

- [263] W. KORRES, T.G. REICHENAU, et al. “Spatio-temporal soil moisture patterns - A meta-analysis using plot to catchment scale data.” In: *Journal of Hydrology* **520**(0) (Jan. 2015), pp. 326–341.  
DOI: [10.1016/j.jhydrol.2014.11.042](https://doi.org/10.1016/j.jhydrol.2014.11.042).
- [SK2018] M. SCHRÖN, R. ROSOLEM, et al. “Cosmic-ray Neutron Rover Surveys of Field Soil Moisture and the Influence of Roads.” In: *Water Resources Research* **54**(9) (May 2018), pp. 6441–6459.  
DOI: [10.1029/2017WR021719](https://doi.org/10.1029/2017WR021719).
- [K2016b] M. KÖHLI, M. KLEIN, F. ALLMENDINGER, A.-K. PERREVOORT, T. SCHRÖDER, N. MARTIN, C.J. SCHMIDT, and U. SCHMIDT. “CASCADE - a multi-layer Boron-10 neutron detection system.” In: *Journal of Physics: Conference Series* **746**(1) (Sept. 2016), p. 012003.  
DOI: [10.1088/1742-6596/746/1/012003](https://doi.org/10.1088/1742-6596/746/1/012003).
- [264] M. HENSKE, M. KLEIN, M. KÖHLI, P. LENNERT, G. MODZEL, C.J. SCHMIDT, and U. SCHMIDT. “The  $^{10}\text{B}$  based Jalousie neutron detector: An alternative for  $^3\text{He}$  filled position sensitive counter tubes.” In: *Nuclear Instruments and Methods in Physics Research Section A: Accelerators, Spectrometers, Detectors and Associated Equipment* **686** (Sept. 2012), pp. 151–155.  
DOI: [10.1016/j.nima.2012.05.075](https://doi.org/10.1016/j.nima.2012.05.075).
- [265] G. MODZEL, M. HENSKE, A. HOUBEN, M. KLEIN, M. KÖHLI, P. LENNERT, M. MEVEN, C.J. SCHMIDT, U. SCHMIDT, and W. SCHWEIKA. “Absolute efficiency measurements with the  $^{10}\text{B}$  based Jalousie detector.” In: *Nuclear Instruments and Methods in Physics Research Section A: Accelerators, Spectrometers, Detectors and Associated Equipment* **743** (Apr. 2014), pp. 90–95.  
DOI: [10.1016/j.nima.2014.01.007](https://doi.org/10.1016/j.nima.2014.01.007).
- [SK2015] M. SCHRÖN, S.ZACHARIAS, M. KÖHLI, J. WEIMAR, and P. DIETRICH. “Monitoring Environmental Water with Ground Albedo Neutrons and Correction for Incoming Cosmic Rays with Neutron Monitor Data.” In: *PoS Proceedings of Science* **231** (Aug. 2015). The 34<sup>th</sup> International Cosmic Ray Conference, pp. 101–104.  
DOI: [10.1063/1.2825756](https://doi.org/10.1063/1.2825756).
- [284] I. MAUCH. “Aufbau eines Praktikumsversuchs und neutronenphysikalische Experimente.” Staatsexamen. Physikalisches Institut, Heidelberg University, 1998. 46 pp.
- [285] F. JAMES. *MINUIT - Function Minimization and Error Analysis*. Manual. D506. CERN. Geneva, Switzerland, Mar. 1994. 56 pp.  
URL: <https://root.cern.ch/sites/d35c7d8c.web.cern.ch/files/minuit.pdf>.





## ADDENDUM

---

B.1.1 | GEOMETRICAL CALCULATIONS

The following calculations are based on the mixed geometry definition of cartesian support and spherical direction vectors

$$\vec{x} = \begin{pmatrix} x \\ y \\ z \end{pmatrix} \quad \text{and} \quad \vec{r} = \begin{pmatrix} r \\ \vartheta \\ \phi \end{pmatrix}.$$

B.1.1.1 DISTANCE TO A VERTICAL LINE

Assuming a vertical line  $L$  through point  $\vec{P} = (x_P, y_P, z_P)$  one can define regarding  $\vec{x}$  the following quantities

$$\begin{aligned} n_x &= \sin(\vartheta) \sin(\phi), \\ n_y &= -\sin(\vartheta) \cos(\phi) \end{aligned} \tag{156}$$

and hence the distance to the line  $d_L$  is calculated by

$$d_L = \frac{\|(x - x_P)n_x + (y - y_P)n_y\|}{\sqrt{n_x^2 + n_y^2}}. \tag{157}$$

B.1.1.2 DISTANCE TO A POINT

Assuming the point  $\vec{P}$  has the coordinates  $(x_P, y_P, z_P)$  one can define regarding  $\vec{x}$  the following quantities

$$\begin{aligned} g_x &= \sin(\vartheta) \cos(\phi), \\ g_y &= \sin(\vartheta) \sin(\phi), \\ g_z &= \cos(\vartheta), \\ k_{rx} &= g_y(z - z_P) - g_z(y - y_P), \\ k_{ry} &= g_z(x - x_P) - g_x(z - z_P), \\ k_{rz} &= g_x(y - y_P) - g_y(x - x_P), \end{aligned} \tag{158}$$

and hence the distance to the point  $d_P$  is calculated by

$$d_P = \frac{\sqrt{k_{rx}^2 + k_{ry}^2 + k_{rz}^2}}{\sqrt{g_x^2 + g_y^2 + g_z^2}}. \tag{159}$$

The database of URANOS materials relies on a library of predefined elements. Such are described by ENDF cards, which are extracted from the existing sources mentioned in chapter 5.1.4 and stored individually. The following tab. 14 is a comprehensive list of isotopes, which have been selected and implemented.

Isotope	Elastic	Inelastic	Absorption and others
<sup>1</sup> H	MT=2 (MF=3, 4)	n/A	MT=5, 102, 208-210
<sup>3</sup> He	MT=2 (MF=3, 4)	n/A	MT=102, 103, 104
<sup>10</sup> B	MT=2 (MF=3, 4)	MT=51-54	MT=107
<sup>11</sup> B	MT=2 (MF=3, 4)	MT=51-54	MT=107
<sup>12</sup> C	MT=2 (MF=3, 4)	MT=51-58	MT=5, 102, 103, 107
<sup>14</sup> N	MT=2 (MF=3, 4)	MT=51-60	MT=5, 102-108, 208-210
<sup>16</sup> O	MT=2 (MF=3, 4)	MT=51-70	MT=5, 102, 103, 105, 107, 208-210
<sup>19</sup> F	MT=2 (MF=3, 4)	MT=51-54	MT=102, 103, 107
<sup>23</sup> Na	MT=2 (MF=3, 4)	MT=51-56	MT=5, 102, 103, 107
<sup>27</sup> Al	MT=2 (MF=3, 4)	MT=51-58	MT=5, 102, 103, 107, 208-210
<sup>28</sup> Si	MT=2 (MF=3, 4)	MT=51-58	MT=5, 102, 103, 107, 208-210
<sup>32</sup> S	MT=2 (MF=3, 4)	MT=51-55	MT=5, 102, 103, 107
<sup>35</sup> Cl	MT=2 (MF=3, 4)	MT=51-56	MT=5, 102, 103, 107
<sup>40</sup> Ar	MT=2 (MF=3, 4)	MT=51-55	MT=5, 102, 103, 107, 208-210
<sup>52</sup> Cr	MT=2 (MF=3, 4)	MT=51-55	MT=5, 102, 103, 107
<sup>53</sup> Cr	MT=2 (MF=3, 4)	MT=51-55	MT=5, 102, 103, 107
<sup>56</sup> Fe	MT=2 (MF=3, 4)	MT=51-58	MT=5, 102, 103, 107, 208-210
<sup>58</sup> Ni	MT=2 (MF=3, 4)	MT=51-54	MT=5, 102, 103, 107
<sup>63</sup> Cu	MT=2 (MF=3, 4)	-	MT=102
<sup>65</sup> Cu	MT=2 (MF=3, 4)	-	MT=102
<sup>155</sup> Gd	MT=2 (MF=3, 4)	MT=51-54	MT=102
<sup>157</sup> Gd	MT=2 (MF=3, 4)	MT=51-54	MT=102

Table 14: Available isotopes in URANOS and cross sections used, identifiers according to [99] and chapter 5.1.4.1.

URANOS provides a list of already predefined materials, which are combinations of elements described in section B.1.2. Tab. 15 summarizes all available compositions which are implemented as materials.

Table 15: List of preconfigured materials available in URANOS with their composition and density.

Material	Density	Description
Helium	0.125 kg/m <sup>3</sup>	<sup>3</sup> He enriched gas
<b>Boron</b>	2.34 g/cm <sup>3</sup>	97 % <sup>10</sup> B enriched
Boron natural	2.46 g/cm <sup>3</sup>	80.1 % <sup>10</sup> B, 19.9 % <sup>11</sup> B
Boron carbide	2.42 g/cm <sup>3</sup>	<sup>10</sup> B enriched B <sub>4</sub> C
Boron carbide	2.51 g/cm <sup>3</sup>	B <sub>4</sub> C with natural boron
Boron trifluoride	2.76 kg/m <sup>3</sup>	<sup>10</sup> B enriched BF <sub>3</sub> gas
Methane	0.656 kg/m <sup>3</sup>	CH <sub>4</sub> gas
Detector gas	1.8 kg/m <sup>3</sup>	ArCO <sub>2</sub> gas (70:30, 80:20)
Aluminum	2.66 g/cm <sup>3</sup>	
Aluminum oxide	3.94 g/cm <sup>3</sup>	Al <sub>2</sub> O <sub>3</sub>
Iron	7.87 g/cm <sup>3</sup>	
Steel (304L)	8.03 g/cm <sup>3</sup>	with 72 % <sup>56</sup> Fe, 16.34 % <sup>52</sup> Cr, 2.66 % <sup>53</sup> Cr, 9 % <sup>58</sup> Ni
Copper	8.94 g/cm <sup>3</sup>	
Salt	2.16 g/cm <sup>3</sup>	
Gadolinium oxide	7.41 g/cm <sup>3</sup>	Gd <sub>2</sub> O <sub>3</sub> with 14.8 % <sup>155</sup> Gd, 15.65 % <sup>157</sup> Gd
<b>Polyethylene</b>	0.95 g/cm <sup>3</sup>	HDPE, CH <sub>2</sub>
PE boronated	0.95 g/cm <sup>3</sup>	HDPE with 3 % natural boron
<b>Polyimide</b>	1.43 g/cm <sup>3</sup>	C <sub>22</sub> H <sub>10</sub> N <sub>2</sub> O <sub>5</sub>
Quartz	2.5 g/cm <sup>3</sup>	SiO <sub>2</sub>
<b>Stones</b>	1.43 g/cm <sup>3</sup>	75 % SiO <sub>2</sub> , 25 % Al <sub>2</sub> O <sub>3</sub>
<b>Water</b>	1.0 g/cm <sup>3</sup>	H <sub>2</sub> O
<b>Soil</b>	>1.43 g/cm <sup>3</sup>	50 % stones, (0-50) % water
<b>Air</b>	1.2 kg/m <sup>3</sup>	78 % N <sub>2</sub> , 21 % O <sub>2</sub> , 1 % Ar
Concrete	2.0 g/cm <sup>3</sup>	50 % stones, 10 % water
Cat litter	1.1 g/cm <sup>3</sup>	44 % H, 44 % O, 12 % Si
Asphalt pavement	2.58 g/cm <sup>3</sup>	14 % H, 50 % O, 11 % C, 25 % Si
Plants	>2.2 kg/m <sup>3</sup>	14 % H, 72 % O, 14 % C, plus air
Wood	0.5 g/cm <sup>3</sup>	like plants
Snow new	0.03 g/cm <sup>3</sup>	like water
Snow old	0.3 g/cm <sup>3</sup>	like water
Ice	0.85 g/cm <sup>3</sup>	like water

The parameters for (68), (69) and (70) in sec. 3.2 published in [66] are the following:

$$\begin{aligned}
 a_1(r_c) &= 12.9 + \frac{15.7}{1 + \exp\left(\frac{r_c - 5.62}{1.79}\right)}, \\
 a_2(r_c) &= 0.00706 + \frac{0.00057}{1 + \exp\left(\frac{r_c - 5.99}{1.94}\right)}, \\
 a_3(r_c) &= 0.975 - \frac{0.210}{1 + \exp\left(\frac{r_c - 0.99}{2.24}\right)}, \\
 a_4(r_c) &= 0.0084 + \frac{0.00441}{1 + \exp\left(\frac{r_c - 2.24}{2.66}\right)}, \\
 a_5(r_c) &= -0.00701 + \frac{0.0258}{1 + \exp\left(\frac{r_c - 10.9}{2.38}\right)}, \\
 a_9(r_c) &= 642 + \frac{189}{1 + \exp\left(\frac{r_c - 2.32}{0.897}\right)}, \\
 a_{10}(r_c) &= 0.00112 + \frac{0.000181}{1 + \exp\left(\frac{r_c - 8.84}{0.587}\right)}, \\
 a_{11}(r_c) &= 1.26 + \frac{0.958}{1 + \exp\left(\frac{r_c - 3.18}{1.47}\right)}, \\
 c_4(d) &= a_5(r_c) + \frac{0.000171d}{1 + 0.53 \exp(0.00136d)}, \\
 c_{12}(d) &= a_9(r_c) \exp(-a_{10}(r_c)d) + a_{11}(r_c) \exp(-0.0133d), \\
 g_3(w) &= -25.2 + \frac{2.73}{w + 0.0715}, \\
 g_5(w) &= 0.348 + 3.35w - 1.57w^2.
 \end{aligned} \tag{160}$$

In the original publication [66]  $g_3(w)$  has been denoted as a multiplication, but it is supposed to be a sum like presented above.

## B.1.5 | SIMULATION MODELS OF THE CRNS DETECTORS

### B.1.5.1 DETECTOR VOXEL MODELS

In sec. 8 the efficiency of commonly used detectors for CRNS has been calculated as well as their angular sensitivity. The evaluation was carried out for each face individually, see also Fig. 56. The rover model has been presented in the respective chapter, e.g. Fig. 54, therefore here the other two types are shown.

The CRS1000 consists of a 400 mm × 100 mm × 100 mm polyethylene casing with a wall thickness of 25 mm. It encloses a stainless steel proportional counter tube with a wall thickness of 2 mm filled with 1.5 bar of helium-3. For reasons of simplicity the tube has been modeled in rectangular shape and the gas pressure was scaled by  $\pi/4$ . The CRS1000/B consists of a cylindrical polyethylene casing of 25 mm width at a diameter of 104 mm and a length of 900 mm. It encloses an 850 mm long stainless steel proportional counter tube with a wall thickness of 2 mm filled with 0.5 bar of  $\text{BF}_3$ . For the material definitions see appendix B.1.3.

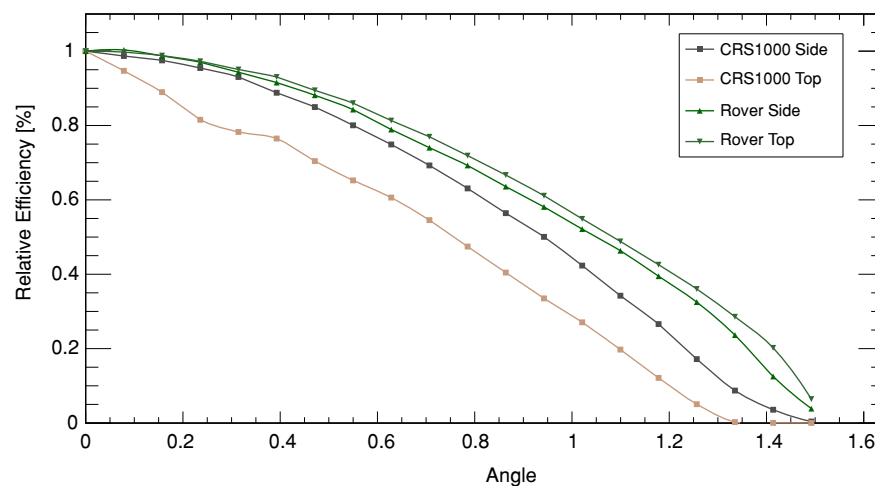


Figure 89: Cross sections of the detector models for the CRS1000 (bottom) and 1000/B (top) detectors with their proportional counter tube (1) in a stainless steel housing (2), surrounded by a polyethylene moderator. The grayscale pictures are the actual geometry input files.

### B.1.5.2 ANGULAR DEPENDENCE

The angular sensitivity component of the response function (140) is shown in Fig. 90, averaged over all energies and the detector face area. The angle  $\vartheta = 0$  is oriented perpendicular to the respective surface and efficiencies are normalized to  $g(\vartheta = 0) = 1$ .

Figure 90: Relative counting efficiency for some selected detector models and faces as a function of inclination angle of the incoming flux representing the angular term of (140). [KS2018]



The detectors show lowest sensitivity to neutrons from directions parallel to the surface, as for slant angles ( $\vartheta = \pi/2$  or  $90^\circ$ ) the probability of detection drops to zero. Highest sensitivity for all detectors is achieved for orthogonal incidence with  $\vartheta = 0$ . This result stresses the importance of accounting for neutron fluxes directly from atmospheric cosmic rays and directly from beneath the sensor. An analytical approximation for the angular distribution of the large faces can be given as:

$$g(\vartheta) = 1.24 - 0.254 \exp(1.087 \vartheta). \quad (161)$$

Yet, for the CRS1000 top face a linear model is sufficient. Like discussed above, the geometric arrangement of the moderator has a minor influence on the response function. For energies in the epithermal to fast regime the angular response does not change significantly.

### B.1.6 | SIMULATION OF THE NEUTRON SOURCE ROOM

A simplified version of the radiation environment of the neutron source within its room has been simulated by URANOS. The room, which is sketched in Fig. 91, consists of the following elements, see also the material compendium in appendix B.1.3: air with  $5 \text{ g/m}^3$  humidity, concrete floor, walls and ceiling, two aluminum tables with boronated rubber mats and vertical polyethylene absorbers covered by boronated rubber mats, one wooden table, a fused silica window, wooden and steal doors. The source itself consists of a large block of boronated and non-boronated polyethylene. Beamport A is open. At its inner center face, which is the moderator of the californium source, a moderated spectrum (??), based on simulations by U. Schmidt, is released in port direction into  $2\pi$ . A more detailed description of the simulations and the source buildup can also be found in [284].

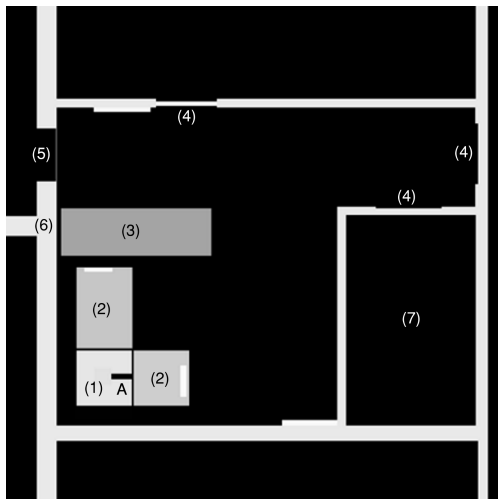


Figure 91: Setup for the source room simulation: (1) Moderated shielded source with spectrum (??) through beamport A, (2) aluminium tables with boron rubber mat covers and vertical absorbers, (3) wooden table, (4) doors, (5) window, (6) concrete wall and (7) isotope storage room.

The goal was to analyze whether an additional thermal shielding on the outside of the source buildup would reduce the background for measurements. The result of this simulation is, that covering the source by an additional absorber has no significant influence on the overall thermal neutron background. The reason can be easily identified in Fig. 92. The background, which can be measured for experimental setups on the tables (2), is not due to neutrons leaking out of the source, but rather originates from the fast neutron, which are scattered within the room and thermalize elsewhere. As the source partly consists of boronated polyethylene, there is no direct contribution from thermal neutrons coming from the source moderator, but instead from all other objects

in the room. In that case, the best background suppression can be achieved by placing the detector as far as possible from any large object. However, the example here is only for qualitative evaluation of the radiation background in the source room.

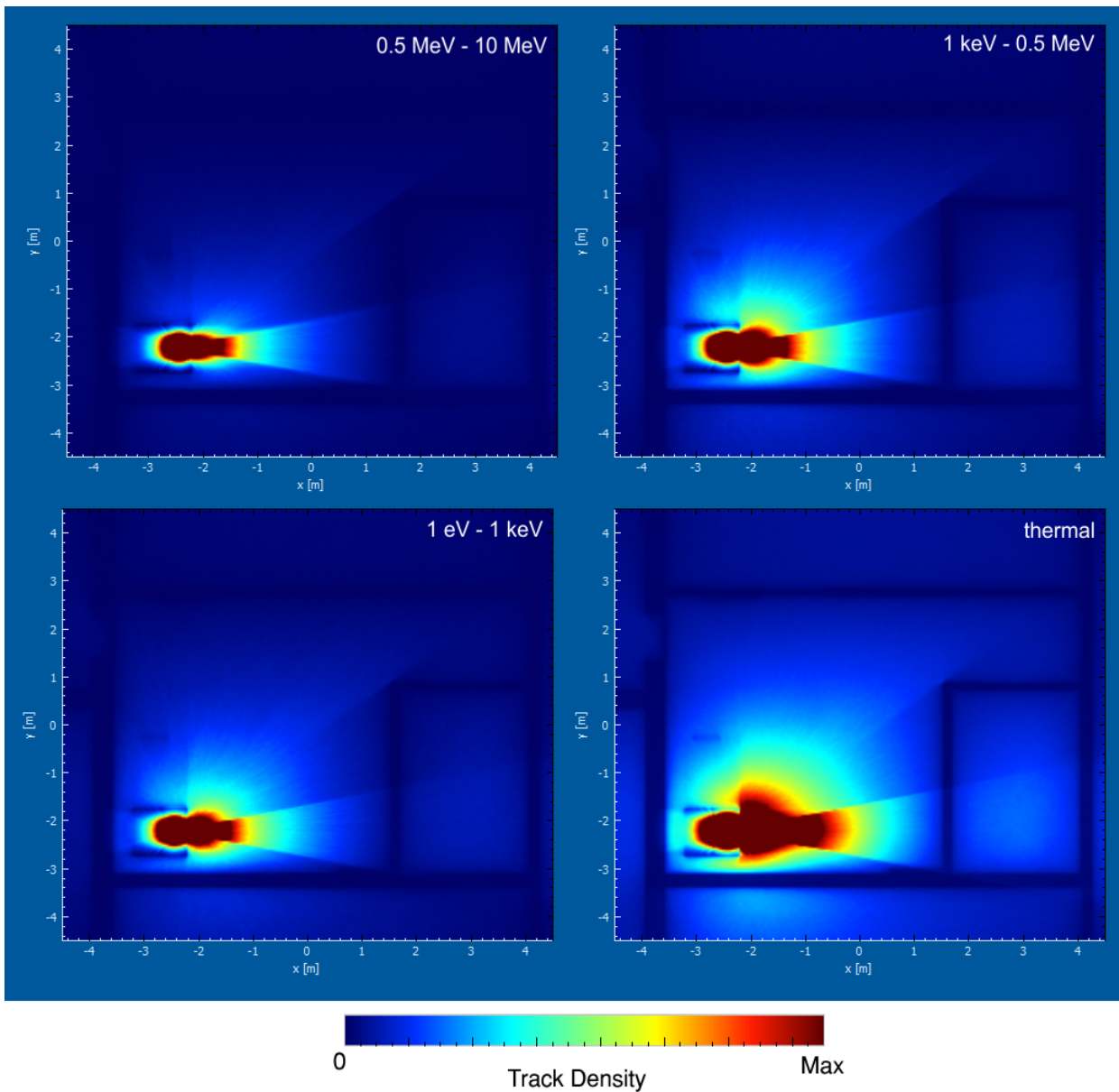


Figure 92: URANOS simulation of the radiation environment in the room of the neutron source with one beamport open for four different energy ranges (scaled relatively to the respective maximum). The source spectrum is modeled by a modified Westcott function (??). The track density is displayed only in air and integrated over the room height.



B.2.1 | MODELING THE FOOTPRINT

In sec. 9.2.3 the footprint weighting function has been introduced and characterized as a sum of exponential functions. This section describes more in detail the procedure to find the analytical relation (151) by the following steps: For all data sets the  $F_i$  coefficients of  $W_r$  and the intensity  $I_0$  were plotted as a function of soil moisture. Then, for each  $F_i$  an individual function with a minimal set of parameters was constructed. One result is exemplarily shown in Fig. 94 for  $h = 10 \text{ g/m}^3$ . Although some parameters have a physical meaning, in general it should be regarded as an empirical model to mathematically model the range distribution. Then the procedure was repeated for all air humidities and the functional dependency on that variable was studied. However, as previously mentioned, the scaling of the weighting function is not independent of the different water pools. Hence, only a multivariate fit in the  $\theta, h$ -space can cope with the problem. Such a plot with the correlated soil moisture and air humidity representation is exemplarily shown for the far-field terms in Fig. 96 for  $I_0$  and Fig. 97 for the parameters of the weighting function.

In order to validate the functional dependencies, all range distribution histograms were fitted by  $I_0 \cdot W_r$  (151). The fitted exponential functions, shown exemplarily in Fig. 93, agree well with the data from the transport modeling. As mentioned above, at around 50 m the analytical description starts to deviate from the data (right panel), which is especially visible for the top curve, that describes the practically not relevant case of 0 % soil moisture. For this reason the value of 50 m has been chosen as a delimiter for both regimes. Although the above described functional dependency of  $W_r$  has mainly been motivated from the far-field transport theory, the agreement in the near-field with the model data is also very good.

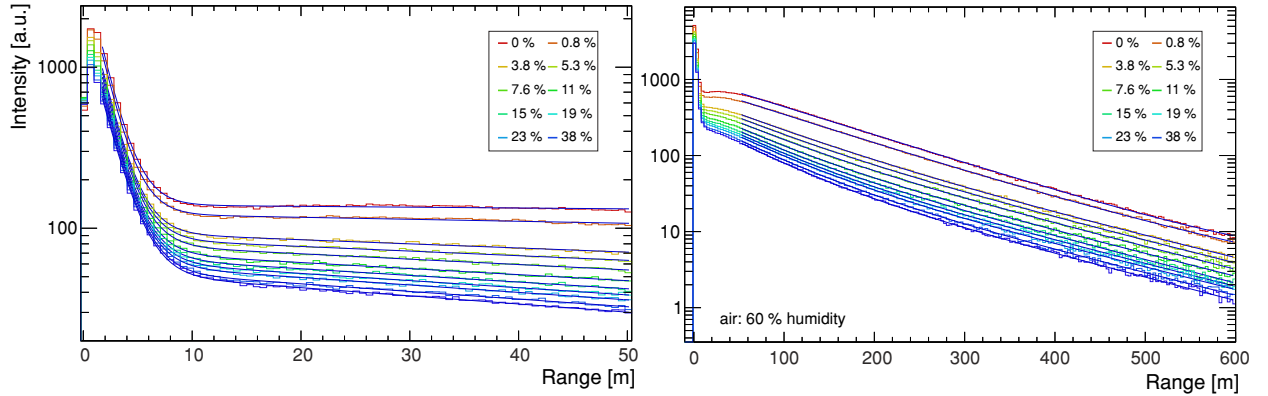


Figure 93: Range distribution histograms and fitted exponential functions according to (151) in the near-field (left) and the far-field regime (right).

For some dependencies a linear correlation between both observables can be assumed, but in most cases more complicated relations have to be used. In general, the goal was set to reduce the amount of free parameters as much as possible - although the fit could still be improved by adding polynomials of arbitrary order, the choice was to keep the congruency of the model and data integrals to yield an error not larger than 5 m on the quantile, especially  $Q_{86}$ .

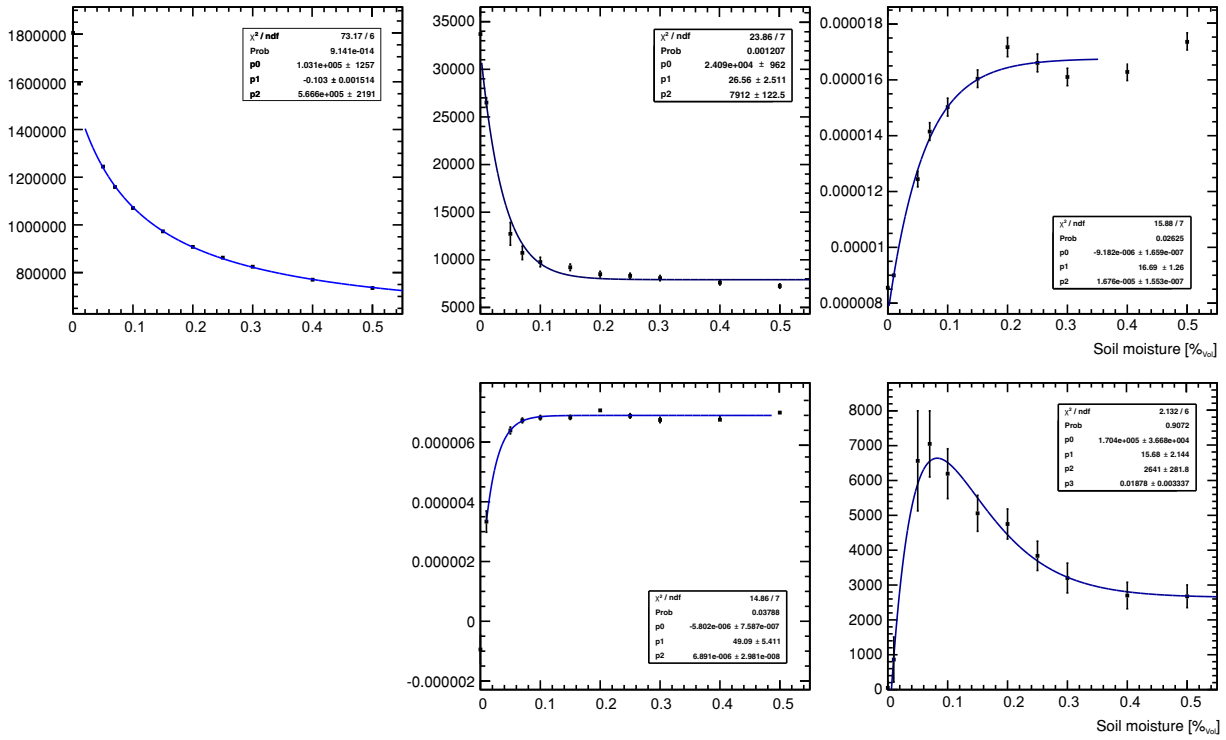


Figure 94: Parameters from the fits for the far-field term of (151) (black dots with statistical errors) for  $h = 10 \text{ g/m}^3$ . From the top left to the lower right panel:  $I_0$ ,  $F_5$ ,  $F_6$ ,  $F_7$  and  $F_8$ . To each set, plotted here depending on soil moisture, the functions (162) are fitted.

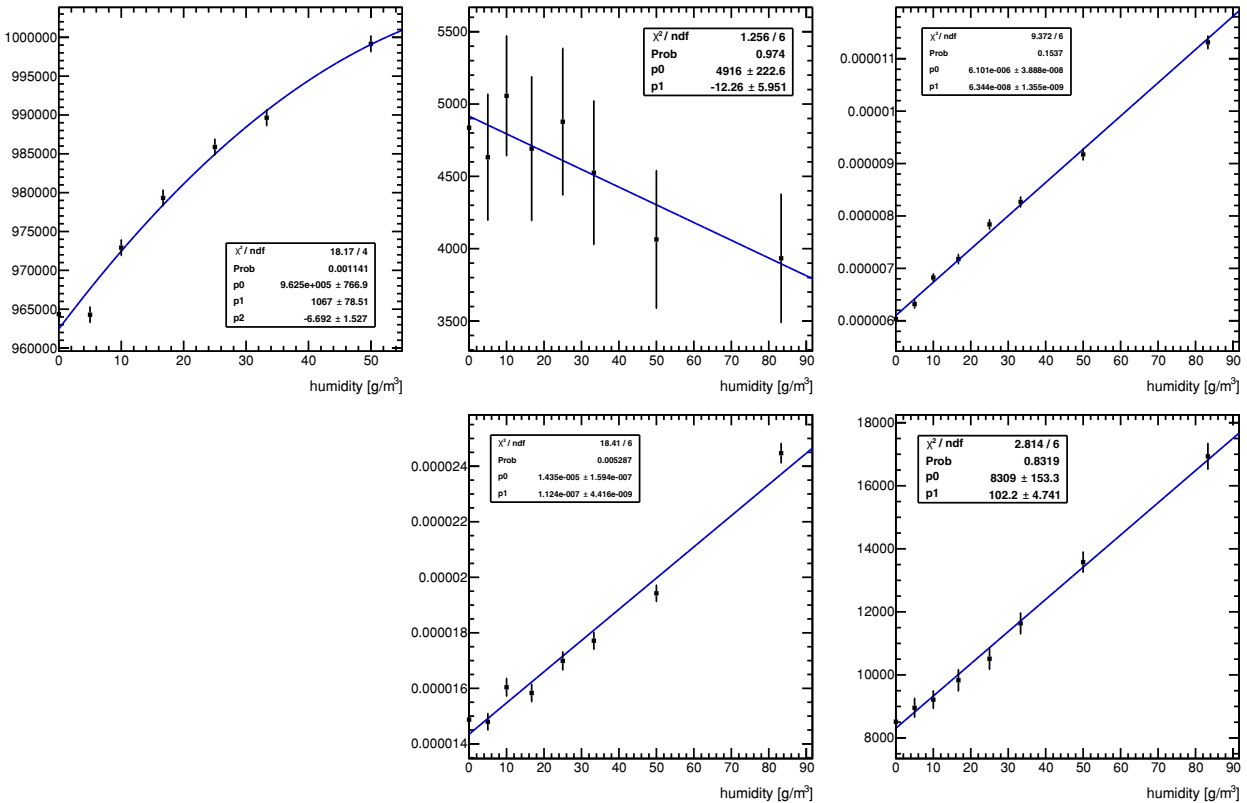


Figure 95: Parameters from the fits for the far-field term of (151) (black dots with statistical errors) for  $\theta = 11 \%$ . From the top left to the lower right panel:  $I_0$ ,  $F_5$ ,  $F_6$ ,  $F_7$  and  $F_8$ . To each set, plotted here depending on air humidity, the functions (162) are fitted.

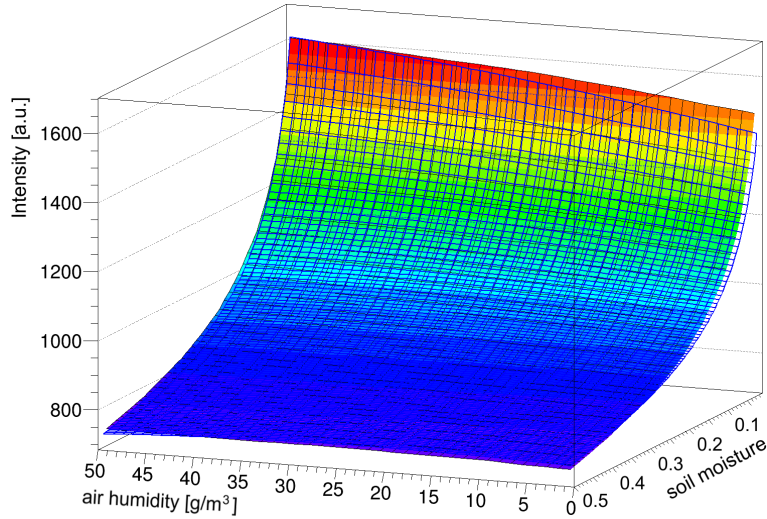


Figure 96: Fitting of the footprint parameters: Intensity  $I_0$  in (151) as a function of volumetric soil moisture fractions and air humidity. The colored hypersurface represents the interpolation of the results from the parameter fits of the range distribution function like in Fig. 94, the grid (blue) represents the modeled function.

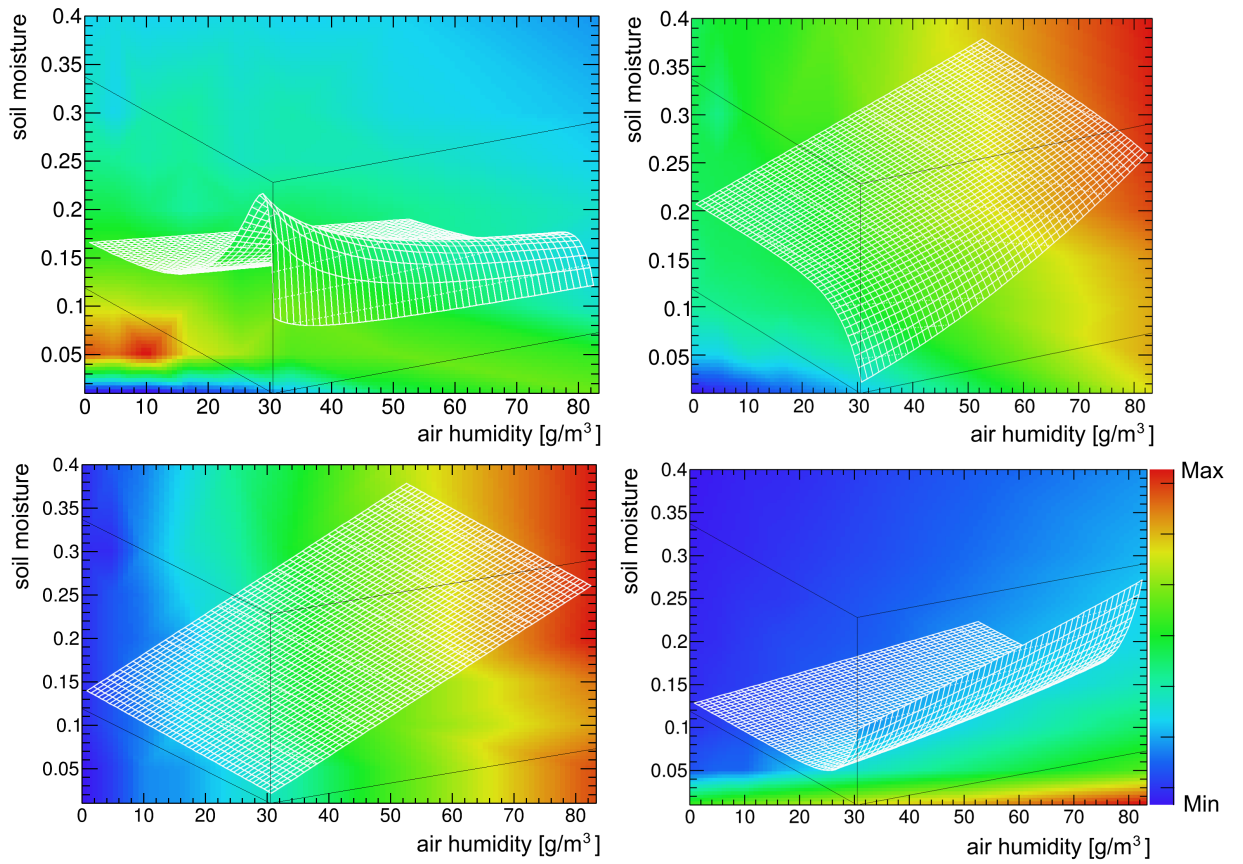
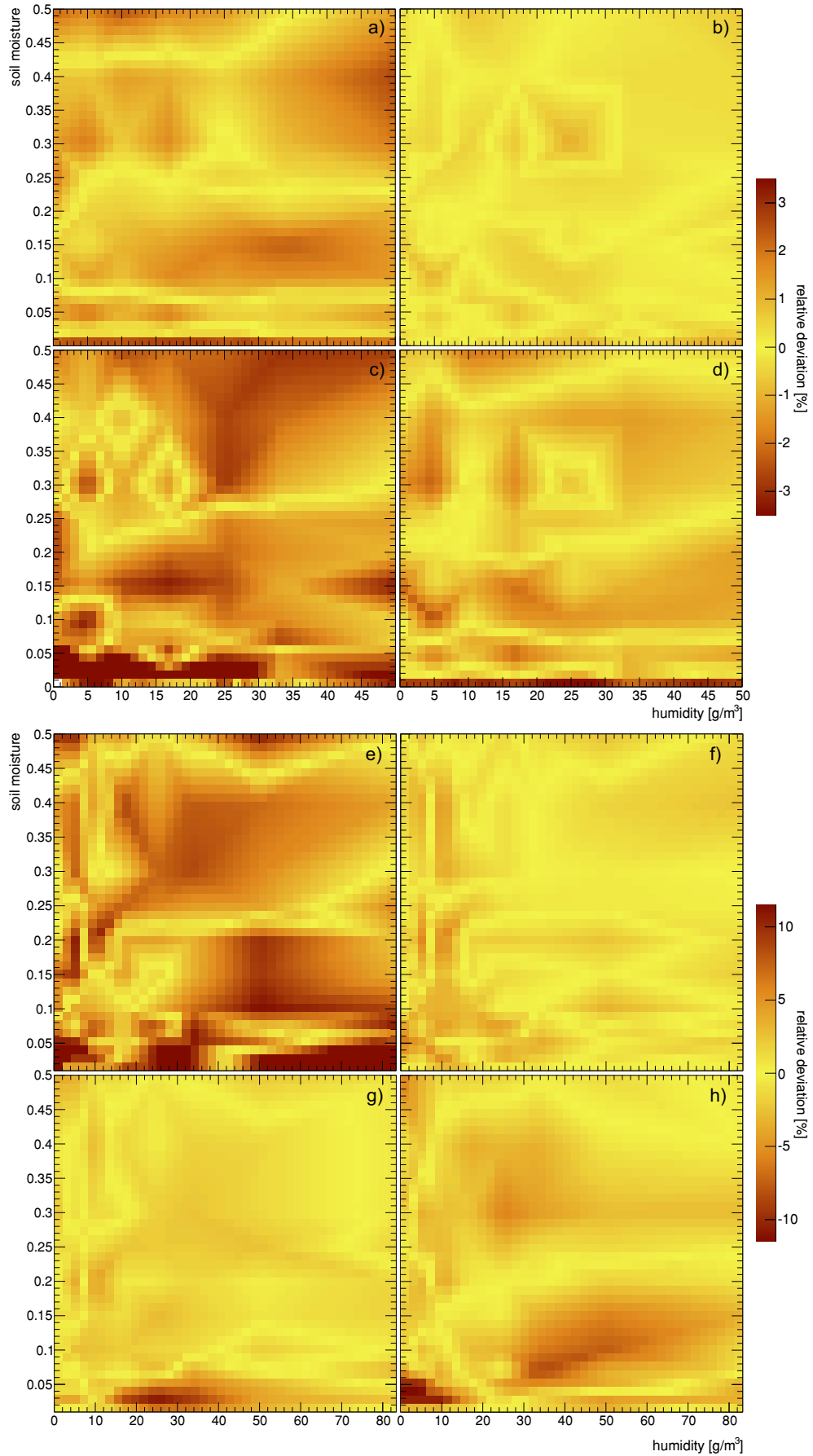


Figure 97: Fitting of the footprint parameters: from the top left to lower right panel as a function of volumetric soil moisture fractions and air humidity:  $F_5$ ,  $F_6$ ,  $F_7$  and  $F_8$ . The plots show an interpolation of the results from the parameter fits from (151) like in the previous Fig. 96 shown as a hypersurface. The rainbow scaled color code shows the relative differences necessary for constructing the functional dependencies. The grid (white) represents the finally modeled function (162).

Figure 98: Fitting of the footprint parameters: Relative deviation of the fitted parameters of function (151) to the values evaluated from the simulation, e.g. the colored hypersurface of Fig. 97, as a function of volumetric soil moisture fractions and air humidity. The four top panels a) to d) present the residuals of parameters  $F_1$  to  $F_4$  in (151), which model the near-field terms. Panels e) to h) present the residuals of parameters  $F_5$  to  $F_8$  in (151), which model the far-field terms. Deviations are mostly due to statistical variations.



The following expressions have been found for modeling the radial weighting function:

$$\begin{aligned}
F_0 &= p_0, \\
F_1 &= p_0 (1 + p_3 h) e^{-p_1 \theta} + p_2 (1 + p_5 h) - p_4 \theta, \\
F_2 &= \left( (p_4 h - p_0) e^{-\frac{p_1 \theta}{1 + p_5 \theta}} + p_2 \right) (1 + p_3 h), \\
F_3 &= p_0 (1 + p_3 h) e^{-p_1 \theta} + p_2 - p_4 \theta, \\
F_4 &= p_0 e^{-p_1 \theta} + p_2 - p_3 \theta + p_4 h, \\
F_5 &= p_0 \left( 0.02 - p_5^{-1} \frac{1}{h + p_5 + p_6 \theta} \right) (\theta - p_4) e^{-p_1 (\theta - p_4)} + p_2 (0.7 - p_3 h \theta), \\
F_6 &= p_0 (h + p_1) + p_2 \theta, \\
F_7 &= \left( p_0 (1 - p_6 h) e^{-p_1 \theta (1 - p_6 h)} + p_2 - p_5 \theta \right) (2 + p_3 h), \\
F_8 &= \left( (p_4 h - p_0) e^{-\frac{p_1 \theta}{1 + p_5 h + p_6 \theta}} + p_2 \right) (2 + p_3 h), \\
F_p &= p_0 / \left( p_1 - e^{-p / (1013 \text{ mbar})} \right).
\end{aligned} \tag{162}$$

with air pressure  $p$ , nondimensionalized air humidity  $h$  and volumetric soil moisture  $\theta$  and with the parameters<sup>[a]</sup>:

	$p_0$	$p_1$	$p_2$	$p_3$	$p_4$	$p_5$	$p_6$
$F_0$	3.7						
$F_1$	8734.92	17.176	11720	0.00978	7045	0.003632	
$F_2$	0.027925	5.0399	0.028544	0.002455	$6.851 \cdot 10^{-5}$	9.293	
$F_3$	247970	17.632	374655	0.00191	195725		
$F_4$	0.054818	15.9213	0.6373	0.0599	$5.425 \cdot 10^{-4}$		
$F_5$	-1383700	4.15586	5324.65	0.002377	0.015635	-0.13	1520.6
$F_6$	$6.03 \cdot 10^{-5}$	98.5	0.001046				
$F_7$	11747	41.66	4521	0.01998	0.006038	2534.36	0.004751
$F_8$	0.01543	10.0555	0.01807	0.0011	$8.08 \cdot 10^{-5}$	0.04052	20.242
$F_p$	0.4922	0.86					
$D_{86}$	8.321	0.14249	0.96655	0.01	20.0	0.0429	

Table 16: Numerical values for the parameters for the horizontal weighting function (162) in (151)

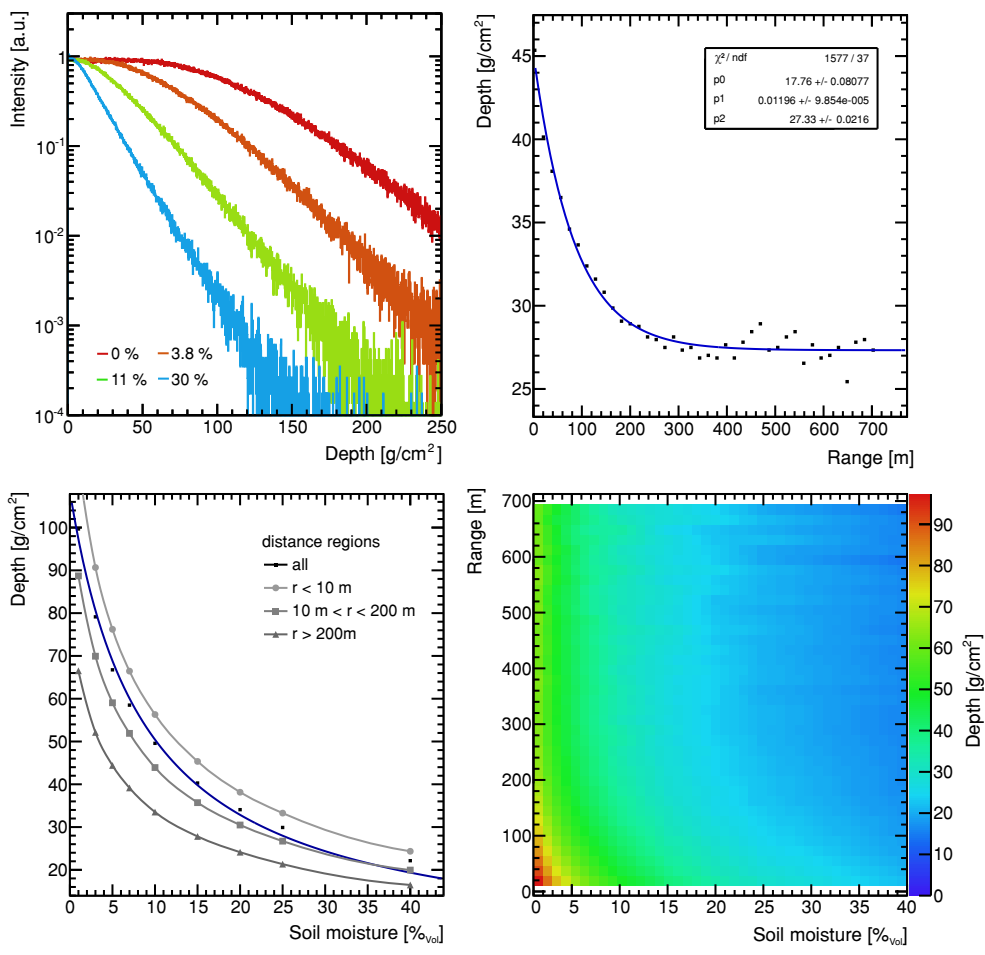
This function allows to describe the neutron transport problem for the footprint investigation analytically.

## B.2.2 | MODELING THE DEPTH DISTRIBUTION

In sec. 9.2.4 the depth penetration function has been introduced. In order to find a suitable parametrization, the procedure was similar to the footprint evaluation in sec. 9.2.3 and described in sec. B.2.1. For each setup the  $D_{86}$  quantiles were calculated additionally as a function of the impact distance to the sensor. Fig. 99 shows exemplarily such distributions additionally to Fig. 75. One can also see, that the maximum penetration depth (top left panel) is much different to the mean penetration. However, this value shall only be taken into account as a limit, not as a probe depth.

[a] It has to be noted, that a few constant numbers had to be inserted in the equations, like the 0.13 in  $F_5$ , in order to stabilize the multidimensional fit of TMinuit [285].

Figure 99: Penetration depth distribution characterization in the ground at a humidity of  $h = 10 \text{ g/m}^3$ . Top row: Scattering center distribution with only the maximum penetration depth scored (left) for different soil moistures and (right) penetration depth quantile  $D_{86}$  for 15% $_{\text{Vol}}$  as a function of impact distance with an exponential fit  $p_0 \exp(-p_1 r) + p_2$  (right). Bottom row: Depth quantile as a function of soil moisture for different impact distance regions (left) and penetration depth quantile  $D_{86}$  as a function of impact distance and soil moisture (right). The  $D_{86}$  distribution is fitted by (153) with the parameters from tab. 17.



	$p_0$	$p_1$	$p_2$	$p_3$ [1/m]	$p_4$ [m³/m³]	$p_5$ [m³/m³]
$D_{86}$	8.321	0.14249	0.96655	0.01	20.0	0.0429

Table 17: Parameters for the depth weighting function (153) using the scheme of (151)

### B.2.3 | UNCERTAINTY ANALYSIS OF THE CRNS TRANSPORT PROBLEM

In the simulated system containing soil, atmosphere, and a detector, uncertainties propagate non-linearly due to the variety of neutron interactions involved. As an indication of their total effect, uncertainties of the calculations were analyzed by means of the influence on the footprint radius  $R_{86}$ .

#### B.2.3.1 ERRORS ON CROSS SECTIONS

Table 18: Relative uncertainties of cross sections in % according to ENDF/B-VII.1 at thermal energy and 10 MeV.

Element	elastic		inel.	absorption		MT107
	$\Delta_{\sigma(\text{th})}$	$\Delta_{\sigma(10 \text{ MeV})}$	$\Delta_{\sigma(10 \text{ MeV})}$	$\Delta_{\sigma(\text{th})}$	$\Delta_{\sigma(10 \text{ MeV})}$	$\Delta_{\sigma(\text{MeV})}$
$^1\text{H}$	0.3	2.4	N/A	2.6	20	N/A
$^{12}\text{C}$	0.5	10	-	3	20	10
$^{14}\text{N}$	4	2	-	30	7.5	
$^{16}\text{O}$	2	4	-	10	-	10
$^{27}\text{Al}$	1.8	13	-	1.7	60	-
$^{28}\text{Si}$	1	8	30	20	40	25

Here exemplary uncertainties are given representative for specific energy ranges. Typically, errors on cross sections listed in the ENDF data base do not vary significantly in the elastic scattering region. Therefore, uncertainties in the thermal and the MeV regime are chosen.

### B.2.3.2 ERROR ESTIMATION ON THE FOOTPRINT RANGE

To estimate the influence of uncertainties in the cross sections, calculations have been carried out by modifying the cross section sets obtained from the data base. Here the results are presented for changes by one and two standard deviations.

moisture [% <sub>Vol</sub> ]	86 % quantile of range distribution [m]				
	base	+1 Δ CS	-1 Δ CS	+2 Δ CS	-2 Δ CS
2.3	223.6(2)	216.4	233.6	208.9	241.3
7	202.7(3)	195.7	209.6	189.8	215.2
30	166.3(3)	162.7	170.3	157.5	176.6

Table 19: Error estimation for  $h = 10 \text{ g/m}^3$ . Statistical errors on range quantiles are 0.3% of the value for 4% soil moisture and 0.7% otherwise.

moisture [% <sub>Vol</sub> ]	base [m]	rel. deviations to base range quantile [%]			
		+1 Δ CS	-1 Δ CS	+2 Δ CS	-2 Δ CS
2.3	223.6(2)	-3.2	4.5	-6.6	7.9
7	202.7(3)	-3.4	3.4	-6.3	6.2
30	166.3(3)	-2.1	2.4	-5.3	6.2

Table 20: Error estimation for  $h = 10 \text{ g/m}^3$ . Relative deviations on range quantiles for varying cross section. Errors on deviations are 0.4% for 4% soil moisture and 0.7% otherwise.

### B.2.3.3 UNCERTAINTIES INDUCED BY THE CHOICE OF THE ENERGY SENSITIVITY

The evaluation of the footprint was carried out mainly using the canonical limits for the energy sensitivity of 100 eV to 10 keV, which represents the mean energy for neutrons slowing down from evaporation to thermal energies. As the prior analysis showed the travel distance of neutrons in the soil-air interface depends significantly on the amount of environmental water. However, the average relevant transport range barely depends on the choice of the sensitive energy range. Fig. 100 shows the lethargy-averaged mean range of neutrons recorded by a single detector entity exemplarily for three different soil moisture conditions.

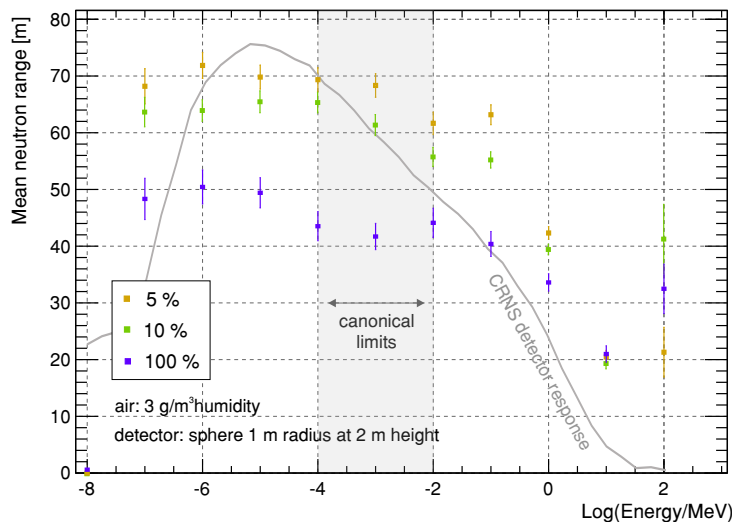


Figure 100: Range evaluation using a spherical detector with 1 m radius in a 600 m domain and  $950 \cdot 10^6$  neutrons for three different soil moisture conditions. As a comparison the simulated detector response is plotted together with the energy threshold as chosen for the footprint evaluation.

Within the water-sensitive domain of 1 eV to 0.1 MeV the transport distance stays remarkably constant as a function of neutron energy. Within this regime one obtains a maximum change of 10 %, however, taking into account to the actual detector sensitivity, this variation averages out. Especially the chosen threshold energies center around the inflection point of this plateau. Therefore, considering a thermally shielded detector which does not record neutrons below 0.5 eV, one can assume an error of 2 % on the footprint attributed to the choice of the used detection thresholds.

#### B.2.3.4 UNCERTAINTIES INDUCED BY THE CHOICE OF THE INPUT SPECTRUM

In a test case of 13 % soil moisture the influence of errors of the input model on the footprint was investigated. Assuming high energetic neutrons to impinge perpendicular to the surface, instead of the sampling from the distribution given by Nesterenok, leads to a  $(2.3 \pm 0.2)$  % decrement of the  $Q_{86}$  radius. Assuming a perpendicular incidence for low energetic neutrons instead of an isotropic distribution leads to a  $(3.1 \pm 0.2)$  % decrement. Furthermore, modifications of the energy dependent function  $Cf(E)$  generating the source from the Sato spectrum have been studied. Overcompensation, i.e. increasing  $Cf(E)$ , by 50 % leads to  $(7.1 \pm 0.2)$  % increase of the footprint radius, whereas underestimation by 50 % leads to a  $(5.0 \pm 0.2)$  % decrease. Taking the unmodified Sato pure water spectrum as a source reduces the footprint radius by  $(9.2 \pm 0.3)$  %.

input model	86 % quantile of range distribution			
	$r_{Q86}$ [m]	$\Delta_{r(Q86)}$ [m]	rel. [%]	$\Delta_{rel.}$ [%]
Low energy: all $0^\circ$	196.4	0.4	-3.1	0.2
High energy: all $0^\circ$	198.0	0.4	-2.3	0.2
Corr x 0	184.1	0.4	-9.2	0.3
Corr x 0.5	192.6	0.4	-5.2	0.2
Corr x 0.8	198.3	0.4	-2.2	0.2
Corr x 1.5	217.1	0.4	7.1	0.2
Corr x 2.5	240.9	0.4	18.9	0.3

Table 21: Error estimation for  $h = 10 \text{ g/m}^3$  and 10 % soil moisture. Relative deviations on range quantiles for varying input model. The following assumptions were evaluated: all low/high energetic neutrons are released with an angle of  $0^\circ$  instead of the distribution used and the correction function, which generates the incoming-only function from the total flux spectrum (6.7), was changed by larger factors.

#### 3.5 UNCERTAINTY ANALYSIS SUMMARIZED

Variations of cross sections by their standard deviation, given in the ENDF data base, lead to changes of  $R_{86}$  by 4 %, 3 %, and 2 % for  $\theta = 3$  %, 10 % and 40 %, respectively. The effect of elastic scattering dominates the budget by approximately 70 %. The errors of the cross sections can be considered as systematic for neutron transport simulations in general. The impact of different source spectra as model input in a test case with 10 % soil moisture and  $5 \text{ g/m}^3$  air humidity was also analyzed. As explained in sec. 9.1.1 the incident spectrum was generated over water by subtracting the soil response from the original mixed spectrum. Variations of this soil response spectrum by 20 % alters  $R_{86}$  by 2.5 %. If the emission angles of source neutrons were not set according to their angular distributions, but chosen perpendicular to the surface, the change of the footprint radius would be 2.5 % applied to high energetic neutrons only and 3.0 % also including sub-MeV neutrons. Compared to the uncertainties involved in the calculations the impact of other source spectrum models can be much higher. The integration of the counted particles further leads to statistical uncertainties on  $R_{86}$  in the order of 0.2 % for  $10^7$  neutrons. For the final fit model Fig. 98 shows the residuals of the fit function (162) to the base data set. Except for extremely low environmental water conditions there are no significant or systematic deviations to the underlying data. Most of the variations in Fig. 98 are due to statistical errors. For example the overall integral of the near-field terms of the weighting function (151) leads to an error in the order of 0.5 %.



## B.2.4 | THE ROAD CORRECTION FUNCTION

The function, which has been developed with M. Schrön for correcting the road bias presented in sec. 9.3.5, is

$$C_{\text{Corr}}(\theta_{\text{field}}, \theta_{\text{road}}, w, x_c) = 1 + c_0 \left(1 - c_1 \frac{w}{\text{m}}\right) (\theta_{\text{field}} - \theta_{\text{road}}) \frac{c_2 - c_3 \theta_{\text{road}}}{\theta_{\text{field}} - c_4 \theta_{\text{road}} + c_5} \cdot \left( c_6 \exp\left(-c_7 \left(\frac{w}{\text{m}}\right)^{-c_8} \left(\frac{x_c}{\text{m}}\right)^4\right) + (1 - c_6) \exp\left(-c_9 \frac{x_c}{\text{m}}\right) \right). \quad (163)$$

The data from the simulation were fitted by (163). The resulting parameters are summarized in tab. 22:

$c_0$	$c_1$	$c_2$ [ $\text{m}^3/\text{m}^3$ ]	$c_3$	$c_4$	$c_5$ [ $\text{m}^3/\text{m}^3$ ]	$c_6$	$c_7$	$c_8$	$c_9$
0.42	0.50	1.11	4.11	1.78	0.30	0.94	1.10	2.70	0.01

Table 22: Numerical values for the parameters of the road bias correction function (163).

The function describes roads of widths below approximately 7 m, as for wider roads the neutron density saturates around the center at a peak value. Furthermore, this function is limited to effective values for  $\theta_{\text{road}}$  between 1 % and 16 % and requires a prior knowledge about the field moisture conditions. A more detailed analysis is presented in [SK2018].

In collaboration with the Helmholtz Centre for Environmental Research - UFZ, Leipzig, and especially M. Schrön, a graphical user interface (GUI) for URANOS has been developed, which specifically targets the needs of environmental sciences. URANOSGUI allows to run the Monte Carlo with the full feature list described in sec. 6 except for the readout simulation for gaseous detector. It enables researchers to carry out neutron transport simulations without the need of configuring the setup by text files<sup>[b]</sup>, which is the usual modus operandi for the codes mentioned in sec. 5.2. It especially does not require profound knowledge of the internal software buildup, as the relevant features and settings are all accessible from the graphical frontend. Instead of drop-down menus or child windows it uses a tabbed document interface, which is functionally split into two parts horizontally partitioned by the golden ratio. The left side functionally controls the program, its general settings and problem-related configurations. The right side tabs provides a direct insight into the ongoing computation. It shows the actual neutron density and track distribution, interaction range and depth and detector scoring results. The top bar represents the dashboard for starting and stopping the simulation as well as exporting the results. It also shows the expected time to accomplish the actual job. A simulation, like presented in the following screenshots of the UFZ site Fig. 101 to Fig. 104, is carried out by creating a layer structure, setting vertical positions and defining a ground layer, a source layer and a detector layer for scoring. The GUI then automatically loads *n.png* or *n.dat* files, with *n* being the layer number, placed in the configured work directory. According to the pixel or ASCII matrix voxels are extruded based on the predefined material codes of sec. B.1.3.

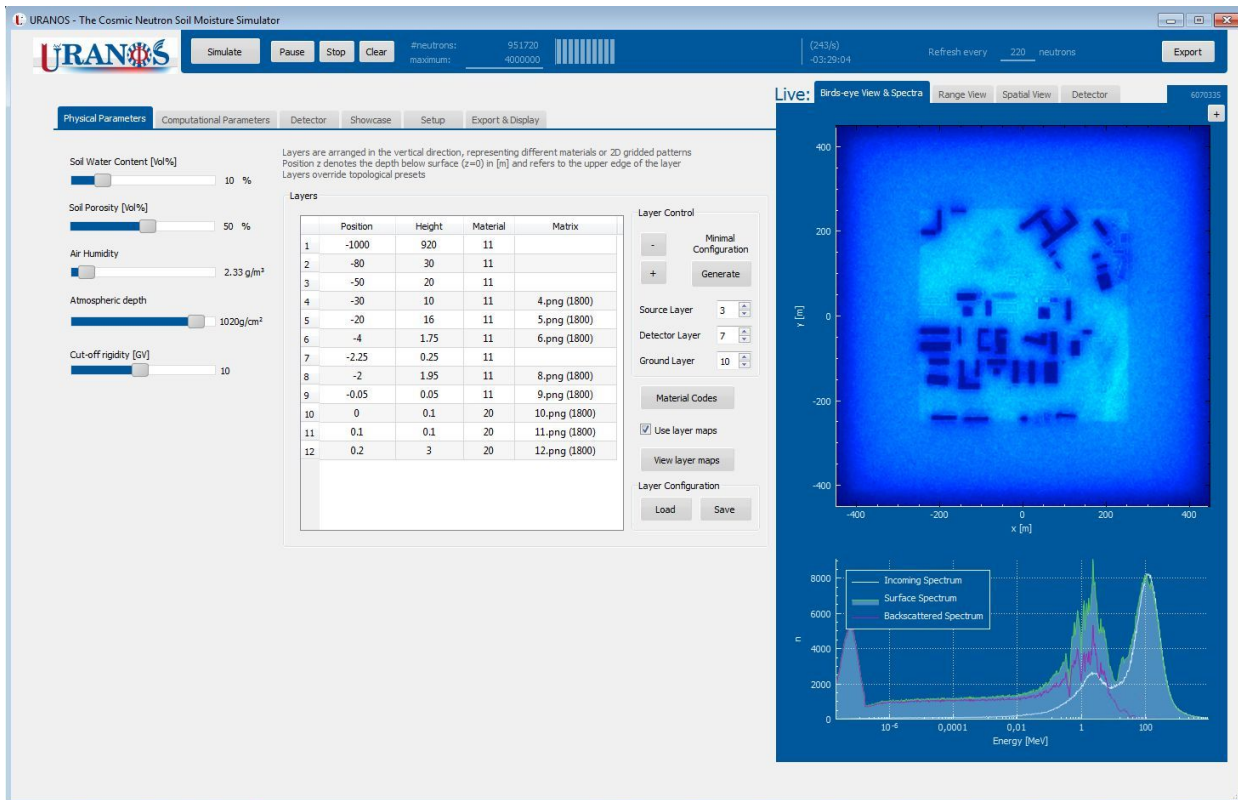


Figure 101: URANOS GUI main tabs: Setup for the layer arrangement for the vertical geometry and environmental parameters (left) and birds-eye view with the above-ground neutron spectrum (right).

[b] It also offers for advanced users a command line option to be configured and run by steering files, which also provide access to features not available in the GUI.

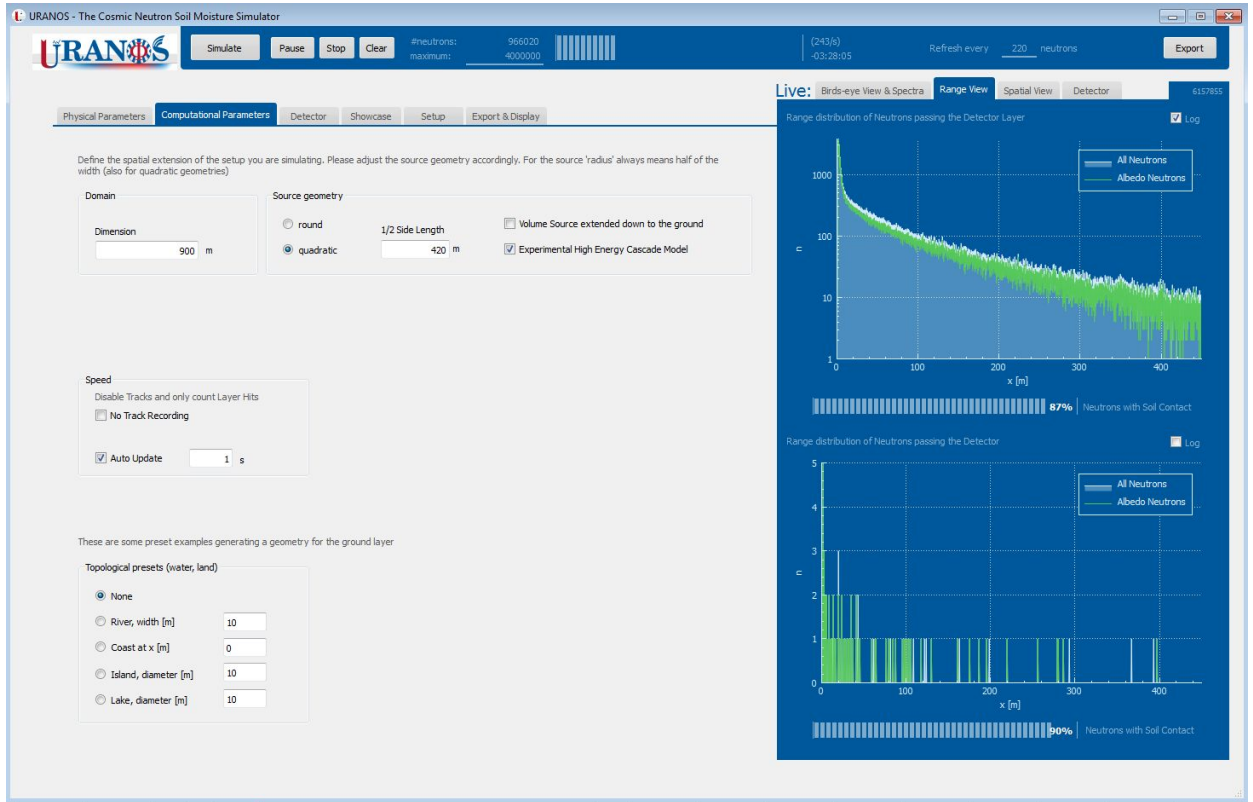


Figure 102: URANOS GUI main tabs: Setup for the general domain geometry and computation (left) and live view for the range distribution in the detector layer and the virtual detector (right).

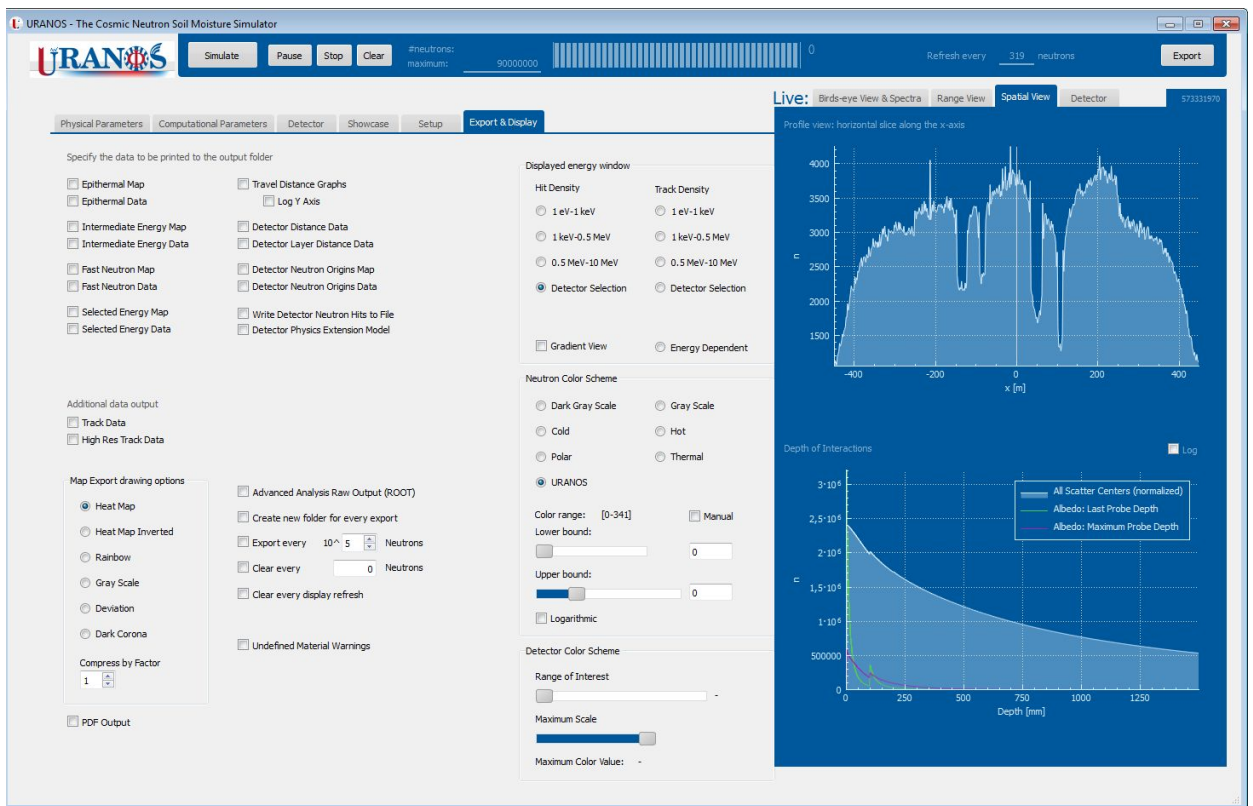


Figure 103: URANOS GUI main tabs: Export options and configurations of the live-view display (left) and spatial neutron distributions (right). The top panel shows the horizontal neutron density in the detector layer by cut view through the center of the domain and the bottom panel show the vertical interaction depth distribution in the ground.

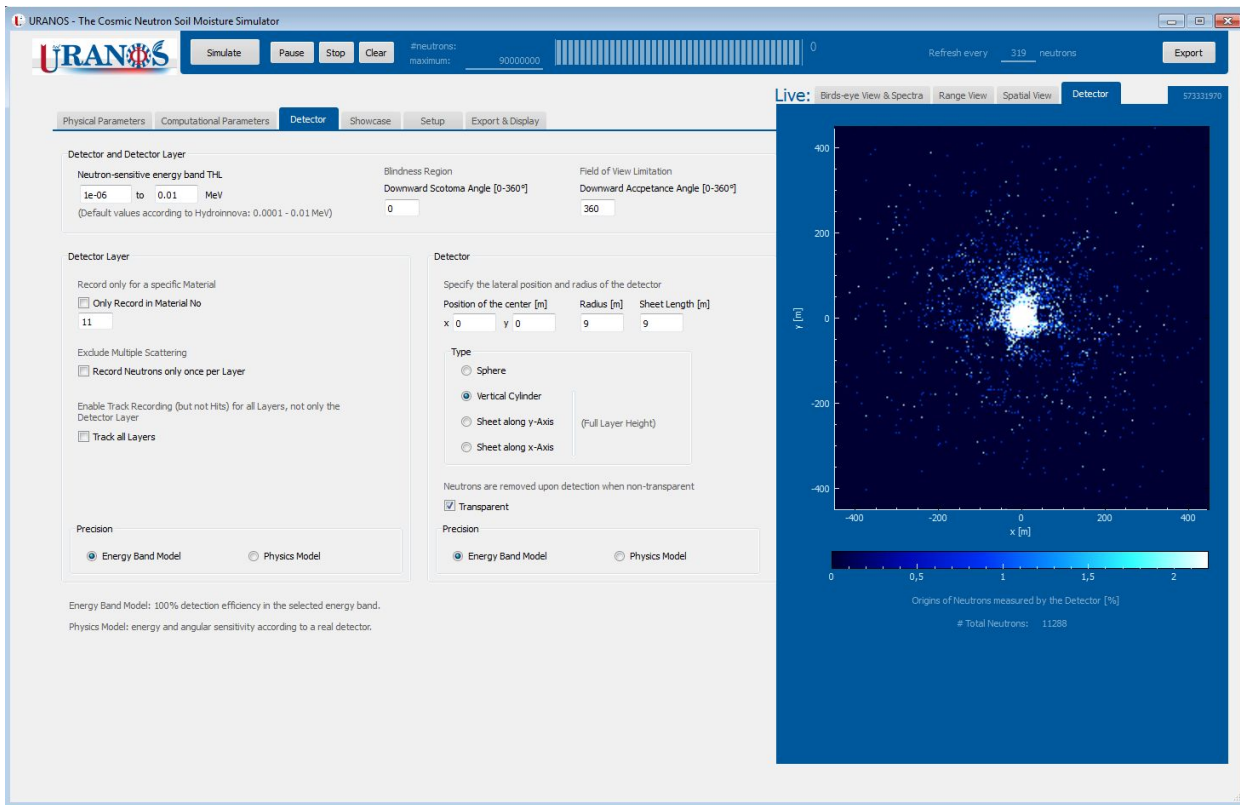


Figure 104: URANOS GUI main tabs: Setup for the scoring of the detector and detector layer (left) and distribution of neutron origins recorded by the virtual detector (right).

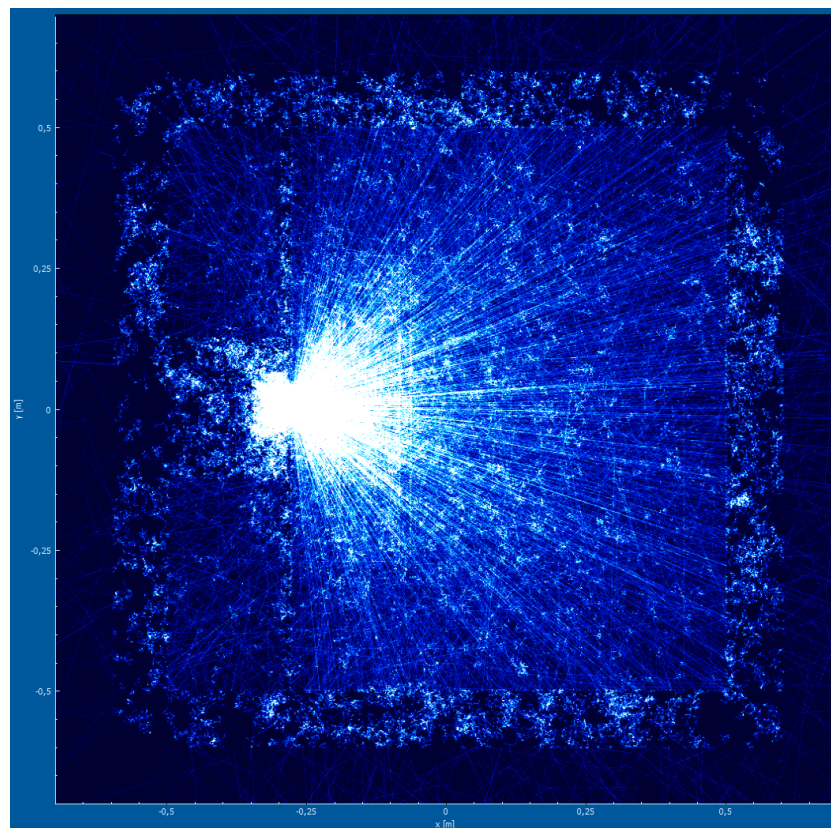


Figure 105: URANOS GUI high resolution track view with histories of thermal neutrons integrated over 1 s: Example of the simulation of a thermal neutron source inside a polyethylene detector test box.

## ACKNOWLEDGEMENTS

---

This work could not have been realized without the financial support during many years of research and experiments. The largest part of the funding has been provided by the Bundesministerium für Bildung und Forschung (BMBF) in the frame of the project „Neutron Detectors for the MIEZE method“. Further contributions came from the Physikalisches Institut, Heidelberg University, from the Deutsche Forschungsgemeinschaft (DFG), from the Helmholtz Centre for Environmental Research-UFZ, Leipzig. Beam times at large-scale research facilities were additionally supported by the Technical University Munich and the Institute of Nuclear Chemistry of the Mainz University. Part of the measurements were performed at the single crystal diffractometer, which is jointly operated by the RWTH Aachen University Institute of Crystallography and the Jülich Centre for Neutron Science (JCNS) as well as the RESEDA Spin Echo spectrometer, operated by the Technical University Munich, both located at the Heinz Maier-Leibnitz Zentrum (MLZ) in Garching.

Furthermost I want to thank my collaborator Martin Schrön at the UFZ, Leipzig: six joint papers and more to come, numerous conferences and approximately 4700 mutual emails in total within approximately six years (which makes a remarkable 2.5 emails per day, including the non-stop weekends) speak by itself.

I am grateful for having nice, supportive and sometimes critical colleagues around me at the Physikalisches Institut: Fabian Allmendinger, Matthias Janke, Peter Augenstein, Jannis Weimar, Christoph Roick, Manuel Fohler, Peter Vivell, Lukas Raffelt, Dirk Wiedner, Gerd Modzel, Max Lamparth, Carmen Ziener, Christian Färber, Martin Klein and Maarten DeKieviet.

Among my students I especially want to acknowledge Michael Liebig, Boris Rivkin, Jan Hammerich and Fabian Schmidt for the good teamwork in the office and the laboratory. Many thanks also go to the excellent team of the electronics and mechanics workshop of the Physikalisches Institut as well as for the technical support of Markus Henske. At the UFZ my thanks go to Steffen Zacharias and Peter Dietrich.

Also I want to thank the meanwhile numerous scientists in team of the RESEDA and the MIRA instrument at the FRM II: Wolfgang Häußler, Christian Franz, Franz Haslbeck, Olaf Soltwedel, Steffen Säubert, Stefan Söllradl, Nicolas Martin, Thorsten Schröder, Tobias Weber and Robert Georgii along with Martin Meven, instrument scientist at HEiDi, and Malgorzata Makowska, instrument scientist at NECTAR.

Honorable mentions for my beam times at the TRIGA reactor: Christian Stieghorst.

This acknowledgment should not close without a special mention to my international collaboration partners in Cosmic-Ray Neutron Sensing: Marek Zreda, Darin Desilets, Paul Schattan and Tatsuhiko Sato.

Special thanks go to Ernst Peter Fischer, author and science historian, for his inspiring lectures and his contributions in my seminar „The most important mistakes in physics' history“.

Last, but not least, my supervisor Ulrich Schmidt, whom I would like to thank with the following poem:

### **Eternal**

I am in the corridor of days enclosed  
and burdened even by the skies.  
I look into centuries, but live in minutes  
waiting for the Saturday of Saturdays.

The end of troubles in my fate,  
blind wanderings of the soul.  
O day, come, deign me sight  
with all bizarre to be known.

I will get another soul  
with all the worries vault'd.  
I will bless the golden road  
to the Sun from the soiled.

And he, who walked by my paths  
in thunder and meek silence,  
who was cruel to my pleasures  
and merciful to my flaws,

who taught to fight and to bear  
and of all the ancient wisdom profound,  
will lower the staff, turn around,  
and simply say: We are here.

Nikolay S. GUMILËV

translation from Гумилёв, Вечное (1912),  
with special thanks to Джетъ - Антология (2007).



Vente, gresle, gelle,  
j'ay mon pain cuit.

François VILLON